



# ATLAS NOTE

April 1, 2011



## SUSY searches with dileptons and high missing transverse momentum.

P. Bechtle<sup>7</sup>, M. Boehler<sup>7</sup>, X. Chen<sup>9</sup>, C. Clement<sup>11</sup>, W. Ehrenfeld<sup>7</sup>, J. Firmino da Costa<sup>7</sup>, S. T. French<sup>16</sup>, J. A. Frost<sup>16</sup>, M-H. Genest<sup>13</sup>, C. Giuliani<sup>14,8</sup>, B. K. Gjelsten<sup>2</sup>, E. Gramstad<sup>2</sup>, D. Harper<sup>1</sup>, S. Hillert<sup>11,20</sup>, S. Jin<sup>22</sup>, T. Lari<sup>14</sup>, S.-C. Lee<sup>4</sup>, F. Legger<sup>13</sup>, C. G. Lester<sup>16</sup>, J. Lundberg<sup>11</sup>, M. Lungwitz<sup>12</sup>, B. Meirose<sup>18</sup>, B. Mellado<sup>9</sup>, T. Mueller<sup>13</sup>, F. Ould-Saada<sup>2</sup>, H. Okawa<sup>3</sup>, Y. Pan<sup>9</sup>, N. Panikashvili<sup>1</sup>, M. A. Parker<sup>16</sup>, S. Pataraia<sup>9</sup>, M. Pedersen<sup>2</sup>, G. Polesello<sup>17</sup>, J. Qian<sup>1</sup>, T.C. Rave<sup>19</sup>, T. Sarangi<sup>9</sup>, A. Taffard<sup>3</sup>, B. Toggerson<sup>3</sup>, J. P. Torres<sup>9</sup>, C. Troncon<sup>14</sup>, F. C. Ungaro<sup>14,8</sup>, M. Uslenghi<sup>15,17</sup>, S.-M. Wang<sup>4</sup>, Z. Weng<sup>4,6</sup>, D. Whiteson<sup>3</sup>, S. L. Wu<sup>9</sup>, Z. Yang<sup>11</sup>, Z. Zhan<sup>21</sup>, X.Zhang<sup>21</sup>, J. Zhong<sup>4,5</sup>, and N. Zhou<sup>3</sup>

<sup>4</sup>Academia Sinica, Taipei

<sup>7</sup>DESY

<sup>14</sup>INFN, Sezione di Milano

<sup>15</sup>INFN, Sezione di Pavia

<sup>22</sup>Institute of High Energy Physics

<sup>13</sup>LMU München

<sup>18</sup>Lund University

<sup>5</sup>Nanjing University

<sup>21</sup>Shandong University

<sup>11</sup>Stockholm University

<sup>6</sup>Sun Yat-sen University

<sup>20</sup>University of Bonn

<sup>3</sup>University of California, Irvine

<sup>16</sup>University of Cambridge

<sup>19</sup>University of Freiburg

<sup>12</sup>University of Mainz

<sup>1</sup>University of Michigan

<sup>8</sup>Universita' degli studi di Milano, Dipartimento di Fisica

<sup>17</sup>Universita' degli studi di Pavia, Dipartimento di Fisica nucleare e teorica

<sup>2</sup>University of Oslo

<sup>9</sup>University of Wisconsin

## **Abstract**

This note contains supporting material for SUSY searches with dilepton +  $E_T^{\text{miss}}$  final states note.

A search for R-parity conserving supersymmetry using the ATLAS detector is described. Two lepton events with high missing transverse momentum are studied. Results are based on data collected with the ATLAS detector in 2010, corresponding to  $35\text{pb}^{-1}$  of integrated luminosity.

# Contents

<b>1</b>	<b>Introduction</b>	<b>4</b>
1.1	MSSM and mSUGRA Test Points and Grids . . . . .	5
1.1.1	mSUGRA . . . . .	5
1.1.2	MSSM Models . . . . .	6
<b>2</b>	<b>Analysis Overview</b>	<b>7</b>
2.1	Signal Regions . . . . .	7
2.2	Background Estimation Techniques . . . . .	8
2.2.1	Fake Rate Determination . . . . .	9
2.2.2	Cosmics contamination . . . . .	9
2.2.3	$Z/\gamma \rightarrow ll + \text{jets}$ Background Determination . . . . .	9
2.2.4	Fully-leptonic $t\bar{t}$ Background Determination . . . . .	9
2.3	Interpretation of Results . . . . .	10
<b>3</b>	<b>Data and Monte Carlo Samples</b>	<b>10</b>
3.1	Data Sets . . . . .	10
3.2	Monte Carlo Samples . . . . .	11
<b>4</b>	<b>Object Definitions</b>	<b>14</b>
<b>5</b>	<b>Systematic Uncertainties</b>	<b>15</b>
<b>6</b>	<b>Trigger and Event Selection</b>	<b>16</b>
6.1	Trigger . . . . .	16
6.2	Pile-up re-weighting . . . . .	17
6.3	Event Selection . . . . .	19
6.3.1	Pre-selection . . . . .	19
6.3.2	Selection . . . . .	19
<b>7</b>	<b>Background Determination</b>	<b>36</b>
7.1	Summary . . . . .	36
7.2	Data Driven Fake Background estimation: Methods . . . . .	37
7.2.1	Matrix Method : Di-Electron channel . . . . .	38
7.2.2	Fake Rate . . . . .	38
7.2.3	Signal Efficiency . . . . .	38
7.2.4	Uncertainty Estimation . . . . .	38
7.2.5	Collision Data Validation . . . . .	42
7.2.6	$\mu\mu$ channel . . . . .	42
7.2.7	Simplified Matrix Method . . . . .	42
7.2.8	Fake rate . . . . .	43
7.2.9	Signal Efficiency . . . . .	45
7.2.10	Uncertainty estimation . . . . .	45
7.2.11	$e\mu$ channel . . . . .	45
7.2.12	Validation with Low Pt Collision Data . . . . .	46
7.2.13	High Pt Collision Data . . . . .	46
7.3	Data Driven Fake Background estimation: Results . . . . .	46
7.3.1	Opposite Sign Di-Electron Channel . . . . .	46

7.3.2	Same Sign Di-Electron Channel . . . . .	47
7.3.3	Opposite Sign Di-Muon Channel . . . . .	47
7.3.4	Same Sign Di-Muon Channel . . . . .	48
7.3.5	Opposite Sign Electron-Muon Channel . . . . .	48
7.3.6	Same Sign Electron-Muon Channel . . . . .	48
7.4	$t\bar{t}$ background in SS due to charge flip . . . . .	48
7.5	Cosmics Contamination . . . . .	50
7.6	$t\bar{t}$ background . . . . .	53
7.7	Z+jets background . . . . .	58
<b>8</b>	<b>Results and Interpretation</b>	<b>61</b>
8.1	Same-Sign Analysis Results . . . . .	61
8.1.1	Expected and Observed Limits . . . . .	61
8.2	Opposite-Sign Analysis Results . . . . .	65
8.2.1	Expected and Observed Limits . . . . .	66
8.3	Flavour Subtraction Results . . . . .	68
8.3.1	Summary . . . . .	68
8.3.2	Method . . . . .	69
8.3.3	The Determination of $\beta$ , $\tau_e$ and $\tau_\mu$ . . . . .	69
8.3.4	Experimental and Theoretical Uncertainties . . . . .	71
8.4	Results . . . . .	74
8.4.1	Data-driven Prediction . . . . .	75
8.4.2	Monte Carlo Prediction . . . . .	77
8.4.3	Observation from Data . . . . .	79
8.4.4	Confidence Limits and Interpretation . . . . .	80
<b>9</b>	<b>Summary and Conclusions</b>	<b>93</b>
<b>10</b>	<b>Acknowledgements</b>	<b>93</b>
<b>A</b>	<b>Same Sign Distributions by Flavour</b>	<b>96</b>
<b>B</b>	<b>Opposite-Sign/Flavour-Subtraction Signal Region Events</b>	<b>103</b>
<b>C</b>	<b>Notes on the Flavour Subtraction Analysis</b>	<b>104</b>
C.1	The Expression $\mathcal{S}$ . . . . .	104
C.2	Determining Uncertainties . . . . .	104
<b>D</b>	<b>Systematic uncertainty on <math>\beta</math> the ratio of the lepton reconstruction efficiencies</b>	<b>105</b>
D.1	Systematics on $\beta$ analyzed for different processes . . . . .	105
D.2	Data-driven $\beta$ determination in the Z control region . . . . .	107
D.3	Data-driven $\beta$ determination in the Z control region checking $p_T$ dependency . . . . .	108
D.4	Summary . . . . .	109
<b>E</b>	<b>SUSY signal models</b>	<b>110</b>
E.1	Theoretical uncertainties on mSUGRA grid . . . . .	110
E.1.1	Acceptance . . . . .	110
E.1.2	Scale and PDF uncertainties . . . . .	112
E.2	Theoretical uncertainties on pheno grids . . . . .	115
E.3	Reconstruction efficiency for the mSUGRA grid . . . . .	119

E.3.1	Systematics . . . . .	119
E.4	Reconstruction efficiency for the PhenoGrids . . . . .	122
E.4.1	Systematics . . . . .	124
<b>F</b>	<b>Charge misidentification rate</b>	<b>128</b>
F.1	Tag-and-Probe Method . . . . .	128
F.2	Electron Charge Mis-identification Rate . . . . .	128
F.3	Statistical and Systematic Uncertainties . . . . .	128
F.4	Conclusion . . . . .	131
<b>G</b>	<b>Complementary results on fake background estimation using the matrix method</b>	<b>132</b>
G.1	Introduction . . . . .	132
G.2	Validation plots for the real lepton control region . . . . .	134
G.3	Validation plots for the same-sign QCD region . . . . .	135
G.4	Validation plots for the 1-lepton QCD region . . . . .	136
G.5	Efficiencies from the real and fake control regions . . . . .	137
G.6	Efficiency and fake-rate for the selected same-sign QCD Control region versus $\eta$ , $p_T$ and $E_T^{\text{miss}}$ . . . . .	137
G.7	Resulting fake estimation using constant efficiency and fake-rate . . . . .	140
G.7.1	Fake background estimations varying the fake-rate . . . . .	143
<b>H</b>	<b>Alternative top background estimates</b>	<b>144</b>
H.1	Signal to control region ratio with alternative control regions . . . . .	144
H.2	Matrix method using the kinematic top tagger . . . . .	147

# 1 Introduction

The two-lepton signature is a very promising venue for the discovery and measurement of Supersymmetry. Many studies have been devoted to this signature in the last fifteen years. The channels characterised by the presence of two leptons in the final state are the best channels for the measurement of SUSY particle properties. The two-lepton signature typically suffers from lower statistics than the zero lepton [1] and one lepton [2] analyses. On the other hand, there are advantages due to the reduced standard model background. This note documents three different two-lepton analyses.

If R-parity is conserved, two sparticles are produced in each SUSY event, each of which cascades to the Lightest Supersymmetric Particle (LSP). We call each of the two cascades a ‘leg’ of the event. Neglecting decays involving the top quark, leptons are produced in SUSY cascade through the decays of the charginos and neutralinos. The main processes through which they occur are:

- a)  $\tilde{\chi}_i^0 \rightarrow \ell^\pm \nu \tilde{\chi}_j^\mp$
- b)  $\tilde{\chi}_i^\pm \rightarrow \ell^\pm \nu \tilde{\chi}_j^0$
- c)  $\tilde{\chi}_i^0 \rightarrow \ell^\pm \ell^\mp \tilde{\chi}_j^0$
- d)  $\tilde{\chi}_i^\pm \rightarrow \ell^\pm \ell^\mp \tilde{\chi}_j^\pm$

A two-lepton event can be obtained either through decays c) and d) on a single leg or decays a) and b) on both legs. The two final state leptons can have equal or opposite sign, and equal or different flavour, thus yielding four possible configurations. By selecting a specific configuration, one selects a specific mix of the four decays above. This feature has been exploited by developing three independent analyses which have different and complementary discovery potentials depending on the SUSY model (though share a common set of object definitions, and event selection criteria).

- One analysis searches for same-sign lepton pairs. This signature can only be produced by having single-lepton decays a) and b) on both legs of the event. This happens either through the production of two same-sign squarks, or through initial states involving gluinos. Gluinos are Majorana particles and decay with equal probability into a particle-antiparticle pair or a sparticle-antiparticle pair. Therefore in models where sparticle production is dominated by the production of at least one gluino, there can be significant same-sign signal. This is not true in the standard model, where same-sign leptons can only be produced through the decay of heavy quarks, or in processes implying the production of three leptons. The requirement that the two leptons be produced in two different legs of the event may reduce the statistical power of this analysis, if squarks and gluinos have low BR into a single lepton.
- The second analysis searches for inclusive opposite-sign leptons. In this case the Standard Model backgrounds are significantly higher, but the signal can be higher too, as all of the possible decay chains contribute.
- When two leptons are produced in the same leg through decays c) and d), if we assume lepton flavour conservation, they must have the same-flavour. A ‘flavour subtraction’ analysis exploits this fact, and looks to find an excess of same-flavour over different-flavour events. In fact for all of the standard model backgrounds – except the ones involving Z boson production – one should produce the same number of same-flavour and opposite-flavour lepton pairs. Therefore simply subtracting opposite flavour from same-flavour events may lead to the emergence of supersymmetry, in an analysis which reduces the systematic uncertainties associated with an inclusive search, at the price of a part of the signal statistics.

These three search modes (i) same-sign, (ii) opposite-sign inclusive and (iii) opposite-sign flavour-subtraction have different strengths and address different supersymmetry signatures. They are thus pursued in parallel. Full details of these three analyses are given in the sections which follow. The object definitions, event selections and signal regions are shared by the three analyses.

## 1.1 MSSM and mSUGRA Test Points and Grids

The definition of a selection strategy is more complex in the case of two-lepton searches than in the case of zero-lepton, and also of one-lepton signatures. In fact, whereas high  $E_T^{\text{miss}}$  and multi-jets are a generic feature of SUSY models with R-parity conservation, the rate of the leptons in the decay chains is strongly dependent on the detailed model features.

A generic minimal Supersymmetric model has a very large number of parameters, so that the complete exploration of the parameter space is impossible. The standard technique typically used to tackle this problem is to assume a dynamical origin for the Supersymmetry breaking. This normally implies on one side an ordering principle which allows one to express all of the soft susy-breaking parameters in terms of typically a handful of parameters. On the other side the correlation among parameters thus induced only select specific mass hierarchies and decay patterns, thus seriously affecting the generality of the results.

In the following analyses, given the large theory space addressed, we avoided optimisation of the analyses based on consideration of specific models, and we set the baseline selection requirements based on consideration of Standard Model backgrounds. However, the usage of some specific SUSY benchmark points providing some loose guidance on the relevant variables is necessary. Moreover, the results of the analysis must be interpreted in terms of the coverage in some theoretical or kinematic parameter space. We therefore considered two different models: a constrained MSSM based on the assumption of a SUSY breaking induced by gravitational interactions (mSUGRA), which allows comparison with previous studies, and a 24-parameters generic MSSM. For both models we have studied specific benchmark points, and produced grids in parameter space.

### 1.1.1 mSUGRA

The mSUGRA model has been for many years the canonical benchmark for SUSY analyses. We use the definition of the model as provided in the ISAWIG spectrum generator. The parameters are the masses of the SUSY scalars and fermions at the SUSY breaking scale, respectively  $M_0$  and  $M_{1/2}$ ,  $\tan\beta$ , the ratio of the vacuum expectation values of the two Higgs doublets in the model,  $A$ , the common trilinear term, and the sign of  $\mu$ , the higgsino mass term. Hadron collider phenomenology mostly depends on  $M_0$  and  $M_{1/2}$ , thus SUSY searches in the past have been reported on an  $(M_0, M_{1/2})$  plane for fixed values of  $\tan\beta$  and  $A$ .

The studies presented in [3] were based on a set of mSUGRA benchmark points. We use in the present study the SU4 point, which was chosen to be close to Tevatron bounds and is expected to be approximately in the sensitive region for analyses on 2010 data. This point is defined by the mSUGRA parameters:

$$M_0 = 200 \text{ GeV}, \quad M_{1/2} = 160 \text{ GeV}, \quad A = -400 \text{ GeV}, \quad \tan\beta = 10, \quad \mu > 0.$$

In order to allow comparison with previous studies, the results of the analyses in this note will be reported on an  $(M_0, M_{1/2})$  plane. To this effect a 220-point grid was generated, spanning a range in  $M_0$  from 40 to 1160 GeV and in  $M_{1/2}$  from 100 to 340 GeV, while keeping the other parameters fixed at  $\tan\beta = 3$ ,  $A_0 = 0$  and  $\mu > 0$ , these values being chosen to match the values used in the Tevatron 3-lepton search which provides the currently best mSUGRA sensitivity. The top mass considered in all calculations is 172.5 GeV

	$m_{\tilde{g}}$	$m_{\tilde{q}}$	$m_{\tilde{\chi}_2^0}$	$m_{\tilde{l}}$	$m_{\tilde{\chi}_1^0}$
MSSM22	420	400	200	150	100
MSSM27	420	400	350	200	100
MSSM29	420	400	350	300	250

Table 1: Sparticle mass values in GeV defining the MSSM benchmark points.

### 1.1.2 MSSM Models

In order to overcome the limitations of mSUGRA, a less constrained model has been considered, with the aim of addressing mass hierarchies and decay patterns suppressed in mSUGRA model. The assumed model is a 24-parameter MSSM as embodied in the ISAWIG spectrum generator.

The following MSSM parameters are set to a fixed value in order to obtain simple decay chains:  $m_A = 1000$  GeV,  $\mu = 1.5 \min(m_{\tilde{g}}, m_{\tilde{q}})$ ,  $\tan\beta = 4$ ,  $A_t = \mu/\tan\beta$ ,  $A_b = \mu \tan\beta$ , and  $A_l = \mu \tan\beta$ . Furthermore, one assumes a common squark mass parameter and a common lepton mass parameter. To reduce heavy-flavour complications in the decay chain,  $\tan\beta$  is set at a low value, and the trilinear couplings  $A_b$ ,  $A_t$  and  $A_l$  are put at a value giving zero left-right mixing. The value of  $m_A$  is chosen to remove the heavy higgses from the decay chains of squarks and gluinos. The choice of  $\mu$ , together with the mass hierarchies described below, ensures that the  $\tilde{\chi}_1^0$  is a pure bino and the  $\tilde{\chi}_2^0$  is a pure gaugino, yielding the following branching ratios:  $\text{BR}(\tilde{q}_L \rightarrow \tilde{\chi}_2^0) = 30\%$ ,  $\text{BR}(\tilde{q}_L \rightarrow \tilde{\chi}_1^+) = 60\%$  and  $\text{BR}(\tilde{q}_R \rightarrow \tilde{\chi}_1^0) = 100\%$ .

Five free parameters thus remain:  $m_{\tilde{g}}$ ,  $m_{\tilde{q}}$ ,  $m_{\tilde{\chi}_1^0}$ ,  $m_{\tilde{\chi}_2^0}$  and  $m_{\tilde{l}}$ .

The spectra of Etmiss and of the transverse momenta of jets and leptons depend on the mass difference squared, and are roughly independent of the squark and gluino masses. To study such dependence we produced a few benchmark points with squark and gluino masses of 400 GeV and a loose scan on the other masses. In the following discussion distributions will be shown for the points labelled MSSM22, MSSM27 and MSSM29, defined by the mass parameters (in GeV) shown in Table 1

In order to define the coverage of the two-lepton signatures, a scan in the quark and gluino masses is also performed with masses ranging from 300 to 600 GeV in steps of 100 GeV, leading to 16 different mass combinations. Given these assumptions we define three grid types, which we call PhenoGrid1, PhenoGrid2 and PhenoGrid3.

- For the first type (PhenoGrid1), no slepton is involved in the squark/gluino decay chains:  $m_{\tilde{l}} = 2000$  GeV,  $m(3\text{rd generation}) = 2000$  GeV, and  $m_{\tilde{q}_R} = m_{\tilde{q}_L}$ . This grid gives a low yield of two-lepton events and will be no further considered in this study.
- The second type (PhenoGrid2) allows the presence of sleptons in the gluino and squark decays chains:  $m(3\text{rd generation}) = 2000$  GeV,  $m_{\tilde{l}_R} = m_{\tilde{l}_L}$ ,  $m_{\tilde{q}_R} = m_{\tilde{q}_L}$ . Two scenarios are considered: a less favourable scenario, PhenoGrid2a with a very compressed spectrum yielding softer values of the discriminant variables, defined by  $m_{\tilde{\chi}_2^0} = M - 50$  GeV,  $m_{\tilde{\chi}_1^0} = M - 150$  GeV and  $m_{\tilde{l}_L} = M - 100$  GeV, where  $M$  is the minimum of the gluino and squark mass, and a more favourable one, PhenoGrid2b with  $m_{\tilde{\chi}_2^0} = M - 100$  GeV,  $m_{\tilde{\chi}_1^0} = 100$  GeV and  $m_{\tilde{l}_L} = M/2$  GeV.
- The third type (PhenoGrid3) further boosts the two-lepton fraction by setting  $m(3\text{rd generation}) = 2000$  GeV,  $m_{\tilde{l}_R} = 2000$  GeV and  $m_{\tilde{q}_R} = 2000$  GeV. In this case as well we consider two kinematic situations PhenoGrid3a and PhenoGrid3b with hierarchies identical to the ones defined for PhenoGrid2.

## 2 Analysis Overview

In this section we briefly introduce the main components of the two lepton analyses. As already noted in Section 1 there are three different analyses:

- A search for opposite-sign di-lepton events with missing transverse energy
- A search for same-sign di-lepton events with missing transverse energy
- A search for an excess of same-flavour opposite-sign di-lepton events with missing transverse energies

For each of these three analyses there are three different channels:

(i) di-electron, (ii) electron-muon and (iii) di-muon

(where in the latter analysis, the three channels in the opposite-sign analysis are combined in a ‘flavour subtraction’ to compute the same-flavour excess).

These three analyses share common object definitions, a common set of event selection criteria and where appropriate they share common background estimation techniques. The only difference in event selection between the opposite-sign and same-sign analyses is the different charge requirements on the leptons in the pairs. The flavour subtraction analysis takes the events in the opposite-sign analysis, and performs a flavour subtraction to search for an excess of same-flavour events. The background estimation techniques used in the opposite-sign analysis are thus also those used in the flavour subtraction analysis. The three analyses are inclusive with regard to jets, no requirement is made on the number of jets in the events. The signal regions (as will be discussed in Section 2.1) are all regions which require events with high missing transverse energy. All three analyses share a signal region ( $E_T^{miss} > 100$  GeV), whilst the opposite-sign analysis also looks at  $E_T^{miss} > 150$  GeV and the same-sign analysis at  $E_T^{miss} > 80$  GeV. The flavour-subtraction analysis only considers the common signal region ( $E_T^{miss} > 100$  GeV).

### 2.1 Signal Regions

There are two different kinds of lepton analysis: opposite-sign and same-sign, and we have seen that they are looking for different phenomenologies and are dominated by different backgrounds. Therefore although they share common object definitions, event selections and where appropriate shared data-driven background estimation techniques – it is not necessarily appropriate for them to share a common signal region. The signals regions used in these analysis are all simple high  $E_T^{miss}$  regions. The motivation for these, for each analysis, are given in this section.

#### • Opposite Sign and Flavour-Subtraction

When defining a signal region for the opposite-sign analysis, we begin by considering the dominant backgrounds to the search. As is clear from Figure 8,  $t\bar{t}$  is the dominant background by one order of magnitude for events with  $E_T^{miss} > 60$  GeV. This implies that a priori requesting additional jets in the signal region will not have a significant impact on the reach. High  $E_T^{miss}$   $t\bar{t}$  events will contain additional hard jets. A request for high multiplicities or high thresholds on jets might indeed help specific SUSY topologies, but in the interests of keeping the analysis as model-independent as possible, we limit ourselves to a simple selection based only on  $E_T^{miss}$ .

The choice of baseline signal region arises from some consideration of the signals themselves. In the introduction, three points were considered: MSSM22, MSSM27 and MSSM29. These correspond to  $m(\tilde{q}) = m(\tilde{g})$  and cover a rather broad range of mass hierarchies. Depending on

the assumed uncertainty on the prediction of the top background, points MSSM22 and MSSM27 would be discoverable for a cut on  $E_T^{\text{miss}}$  between 100 and 120 GeV. The optimal sensitivity would be for a cut at 150 GeV. Such uncertainty, for some of the proposed data-driven techniques, will depend on the statistics in the signal region.

Based on the considerations above, the opposite-sign (and thus flavour-subtraction analysis) considers a signal region defined by an  $E_T^{\text{miss}}$  cut of 100 GeV. This signal region is then optimised, by tightening the  $E_T^{\text{miss}}$  cut, when the parameter spaces of specific models are considered.

- **Same Sign**

Similarly in the same-sign analysis, the cut on missing energy has been motivated by looking at the number of Monte Carlo events from the different standard model background processes and a benchmark signal point – SU4. As you can see in Figure 8, a cut of  $E_T^{\text{miss}} > 100$  GeV reasonably reduces the standard model background, without removing too much signal. As it can be seen from Table 15, the  $E_T^{\text{miss}} > 100$  GeV cut removes more than 98% of the background events while keeping 60% of the signal SU4 events. The results of an  $E_T^{\text{miss}}$  only selection criteria have then been compared to selection criteria which also require jets in the final states. The comparison yields are similar (see figure-of-merit based on this study in [4]). Therefore the decision is made to use a simple missing energy based selection to match with the opposite-sign analysis. This is useful for the statistical combination of the two channels which is discussed later in this note. In some instances we quote two different cuts on missing energy ( $E_T^{\text{miss}} > 80$  GeV,  $E_T^{\text{miss}} > 100$  GeV) in order to show that the same-sign channel is heavily affected by statistics and that any optimisation might lead to a bias in the analysis.

## 2.2 Background Estimation Techniques

The backgrounds to a di-lepton search include:

- $Z/\gamma \rightarrow ll + \text{jets}$  background
- Fully-leptonic  $t\bar{t}$  background
- Dibosons
- Fakes (from single top,  $W \rightarrow l\nu + \text{jets}$ , QCD, semi-leptonic  $t\bar{t}$  and so on)
- Cosmics

In the same-sign analysis the majority of the background arises from fakes and thus the significant background to estimate in this analysis is the contribution to the observed event-rates in the signal region from fake events. Fakes will also contribute to the observed event rates in the opposite-sign signal region, and so the techniques used to estimate the fake-rate are shared between these two analyses (and so also the flavour subtraction analysis). A common technique is used to estimate the contamination from cosmics in both the opposite-sign and same-sign analyses. Additionally, the opposite-sign and flavour subtraction analyses use shared estimates of the  $Z/\gamma \rightarrow ll + \text{jets}$  and  $t\bar{t}$  backgrounds from data, and an estimate of the diboson event rates from Monte Carlo. All data-driven background estimations are complemented by Monte Carlo estimates. In some cases, particularly fake-rate determination from QCD, Monte Carlo estimates are inadequate - in other cases they agree very reasonably with data-driven predictions.

### 2.2.1 Fake Rate Determination

The data-driven fake background estimation is designed to predict separately the contribution to the event counts after selection, and in the signal region, from events with a) one-fake lepton and b) two-fake leptons.  $W/Z+jets$  events can be one-fake lepton events, whilst  $b\bar{b}$  and  $c\bar{c}$  events are sources of double-fake events.

In the di-electron channels, the magnitudes of these two fake lepton backgrounds can be estimated by measuring two probabilities: (i) the probability of a real lepton passing our selection, and (ii) the probability of a fake lepton passing our selection. A matrix is setup which relates the ‘true’ composition of sample in terms of real and fake leptons, to its ‘observable’ composition in terms of leptons which fail selection, and leptons with pass selection. An inversion of this matrix gives the necessary data-driven background estimates of the one-fake and two-fake lepton rates. Similar techniques can be used to derive the contribution to event rates in the di-muon channels, and then similarly event rates in the electron-muon channels.

### 2.2.2 Cosmics contamination

Matrix methods are also used to estimate the contamination in the signal regions from cosmic events. The predicted cosmic rates in each of the channels can be predicted by solving equations which relate the number of cosmic and collision events in each channel to the observed number of events passing the baseline two-lepton selection and the number of events in an enhanced cosmics sample. The `CosmicCalo` stream is used to study cosmic candidates.

### 2.2.3 $Z/\gamma \rightarrow ll+jets$ Background Determination

The background from  $Z/\gamma \rightarrow ll+jets$  events is estimated using semi-data driven techniques. In this estimation technique a scale-factor,  $\beta$ , is defined which relates the number of estimated events in the signal-region,  $N_{Z/\gamma^*}^{est,SR}$  to the total number of  $Z/\gamma^*$  events observed in data,  $N_{Z/\gamma^*,data}$ :

$$N_{Z/\gamma^*}^{est,SR} = \beta \cdot N_{Z/\gamma^*,data} \quad (1)$$

The scale factor  $\beta$  is obtained as the ratio of the number of high- $E_T^{miss}$  events with any  $m_{ll}$  to the number of low- $E_T^{miss}$  events with  $81 < m_{ll} < 100$  GeV in Monte Carlo and  $N_{Z/\gamma^*,data}$  is the number of data events in the low  $E_T^{miss}$  events with  $81 \text{ GeV} < m_{ll} < 101$  GeV after subtracting the expected non- $Z$  MC events in that region.

### 2.2.4 Fully-leptonic $t\bar{t}$ Background Determination

In a signal region selected with two opposite sign leptons and  $E_T^{miss} > 100$  GeV,  $t\bar{t}$  events where both  $W$ 's decay leptonically make up more than 85% of the selected sample. A small fraction of the  $t\bar{t}$  dilepton events arises from semi-leptonic  $t\bar{t}$  events, where one of the isolated leptons is a fake isolated lepton, rather than from the chain  $t \rightarrow W \rightarrow \ell\nu$ . These semi-leptonic  $t\bar{t}$  events have one fake isolated lepton and are therefore taken into account by the data-driven estimate of the fake-lepton backgrounds. The data-driven  $t\bar{t}$  estimates therefore focus specifically on the determination of the background from  $t\bar{t} \rightarrow (W^+b)(W^-\bar{b}) \rightarrow (\ell^+ \nu_\ell b)(\ell^- \bar{\nu}_\ell \bar{b})$ .

Each data-driven technique is designed to address a specific type of background, and has inherent assumptions. Thanks to orthogonal systematics and assumptions, the different methods complement each other and allow to reach a solid understanding of the  $t\bar{t} \rightarrow \ell\ell$  background. The methods described

Table 2: The data-taking periods analysed in this note, with the integrated luminosity,  $\int \mathcal{L} dt$ , recorded in each after good run list selection. In total,  $34.3 \text{ pb}^{-1}$  of integrated luminosity is analysed, the majority of which is from the data-taking period I.

Period	Run number	$\int \mathcal{L} dt (\text{pb}^{-1})$ after GRL
E	160387–161946	0.937
F	162347–162882	1.728
G	165591–166383	5.659
H	166466–166964	7.057
I	167575–167844	19.002
Total		34.3

below use two different so-called “top-taggers” which are discriminating variables designed to test the consistency of the event kinematics with that of a  $t\bar{t} \rightarrow (W^+ b)(W^- \bar{b}) \rightarrow (\ell^+ \nu_\ell b) (\ell^- \bar{\nu}_\ell \bar{b})$  event.

### 2.3 Interpretation of Results

After having estimated using data-driven techniques the number of background events of each different type in the opposite-sign and same-sign signal regions these predictions can be used to set a limit. Limits are set using a profile-likelihood method [1].

A different limit setting procedure has been adopted for the flavour subtraction analysis. In fact the distribution of possible observations is in this case not a simple Poisson, but instead a ‘Skellam’ distribution. Therefore two approaches have been explored: a profile likelihood method taking a skellam and not a Poisson, and the use of Toy Monte Carlo experiment. The final limits are given in terms of this latter approach.

## 3 Data and Monte Carlo Samples

### 3.1 Data Sets

The data used in this analysis were collected between 24th June 2010, and the end of  $\sqrt{s} = 7 \text{ TeV}$  running in late October 2010. These data correspond to the data taking periods E through to I. The total integrated luminosity, after good run list (GRL) selection, of this data is  $\int \mathcal{L} dt = 34.3 \text{ pb}^{-1}$ .

The data which pass the GRL selection are the data for which the LHC declared stable beams and the ATLAS detector was at nominal high voltage. The solenoid and toroid fields were required to be both on and at nominal conditions (for good muon and electron momentum measurements). The sub-detectors were also recording good data quality so that the electron, muon and jet identification and reconstruction algorithms give results which do not deviate significantly from expectation.

In Table 2 each data period is listed and the luminosity of each given after GRL selection. In these analyses, events are taken from both the **Egamma** stream and the **Muon** stream. All centrally produced AODs have been converted into SUSYD3PDs using the **SUSYD3PDMaker** package version **00-06-20**. This analysis has been carried out on these D3PDs. All data samples are from **r15**.

Table 3: The  $W$ +jets **mc09** Monte Carlo samples used in this analyses. The dataset name, the generator with which it was produced, the cross-section and the k-factor are given. In addition, the total number of events generated ( $N_{gen}$ ) for each sample are listed.

ID	Name	Generator	Cross Section (pb)	k-factor	$N_{gen}$
107680	WenuNp0_pt20	AlpgenJimmy	6913.3	1.199	1381531
107681	WenuNp1_pt20	AlpgenJimmy	1293.0	1.199	257958
107682	WenuNp2_pt20	AlpgenJimmy	377.1	1.199	188896
107683	WenuNp3_pt20	AlpgenJimmy	100.9	1.199	49978
107684	WenuNp4_pt20	AlpgenJimmy	25.3	1.199	12991
107685	WenuNp5_pt20	AlpgenJimmy	6.9	1.199	3449
107690	WmunuNp0_pt20	AlpgenJimmy	6913.3	1.199	1386038
107691	WmunuNp1_pt20	AlpgenJimmy	1293.0	1.199	254959
107692	WmunuNp2_pt20	AlpgenJimmy	377.1	1.199	187860
107693	WmunuNp3_pt20	AlpgenJimmy	100.9	1.199	49887
107694	WmunuNp4_pt20	AlpgenJimmy	25.3	1.199	12991
107695	WmunuNp5_pt20	AlpgenJimmy	6.9	1.199	3498
107700	WtaunuNp0_pt20	AlpgenJimmy	6913.3	1.199	131846
107701	WtaunuNp1_pt20	AlpgenJimmy	1293.0	1.199	254753
107702	WtaunuNp2_pt20	AlpgenJimmy	377.1	1.199	188446
107703	WtaunuNp3_pt20	AlpgenJimmy	100.9	1.199	49972
107704	WtaunuNp4_pt20	AlpgenJimmy	25.3	1.199	12996
107705	WtaunuNp5_pt20	AlpgenJimmy	6.9	1.199	3998
106280	WbbNp0	AlpgenJimmy	3.2	1.22	6499
106281	WbbNp1	AlpgenJimmy	2.6	1.22	5500
106282	WbbNp2	AlpgenJimmy	1.4	1.22	2997
106283	WbbNp3	AlpgenJimmy	0.6	1.22	1500

### 3.2 Monte Carlo Samples

The official **mc09** Monte Carlo samples have been used in this analysis. The last OTX map is used with these Monte Carlo samples. Pile-up (Section 6.2) samples are used where possible (tag `r1430_r1429`). These samples are generated with on average two primary interactions per event. The Monte Carlo datasets unavailable with pile-up include: **Herwig** dibosons, **Pythia** dijet and low-mass Drell Yan samples. The  $W$ +jets and  $Z$ +jets/Drell Yan samples are detailed in Tables 3 and 4. The  $t\bar{t}$ , QCD and diboson samples used are detailed in Table 5. In these tables, where the k-factor column is left blank – either one has not been applied, or it has been incorporated into the cross-section.

The top pair-production cross-section is calculated at NNLO precision and is 160.79 pb. The NNLO cross-section,  $10.46 \pm 0.52$  nb is used for  $W$ +jets production along with the NNLO cross-section. For  $Z$ +jets production, the NNLO cross-section  $1.070 \pm 0.054$  nb is used. The diboson cross-sections are calculated up to NLO. The cross-section for  $WW$  production is  $44.9 \pm 2.2$  pb, the cross-section for  $WZ$  production  $18.0 \pm 1.3$  pb and the cross-section for  $ZZ$  production  $5.96 \pm 0.32$  pb [5].

In the  $ee$  channels, the **PythiaB\_bbe15X** heavy flavour sample is used for QCD. In the  $e\mu$  and  $\mu\mu$  channels, the filtered **Pythia Jx** samples were used for QCD.

Table 4: The Z+jets mc09 Monte Carlo samples used in this analyses. The dataset name, the generator with which it was produced, the cross-section and the k-factor are given. In addition, the total number of events generated ( $N_{gen}$ ) for each sample are listed.

ID	Name	Generator	Cross Section (pb)	k-factor	$N_{gen}$
107650	ZeeNp0_pt20	AlpgenJimmy	664.1	1.25	303966
107651	ZeeNp1_pt20	AlpgenJimmy	133.0	1.25	62491
107652	ZeeNp2_pt20	AlpgenJimmy	40.23	1.25	18997
107653	ZeeNp3_pt20	AlpgenJimmy	11.14	1.25	5499
107654	ZeeNp4_pt20	AlpgenJimmy	2.899	1.25	1499
107655	ZeeNp5_pt20	AlpgenJimmy	0.753	1.25	500
107660	ZmumuNp0_pt20	AlpgenJimmy	664.1	1.25	303947
107661	ZmumuNp1_pt20	AlpgenJimmy	133.0	1.25	62996
107662	ZmumuNp2_pt20	AlpgenJimmy	40.23	1.25	18993
107663	ZmumuNp3_pt20	AlpgenJimmy	11.14	1.25	5497
107664	ZmumuNp4_pt20	AlpgenJimmy	2.899	1.25	1499
107665	ZmumuNp5_pt20	AlpgenJimmy	0.753	1.25	499
107670	ZtautauNp0_pt20	AlpgenJimmy	664.1	1.25	302959
107671	ZtautauNp1_pt20	AlpgenJimmy	133.0	1.25	62981
107672	ZtautauNp2_pt20	AlpgenJimmy	40.23	1.25	18993
107673	ZtautauNp3_pt20	AlpgenJimmy	11.14	1.25	5497
107674	ZtautauNp4_pt20	AlpgenJimmy	2.899	1.25	1499
107675	ZtautauNp5_pt20	AlpgenJimmy	0.753	1.25	499
108319	DrellYan_mumu	Pythia	1252.9	none	999969
108320	DrellYan_ee	Pythia	1253.0	none	999503
108321	DrellYanLowM_mu3	Pythia	4407.0	none	499925
108322	DrellYanLowM_ee3	Pythia	4406.1	none	499931

Table 5:  $t\bar{t}$ , diboson and QCD mc09 Monte Carlo samples used in this analyses. The dataset name, the generator with which it was produced, the cross-section and the k-factor are given. In addition, the total number of events generated ( $N_{gen}$ ) for each sample are listed.

ID	Name	Generator	Cross Section (pb)	k-factor	$N_{gen}$
105200	T1	MC@NLO Jimmy	89.40	NNLO calculation	154976
108340	st_tchan_enu	MC@NLO Jimmy	7.0	NNLO calculation	9993
108341	st_tchan_munu	MC@NLO Jimmy	7.0	NNLO calculation	9997
108342	st_tchan_taunu	MC@NLO Jimmy	7.0	NNLO calculation	10000
108343	st_schan_enu	MC@NLO Jimmy	0.47	NNLO calculation	9950
108344	st_schan_munu	MC@NLO Jimmy	0.47	NNLO calculation	9996
108345	st_schan_taunu	MC@NLO Jimmy	0.47	NNLO calculation	9996
108346	st_Wt	MC@NLO Jimmy	13	NNLO calculation	14995
109276	J0_jetjet_1muon	Pythia	843.78	none	1996528
109277	J1_jetjet_1muon	Pythia	821.17	none	1769626
109278	J2_jetjet_1muon	Pythia	222.50	none	399911
109279	J3_jetjet_1muon	Pythia	28.62	none	1999427
109280	J4_jetjet_1muon	Pythia	1.960	none	199857
109281	J5_jetjet_1muon	Pythia	0.071	none	499174
108326	PythiaB_bbe15X	Pythia	75126.6	none	4447997
105985	WW	Herwig	17.43	NLO calculation	249837
105986	ZZ	Herwig	1.265	NLO calculation	249725
105987	WZ	Herwig	5.553	NLO calculation	249830

## 4 Object Definitions

- Jets are reconstructed using the anti- $k_T$  jet clustering algorithm with  $R = 0.4$  based on topological clusters. The energy is first measured at the EM-scale before jet energy scales are applied as a function of  $p_T$  and  $\eta$ . Jets must have  $p_T > 20$  GeV and  $|\eta| < 2.5$ . If any of these selected jets overlap within  $\Delta R < 0.2$  with an electron then the jet is removed. These jet selection criteria are in-line with JetEtmiss performance group recommendations [6].
- Electrons are selected which are AuthorElectron, and which satisfy RobustMedium electron identification requirements. The *object p<sub>T</sub>* of each electron must be greater than 20 GeV, and the electron must lie in the region  $|\eta_{cl}| < 2.47$  where  $\eta_{cl}$  is the pseudo-rapidity of the cluster. Each selected electron must not touch a dead OTX region (the latest OTX map is used for Monte Carlo). If an electron overlaps with a jet ( $0.2 < \Delta R < 0.4$ ), then the electron candidate is rejected. These electron definitions are as used in [7]. When in the analysis electrons are further required to be ‘tight’, this refers to the requirement that the electrons pass the RobusterTight identification requirements. When in the analysis electrons are also required to be isolated, this refers to the requirement that  $E_{T\text{cone}20}/p_T < 0.15$ . In the object definitions, electrons are required to be neither tight nor isolated. These two requirements are imposed after initial object selection, after overlap removal but during later analysis.
- Muons are, as recommended by the Muon Combined Performance group [8], selected using the STACO algorithm (combined or segment-tagged). They must have  $p_T > 20$  GeV and  $|\eta| < 2.4$ . As recommended in [8] each component of a Monte Carlo muon’s  $p_T$  is shifted and smeared in order to reproduce the  $p_T$  resolution in data. This smearing is only applied to Monte Carlo. Additionally, all muons must have at least 1 pixel hit and 6 SCT hits in the inner detector. Each muon must pass the following track quality requirements:  
 If  $|\eta| < 1.9$ :  $n_{\text{TRT}}^{\text{outliers}} \geq 6$  and  $n_{\text{TRT}}^{\text{outliers}} < 0.9n_{\text{TRT}}$   
 If  $|\eta| \geq 1.9$  and  $n_{\text{TRT}} \geq 6$ :  $n_{\text{TRT}}^{\text{outliers}} < 0.9n_{\text{TRT}}$   
 The track quality match ( $\chi^2$ ) must be less than 150, and combined muons must in addition to these cuts satisfy:  
 $p_{T,\text{MS}} < 50$  GeV:  $p_{\text{MS}}^{\text{extrap.}} - p_{\text{ID}} < 0.4p_{\text{ID}}$   
 The selected muons must be isolated with the total  $p_T$  in a cone of size 0.2 less than 1.8 GeV. If any muon falls within  $\Delta R$  of 0.4 of a jet (which is not removed by jet overlap with electrons), then the muon is rejected. In order to veto against cosmics,  $|z_\mu - z_{PV}| < 10$  mm.

- No specific photon selection is used, which means that photons are not ignored but are treated as jets.

- SimplifiedRefFinal is used for missing transverse energy (corresponding to the variable: MET\_EMJES\_RefFinal\_CellOutEM

in the D3PDs). This variable is the sum of five terms:

- RefJet(EMJES): Missing transverse energy from jets using EM scale plus jet energy scale calibration
- RefEle: Missing transverse energy from electrons
- MuonBoy\_Track: Missing transverse energy from isolated STACO muons
- MuonBoy\_Spectro: Missing transverse energy from non-isolated STACO muons
- CellOut(EM): Missing transverse energy from cells not belonging to any electron or jet cluster using the EM-scale

The MuonBoy terms are replaced with all isolated and non-isolated selected muons. During calculation of the RefJet and RefEle terms Medium quality, and not RobustMedium quality, electrons were used. An offline correction for events which contain electrons which are RobustMedium but

not **Medium** is applied. This correction, as devised by the SUSY working group ensures that the contribution from jets which overlap with the new electrons to be included after correction are replaced with the electron contribution. During this correction electrons passing object definitions, but with  $p_T > 10$  GeV are considered.

## 5 Systematic Uncertainties

In the sections which follow the impact of various systematic uncertainties on the analyses (in addition to the statistical uncertainty due to limited Monte Carlo statistics, often denoted *stat.*) will be considered. The uncertainties which will be considered are detailed below.

- o Luminosity

The uncertainty on the luminosity is taken to be 11%.

- o Cross Section

The uncertainty due to the cross-section is taken to be 5% for most Monte Carlo samples considered - this being consistent with the quoted cross-section uncertainties in Section 3.2. The two exceptions to this are: QCD and  $t\bar{t}$ . For QCD, we assign a cross-section uncertainty of 100% to account for the expected poor-modelling of fake events in Monte Carlo. We assign +6.9%, -9.5% uncertainty on the  $t\bar{t}$  cross-section based [9, 10] ( $164.6 \text{ pb}_{-15.7}^{+11.4}$ ). Larger uncertainties are applied to the SUSY Monte Carlos (see Appendix E).

- o JES<sub>up/down</sub>

This is the asymmetric uncertainty due to the scaling of the jet energy *up* or *down*. The uncertainty due to the jet energy scale is evaluated using the `JESUncertaintyProvider` [11], which gives the uncertainties on the jet energy scale as a function of jet  $p_T$  and  $\eta$ . On average the energy is scaled by 8% [12].

- o JER

This systematic considers the impact of additional jet energy resolution. It is evaluated following the recommendations given in [13]. Each jet is smeared according to a Gaussian distribution, with unit mean, and a width, sigma, given by the  $p_T$  (where  $p_T$  is given in units of GeV) dependant resolution function (Equation 2):

$$0.55 \sqrt{\frac{(4.6)^2}{p_T^2} + \frac{0.846^2}{p_T} + 0.064^2} \quad (2)$$

For a jet with  $p_T$  of 30 GeV, this gives a width of 12%.

- o  $E_{e,up/down}$

This is an asymmetric uncertainty due to the scaling *up* or *down* of the electron energy scale. This is taken to be 3% for all electrons (regardless of their  $p_T$  and  $\eta$ ) [14].

- o  $\mu_{MS,up/down}$  and  $\mu_{ID,up/down}$

These are the asymmetric uncertainties from varying the MS and ID components of muon  $p_T$  [15]. These uncertainties are small.

- o  $\text{res}_e$

This uncertainty considers the impact of additional electron energy resolution. The electron energy is smeared using a Gaussian with  $p_T$  (in GeV) and  $\eta$  dependent sigma [14]. This function

Table 6: Trigger chains and their corresponding L1, L2 and EF trigger items used for the different data-taking period in this analysis.

Data Period	L1 item	L2 trigger	EF trigger
E	L1_EM10	L2_g17_etcut	EF_g17_etcut
F-I	L1_EM10	L2_e15_medium	EF_e15_medium

Table 7: The muon triggers used for the different data-taking periods in this analysis.

Data Period	Trigger
E-F	EF_mu10_MSonly
G-H	EF_mu13
I	EF_mu13_tight

(Equation 3) is given by:

$$\sqrt{(S(1 + \Delta S)\sqrt{E_{cl}})^2 + (C(1 + \Delta C)E_{cl})^2 - (S\sqrt{E_{cl}})^2 - (CE_{cl})^2} \quad (3)$$

where  $S$  and  $C$  are the sampling and constant terms, 0.1 and 0.007 respectively. The uncertainty on the sampling term,  $\Delta S$ , is 0.2, and the uncertainty on the constant term,  $\Delta C$ , 1% in the barrel and 4% in the end-cap.

- o pdf

This is the uncertainty due to uncertainties in the parton distribution functions. The way in which this uncertainty is evaluated varies slightly between the opposite/same sign analyses, and the flavour subtraction analysis. The reader is therefore referred to the appropriate sections in the different analysis sections where this uncertainty is considered for precise details. In all figures the pdf uncertainty is taken to be a conservative 5%. A larger uncertainty is applied to SUSY Monte Carlos (see Appendix E).

For all the uncertainties which affect object definitions, the missing transverse energy is corrected accordingly. This means that each object in the container is removed (vectorially) from the missing energy (via its and the objects  $x$  and  $y$  components), and the object added back in, but with corrected contributions to the  $x$  and  $y$  components.

## 6 Trigger and Event Selection

### 6.1 Trigger

The electron triggers used, by data-taking period, are illustrated in Table 6. In Table 7 the equivalent details are given for the muon triggers. For detailed studies of the efficiencies of these triggers, their turn-on curves as functions of  $p_T$  and  $\eta$  and other studies – the reader is referred to the supporting note of the one-lepton search [2]. An evaluation of the overall trigger efficiencies is also give in Section 8.3.3 where they are used in the flavour subtraction analysis. These triggers are all un-prescaled, and at plateau for  $p_T > 20$  GeV leptons (which are the leptons considered in this analysis).

For both the opposite-sign, flavour-subtraction and same-sign analyses – in order to avoid duplicating events, a scheme is adopted by which  $ee$  events are taken from the electron triggered streams,  $\mu\mu$  from the muon triggered streams and  $e\mu$  events from the muon stream only if they are events not triggered by an electron trigger (and thus are in the egamma stream).

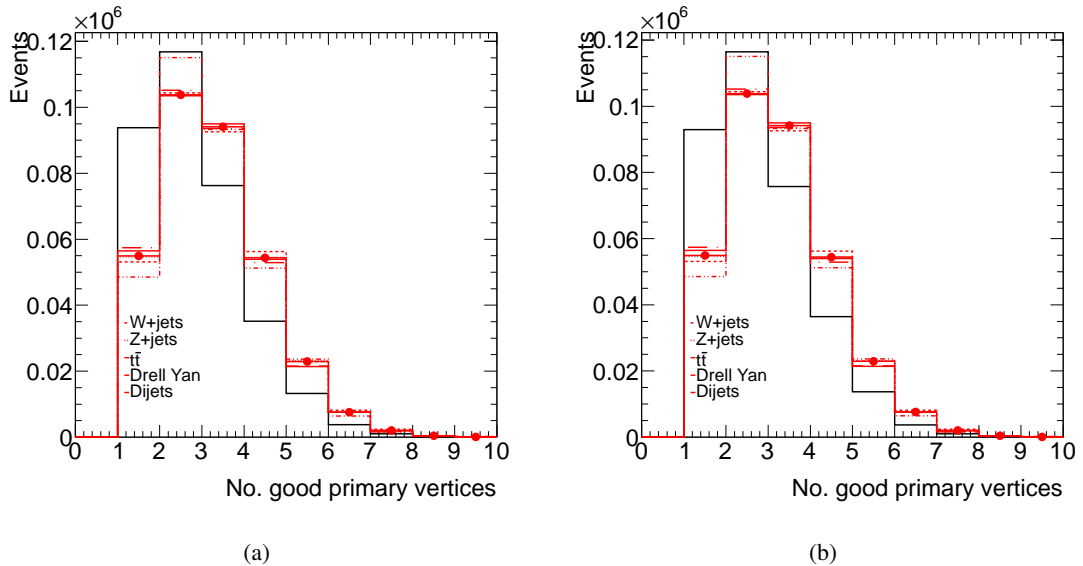


Figure 1: The number of good primary vertices (defined as vertices associated with at least five tracks) in data ((a) `egamma` stream and (b) `muon` stream), compared to Monte Carlo which is generated with an average of two additional primary interactions per event. The overall Monte Carlo is illustrated, along with the distributions for the different types of Monte Carlo (to demonstrate that there is no difference). In these figures the good vertex distribution in data is normalised to Monte Carlo. Data is given by the black histogram.

## 6.2 Pile-up re-weighting

The number of additional interactions for the  $\sqrt{s} = 7$  TeV data is typically between one and three extra interactions per event. The Monte Carlo samples used in this study were (see Section 3.2) generated with on average two primary interactions per event, the resulting distribution of good vertices for these events is thus a Poisson distribution with mean two. The number of good primary vertices (defined as vertices associated with at least five tracks) for  $\sqrt{s} = 7$  TeV data is illustrated in Figure 1, where it is compared with the distribution in Monte Carlo. As expected the two distributions are very different. In Figure 1, the data is separated into the egamma stream (a), and the muon stream (b). There is, again as anticipated, no difference between the two data distributions. The Monte Carlo distributions illustrated, and the Monte Carlo events thus used to derive suitable weights to correct for the differences between data and Monte Carlo, are the events in both data and Monte Carlo which pass all but the  $m_{ll}$  event selection criteria (Section 6.3).

The discrepancies between data and Monte Carlo are corrected for by re-weighting the primary vertex multiplicity distribution in Monte Carlo, to match that in data. In Figure 2 the necessary weights, as a function of the number of good primary vertices, are illustrated. In Figure 3 the resulting Monte Carlo distribution, which now by construction, matches the data distribution is illustrated. The used weights are also tabulated in Table 8, where it is noted that a single weight is applied for events with  $\geq 8$  primary vertices (Figure 2 illustrates the increased statistical error on the weight when considering numbers of primary vertices beyond this). After pile-up re-weighting each sample is then further re-weighted to restore the cross-section to its original value. This additional re-weighting is necessary because the primary vertex distributions are not *exactly* identical for each sample, and so the weights based on all the Monte Carlo may not precisely conserve each samples' cross-section.

For the few Monte Carlo Standard Model processes for which events with a mean of two additional

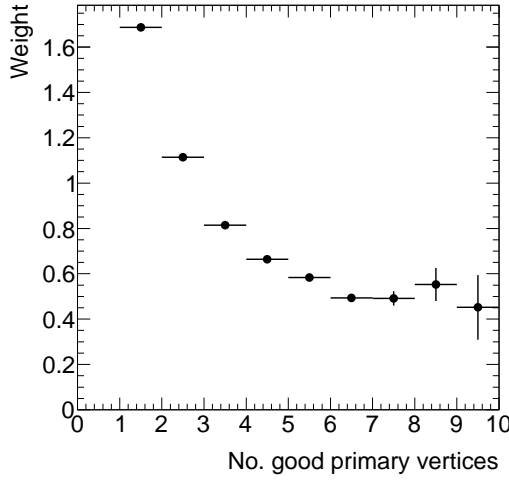


Figure 2: The weights to be applied to Monte Carlo samples with pile-up, as a function of the number of good primary vertices (defined as vertices associated with at least five tracks). The last two bins are combined with the over-flow bin, and a common weight of  $\sim 0.6$  is applied to events with  $\geq 8$  primary vertices.

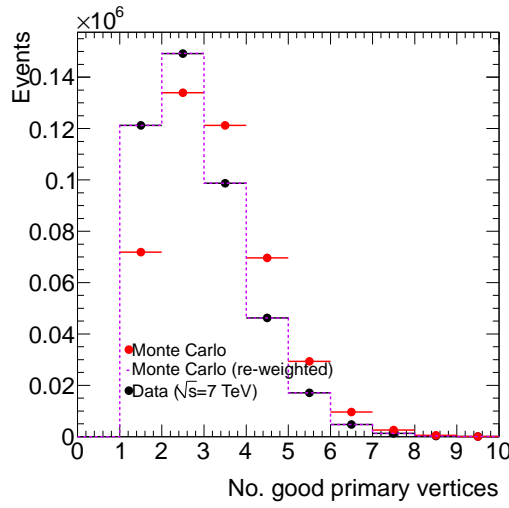


Figure 3: Monte Carlo event numbers as a function of the number of good primary vertices (defined as vertices associated with at least five tracks), before (red) and after (magenta) pile-up re-weighting. In this figure data is normalised to Monte Carlo.

Table 8: The weights to be applied to Monte Carlo samples with pile-up, as a function of the number of good primary vertices (defined as vertices associated with at least five tracks). A single weight is applied to events with  $\geq 8$  good primary vertices, here the statistics become small.

No. good vertices	Weight
1	1.68
2	1.11
3	0.81
4	0.66
5	0.58
6	0.49
7	0.48
$\geq 8$	0.56

interactions (as already noted in Section 3.2 these are the  $WW$ ,  $WZ$  and  $ZZ$ , low-mass Drell Yan, and the **Pythia** heavy flavour electron samples), Monte Carlo events with always no additional interactions were used, and no pile-up weights applied.

## 6.3 Event Selection

### 6.3.1 Pre-selection

Before any requirements are made on the number of leptons in the event, the following event ‘cleaning’ cuts are made:

- If any jets are classified as ‘loose bad’ [16] then the event is not considered. In loose cleaning the following variables are considered –  $f_{em}$  (the energy fraction in the electromagnetic calorimeter),  $f_{hec}$  (the energy fraction in the hadronic end-cap calorimeter (HEC)),  $n_{90}$  (the minimum number of cells containing at least 90 % of the cluster energy),  $f_Q$  (the fraction of LAr cells with a cell Q-factor greater than 4000),  $t_{jet}$  (jet timing computed as the energy squared cells mean time) and finally  $f_{max}$  (the maximum energy fraction in one calorimeter layer).
- Any events with a selected electron (before overlap removal) in the transition region of the detector ( $1.37 < |\eta_{cl}| < 1.52$ ) are removed. If an electron touches a dead OTX region, the electron is vetoed but the event is still accepted.
- If any event contains a cosmic muon, as detailed in Section 4, the event is rejected.
- All events must have at least one primary vertex associated to at least five tracks.

### 6.3.2 Selection

After pre-selection, events are required to have exactly two selected leptons (satisfying the object definitions, and overlap-removal criteria, defined in Section 4). These events will fall into one of three categories:

- Di-electron ( $ee$ )
- Electron-muon ( $e\mu$ )

- Di-muon ( $\mu\mu$ )

If the two leptons are of opposite-sign ( $l^\pm l^\mp; l = e, \mu$ ) the event is included in the opposite-sign and flavour-subtraction analyses. If the two leptons have the same-sign ( $l^\pm l^\pm; l = e, \mu$ ) then the event is included in the same-sign analysis. For both the two-lepton events in the opposite-sign/flavour-subtraction analyses and the two-lepton events in the same-sign analysis the following additional requirements are made:

- The invariant mass of the two-leptons ( $m_{ll}$ ) must exceed 5 GeV
- Any electrons in the pair must be both tight and isolated (see Section 4).

Events in Monte Carlo which pass this selection, and contain electrons, are re-weighted using global event weights which correct for differences in electron reconstruction efficiencies between data and Monte Carlo. The weights for RobusterTight electrons are applied, as detailed in [17].

Events with high  $E_T^{miss}$  fall into the signal-regions. The opposite-sign, same-sign and flavour-subtraction analyses share an  $E_T^{miss} > 100$  GeV signal region. In addition to this region, the opposite-sign analysis looks at the  $E_T^{miss} > 150$  GeV signal region and the same-sign analysis looks at the  $E_T^{miss} > 80$  GeV signal region. These signal regions are as motivated in Section 2.1.

In Table 9 the numbers of events in the `egamma` stream after pre-selection are given by period. These  $ee$  events are then detailed at different stages of event selection and separated into opposite-sign and same-sign events.

Table 9: The number of events in the `egamma` stream at various stages of event selection, separated by run period. The total number of  $ee$  events in each signal region are also detailed. All  $ee$  events are derived from the `egamma` stream.

Cuts	periodE	periodF	periodG	periodH	periodI	Total
preselection	5524787	351371	1171807	1465451	3952418	12465834
$ee$	268	455	1587	2007	5494	9811
$m_{ee} > 5\text{GeV}$ (isolated tight $e$ )	160	298	1015	1305	3534	6312
OS $ee$	159	296	1006	1294	3495	6250
$E_T^{miss} > 100\text{GeV}$	0	0	1	1	2	4
$E_T^{miss} > 150\text{GeV}$	0	0	0	0	1	1
SS $ee$	1	2	9	11	39	62
$E_T^{miss} > 80\text{GeV}$	0	0	0	0	0	0
$E_T^{miss} > 100\text{GeV}$	0	0	0	0	0	0

In Table 10 details are given of the number of  $\mu\mu$  events in the `muon` stream by run period. These are also broken down into opposite-sign and same-sign events.

Finally, Table 11 details the  $e\mu$  events, which are derived from both the `egamma` and `muon` stream, as described. These are also separated into the different run periods.

Table 10: The total number of  $\mu\mu$  events at various stages of selection, by run period. These are then divided into opposite-sign and same-sign lepton pairs. All  $\mu\mu$  events are derived from the muon stream.

Cuts	periodE	periodF	periodG	periodH	periodI	Total
preselection	1701620	4598842	780792	992314	2587217	10660785
$\mu\mu$	381	563	2157	2635	7041	12777
$m_{\mu\mu} > 5GeV$	381	562	2157	2634	7041	12775
OS $\mu\mu$	381	562	2156	2633	7040	12772
$E_T^{miss} > 100GeV$	0	0	5	0	8	13
$E_T^{miss} > 150GeV$	0	0	2	0	2	4
SS $\mu\mu$	0	0	1	1	1	3
$E_T^{miss} > 80GeV$	0	0	0	0	0	0
$E_T^{miss} > 100GeV$	0	0	0	0	0	0

Table 11: The total number of  $e\mu$  events at various stages of the event selection, by run period. These  $e\mu$  events are divided into opposite-sign and same-sign pairs.

Cuts	periodE	periodF	periodG	periodH	periodI	Total
$e\mu$	17	32	87	120	341	597
$m_{e\mu} > 5GeV$	2	4	18	32	80	136
(isolated tight $e$ )						
OS $e\mu$	2	4	17	31	77	131
$E_T^{miss} > 100GeV$	0	2	3	0	8	13
$E_T^{miss} > 150GeV$	0	0	1	0	3	4
SS $e\mu$	0	0	1	1	3	5
$E_T^{miss} > 80GeV$	0	0	0	0	0	0
$E_T^{miss} > 100GeV$	0	0	0	0	0	0

The events which fall into the opposite-sign/flavour-subtraction analysis signal regions are detailed in Appendix B. The total number of opposite-sign data events, at pre-selection, event selection and signal selection, are compared with Monte Carlo in Table 12. In this table the agreement between data and Monte Carlo is reasonable. The systematic errors on the counts in the 100 GeV signal region are detailed in Table 13 (these uncertainties are detailed in Section 5). The corresponding uncertainties for the 150 GeV signal region are detailed in Table 14.

The total number of same-sign data events at pre-selection, event selection and signal section, are compared with Monte Carlo in Table 15. There are no data in events in either of the same-sign signal regions (in any channel), as one would expect from the Monte Carlo predictions at this luminosity. The systematic uncertainties are detailed in Table 16.

In the figures which follow, comparisons are made between data and Monte Carlo of a variety of event variables. The illustrated uncertainty band includes the uncertainties on each cross-section, the luminosity, energy scale and resolution uncertainties and the statistical sum-of-weights uncertainty which arises from limited Monte Carlo statistics. These uncertainties are as detailed in Section 5. All standard model Monte Carlo events are illustrated along with data and then two signal points: (i) SU4, and (ii) MSSM27, combined with the total standard model contribution.

Figure 4 illustrates for the opposite-sign and same-sign selected channels separately the  $p_T$  of the leading lepton in selected events, whilst Figure 6 illustrates the  $p_T$  of the sub-leading lepton for these events. The agreement between data and Monte Carlo is good for all three opposite-sign channels, for both leading and sub-leading  $p_T$ . The same-sign distributions suffer from an expected lack of statistics, but there is no obvious disagreement between the distributions and as Table 15 illustrates the observed number of selected two-lepton events are in-line with expectation. In the same-sign electron distribution, but not the electron-muon or muon pair distributions, the leading  $p_T$  peaks at  $\sim 40$  GeV. In the  $e^\pm e^\mp$  channel,  $Z \rightarrow e^\pm e^\mp$  trident events result in the peak in this distribution at 40 GeV. Trident events are not significant in the  $\mu^\pm \mu^\pm$  distribution.

In Figures 5 and 7, again for both opposite-sign and same-sign events, the  $p_T$  and invariant masses of all selected lepton pairs are illustrated. The agreement is again sound. The  $E_T^{miss}$  of each selected event and the  $M_T$  formed from the leading lepton  $p_T$  and  $E_T^{miss}$  of these events are illustrated in Figures 8 and 9. The total number of jets in each event are illustrated in Figure 10. In all these distributions the agreement between data and Monte Carlo is good in the same-sign electron channel, where there are reasonable statistics. The same-sign electron-muon and muon distributions suffer from the expected lack of statistics, but as seen in Table 15 there is no significant or unusual disagreement between the expected event rates in these distribution and the observed. The final plots (Figure 11) illustrate event  $M_{T2}$  for the selected two lepton events.

(a)  $e^\pm e^\mp$ 

	2 Leptons	$m_{ll} > 5 \text{ GeV}$	$E_T^{\text{miss}} > 100 \text{ GeV}$	$E_T^{\text{miss}} > 150 \text{ GeV}$
Data	$6250^{+80}_{-79}$	$6250^{+80}_{-79}$	$4^{+3}_{-2}$	$1^{+2}_{-1}$
Z+jets	$6023.09 \pm 24.97$	$6023.09 \pm 24.97$	$0.38 \pm 0.16$	$0.20 \pm 0.12$
W+jets	$2.45 \pm 0.60$	$2.45 \pm 0.60$	$0.00 \pm 0.00$	$0.00 \pm 0.00$
Drell Yan	$22.5 \pm 1.3$	$22.5 \pm 1.3$	$0.0 \pm 0.0$	$0.0 \pm 0.0$
$t\bar{t}$	$20.2 \pm 0.8$	$20.2 \pm 0.8$	$3.7 \pm 0.3$	$0.9 \pm 0.2$
Dibosons	$11.88 \pm 0.12$	$11.88 \pm 0.12$	$0.30 \pm 0.02$	$0.09 \pm 0.01$
Dijets	$49.3 \pm 5.3$	$49.3 \pm 5.3$	$0.0 \pm 0.0$	$0.0 \pm 0.0$
Single Top	$1.6 \pm 0.3$	$1.6 \pm 0.3$	$0.1 \pm 0.1$	$0.0 \pm 0.0$
SM	$6131.1 \pm 25.6$	$6131.1 \pm 25.6$	$4.5 \pm 0.4$	$1.2 \pm 0.2$
SU4	$5.8 \pm 0.5$	$5.8 \pm 0.5$	$3.2 \pm 0.4$	$2.2 \pm 0.3$

(b)  $e^\pm \mu^\mp$ 

	2 Leptons	$m_{ll} > 5 \text{ GeV}$	$E_T^{\text{miss}} > 100 \text{ GeV}$	$E_T^{\text{miss}} > 150 \text{ GeV}$
Data	$131^{+12}_{-11}$	$131^{+12}_{-11}$	$13^{+5}_{-4}$	$4^{+3}_{-2}$
Z+jets	$37.39 \pm 1.98$	$37.39 \pm 1.98$	$0.36 \pm 0.16$	$0.08 \pm 0.08$
W+jets	$2.75 \pm 0.70$	$2.75 \pm 0.70$	$0.00 \pm 0.00$	$0.00 \pm 0.00$
Drell Yan	$0.0 \pm 0.0$	$0.0 \pm 0.0$	$0.0 \pm 0.0$	$0.0 \pm 0.0$
$t\bar{t}$	$51.7 \pm 1.2$	$51.7 \pm 1.2$	$9.8 \pm 0.5$	$1.8 \pm 0.2$
Dibosons	$12.77 \pm 0.17$	$12.77 \pm 0.17$	$0.36 \pm 0.03$	$0.06 \pm 0.01$
Dijets	$53.2 \pm 35.0$	$53.2 \pm 35.0$	$0.0 \pm 0.0$	$0.0 \pm 0.0$
Single Top	$4.5 \pm 0.4$	$4.5 \pm 0.4$	$0.8 \pm 0.2$	$0.1 \pm 0.0$
SM	$162.3 \pm 35.1$	$162.3 \pm 35.1$	$11.3 \pm 0.6$	$2.0 \pm 0.3$
SU4	$9.5 \pm 0.6$	$9.5 \pm 0.6$	$6.0 \pm 0.5$	$3.7 \pm 0.4$

(c)  $\mu^\pm \mu^\mp$ 

	2 Leptons	$m_{ll} > 5 \text{ GeV}$	$E_T^{\text{miss}} > 100 \text{ GeV}$	$E_T^{\text{miss}} > 150 \text{ GeV}$
Data	$12774^{+114}_{-113}$	$12772^{+114}_{-113}$	$13^{+5}_{-4}$	$4^{+3}_{-2}$
Z+jets	$13011.08 \pm 36.94$	$13011.08 \pm 36.94$	$0.97 \pm 0.29$	$0.15 \pm 0.11$
W+jets	$0.64 \pm 0.30$	$0.64 \pm 0.30$	$0.00 \pm 0.00$	$0.00 \pm 0.00$
Drell Yan	$56.7 \pm 2.0$	$56.7 \pm 2.0$	$0.0 \pm 0.0$	$0.0 \pm 0.0$
$t\bar{t}$	$34.8 \pm 1.0$	$34.8 \pm 1.0$	$7.0 \pm 0.4$	$1.5 \pm 0.2$
Dibosons	$23.94 \pm 0.17$	$23.94 \pm 0.17$	$0.61 \pm 0.03$	$0.15 \pm 0.01$
Dijets	$214.7 \pm 61.1$	$214.7 \pm 61.1$	$0.0 \pm 0.0$	$0.0 \pm 0.0$
Single Top	$3.4 \pm 0.4$	$3.4 \pm 0.4$	$0.7 \pm 0.2$	$0.1 \pm 0.1$
SM	$13345.3 \pm 71.4$	$13345.3 \pm 71.4$	$9.2 \pm 0.6$	$1.9 \pm 0.2$
SU4	$10.9 \pm 0.7$	$10.9 \pm 0.7$	$5.9 \pm 0.5$	$3.5 \pm 0.4$

Table 12: Number of events in the opposite-sign channels at  $34.3 \text{ pb}^{-1}$  at various event selection levels. Errors on the Monte Carlo prediction are purely statistical.

	Events	JES $_{\uparrow}$	JES $_{\downarrow}$	JER	$E_{e,\downarrow}$	$E_{e,\uparrow}$	res $_e$	$\mu_{MS,\uparrow}$	$\mu_{MS,\downarrow}$	$\mu_{ID,\uparrow}$	$\mu_{ID,\downarrow}$	Lumi.	$\sigma$	pdf.	Total.	Stat.
Z+jets	0.383	0.129	-0.058	0.251	0.197	0.001	0.059	0	0	0	0	0.042	0.019	0.019	0.353	0.163
$t\bar{t}$	3.718	0.872	-0.665	0.145	0.257	-0.408	-0.043	0	0	0	0	0.409	0.186	0.186	1.089	0.311
Dibosons	0.303	0.089	-0.061	0.012	0.046	-0.031	0.003	0	0	0	0	0.033	0.015	0.015	0.108	0.019
Single Top	0.127	0	0	0	0.056	0	0	0	0	0	0	0.014	0.006	0.006	0.059	0.064

(b)  $e^{\pm} \mu^{\mp}$ 

	Events	JES $_{\uparrow}$	JES $_{\downarrow}$	JER	$E_{e,\downarrow}$	$E_{e,\uparrow}$	res $_e$	$\mu_{MS,\uparrow}$	$\mu_{MS,\downarrow}$	$\mu_{ID,\uparrow}$	$\mu_{ID,\downarrow}$	Lumi.	$\sigma$	pdf.	Total.	Stat.
Z+jets	0.356	0.100	-0.117	-0.058	0	0	0	0	0	0	0	0.039	0.018	0.018	0.139	0.161
$t\bar{t}$	9.799	1.646	-1.946	-0.086	0.730	-0.641	0.086	0.010	-0.022	0.006	0	1.078	0.490	0.490	2.445	0.530
Dibosons	0.359	0.084	-0.049	0.022	0.025	-0.022	0.005	0.005	-0.002	0.007	0	0.039	0.018	0.018	0.103	0.028
Single Top	0.755	0.138	0.019	0.035	0.054	-0.023	-0.028	0	0	0	0	0.083	0.038	0.038	0.184	0.172

(c)  $\mu^{\pm} \mu^{\mp}$ 

	Events	JES $_{\uparrow}$	JES $_{\downarrow}$	JER	$E_{e,\downarrow}$	$E_{e,\uparrow}$	res $_e$	$\mu_{MS,\uparrow}$	$\mu_{MS,\downarrow}$	$\mu_{ID,\uparrow}$	$\mu_{ID,\downarrow}$	Lumi.	$\sigma$	pdf.	Total.	Stat.
Z+jets	0.972	0.238	-0.131	-0.073	-0.041	-0.131	-0.057	0	-0.098	0	0	0.107	0.049	0.049	0.329	0.286
$t\bar{t}$	6.985	0.827	-1.233	0.137	0.233	-0.373	-0.050	0	-0.068	0.013	0.013	0.768	0.349	0.349	1.588	0.443
Dibosons	0.605	0.056	-0.024	0.006	0.014	-0.005	-0.001	0.016	-0.003	0.004	-0.002	0.067	0.030	0.030	0.100	0.027
Single Top	0.674	0.263	0	-0.027	-0.019	-0.027	0	0	0	0	0	0.074	0.034	0.034	0.280	0.176

Table 13: Number of events in the signal region ( $E_T^{miss} > 100$  GeV) for each opposite-sign channel at 34.3 pb $^{-1}$ , with breakdown of systematic error. The largest members of the JES $_{\uparrow/\downarrow}$ ,  $\mu_{MS//ID,\uparrow/\downarrow}$  and  $E_{e,\uparrow/\downarrow}$  pairs are used to compute the total systematic.

	Events	JES $\uparrow$	JES $\downarrow$	JER	E $_{e,\uparrow}$	E $_{e,\downarrow}$	res $_e$	$\mu_{MS,\uparrow}$	$\mu_{MS,\downarrow}$	$\mu_{ID,\uparrow}$	$\mu_{ID,\downarrow}$	Lumi.	$\sigma$	pdf.	Total.	Stat.
Z+jets	0.204	0.000	0.000	0.043	0.056	-0.099	0.000	0.000	0.000	0.000	0.000	0.022	0.010	0.010	0.111	0.124
$t\bar{t}$	0.923	0.141	-0.288	0.066	-0.185	0.022	0.000	0.000	0.000	0.000	0.000	0.102	0.046	0.046	0.409	0.151
Dibosons	0.087	0.024	-0.017	0.002	0.011	-0.007	0.005	0.000	0.000	0.000	0.000	0.010	0.004	0.004	0.029	0.010
Single Top	0.026	0.000	-0.026	0.000	0.000	-0.026	0.000	0.000	0.000	0.000	0.000	0.003	0.001	0.001	0.046	0.026

	Events	JES $\uparrow$	JES $\downarrow$	JER	E $_{e,\uparrow}$	E $_{e,\downarrow}$	res $_e$	$\mu_{MS,\uparrow}$	$\mu_{MS,\downarrow}$	$\mu_{ID,\uparrow}$	$\mu_{ID,\downarrow}$	Lumi.	$\sigma$	pdf.	Total.	Stat.
Z+jets	0.083	0.000	0.000	0.000	0.000	0.000	0.000	0.000	0.000	0.000	0.000	0.009	0.004	0.004	0.011	0.083
$t\bar{t}$	1.832	0.622	-0.381	-0.010	0.177	-0.203	-0.052	0.000	-0.016	0.000	0.012	0.202	0.092	0.092	0.699	0.237
Dibosons	0.057	0.022	-0.010	0.012	0.007	-0.008	-0.002	0.003	-0.005	-0.002	0.000	0.006	0.003	0.003	0.028	0.011
Single Top	0.061	0.059	0.000	0.000	0.022	0.000	0.000	0.000	0.000	0.000	0.007	0.003	0.003	0.003	0.064	0.045

	Events	JES $\uparrow$	JES $\downarrow$	JER	E $_{e,\uparrow}$	E $_{e,\downarrow}$	res $_e$	$\mu_{MS,\uparrow}$	$\mu_{MS,\downarrow}$	$\mu_{ID,\uparrow}$	$\mu_{ID,\downarrow}$	Lumi.	$\sigma$	pdf.	Total.	Stat.
Z+jets	0.151	0.000	0.102	0.000	0.000	0.102	0.000	0.000	0.000	0.000	0.017	0.008	0.008	0.145	0.107	
$t\bar{t}$	1.484	0.375	-0.386	0.161	0.110	-0.148	-0.104	-0.022	0.000	0.000	0.163	0.074	0.074	0.496	0.196	
Dibosons	0.149	0.010	-0.010	0.001	0.009	-0.002	0.001	0.002	-0.001	0.000	0.016	0.007	0.007	0.024	0.011	
Single Top	0.097	0.000	0.000	0.038	0.000	0.000	0.000	0.000	0.000	0.011	0.005	0.005	0.005	0.040	0.058	

Table 14: Number of events in the signal region ( $E_T^{miss} > 150$  GeV) for each opposite-sign channel at 34.3 pb $^{-1}$ , with breakdown of systematic error. The largest members of the JES $_{uparrow/\downarrow}$ ,  $\mu_{MS,uparrow/\downarrow}$  and  $E_{e,uparrow/\downarrow}$  pairs are used to compute the total systematic.

(a)  $e^\pm e^\pm$ 

	2 Leptons	$m_{ll} > 5 \text{ GeV}$	$E_T^{miss} > 100 \text{ GeV}$
Data	$62^{+9}_{-8}$	$62^{+9}_{-8}$	$0^{+2}_{-0}$
Z+jets	$66\pm3$	$66\pm3$	$0\pm0$
W+jets	$0.5\pm0.2$	$0.5\pm0.2$	$0.0\pm0.0$
Drell Yan	$0.3\pm0.2$	$0.3\pm0.2$	$0.0\pm0.0$
$t\bar{t}$	$0.4\pm0.1$	$0.4\pm0.1$	$0.1\pm0.1$
Dibosons	$0.37\pm0.02$	$0.37\pm0.02$	$0.01\pm0.00$
Dijets	$1.2\pm0.8$	$1.2\pm0.8$	$0.0\pm0.0$
Wbb	$0.02\pm0.02$	$0.02\pm0.02$	$0.00\pm0.00$
Single Top	$0.06\pm0.04$	$0.06\pm0.04$	$0.00\pm0.00$
SM	$68.80\pm2.74$	$68.80\pm2.74$	$0.14\pm0.06$
SU4	$1.5\pm0.2$	$1.5\pm0.2$	$0.9\pm0.2$

(b)  $e^\pm \mu^\pm$ 

	2 Leptons	$m_{ll} > 5 \text{ GeV}$	$E_T^{miss} > 100 \text{ GeV}$
Data	$11^{+4}_{-3}$	$5^{+3}_{-2}$	$0^{+2}_{-0}$
Z+jets	$2\pm0$	$1\pm0$	$0\pm0$
W+jets	$6.5\pm1.2$	$1.7\pm0.6$	$0.1\pm0.1$
Drell Yan	$0.0\pm0.0$	$0.0\pm0.0$	$0.0\pm0.0$
$t\bar{t}$	$0.7\pm0.1$	$0.6\pm0.1$	$0.1\pm0.1$
Dibosons	$0.84\pm0.03$	$0.81\pm0.03$	$0.03\pm0.01$
Dijets	$0.0\pm0.0$	$0.0\pm0.0$	$0.0\pm0.0$
Wbb	$0.12\pm0.06$	$0.08\pm0.05$	$0.03\pm0.03$
Single Top	$0.09\pm0.06$	$0.07\pm0.06$	$0.00\pm0.00$
SM	$10.15\pm1.25$	$4.49\pm0.66$	$0.21\pm0.08$
SU4	$2.5\pm0.3$	$2.5\pm0.3$	$1.5\pm0.2$

(c)  $\mu^\pm \mu^\pm$ 

	2 Leptons	$m_{ll} > 5 \text{ GeV}$	$E_T^{miss} > 100 \text{ GeV}$
Data	$3^{+3}_{-2}$	$3^{+3}_{-2}$	$0^{+2}_{-0}$
Z+jets	$0\pm0$	$0\pm0$	$0\pm0$
W+jets	$0.2\pm0.2$	$0.2\pm0.2$	$0.0\pm0.0$
Drell Yan	$0.0\pm0.0$	$0.0\pm0.0$	$0.0\pm0.0$
$t\bar{t}$	$0.1\pm0.1$	$0.1\pm0.1$	$0.0\pm0.0$
Dibosons	$0.45\pm0.02$	$0.45\pm0.02$	$0.02\pm0.00$
Dijets	$3.1\pm3.1$	$3.1\pm3.1$	$0.0\pm0.0$
Wbb	$0.00\pm0.00$	$0.00\pm0.00$	$0.00\pm0.00$
Single Top	$0.05\pm0.04$	$0.05\pm0.04$	$0.00\pm0.00$
SM	$3.98\pm3.14$	$3.98\pm3.14$	$0.02\pm0.00$
SU4	$1.9\pm0.3$	$1.9\pm0.3$	$1.2\pm0.2$

Table 15: Number of events in the same-sign channels at  $34.3 \text{ pb}^{-1}$  at various event selection levels. Errors on the Monte Carlo prediction are purely statistical.

	Events	$\text{JES}_{\uparrow}$	$\text{JES}_{\downarrow}$	JER	$E_{e,\uparrow}$	$E_{e,\downarrow}$	$\text{res}_e$	$\mu_{MS,\uparrow}$	$\mu_{MS,\downarrow}$	$\mu_{ID,\uparrow}$	$\mu_{ID,\downarrow}$	Lumi.	$\sigma$	pdf.	Total.	Stat.
$t\bar{t}$	0.12	0.01	-0.01	0.01	0	0	0	0	0	0	0	0.01	0.01	0.01	0.02	0.06
Dibosons	0.015	0.005	-0.006	0.003	0	-0.001	0.001	0	0	0	0	0.002	0.001	0.001	0.007	0.004
(a) $e^{\pm}e^{\pm}$																
	Events	$\text{JES}_{\uparrow}$	$\text{JES}_{\downarrow}$	JER	$E_{e,\uparrow}$	$E_{e,\downarrow}$	$\text{res}_e$	$\mu_{MS,\uparrow}$	$\mu_{MS,\downarrow}$	$\mu_{ID,\uparrow}$	$\mu_{ID,\downarrow}$	Lumi.	$\sigma$	pdf.	Total.	Stat.
$W+\text{jets}$	0.06	0	0	0	0	0	0	0	0	0	0	0.01	0	0	0	0.06
$t\bar{t}$	0.08	0	-0.03	0	0	0	0	0	0	0	0	0.01	0	0	0.03	0.06
Dibosons	0.035	0.008	-0.010	0.002	0.001	-0.006	0.002	-0.002	-0.001	0	0	0.004	0.004	0.002	0.002	0.005
Whb	0.03	0	0	0	0	0	0	0	0	0	0	0	0	0	0	0.03
(b) $e^{\pm}\mu^{\pm}$																
	Events	$\text{JES}_{\uparrow}$	$\text{JES}_{\downarrow}$	JER	$E_{e,\uparrow}$	$E_{e,\downarrow}$	$\text{res}_e$	$\mu_{MS,\uparrow}$	$\mu_{MS,\downarrow}$	$\mu_{ID,\uparrow}$	$\mu_{ID,\downarrow}$	Lumi.	$\sigma$	pdf.	Total.	Stat.
$W+\text{jets}$	0	0.13	0	0	0	0	0	0	0	0	0	0	0	0	0	0
$t\bar{t}$	0	0	0.01	0	0	0	0	0	0	0	0	0	0	0	0.01	0
Dibosons	0.021	0.001	-0.004	0	0.001	-0.002	0	0	-0.001	0	0	0.002	0.001	0.001	0.005	0.004
(c) $\mu^{\pm}\mu^{\pm}$																
	Events	$\text{JES}_{\uparrow}$	$\text{JES}_{\downarrow}$	JER	$E_{e,\uparrow}$	$E_{e,\downarrow}$	$\text{res}_e$	$\mu_{MS,\uparrow}$	$\mu_{MS,\downarrow}$	$\mu_{ID,\uparrow}$	$\mu_{ID,\downarrow}$	Lumi.	$\sigma$	pdf.	Total.	Stat.
$W+\text{jets}$	0	0.13	0	0	0	0	0	0	0	0	0	0	0	0	0	0
$t\bar{t}$	0	0	0.01	0	0	0	0	0	0	0	0	0	0	0	0.01	0
Dibosons	0.021	0.001	-0.004	0	0.001	-0.002	0	0	-0.001	0	0	0.002	0.001	0.001	0.005	0.004

Table 16: Number of events in the signal region ( $E_T^{\text{miss}} > 100 \text{ GeV}$ ) for each same-sign channel at  $34.3 \text{ pb}^{-1}$  in the signal region, with breakdown of systematic error. The largest members of the  $\text{JES}_{\uparrow/\downarrow}, \mu_{MS/ID,\uparrow/\downarrow}$  and  $E_{e,\uparrow/\downarrow}$  pairs are used to compute the total systematic.

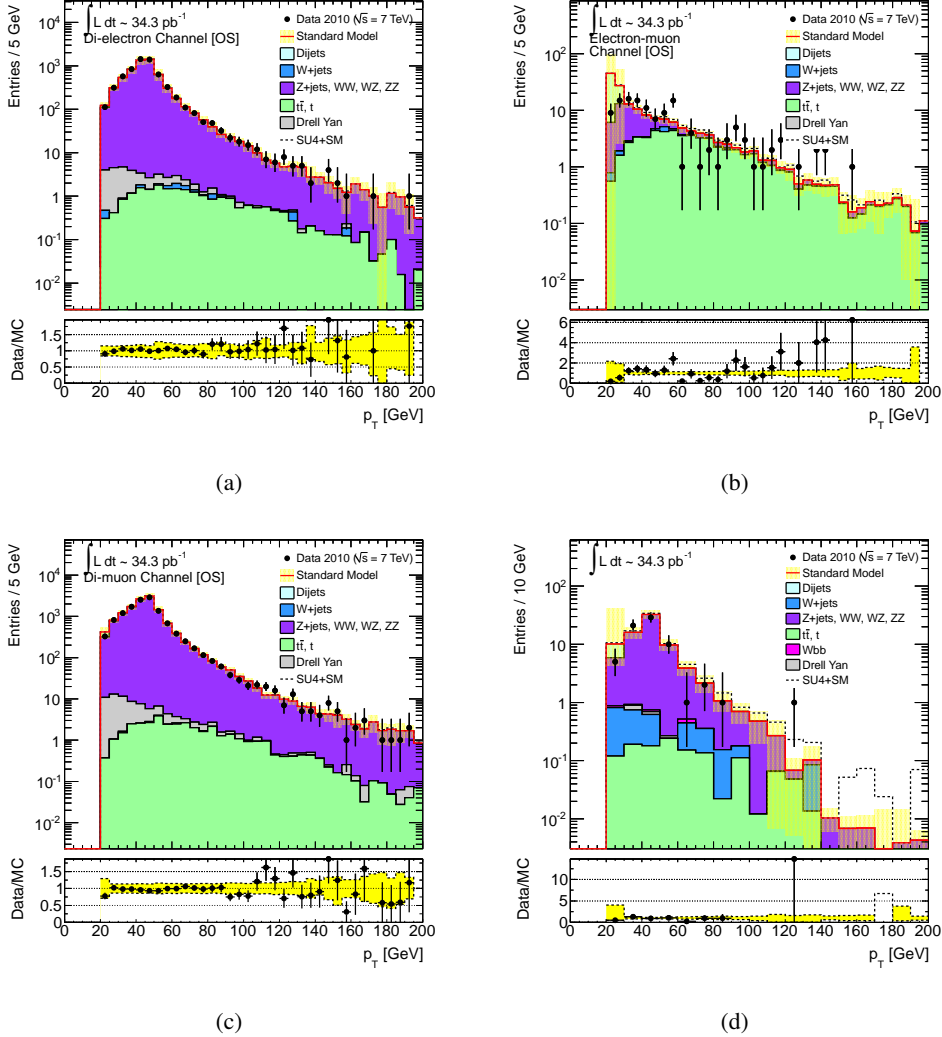


Figure 4: Distributions of the  $p_T$  of the leading lepton in two-lepton events in data and Monte Carlo. The two lepton events are divided into the three opposite-sign and a single same-sign charge channel,  $e^\mp e^\pm$  (a),  $e^\mp \mu^\pm$  (b),  $\mu^\mp \mu^\pm$  (c) and  $l^\mp l^\mp$  (d). Errors on data points are 68% Poisson confidence limits, error band on Monte Carlo represents the statistical, jet energy scale and resolution, lepton energy scale and resolution, cross-section and luminosity uncertainties (as detailed in the text). In the bottom histogram the black data points, and the yellow uncertainty band, have been divided by the total Monte Carlo to show whether the fractional deviation of the data from the Monte Carlo lies within the uncertainty band. The red Monte Carlo line is the sum of all the Standard Model backgrounds.

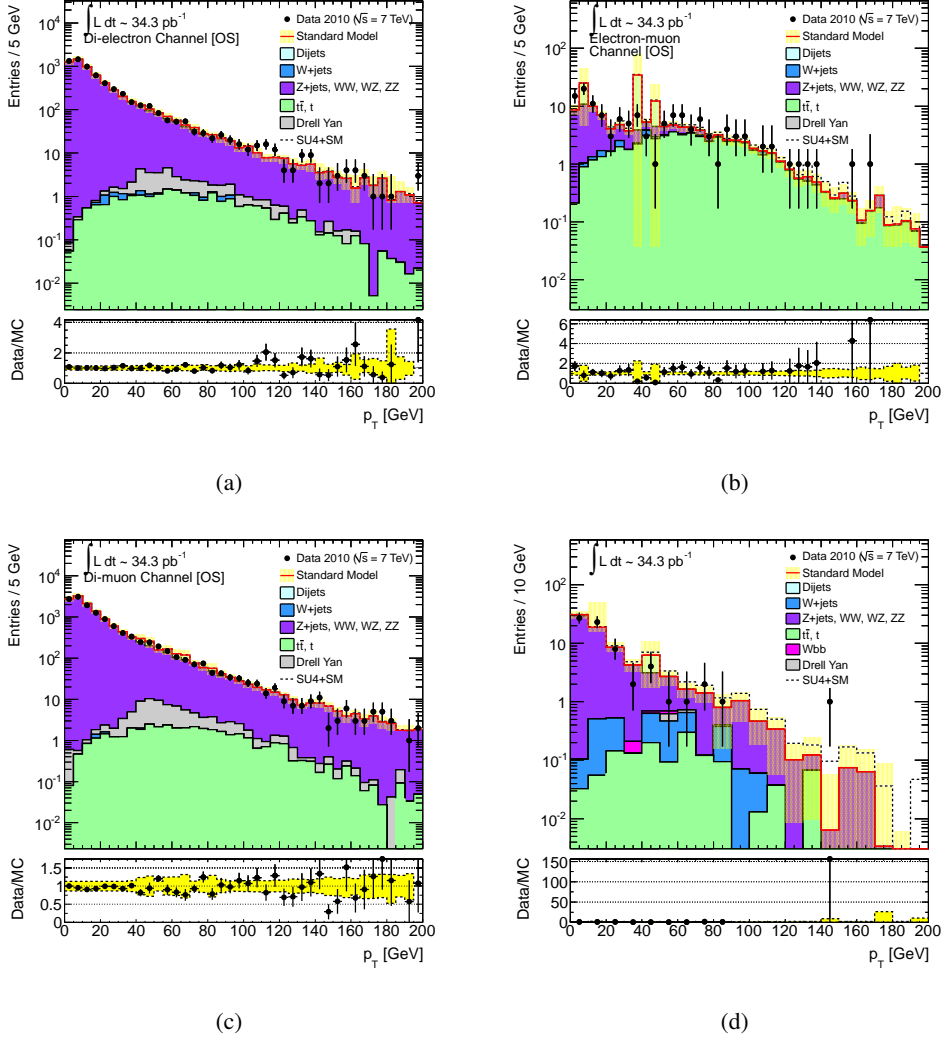


Figure 5: Distributions of the  $p_T$  of the lepton-pair in two-lepton events in data and Monte Carlo. The two lepton events are divided into the three opposite-sign and a single same-sign charge channel,  $e^\mp e^\pm$  (a),  $e^\mp \mu^\pm$  (b),  $\mu^\mp \mu^\pm$  (c) and  $l^\mp l^\mp$  (d). Errors on data points are 68% Poisson confidence limits, error band on Monte Carlo represents the statistical, jet energy scale and resolution, lepton energy scale and resolution, cross-section and luminosity uncertainties (as detailed in the text). In the bottom histogram the black data points, and the yellow uncertainty band, have been divided by the total Monte Carlo to show whether the fractional deviation of the data from the Monte Carlo lies within the uncertainty band. The red Monte Carlo line is the sum of all the Standard Model backgrounds.

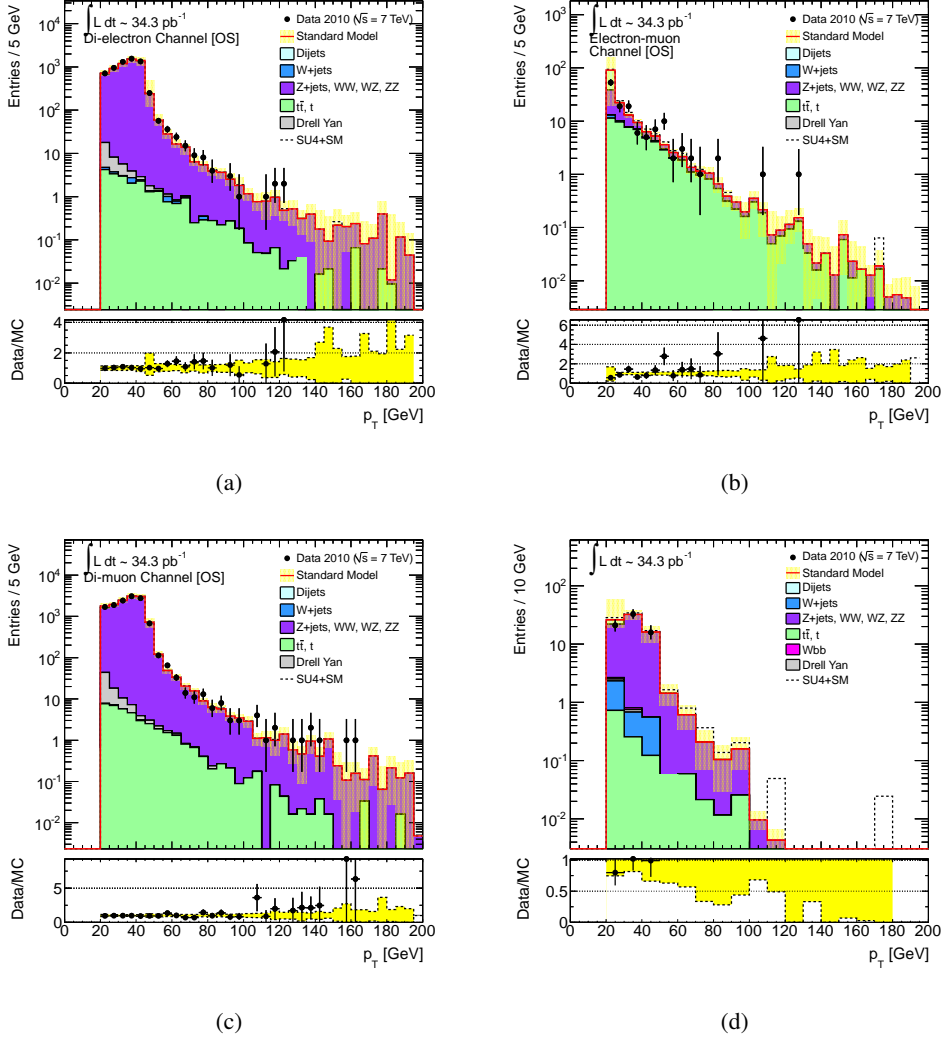


Figure 6: Distributions of the  $p_T$  of the sub-leading lepton in two-lepton events in data and Monte Carlo. The two lepton events are divided into the three opposite-sign and a single same-sign charge channel,  $e^\mp e^\pm$  (a),  $e^\mp \mu^\pm$  (b),  $\mu^\mp \mu^\pm$  (c) and  $l^\mp l^\mp$  (d). Errors on data points are 68% Poisson confidence limits, error band on Monte Carlo represents the statistical, jet energy scale and resolution, lepton energy scale and resolution, cross-section and luminosity uncertainties (as detailed in the text). In the bottom histogram the black data points, and the yellow uncertainty band, have been divided by the total Monte Carlo to show whether the fractional deviation of the data from the Monte Carlo lies within the uncertainty band. The red Monte Carlo line is the sum of all the Standard Model backgrounds.

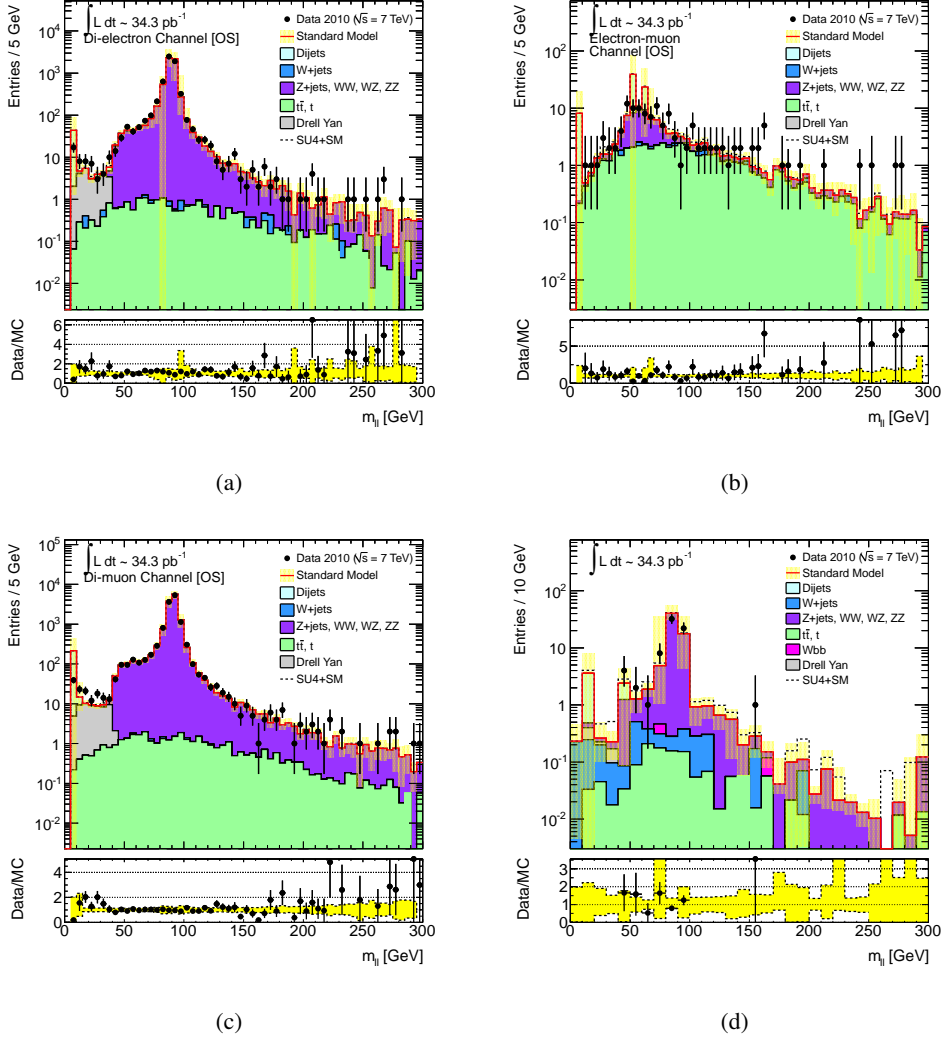


Figure 7: Distributions of the invariant mass of the lepton-pair in two-lepton events in data and Monte Carlo. The two lepton events are divided into the three opposite-sign and a single same-sign charge channel,  $e^\mp e^\pm$  (a),  $e^\mp \mu^\pm$  (b),  $\mu^\mp \mu^\pm$  (c) and  $l^\mp l^\mp$  (d). Errors on data points are 68% Poisson confidence limits, error band on Monte Carlo represents the statistical, jet energy scale and resolution, lepton energy scale and resolution, cross-section and luminosity uncertainties (as detailed in the text). In the bottom histogram the black data points, and the yellow uncertainty band, have been divided by the total Monte Carlo to show whether the fractional deviation of the data from the Monte Carlo lies within the uncertainty band. The red Monte Carlo line is the sum of all the Standard Model backgrounds.

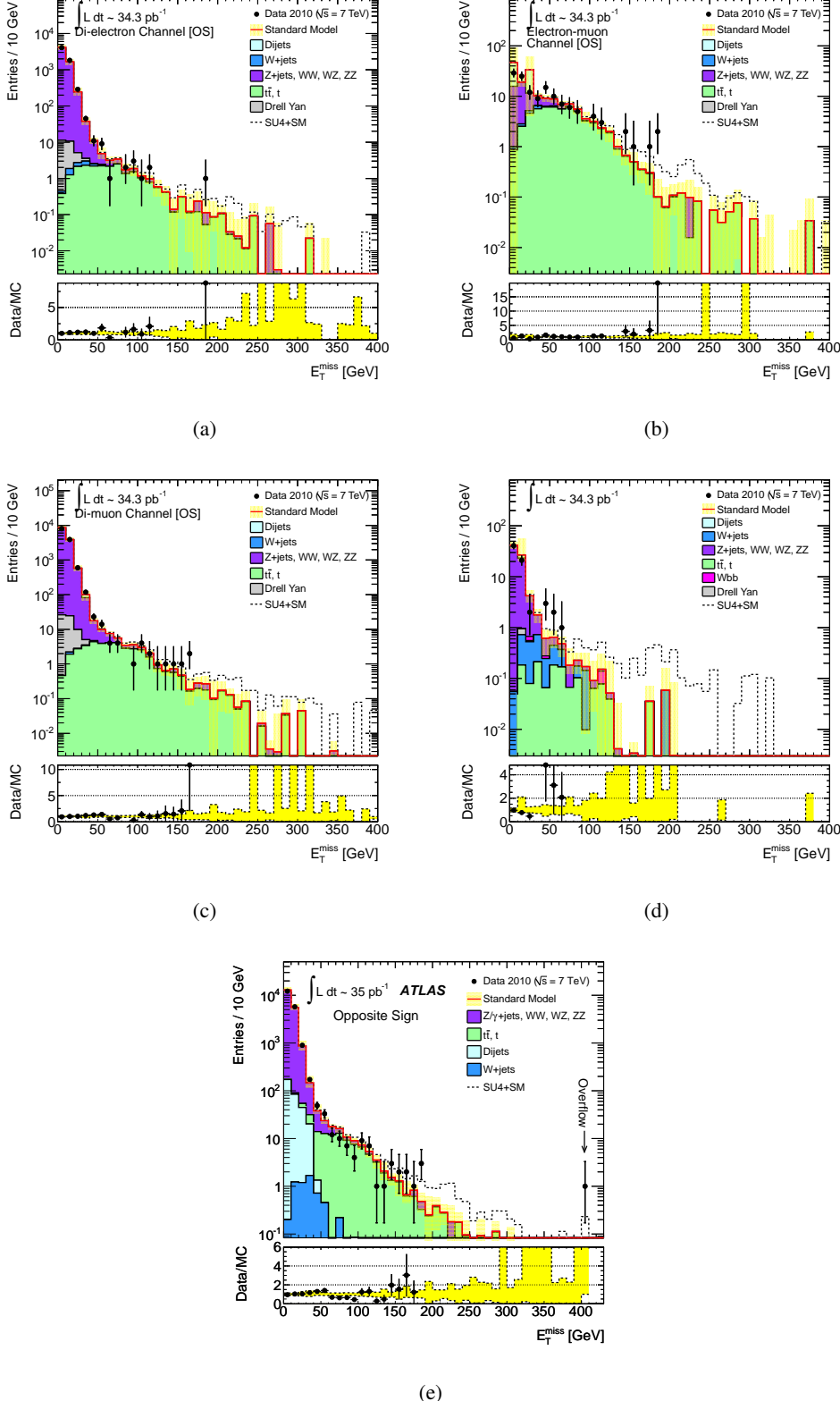


Figure 8: Distributions of the transverse missing energy ( $E_T^{miss}$ ) of two-lepton events in data and Monte Carlo. The two lepton events are divided into the three opposite-sign and a single same-sign charge channel,  $e^{\mp}e^{\pm}$  (a),  $e^{\mp}\mu^{\pm}$  (b),  $\mu^{\mp}\mu^{\pm}$  (c) and  $l^{\mp}l^{\pm}$  (d). (e) shows the  $E_T^{miss}$  distribution for the OS dilepton events. The distribution has an overflow bin which corresponds to a  $\mu\mu$  event with  $E_T^{miss}$  value 600 GeV. Errors on data points are 68% Poisson confidence limits, error band on Monte Carlo represents the statistical, jet energy scale and resolution, lepton energy scale and resolution, cross-section and luminosity uncertainties (as detailed in the text). In the bottom histogram the black data points, and the yellow uncertainty band, have been divided by the total Monte Carlo to show whether the fractional deviation of the data from the Monte Carlo lies within the uncertainty band. The red Monte Carlo line is the sum of all the Standard Model backgrounds.

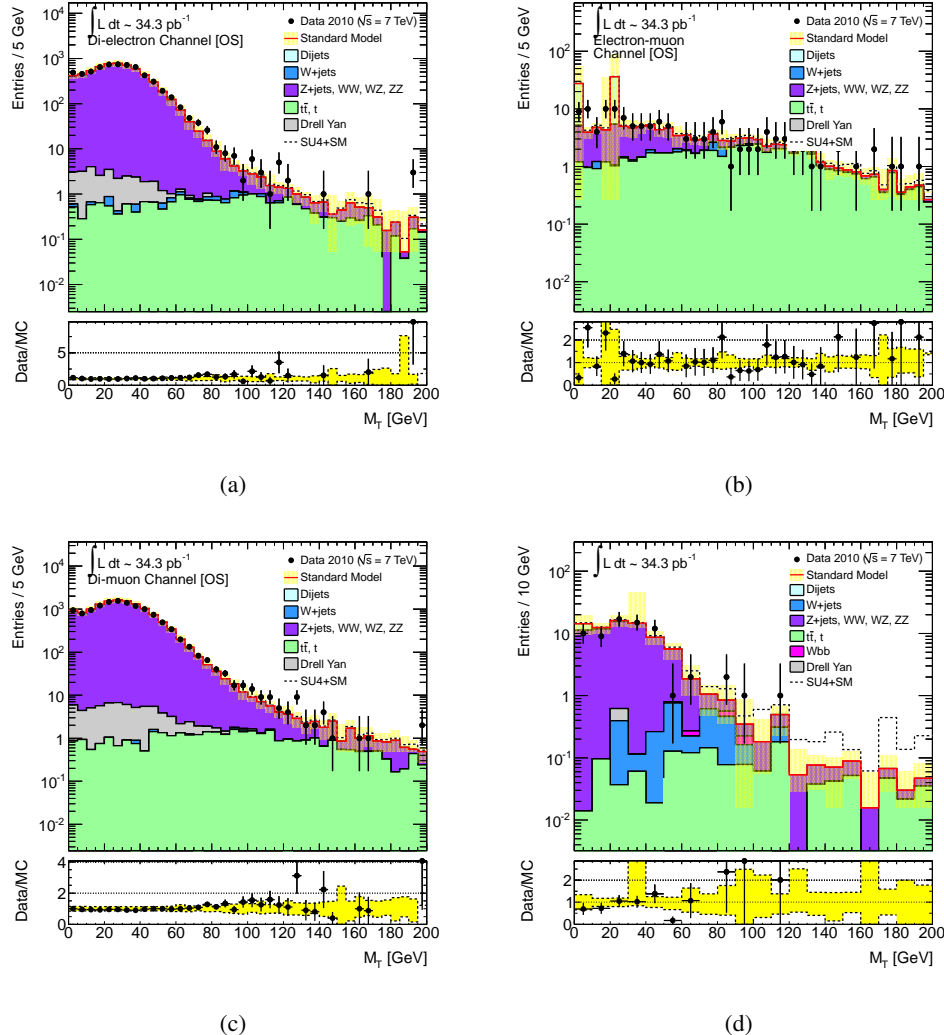


Figure 9: Distributions of the transverse mass ( $M_T$ ) of the highest  $p_T$  lepton in two-lepton events in data and Monte Carlo. The two lepton events are divided into the three opposite-sign and a single same-sign charge channel,  $e^\mp e^\pm$  (a),  $e^\mp \mu^\pm$  (b),  $\mu^\mp \mu^\pm$  (c) and  $l^\mp l^\mp$  (d). Errors on data points are 68% Poisson confidence limits, error band on Monte Carlo represents the statistical, jet energy scale and resolution, lepton energy scale and resolution, cross-section and luminosity uncertainties (as detailed in the text). In the bottom histogram the black data points, and the yellow uncertainty band, have been divided by the total Monte Carlo to show whether the fractional deviation of the data from the Monte Carlo lies within the uncertainty band. The red Monte Carlo line is the sum of all the Standard Model backgrounds.

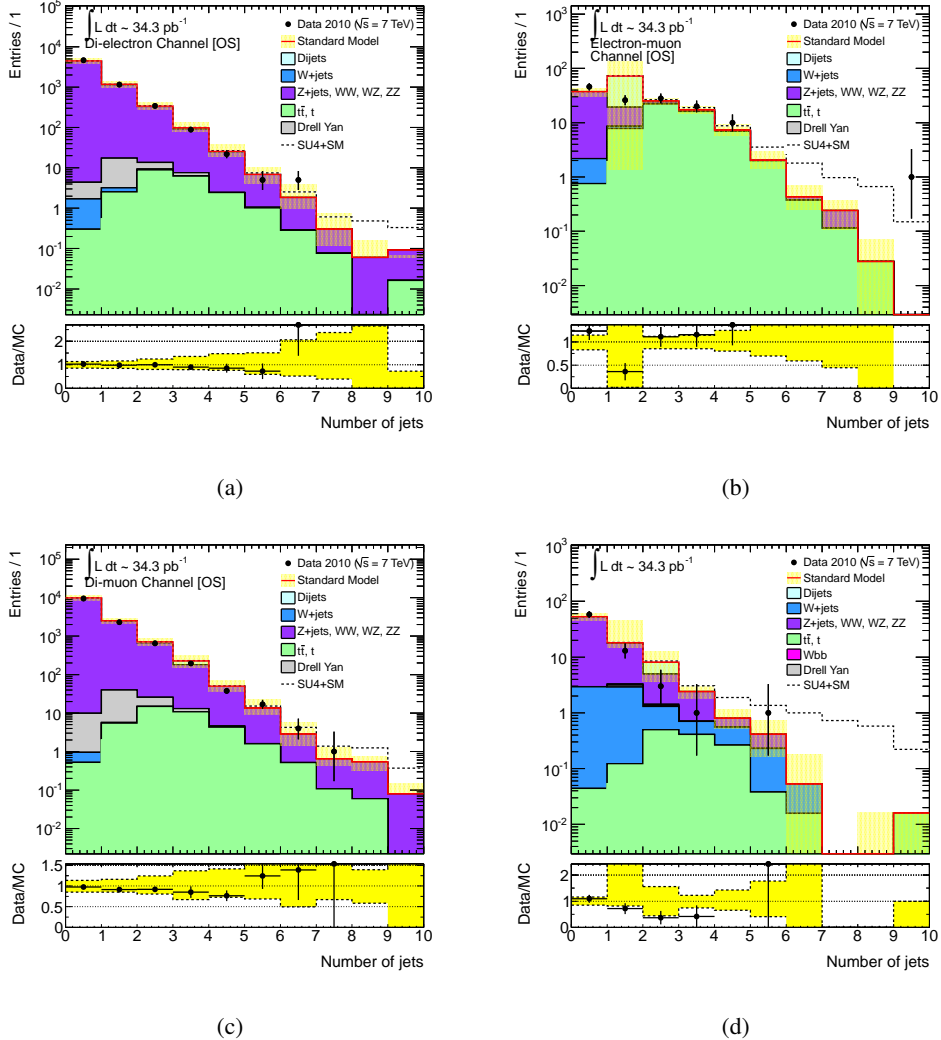


Figure 10: Distributions of the total number of jets in the two-lepton events in data and Monte Carlo. The two lepton events are divided into the three opposite-sign and a single same-sign charge channel,  $e^\mp e^\pm$  (a),  $e^\mp \mu^\pm$  (b),  $\mu^\mp \mu^\pm$  (c) and  $l^\mp l^\mp$  (d). Errors on data points are 68% Poisson confidence limits, error band on Monte Carlo represents the statistical, jet energy scale and resolution, lepton energy scale and resolution, cross-section and luminosity uncertainties (as detailed in the text). In the bottom histogram the black data points, and the yellow uncertainty band, have been divided by the total Monte Carlo to show whether the fractional deviation of the data from the Monte Carlo lies within the uncertainty band. The red Monte Carlo line is the sum of all the Standard Model backgrounds.

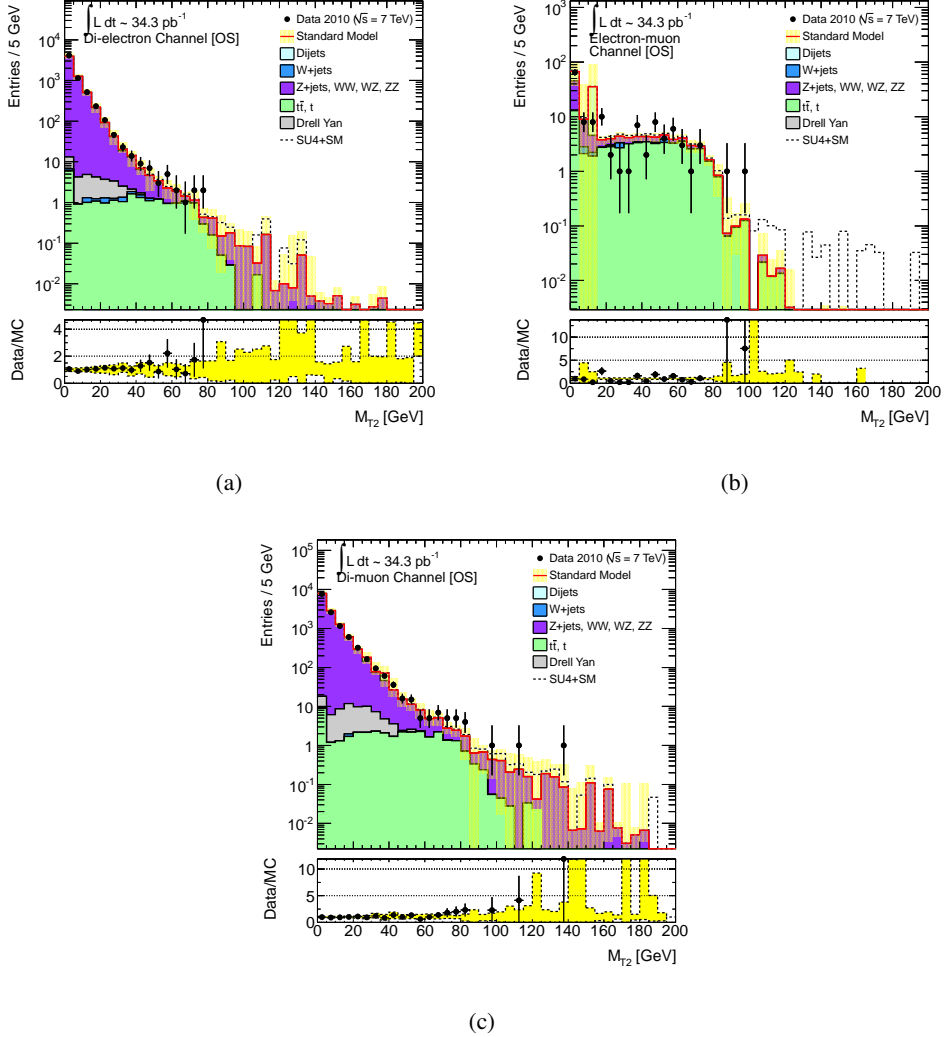


Figure 11: Distributions of event  $M_{T2}$  in the two-lepton events in data and Monte Carlo. The two lepton events are divided into the three opposite-sign and a single same-sign charge channel,  $e^\mp e^\pm$  (a),  $e^\mp \mu^\pm$  (b),  $e^\pm \mu^\pm$  (c) and  $l^\mp l^\mp$  (d). Errors on data points are 68% Poisson confidence limits, error band on Monte Carlo represents the statistical, jet energy scale and resolution, lepton energy scale and resolution, cross-section and luminosity uncertainties (as detailed in the text). In the bottom histogram the black data points, and the yellow uncertainty band, have been divided by the total Monte Carlo to show whether the fractional deviation of the data from the Monte Carlo lies within the uncertainty band. The red Monte Carlo line is the sum of all the Standard Model backgrounds.

## 7 Background Determination

### 7.1 Summary

There are five main backgrounds to a di-lepton search:

- $Z/\gamma \rightarrow ll + \text{jets}$  background
- Fully-leptonic  $t\bar{t}$
- Dibosons
- Fakes (from single top,  $W \rightarrow l\nu + \text{jets}$ , QCD, semi-leptonic  $t\bar{t}$  and so on)
- Cosmics

Completely data-driven methods are used to estimate the contribution from fakes and cosmics. For  $t\bar{t}$  and  $Z/\gamma \rightarrow ll + \text{jets}$  the techniques used are partially data-driven. For diboson and single top, the estimates are purely based on Monte Carlo. Whilst in the opposite-sign channel the background is dominated by true lepton-pairs, most of the standard model backgrounds to the same-sign search involve at least one fake lepton in the final state. We give in this section an overview of the relative importance of these background components for the three analyses.

#### Same-Sign Backgrounds

The dominant background in the signal region for a same-sign analysis is  $t\bar{t}$  production. Here, one lepton originates from a  $W$  decay, the other from a semi-leptonic  $b$  decay.  $t\bar{t}$  production gives events with jets. The semi-leptonic  $W$  and  $b$  decays gives real, but only a moderate amount of missing transverse energy. This background can be suppressed by requiring high missing transverse energy.

The  $W+\text{light-quark jets}$  and  $Wbb+\text{jets}$  processes are also among the major backgrounds in this analysis. In  $W+\text{jets}$  events, one lepton arises from  $W \rightarrow l\nu$  decay, while the other is a light jet faking a lepton. In  $Wbb+\text{jets}$  events, one lepton originates from the decay of the  $W$  whilst the other originates from the decay of either of the two  $b$  quarks.

QCD and  $b\bar{b}$  backgrounds are potentially dangerous because they carry very high cross-sections. There are a few mechanisms in  $b\bar{b}$  decay by which same-sign lepton pairs can be produced. In one mechanism, one of the leptons originates from a semi-leptonic  $b$  decay and the second arises when one of the jets is misidentified as a lepton. In a second mechanism, both gluons in a gluon-gluon event split into a  $b\bar{b}$  pair. This potentially leads to a pair of same-sign leptons in the final state. A small number of other mechanisms *e.g.*  $B^0 - \bar{B}^0$  mixing, also exist. The  $p_T$  spectrum of leptons from semi-leptonic  $b$  decays drops off sharply at high  $p_T$ . By requiring high  $p_T$  leptons,  $b\bar{b} \rightarrow c\bar{c}ll\nu\nu$  background can be suppressed by orders of magnitude. Since a lepton coming from a semi-leptonic  $b$  decay will typically be associated with hadronic depositions, tight isolation criteria will also help to prevent these leptons from contributing to the signal selection.

Diboson events ( $WZ$  and  $ZZ$ ) produce three or more leptons. If, however, one of the leptons is not reconstructed it is possible to obtain a same-sign lepton pair. Because the  $W$  decays to a lepton and a neutrino, such events are also likely to be associated with high missing transverse energy. Two same-sign leptons may arise from  $W^\pm W^\pm$  pair production, but also from  $W^\pm W^\mp$  pair production when one of the

leptons has its charge misidentified ( $< 2\%$  probability of electron charge misidentification). The inclusive cross-section for same-sign  $WW$  production is fairly small [18] and so we expect the contribution from this type of background to be negligible in the signal region.

### Opposite-Sign Backgrounds

The major standard model backgrounds to a general search for two opposite-sign lepton final states are:  $t\bar{t}$ , dibosons, Drell Yan,  $Z$ +jets, single top and  $W$ +jets. The most irreducible of these is usually  $t\bar{t}$ . Estimates of its contribution tend to rely on kinematic reconstruction of the top candidates (which are not particularly numerous at the integrated luminosities considered here).  $W$ +jets and  $Z$ +jets events can often be isolated by exploiting cuts on the transverse mass of the lepton or cuts on the invariant mass of the lepton pair. Data-driven estimates of diboson event rates are difficult at these luminosities. After a high missing energy cut,  $W$ +jets,  $Z$ +jets and Drell Yan backgrounds are considerably reduced. Top pair production is associated with high missing energy final states from the production of two neutrinos, as are  $WW$  and  $WZ$  pair production diboson events – and so these backgrounds dominate high missing transverse energy signal regions.

### Opposite-Sign Backgrounds after Flavour Subtraction

In contrast for an opposite-sign ‘flavour subtraction’ analysis the standard model predicts no excess of same flavour  $t\bar{t}$  events over different flavour  $t\bar{t}$  events, similarly no excess for  $WW$  events. The dominant standard model contributions in the signal region to a two-lepton analysis thus naturally cancel in a flavour subtraction analysis. After flavour subtraction there will be an excess of  $Z$ +jets, Drell Yan and  $WZ$  diboson events (the  $Z$  is reconstructed in preference to the lepton from the  $W$ ) – but in the high missing transverse energy signal region these excesses will be small, as they are for an inclusive two-lepton analysis. The  $WZ$  events will behave slightly differently to  $Z \rightarrow ll$ +jets events in that the escaping neutrino from the  $W$  decay will give rise to events with higher associated missing energy. But the cross-section for  $WZ$  boson pair production is small, and so the expected contribution to a flavour subtraction analysis is small.  $ZZ$  events will contribute negligibly to a flavour subtraction analysis given the small cross-section and the requirement that two of the four leptons fail reconstruction.

The fake background to the same-sign search can be estimated in the same way as the fake background to the opposite-sign search. The techniques used to estimate fake background sources are given next in Sections 7.2 and 7.3. The contribution to the opposite-sign channels from  $Z/\gamma \rightarrow ll$ +jets events is estimated in Section 7.7 and the contribution to these channels from fully-leptonic  $t\bar{t}$  events is estimated in Section 7.6. These background estimations can then be used to set limits for the opposite-sign, same-sign and finally flavour subtraction analyses. In the latter case the estimations in the different opposite-channels will be appropriately subtracted to obtain flavour-subtracted background estimations. The estimates of the subtracted background will be obtained in Section 8.3. The limit setting procedures are fully detailed in Sections 8.2, 8.1 and 8.3.

## 7.2 Data Driven Fake Background estimation: Methods

In the same-sign dilepton channel, most of the SM background processes involves at least one fake lepton in the final state. The fake backgrounds for the di-lepton search include double-fake sources such as  $b\bar{b}$  and  $c\bar{c}$ , as well as true-fake sources such as  $W/Z$ +jets.  $t\bar{t}$  production is also most likely to be a true-fake background for the same-sign channels. Therefore, the following section describes the method for obtaining these background component directly using data.

For backgrounds involving fake leptons, their contributions in the signal region can be estimated from control regions where the leptons failed some of the pre-selection. It worths to notice that here "fake" does not only refer to the particle type. Instead it represents the fact that the object are not supposed to pass the pre-selection. For example, most "fake muons" in the following context are well-reconstructed real muons, except for the fact that at truth level they are not isolated.

### 7.2.1 Matrix Method : Di-Electron channel

For electrons, we preselect candidates passing the selection criteria described in the Section 4.

The matrix method is used to determine the magnitude of the fake lepton backgrounds in the dilepton signal regions. We measure the probabilities  $r$  and  $f$  that a real or fake preselected lepton will pass the tight criteria using purified control regions. The composition of the signal samples can then be extracted by inverting Equation 4, which relates the 'true' composition of the sample in terms of Real ("R") and Fake ("F") leptons to its 'observable' composition in terms of Pass (passing "tight", "T") and NotPass (failing "tight", "L") leptons,

$$\begin{bmatrix} N_{TT} \\ N_{TL} \\ N_{LT} \\ N_{LL} \end{bmatrix} = \begin{bmatrix} rr & rf & fr & ff \\ r(1-r) & r(1-f) & f(1-r) & f(1-f) \\ (1-r)r & (1-r)f & (1-f)r & (1-f)f \\ (1-r)(1-r) & (1-r)(1-f) & (1-f)(1-r) & (1-f)(1-f) \end{bmatrix} \begin{bmatrix} N_{RR} \\ N_{RF} \\ N_{FR} \\ N_{FF} \end{bmatrix} \quad (4)$$

### 7.2.2 Fake Rate

The fake electron control region is obtained using the following selection criteria:

- Exactly one preselected electron is required in the event.
- The  $\Delta\phi$  between  $E_T^{\text{miss}}$  and one of the reconstructed jets smaller than 0.1. A reconstructed jet has  $p_T > 20 \text{ GeV}$  and  $|\eta| < 2.5$ .
- The transverse mass of the electron candidate and  $E_T^{\text{miss}}$  smaller than 60 GeV if electron  $p_T$  is above 30 GeV.

The efficiencies of passing "tight" obtained using these cuts are shown in Figure 12 and compared with Monte Carlo simulations. A good agreement between data and MC can be seen.

The fake rate has some dependence on  $E_T^{\text{miss}}$ ,  $\eta$  and  $H_T$ . We parameterize the fake rate  $f$  as a function of  $\eta$  and  $H_T$ , which reproduces the dependence on  $E_T^{\text{miss}}$ , shown in Figure 13.

### 7.2.3 Signal Efficiency

To create a real electron control region, we select a sample which is highly purified in Z boson events by requiring one tight electron and one opposite-signed preselected electron whose invariant mass lies in the range 86-96 GeV. For each tight electron in the event, we then check whether or not the other electron passes the tight selection cuts. The efficiency of the tight selection is shown in Figure 14.

### 7.2.4 Uncertainty Estimation

For the electron fakes, there are three fake origins: light flavor jets, photon conversion and heavy flavor meson decay. For each electron candidate, we check if it matches to a conversion vertex and if the closest jet has large SV0 b-tagging weight ( $SV0 > 5.72$ ) to distinguish these three fake components.

- heavy flavor enhanced: require large SV0 weight of closest jet

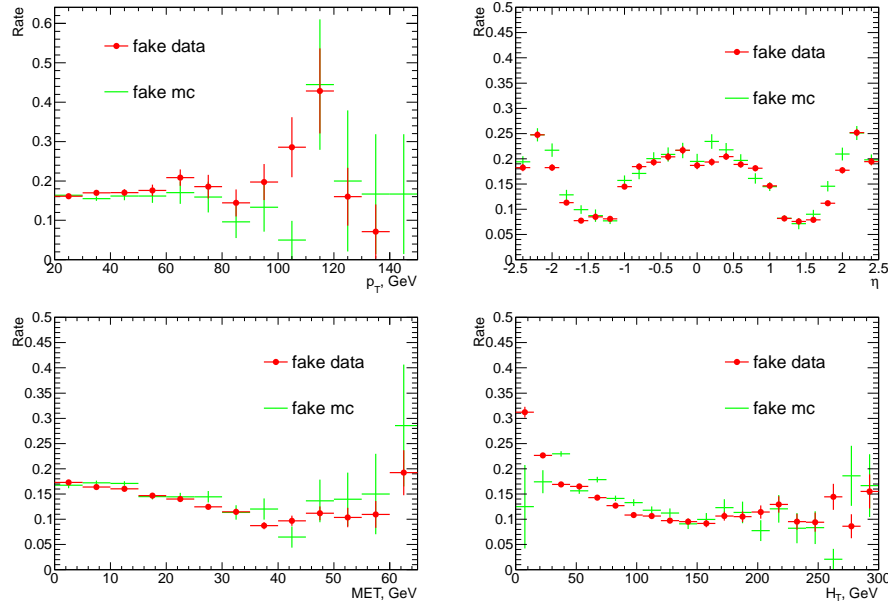


Figure 12: Fake electron passing “tight” rate as a function of  $p_T$ ,  $\eta$ , missing transverse energy and  $H_T$  (the  $p_T$ -sum for jets with  $E_T > 20$  GeV and  $|\eta| < 2.5$ ).

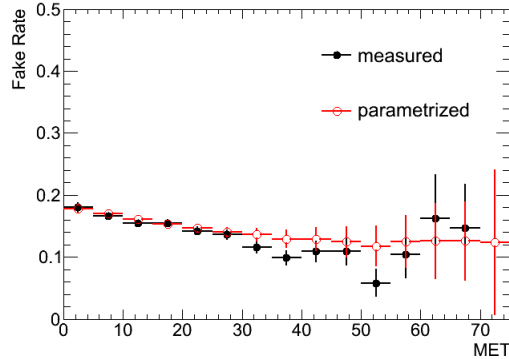


Figure 13: Fake electron passing “tight” rate as a function of  $E_T^{\text{miss}}$  from measurement (black) and parametrization on  $\eta$  and  $H_T$  (red).

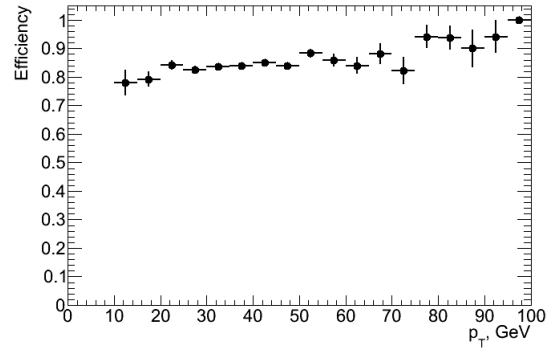


Figure 14: Real electron passing “tight” rate as a function of  $p_T$ .

- conversion enhanced: require match to conversion vertex and small  $S V0$ -weight of closest jet
- light flavor enhanced: require no match to conversion vertex and small  $S V0$  weight of closest jet

The fake rates are measured in each of these control regions are shown in Figure 15.

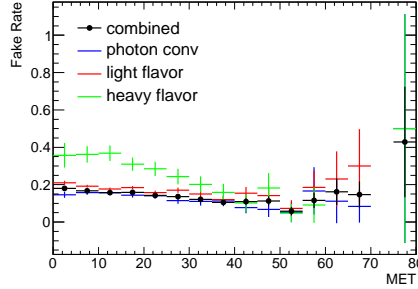


Figure 15: Fake electron passing “tight” rate as a function of  $E_T^{\text{miss}}$  for each fake component.

As can be seen, the fake rate for electrons from heavy flavor meson decay ( $\sim 30\%$ ) is much higher than the others ( $\sim 15\%$ ). It indicates that the overall fake rate is sensitive to the composition of fake electrons in the preselected electron sample. The dominant systematic uncertainty is due to the potential difference among the mixture of different processes that contribute to the fake rate control region and the signal region. Since the control region is dominated by di-jet events, the systematic uncertainty is evaluated by comparing the fraction of di-jet events in the signal region and in the control region.

Figure 16 shows the distribution of  $S V0$  weights of the closest jets to electron candidates in the fake control region and the di-electron signal region. We found  $5.0 \pm 0.1\%$  of electron candidates in the fake control region pass the large  $S V0$  requirement, and the fraction in the same-sign di-electron region is  $7.3 \pm 1.2\%$ .

The  $S V0 > 5.72$  cut has a very large rejection power ( $O(200)$ ) to electrons from light flavor jets and photon conversions. In the  $t\bar{t}, b\bar{b}/c\bar{c}$  Monte Carlo(MC) samples, the fraction of electrons with large  $S V0$  weight varies between 20% and 40%. From the measurement of  $S V0$  b-tagging efficiency, the data/MC scale factor is close to 1, ranging from 0.8 to 1.1, so we can make a rough estimation of the fraction of electrons from heavy flavor jets in the fake control region ( $C_{hf}$ , 12.5%-25%) and in the di-electron signal region( $C_{hf}^*$ , 18.3%-36.5%). Therefore, we have the equations

$$\text{Fake Rate}_{\text{heavy flavor enhanced}} (\sim 30\%) = f_{hf}, \quad (5)$$

$$\text{Fake Rate}_{\text{fake control region}} (\sim 15\%) = (1 - C_{hf}) \cdot f_{lf,pc} + C_{hf} \cdot f_{hf}, \quad (6)$$

$$\text{Fake Rate}_{\text{di-electron region}} = (1 - C_{hf}^*) \cdot f_{lf,pc} + C_{hf}^* \cdot f_{hf}, \quad (7)$$

where  $f_{hf}$  is the fake rate of electrons from heavy flavor meson decay and  $f_{lf,pc}$  is the fake rate of other fake electrons. By varying the  $C_{hf}$  and  $C_{hf}^*$  according to the estimation, the derived fake rate in di-electron region changes by 30% with respect to the fake rate measured in the fake control region. This value is taken as the systematic uncertainty.

Statistical uncertainties on the measured event yields are evaluated as follows. The passing “tight” efficiencies have a binomial statistical error due to limited control region statistics, and a systematic uncertainty to account for any bias caused by the fact that we measure the efficiencies in control regions which may have different lepton kinematics or event topologies than our signal regions. The tight/preselected  $N$ ’s are simply observed event multiplicities, so they are given a Poisson uncertainty. To be conservative, we use the two worst case scenarios to measure the impact of the systematic uncertainty on the real/fake  $N$ ’s, i.e. we shift the real efficiencies up and fake efficiencies down simultaneously to obtain the upwards shift in  $N_{RR}$ , and vice-versa.

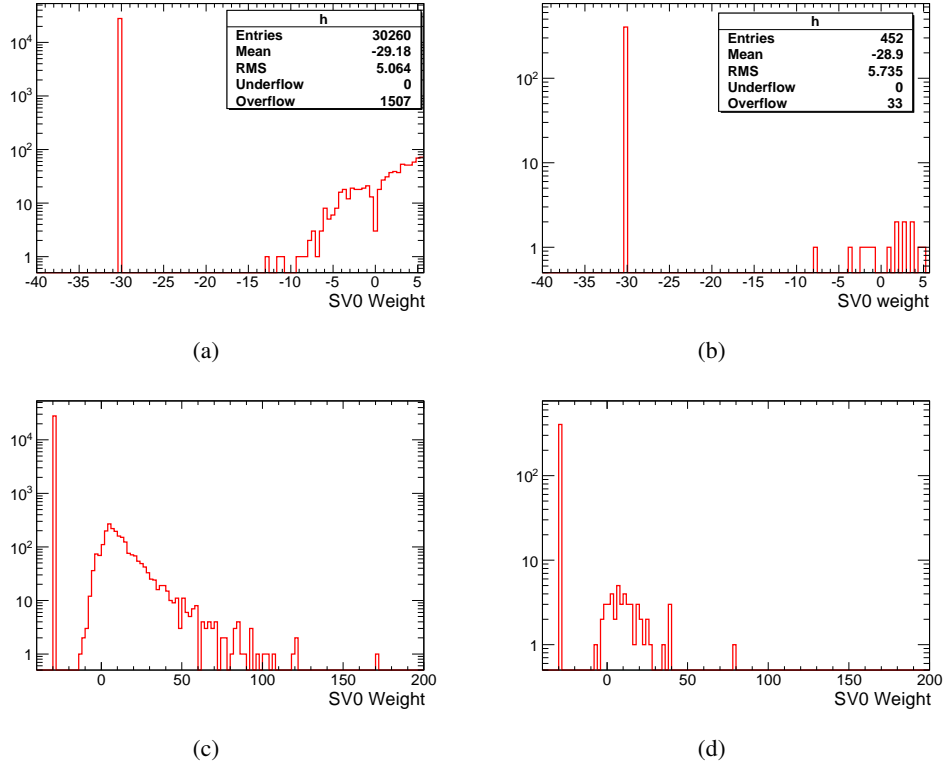


Figure 16: Zoomed in( $SV0 < 5.72$ ) plots for  $SV0$  b-tagging weights of the closest jets to electron candidates in the fake control region (a) and the same-sign di-electron signal region (b), where we get a probability of  $5.0 \pm 0.1\%$  ( $7.3 \pm 1.2\%$ ) for  $SV0$  weight above  $5.72$  in the fake control (the same-sign di-electron signal) region. (c) and (d) are similar plots of  $SV0$ , but in a more wide range.

### 7.2.5 Collision Data Validation

The method is validated with collision data, in a control region where one of the two electrons has  $E_T$  between 10 GeV and 20 GeV and the other still has  $E_T$  above 20 GeV. For period E-I, we observed 29 same-sign events, and predicted  $18.47 \pm 1.99(\text{stat}) \pm 4.60(\text{sys})$  events. The predicted contributions mostly concentrate in low  $E_T^{\text{miss}}$  region, which is consistent with observation, as shown in figure 17. For  $E_T^{\text{miss}}$  above 80 GeV, no event was observed, and the estimation is  $0.05 \pm 0.05(\text{stat}) \pm 0.02(\text{sys})$  events. For  $E_T^{\text{miss}}$  above 100 GeV, the estimation is  $0.05 \pm 0.05(\text{stat}) \pm 0.02(\text{sys})$  events.

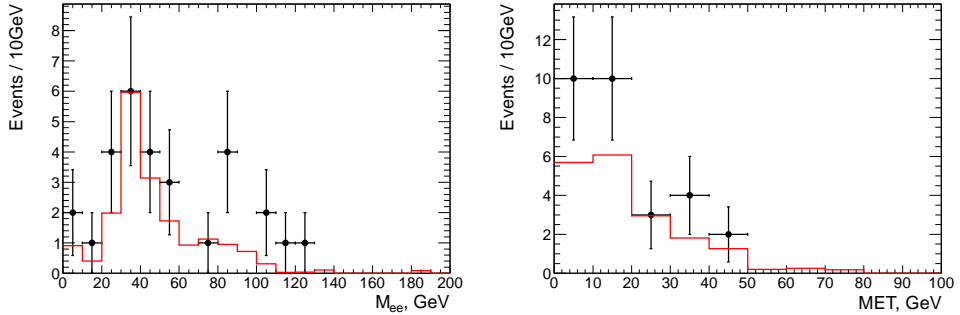


Figure 17: Predicted (red) and observed (black) distribution over invariant mass and  $E_T^{\text{miss}}$ , for low pt SS ee control sample.

### 7.2.6 mu-mu channel

#### 7.2.7 Simplified Matrix Method

In the mu-mu channel, a simplified matrix method, also known as the "pass/fail" method is used. For muons, the "loose" muons are defined as muons passing all selection cuts, except for the isolation requirement, i.e.  $\text{ptcone}20 < 1.8\text{GeV}$  and the muon-jet overlap removal. Such "loose" muons can be further categorized as "pass" (tight) muons and "fail" muons by the isolation cut.

The matrix method can be simplified if the signal efficiency approximates to 100%, which is true with the above definition of "tight" and "loose", as we will see later. As the false negative rate is so low, while the amount of double-real events are not expected to be very high, we can have very clean control samples of fakes, if we require one or both of the same-charge muons failed the isolation cut. From those control samples we can predict the fake contribution in the signal region, by applying the pass/fail ratio upon them. The pass/fail ratio  $k$  is defined as

$$k = \frac{f}{1-f} \quad (8)$$

where  $f$  represents the isolation fake rate, defined in Section 7.2.8 below.

First, we estimate the double-fake contribution with a control sample of same-charge di-muon events, which pass all the cuts as our signal sample, except for the requirement that both muons in the event must fail the isolation cut. We denote this sample as "Sample FF". From this sample, the prediction can be made by applying the pass/fail ratio  $k$  on each muon with formula

$$N_{\text{PP}}^{\text{pred,FF}} = \sum_{i=0}^{N_{\text{FF}}} k(\vec{x}_{1i})k(\vec{x}_{2i}) \quad (9)$$

$\vec{x}$  stands for the variables affecting the fake rate, for each muon respectively.

Next, we get another estimation from a similar control sample, where one muon passed the isolation cut and the other failed. This sample is a mixture of true-fake processes and double-fake ones. We denote this sample as "Sample PF". The prediction can be made by applying the pass/fail ratio on the non-isolated muon, with formula

$$N_{\text{PP}}^{\text{pred\_PF}} = \sum_{i=0}^{N_{\text{PF}}} k(\vec{x}_{fi}) \quad (10)$$

However, for double-fake sources in Sample PF, applying the above formula will lead to double-counted prediction. To be more specific, the fake-fake contribution to Sample PF is:

$$N_{\text{PF}} = \sum_{i=0}^{N_{\text{FF}}} (k(\vec{x}_{1i}) + k(\vec{x}_{2i})) \quad (11)$$

Applying formula 10 on them will lead to prediction:

$$N_{\text{PP}}^{\text{pred\_PF}} = \sum_{i=0}^{N_{\text{PF}}} k(\vec{x}_{fi}) \quad (12)$$

$$= \sum_{i=0}^{N_{\text{FF}}} (k(\vec{x}_{1i}) * k(\vec{x}_{2i}) + k(\vec{x}_{2i}) * k(\vec{x}_{1i})) \quad (13)$$

$$= 2N_{\text{PP}}^{\text{pred\_FF}} \quad (14)$$

Therefore, in order to obtain the correct data-driven prediction for all fake backgrounds, the prediction should be

$$N_{\text{PP}}^{\text{pred}} = N_{\text{PP}}^{\text{pred\_PF}} - N_{\text{PP}}^{\text{pred\_FF}} \quad (15)$$

While the contribution from true-fake source can be derived as

$$N_{\text{PP}}^{\text{pred}} = N_{\text{PP}}^{\text{pred\_PF}} - 2N_{\text{PP}}^{\text{pred\_FF}} \quad (16)$$

### 7.2.8 Fake rate

The isolation fake rate for muons from jet can be estimated from a single-muon control sample, where we require

- No more than one combined muon in the event.
- $E_T^{\text{miss}}$  less than 30GeV
- Muon  $p_T$  less than 40GeV
- Transverse mass  $M_T$  of the muon and  $E_T^{\text{miss}}$  is less than 30GeV.
- $\Delta\phi$  between missing transverse energy and MPT (a missing transverse momentum calculation based on inner detector tracks [19]) is greater than 1.0.
- Pass all our pre-selection cuts other than the isolation requirement.

Instead of obtaining an average fake rate value from this sample, we extract a parameterized fake rate function. The first reason for parameterization is because the kinematic variables affecting the fake rate could have distinct distributions between this single-muon control sample and the di-muon samples. The value averaged over different distributions will suffer large systematic uncertainty. Secondly, if the fake rate depends on the property of the event, such dependence will be shared by the two muons in the events, if both of them are from fake sources. This correlation cannot be handled if an average value is used. Instead, the systematic uncertainties on the background estimation can be reduced by using a proper parametrization.

We choose two variables of the muons for the parameterization of the fake rate function:

- $p_T$ : The transverse momentum of the muons.
- 
- $H_\phi$ : The scalar sum of  $p_T$  projection on the muon's  $\phi$  plane, for all muons, jets and the  $E_T^{\text{miss}}$ . This variable approximate the  $p_T$  of the hard scattering partons, assuming the muon is close to the production plane. It reflects the overall energy activity in the event, as well as the angular dispersion of energetic components.

$$H_\phi(\mu_i) = P_T(\mu_i) + \sum_j P_T(\mu_j) |\cos \phi_{ij}| + \sum_j P_T(jet_j) |\cos \phi_{ij}| + E_T^{\text{miss}} |\cos \phi_{iE_T^{\text{miss}}}| \quad (17)$$

Unlike the parameterization in electron fake rate study, the  $p_T$  and  $H_\phi$  are highly correlated variables. Therefore a Bayesian Neural Network (BNN) is utilized as a generic multivariate function to fit the fake rate in 2D phase space. As the BNN is an unbinned fitting, the information in the input sample can be maximally exploited. Besides, the Bayesian implementation provides a mechanism to control the complexity of the model adaptively, based on the statistical property of the input sample. As a result, the risk of over-fitting is greatly reduced.

The 2-dimensional fake rate function extracted from the single muon control sample, from collision data, can be visualised in Figure 18.

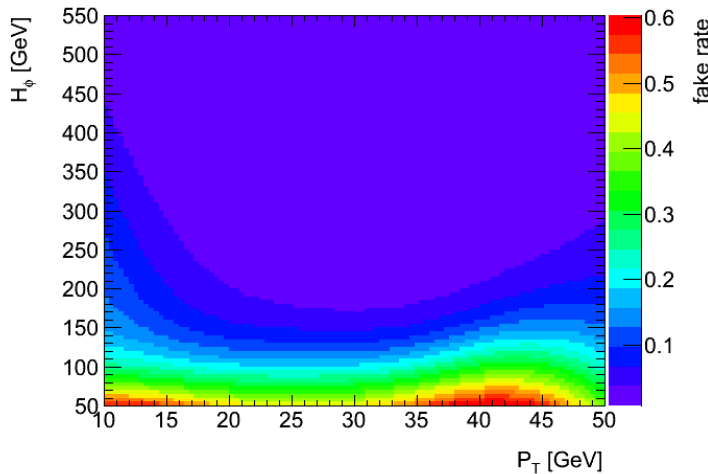


Figure 18: Muon isolation fake rate distribution in the  $p_T$  versus  $H_\phi$  phase space, parameterized by the BNN. Z-value (color) represents the fitted fake rate at each point.

### 7.2.9 Signal Efficiency

The isolation cut has very high efficiency for real-isolated muons. We can estimate the efficiency in collision data, from the control sample of  $Z \rightarrow \mu\mu$  process selected by the tag-and-probe technique. We require opposite sign muon pairs with invariant mass between 86GeV and 96GeV. In addition, at least one muon in the pair must pass the isolation cut as a "tagged" muon. The other "probe" muon can therefore provide a clean sample of real isolated muons, which gives an estimation of the efficiency as 98.2%.

The distributions over the two variables of fake rate parameterization are also examined in figure 19. The signal efficiency is sufficiently high all over the phase space.

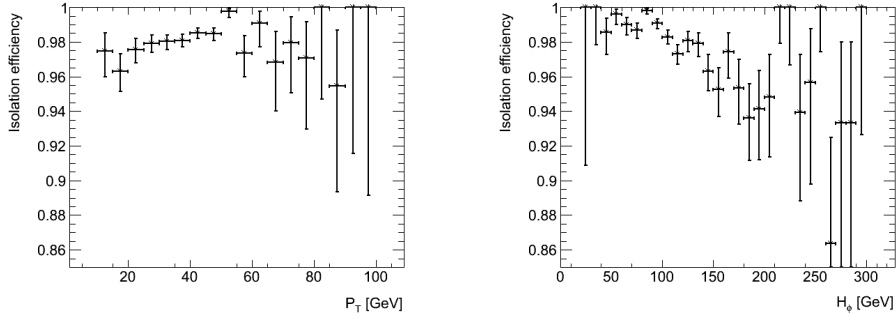


Figure 19: Isolation efficiency for  $Z$ -mass tag-and-probe muons, over muon  $p_T$  (left) and  $H_\phi$  (right).

Generally real isolated muon are much rare comparing to fakes in same-sign di-muon events. With such a high efficiency, their contribution can be negligible in the PF and FF control samples mentioned above. Therefore we assume these control samples are purely fake-involved processes.

### 7.2.10 Uncertainty estimation

- A Poisson fluctuation is considered for each event in the PF and FF control sample. Subsequently, these uncertainties are weighted by the event-by-event weight of the pass/fail ratios. Such uncertainties are considered as statistical uncertainty.
- The Bayesian Neural Network also provides uncertainty to each prediction. This uncertainty covers those due to the fit quality, as well as the statistics of the training sample. These uncertainties are counted as systematic uncertainty.
- There is also uncertainties due to parametrization of the fake rate, arising from the difference in the control samples or the correlation between the muons. This is evaluated from the data as well. We selected events with only two muons of same charge, applying all other "loose" selections, but requiring the sub-leading muons have  $p_T$  between 10GeV and 20GeV. No  $E_T^{\text{miss}}$  cut was applied. We observed 42 such events, with a data-driven prediction of  $42.6 \pm 3.9(\text{BNN}) \pm 5.7(\text{stat})$  events. The difference is well within the statistical fluctuation. We add the BNN and statistical uncertainty in quadrature considering them as uncorrelated and assign this as an additional systematic uncertainty on the method which is approximately 20%. The error due to the BNN in the fake rate prediction is then added in quadrature to the uncertainty from the validation ( $\approx 20\%$ ) in order to quote the total systematic uncertainty on the fake rate estimation method.

### 7.2.11 e-mu channel

The matrix-method is also applied to the e-mu channel, utilizing the parameterized fake rates and efficiencies as mentioned above.

### 7.2.12 Validation with Low Pt Collision Data

Again we validate the method, using a control region where one of the two leptons has  $p_T$  between 10GeV and 20GeV. For period E-I, we observed 62 same-sign e-mu events, with a data-driven prediction of  $64.81 \pm 5.04(stat) \pm 4.26(sys_{electron}) \pm 0.75(sys_{muon})$  events. The predicted distribution over  $E_T^{\text{miss}}$  can be well matched with observation, as shown in figure 20.

2 SS e-mu events with  $E_T^{\text{miss}}$  above 80GeV were observed in this control sample, and the data-driven algorithm predicted  $0.68 \pm 0.26(stat) \pm 0.12(sys_{electron}) \pm 0.05(sys_{muon})$  events. For  $E_T^{\text{miss}}$  greater than 100GeV, the prediction of background contribution is  $0.30 \pm 0.17(stat) \pm 0.05(sys_{electron}) \pm 0.03(sys_{muon})$  events.

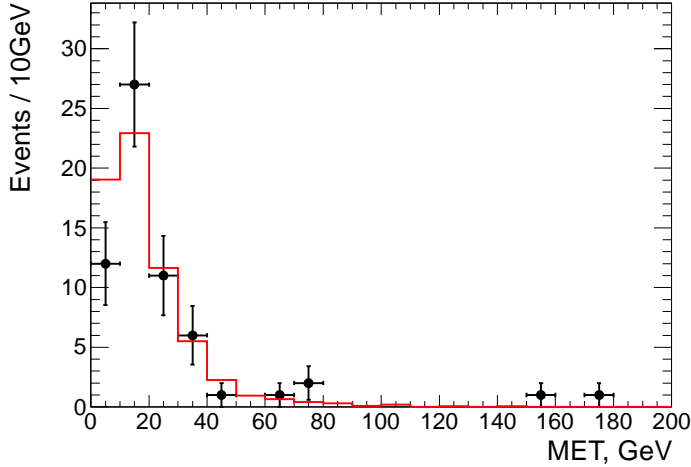


Figure 20: Predicted (red) and observed (black) distribution over  $E_T^{\text{miss}}$ , for low pt SS e-mu control sample.

### 7.2.13 High Pt Collision Data

In the high pt region, with both leptons  $p_T$  greater than 20GeV. Inclusively without any  $E_T^{\text{miss}}$  cut, we predicted  $5.28 \pm 1.10(stat) \pm 0.59(sys_{electron}) \pm 0.10(sys_{muon})$  SS events, with an observation of 5 events. The predicted distribution over  $E_T^{\text{miss}}$  is compared with observation in figure 21.

No SS e-mu event was observed with  $E_T^{\text{miss}}$  greater than 80GeV, and the prediction of background is  $0.028 \pm 0.026(stat) \pm 0.002(sys_{electron}) \pm 0.009(sys_{muon})$  events. For  $E_T^{\text{miss}}$  above 100GeV, the prediction is  $0.030 \pm 0.026(stat) \pm 0.005(sys_{electron}) \pm 0.009(sys_{muon})$  events.

## 7.3 Data Driven Fake Background estimation: Results

### 7.3.1 Opposite Sign Di-Electron Channel

In the opposite-sign dielectron channel, inclusively without any  $E_T^{\text{miss}}$  cut, the data has 6250 events, which is dominated by the Drell-Yan and Z boson production. The estimated fake contribution is  $25.11 \pm 5.51(stat) \pm 8.07(sys)$  events.

For  $E_T^{\text{miss}}$  greater than 100GeV, the data has 4 events, with the largest expected contribution from  $t\bar{t}$  process. The estimated fake background contribution is  $0.31 \pm 0.21(stat) \pm 0.11(sys)$  events. With  $E_T^{\text{miss}}$  above 150GeV, the data has 1 event, and the fake prediction is  $-0.02 \pm 0.02(stat) \pm 0.01(sys)$  events. The negative weight is due to low statistics, since the matrix method prediction is a combination of all the events, some of them provide positive weights, while some others have negative weights.

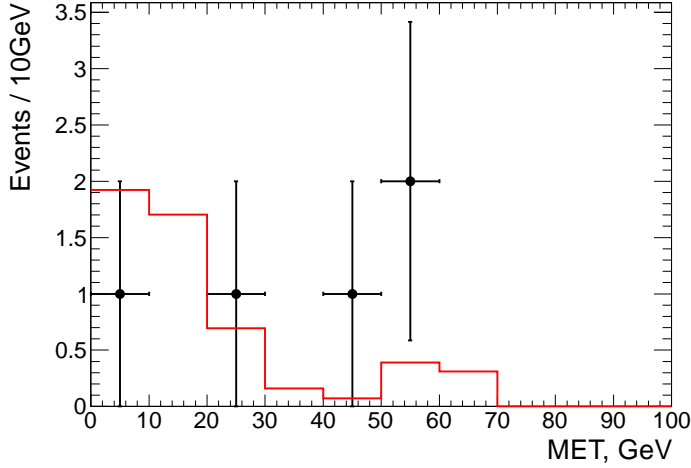


Figure 21: Predicted (red) and observed (black) distribution over  $E_T^{\text{miss}}$ , for high pt SS e-mu sample (before  $E_T^{\text{miss}}$  cut).

### 7.3.2 Same Sign Di-Electron Channel

For period E-I, the data has 62 same-sign di-electron pairs (both  $E_T$  above 20 GeV). The estimated fake contribution is  $11.37 \pm 1.23(\text{stat}) \pm 3.66(\text{sys})$  events. Clearly shown in the invariant mass distribution as figure 22, the estimated fake contribution does not predict the contribution of Z+jets due to trident electrons.<sup>1</sup>

These trident electrons have a higher rate of passing “tight” selection criteria than the measured rate from control region as these are real electrons, and this rate is not modeled in the matrix method. The rate of  $Z \rightarrow ee$  producing same-sign events is a combination of trident and charge mis-identification of the electron charge track, therefore the rate is much higher under the  $Z$  mass peak and very low  $E_T^{\text{miss}}$  region than the high  $E_T^{\text{miss}}$  region which defines the signal region for this SS dilepton analysis.

Out of 62 observed data events in Figure 22, the charge mis-identification study detailed in the Appendix F predicts  $48.3 \pm 7.7(\text{stat.})$  mis-id  $Z \rightarrow ee$  events and the fake rate method predicts  $11.37 \pm 1.23(\text{stat}) \pm 3.66(\text{sys})$  fake background events. The predicted numbers are in good agreement with the observed data events.

For  $E_T^{\text{miss}} > 80\text{GeV}$ , the data has 0 event. The estimated fake contribution is  $0.12 \pm 0.12(\text{stat}) \pm 0.05(\text{sys})$  events. With  $E_T^{\text{miss}}$  cut above  $100\text{GeV}$ , the estimated fake contribution is  $0.12 \pm 0.12(\text{stat}) \pm 0.05(\text{sys})$ .

### 7.3.3 Opposite Sign Di-Muon Channel

13 events with  $E_T^{\text{miss}} > 100$  GeV are observed. Fake sources are estimated to give  $0.014 \pm 0.010(\text{stat}) \pm 0.004(\text{sys})$  events. For  $E_T^{\text{miss}}$  greater than  $150\text{GeV}$ , there is no event left in the non-isolated samples, therefore no valid prediction can be made.

<sup>1</sup>A process of an electron emitting a photon in external (and internal, since the two are not distinguishable) bremsstrahlung traversing the material in the tracking volume and the photon later converts into an  $e^+e^-$  pair, and in the end we detect three tracks coming from the electron, forming a trident pattern. In the hard bremsstrahlung case, for instance,

$$e_{\text{hard}}^- \rightarrow e_{\text{soft}}^- + \gamma_{\text{hard}} \rightarrow e_{\text{soft}}^- + e_{\text{soft}}^- + e_{\text{hard}}^+, \quad (18)$$

the reconstructed positron contains most of the energy of the electron from the  $Z$  decay but with opposite charge, therefore it produces same-sign events in the  $Z$  mass region.

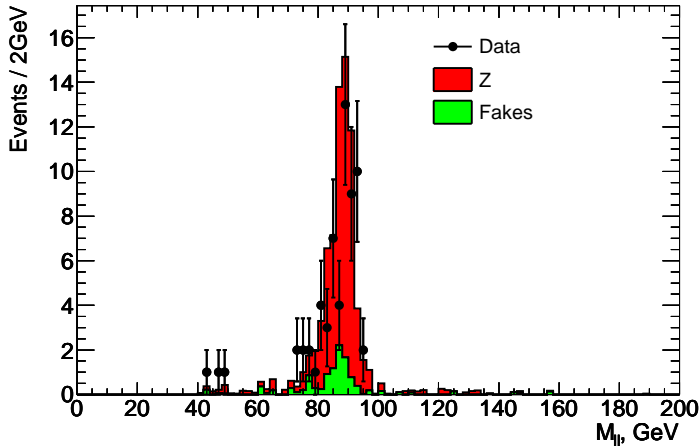


Figure 22: Predicted fake rate(green), Z( $e e$ ) MC (solid red) and observed data(black) distribution over  $M_{ee}$ , for high pt SS ee (no  $E_T^{\text{miss}}$  cut).

### 7.3.4 Same Sign Di-Muon Channel

For  $E_T^{\text{miss}}$  greater than 80GeV,no event was observed, while the data-driven algorithm predicted  $0.095 \pm 0.053(\text{stat}) \pm 0.021(\text{sys})$  SS events from fake sources. For  $E_T^{\text{miss}}$  greater than 100GeV,the prediction of fake contribution is  $0.014 \pm 0.010(\text{stat}) \pm 0.005(\text{sys})$  SS events.

### 7.3.5 Opposite Sign Electron-Muon Channel

In the OS channel, the method predicted  $8.13 \pm 1.41(\text{stat}) \pm 1.95(\text{sys}_{\text{electron}}) \pm 0.12(\text{sys}_{\mu\text{on}})$  fake events inclusively before  $E_T^{\text{miss}}$  cut, and we observed 131 events. With  $E_T^{\text{miss}}$  greater than 100GeV,we predicted  $-0.15 \pm 0.05(\text{stat}) \pm 0.06(\text{sys}_{\text{electron}}) \pm 0.01(\text{sys}_{\mu\text{on}})$  OS events coming from fake sources, and 13 events were observed. There are 4 events observed with  $E_T^{\text{miss}}$  greater than 150GeV, and the prediction is  $-0.05 \pm 0.03(\text{stat}) \pm 0.02(\text{sys}_{\text{electron}}) \pm 0.01(\text{sys}_{\mu\text{on}})$ .

### 7.3.6 Same Sign Electron-Muon Channel

In the high pt region, with both leptons'  $p_T$  greater than 20GeV. Inclusively without any  $E_T^{\text{miss}}$  cut, we predicted  $5.28 \pm 1.10(\text{stat}) \pm 0.59(\text{sys}_{\text{electron}}) \pm 0.10(\text{sys}_{\mu\text{on}})$  SS events coming from fake sources. The observation is 5 SS events.

For  $E_T^{\text{miss}}$  greater than 80GeV,0 event was observed, while the data-driven algorithm predicted  $0.028 \pm 0.026(\text{stat}) \pm 0.002(\text{sys}_{\text{electron}}) \pm 0.009(\text{sys}_{\mu\text{on}})$  SS events from fake sources. For  $E_T^{\text{miss}}$  greater than 100GeV,the prediction of fake contribution is  $0.030 \pm 0.026(\text{stat}) \pm 0.005(\text{sys}_{\text{electron}}) \pm 0.009(\text{sys}_{\mu\text{on}})$  SS events.

## 7.4 $t\bar{t}$ background in SS due to charge flip

The process  $t\bar{t}$  goes to dilepton can be a background to the same sign analysis due to the possibility of charge mis-identification, or charge flip due to hard bremsstrahlung followed by asymmetric pair production ( $e_{\text{hard}}^{\mp} \rightarrow \gamma_{\text{hard}} e_{\text{soft}}^{\mp} \rightarrow e_{\text{soft}}^{\mp} e_{\text{soft}}^{\mp} e_{\text{hard}}^{\pm}$ ), known as trident events. Since the charge flip rate for muons is negligible, dilepton  $t\bar{t}$  is only a significant background for the  $e^{\pm}e^{\pm}$  and  $e^{\pm}\mu^{\pm}$  channels.

Due to limited statistics of same sign events in  $t\bar{t}$  Monte Carlo, we weight opposite sign events based upon the charge flip rate. We match reconstructed electrons in  $Z \rightarrow ee$  Monte Carlo to their

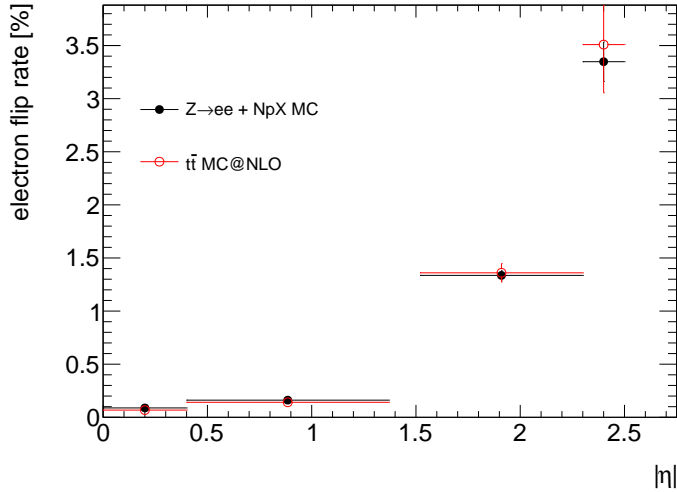


Figure 23: The flip rate as a function of  $|\eta|$  for  $Z \rightarrow ee$  and  $t\bar{t}$  Monte Carlo

corresponding truth particles using the `McTruthClassifier` Tool and determine the charge flip rate as a function of  $|\eta|$ , see Figure 23. We test the closure of our method by comparing the number of same-sign events in  $Z \rightarrow ee$  Monte Carlo with the sum of weighted opposite-sign events as seen in Table 17.

	Events	Statistical error [%]
$Z \rightarrow ee$ MC $e^\pm e^\pm$	65.4	3.69
$Z \rightarrow ee$ MC $e^\pm e^\mp + \text{flip}$	61.3	0.39
data	62	12.7

Table 17: Closure test using the charge flip rate in opposite-sign di-electron events vs. same-sign di-electron events in MC

	$E_T^{\text{miss}} > 100 \text{ GeV}$	
	$e^\pm e^\pm$	$e^\pm \mu^\pm$
$t\bar{t}$ (SS MC)	$0.043 \pm 0.013 \pm 0.010$	$0.057 \pm 0.013 \pm 0.016$
$t\bar{t}$ (OS + flip)	$0.024 \pm 0.001 \pm 0.008$	$0.032 \pm 0.001 \pm 0.011$
$t\bar{t}$ (OS + flip corrected)	$0.019 \pm 0.001 \pm 0.008$	$0.026 \pm 0.001 \pm 0.011$

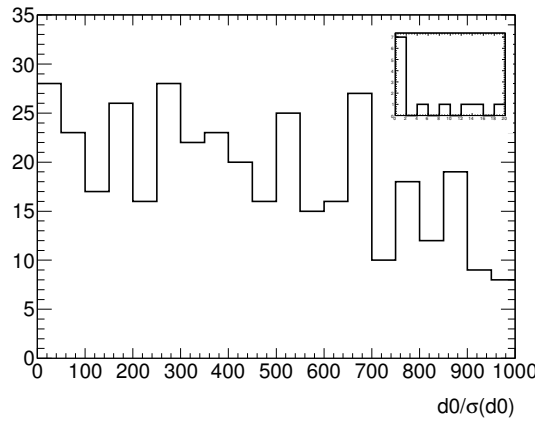
Table 18: The estimate of dilepton  $t\bar{t}$  in the signal region. The correction in the final row removes events that will be included by the matrix method. Systematic uncertainties in the table includes error due to JES, JER, LES, LER, pdf and luminosity measurements.

In estimating the dilepton  $t\bar{t}$  contribution to the signal region, we need to take care not count events as both fake and dilepton  $t\bar{t}$ . A Monte Carlo truth cut requiring only dilepton  $t\bar{t}$  events ensures that our estimate does not include fakes from  $t\bar{t} \rightarrow \ell + \text{jets}$ . However, the  $Z$ -peak in the fake estimate in Figure, indicates that the fake lepton matrix method does include some fraction of trident events. This fraction has been measured to be  $0.812 \pm 0.004$  (see Section 7.3.2). We scale our dilepton  $t\bar{t}$  estimate by this factor to prevent double counting these events. The final estimates for the dilepton  $t\bar{t}$  background to the  $e^\pm e^\pm$  and  $e^\pm \mu^\pm$  channels can be seen in Table 18.

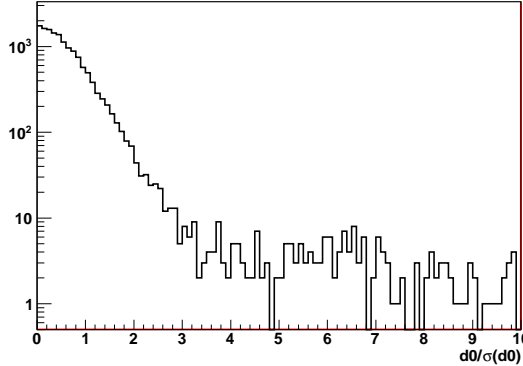
## 7.5 Cosmics Contamination

The longitudinal impact parameter,  $z_0$ , is used to select muons for analysis in all the dilepton channels. Here the transverse impact parameter of the muon w.r.t the primary vertex,  $d_0$ , is used to estimate the contamination in each dilepton channel from cosmic muons. Figure 24 shows the distribution of  $d_0$  significance for cosmic muons and Monte Carlo muons in  $t\bar{t}$ . In order to estimate the cosmic contamination in the selected  $\mu\mu$  and  $e\mu$  samples, we measure the fraction of events selected by the analyses ( $\mu\mu$  and  $e\mu$ ), that also pass the additional selection criterion  $d_0 > 5\sigma_{d_0}$ . This criterion selects preferentially cosmic muons over muons coming from collisions. This measured fraction combined with the knowledge of the  $d_0/\sigma_{d_0}$  distribution in actual cosmic data and in  $t\bar{t}$  Monte Carlo allows an estimate to be made of the actual fraction of cosmic events in the selected data.

The cosmic events are examined by looking at the CosmicCalo data stream for periods A to H. Since a muon originating from a  $b$  quark decay is more likely to deviate from the primary vertex, the  $d_0$  significance in the collision events is investigated with both the  $t\bar{t}$  and the  $1\mu$  filtered QCD samples.



(a)Muons in the CosmicCalo stream



(b)Muons in  $t\bar{t}$  Monte Carlo

Figure 24:  $d_0$  significance in (a) cosmic data from the CosmicCalo stream and in (b)  $t\bar{t}$  Monte Carlo.

For good muons with  $p_T > 20$  GeV,  $\epsilon_{cos} = 0.975 \pm 0.025$ ,  $\epsilon_{coll} = 0.075 \pm 0.011$ , where  $\epsilon_{cos}$  is the efficiency of the reverse selection in the cosmic events, and  $\epsilon_{coll}$  is the efficiency of the reverse selection in the collision events. If requiring  $E_T^{miss} > 100$  GeV,  $\epsilon_{coll} = 0.047 \pm 0.019$ .

Hereafter the standard dilepton selection will be named ‘loose’ selection, and the selection with the additinal requirement that  $d_0 > 5\sigma_{d_0}$  - ‘tight’. The number of cosmic events are estimated for the  $e\mu$  and

$\mu\mu$  channels using matrix methods.

For the  $e\mu$  channel, the number of cosmic events,  $N_{cos}$  is extracted from the following equations:

$$N_L = N_{cos} + N_{coll} \quad (19a)$$

$$N_T = \epsilon_{cos} N_{cos} + \epsilon_{coll} N_{coll} \quad (19b)$$

$$N_{L-T} = N_L - N_T \quad (19c)$$

where,  $N_L$  and  $N_T$  are the number of events passing the loose selection and the tight selection respectively. Since the tight selection is a subset of the loose one, the number of events that fail the tight selection,  $N_{L-T}$  is used instead of  $N_L$  to avoid correlations.

$N_{cos}$  and its variance are:

$$N_{cos} = [N_T - \epsilon_{coll}(N_{L-T} + N_T)] / (\epsilon_{cos} - \epsilon_{coll})$$

$$\sigma_{N_{cos}}^2 = (dN_{cos}/dN_{L-T})^2 \sigma_{N_{L-T}}^2 + (dN_{cos}/dN_T)^2 \sigma_{N_T}^2 + (dN_{cos}/d\epsilon_{cos})^2 \sigma_{\epsilon_{cos}}^2 + (dN_{cos}/d\epsilon_{coll})^2 \sigma_{\epsilon_{coll}}^2$$

where,

$$dN_{cos}/dN_{L-T} = -\epsilon_{cos}/(\epsilon_{cos} - \epsilon_{coll})$$

$$dN_{cos}/dN_T = (1 - \epsilon_{coll})/(\epsilon_{cos} - \epsilon_{coll})$$

$$dN_{cos}/d\epsilon_{cos} = -[N_T - \epsilon_{coll}(N_{L-T} + N_T)] / (\epsilon_{cos} - \epsilon_{coll})^2$$

$$dN_{cos}/d\epsilon_{coll} = [N_T - \epsilon_{cos}(N_{L-T} + N_T)] / (\epsilon_{cos} - \epsilon_{coll})^2$$

The estimated contributions from cosmics in each of the  $e\mu$  channels are thus given in Table 19.

Cuts	Data	Estimated cosmics
OS $e\mu$	131	$-3.14 \pm 3.34$
$E_T^{miss} > 100GeV$	13	$0.42 \pm 1.07$
$E_T^{miss} > 150GeV$	4	$-0.20 \pm 1.18$
SS $e\mu$	5	$0.69 \pm 1.04$
$E_T^{miss} > 80GeV$	0	$0 \pm 1.17$
$E_T^{miss} > 100GeV$	0	$0 \pm 1.17$

Table 19: The estimated contribution from cosmic events in both the opposite-sign and same-sign  $e\mu$  channels.

The  $\mu\mu$  channel is slightly more complex because there are two muons. These are either both from cosmic events,  $N_{2cos}$ , both from collision events,  $N_{2coll}$ , or one from cosmics and the other one from collision,  $N_{1cos,1coll}$ . The efficiency  $\epsilon_{coll}$  for a single muon being a collision candidate in these types of event is simply taken to be the same as that in  $e\mu$  channel. Since there is large contribution from Z+jets before the  $E_T^{miss}$  cut, the efficiency for the opposite-sign di-muon collision events at this stage of selection is re-estimated with  $t\bar{t}$  and Z samples. Figure 25 shows this efficiency in the mixed samples. For  $p_T > 20$  GeV,  $\epsilon_{coll} = 7.95 \times 10^{-4} \pm 1.65 \times 10^{-4}$ .

Similar to the  $e\mu$  channel the matrix to solve is:

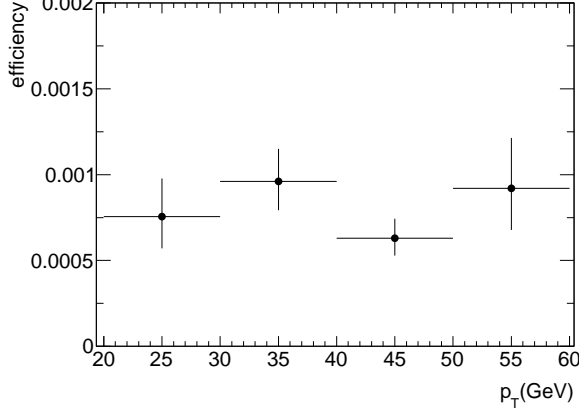


Figure 25: The efficiency of tight selection, as a function of  $p_T$ , for the  $t\bar{t}$  and  $Z+jets$  Monte Carlo samples.

$$(N_{L-T,L-T}, N_{L-T,T}, N_{T,T}) = (N_{2cos}, N_{2coll}, N_{1cos,1coll}) \times$$

$$\begin{pmatrix} (1 - \epsilon_{cos})^2 & 2\epsilon_{cos}(1 - \epsilon_{cos}) & \epsilon_{cos}^2 \\ (1 - \epsilon_{coll})^2 & 2\epsilon_{coll}(1 - \epsilon_{coll}) & \epsilon_{coll}^2 \\ (1 - \epsilon_{cos})(1 - \epsilon_{coll}) & \epsilon_{cos}(1 - \epsilon_{coll}) + \epsilon_{coll}(1 - \epsilon_{cos}) & \epsilon_{cos}\epsilon_{coll} \end{pmatrix}$$

Equation 20 gives the estimated cosmic contamination in the  $\mu\mu$  channel, the results of which are listed in Table 20.

$$N_{1cos,1coll} = \frac{(\epsilon_{cos} + \epsilon_{coll} - 2\epsilon_{cos}\epsilon_{coll})N_{L-T,T} - 2(1 - \epsilon_{cos})(1 - \epsilon_{coll})N_{T,T} - 2\epsilon_{cos}\epsilon_{coll}N_{L-T,L-T}}{(\epsilon_{cos} - \epsilon_{coll})^2} \quad (20a)$$

$$N_{2cos} = \frac{-\epsilon_{coll}(1 - \epsilon_{coll})N_{L-T,T} + (1 - \epsilon_{coll})^2N_{T,T} + \epsilon_{coll}^2N_{L-T,L-T}}{(\epsilon_{cos} - \epsilon_{coll})^2} \quad (20b)$$

Cuts	Data	2 cosmics	1 cosmic
OS $\mu\mu$	12772	$9.39 \pm 3.19$	$86.63 \pm 11.49$
$E_T^{miss} > 100GeV$	13	$0.03 \pm 1.20$	$-1.39 \pm 1.43$
$E_T^{miss} > 150GeV$	4	$0.01 \pm 1.20$	$-0.43 \pm 1.27$
SS $\mu\mu$	3	$2.12 \pm 1.50$	$-0.29 \pm 1.29$
$E_T^{miss} > 80GeV$	0	$0 \pm 1.20$	$0 \pm 1.24$
$E_T^{miss} > 100GeV$	0	$0 \pm 1.20$	$0 \pm 1.24$

Table 20: The estimated number of cosmic events in both the opposite-sign and same-sign  $\mu\mu$  channels.

At  $34.3 \text{ pb}^{-1}$ , the predicted number of cosmic events is negligible in the dilepton signal region in both the  $e\mu$  channels and the  $\mu\mu$  channels.

To enable setting upper limits in the dilepton channel, an alternative method is adopted to get rid of the negative predicted number of cosmic ray events in the signal region. Table 21 shows the good

period	good LBs	live time(ks)
AB	4373	522.1
C	919	106.2
D	3439	407.6
E	3634	429.3
F	2229	263.9
G	2137	244.2
H	972	111.1
I	1274	143.4
A-D	8731	1036.5
E-I	10246	1191.9

Table 21: Good luminosity blocks and live time in period A to I.

luminosity blocks and the corresponding live time in period A to I. Since there is no event surviving the  $E_T^{\text{miss}}$  selection in both the  $e\mu$  and  $\mu\mu$  channels in period A to D, the number of cosmic events in period E to I is  $N_{\text{cos}} < 1.32$  at 68% C.L, and  $N_{\text{cos}} < 3.45$  at 95% C.L.

## 7.6 $t\bar{t}$ background

This section describes the data-driven techniques used to estimate the amount of  $t\bar{t}$  background in the signal region of the Opposite Sign analysis. Here, the  $t\bar{t}$  background is the largest background to supersymmetry. In a signal region selected with two opposite sign leptons and  $E_T^{\text{miss}} > 100$  GeV,  $t\bar{t}$  events where both  $W$ 's decay leptonically make up more than 85% of the selected sample as shown in Table 12. A small fraction of the  $t\bar{t}$  dilepton events arises from semi-leptonic  $t\bar{t}$  events, where one of the isolated leptons is a fake isolated lepton, rather than from the chain  $t \rightarrow W \rightarrow \ell\nu$ . These semi-leptonic  $t\bar{t}$  events have one fake isolated lepton and are therefore taken into account by the data-driven estimate of the fake-lepton backgrounds described in Sec. 7.3.

This section focuses specifically on the determination of the background from  $t\bar{t} \rightarrow (W^+ b)(W^- \bar{b}) \rightarrow (\ell^+ \nu_\ell b) (\ell^- \bar{\nu}_\ell \bar{b})$ . It describes the baseline technique used to estimate the top background in the signal region. Other techniques are reported in Appendix H and provide a important cross check of the baseline estimate.

First a “top tagger” method is described, which is used to select events with a kinematic consistent with that of a  $t\bar{t} \rightarrow (W^+ b)(W^- \bar{b}) \rightarrow (\ell^+ \nu_\ell b) (\ell^- \bar{\nu}_\ell \bar{b})$  event. Then the method used to estimate the top background is described, and finally the results obtained on data and the studies of systematic uncertainties are presented.

### CONTRANSVERSE MASS TAGGER

The contransverse mass was introduced in Ref. [20], it can be defined for two pair produced heavy states  $\delta$  each decaying into an invisible particle  $\alpha$  and visible decay products  $\chi_i$ :

$$m_{\text{CT}}^2(\chi_1, \chi_2) = [E_T(\chi_1) + E_T(\chi_2)]^2 - [\mathbf{p}_T(\chi_1) - \mathbf{p}_T(\chi_2)]^2 \quad (21)$$

If  $m(\chi_1) = m(\chi_2) \equiv m(\chi)$  as is the case of  $t\bar{t}$ ,  $m_{\text{CT}}$  possesses an endpoint:

$$m_{\text{CT}}[m^2(\chi)] < m_{\text{CT}}^{\max}[m^2(\chi)] = \frac{m^2(\chi)}{m(\delta)} + \frac{m^2(\delta) - m^2(\alpha)}{m(\delta)} \quad (22)$$

On each side of a top events one finds one lepton and one jet, therefore  $\chi$  in Equation 22 can be a lepton, a jet, or a lepton-jet combination. The following contransverse masses can thus be constructed  $m_{\text{CT}}(\ell\ell)$ ,  $m_{\text{CT}}(jj)$ ,  $m_{\text{CT}}(jl, jl)$ . For each of these the end-point is given by Equation 22, substituting for  $(\delta, \alpha)$  respectively  $(W, v)$ ,  $(t, W)$ , and  $(t, v)$ . The top-tag is based on the idea that a  $t\bar{t}$  event should fullfill the inequality of Eq. 22 for the three different contransverse mass combinations. The end-point is also a function of the vector sum of transverse momenta of the visible particles upstream of the system for which the cotransverse mass is calculated. This variable which we call  $p_b(\chi)$  is precisely defined in Ref. [21]. Therefore rather than applying a straight upper cut on the  $m_{\text{CT}}$  variables, the top events are required to lie below the appropriate curve in the  $(m_{\text{CT}}(\chi), p_b(\chi))$  plane.

Thus the top-tag is defined by the following algorithm:

1. The event should have at least 2 jets with  $p_T > 20$  GeV
2. Consider all 2 jet permutations  $j_1, j_2$ , such that the two jets have  $p_T > 20$  GeV and  $p_T(j_1) + p_T(j_2) + p_T(\ell_1) + p_T(\ell_2) > 100$  GeV,
3.  $m_{\text{CT}}(\ell_1, \ell_2)$  should be in the allowed area of the  $(m_{\text{CT}}(\ell_1, \ell_2), p_b(\ell\ell))$  plane,
4. Build all pairs  $((j_i\ell_1)(j_j\ell_2))$  such that  $m(j_i\ell_1) < 155$  GeV and  $m(j_j\ell_2) < 155$  GeV.
5. There should be at least one combination with  $m_{\text{CT}}(jj)$  in the allowed area of the  $m_{\text{CT}}(jj), p_b(jj)$  plane.
6. For the combinations passing the previous cuts:  $m_{\text{CT}}(j\ell, j\ell)$  should be compatible with  $t\bar{t}$ .

Events which have one permutation of two jets which fullfill the conditions above is considered as top-tagged. The efficiency of this algorithm for  $t\bar{t}$  MonteCarlo samples is 83% both for the signal regions ( $E_T^{\text{miss}} > 100$  GeV or  $E_T^{\text{miss}} > 150$  GeV) and for the control region selection  $60 \text{ GeV} < E_T^{\text{miss}} < 80 \text{ GeV}$ , see Section 7.6.

In the following sections the cotransverse mass tagger is used to define control regions for the  $t\bar{t}$  background. An other tagger (kinematic top tagger) is described in Appendix H.2 and is used in the alternative  $t\bar{t}$  background estimate described there.

#### DESCRIPTION OF THE METHOD

The method described here estimates the top background in the signal region using the formula

$$(N_{tt})_{SRee} = \left( (N_{\text{data}}^{\text{tag}})_{CR} - (N_{\text{non-}t\bar{t},MC}^{\text{tag}})_{CR} \right) \frac{(N_{\text{top},MC})_{SRee}}{(N_{\text{top},MC})_{CR}} \quad (23)$$

$$(N_{tt})_{SR\mu\mu} = \left( (N_{\text{data}}^{\text{tag}})_{CR} - (N_{\text{non-}t\bar{t},MC}^{\text{tag}})_{CR} \right) \frac{(N_{\text{top},MC})_{SR\mu\mu}}{(N_{\text{top},MC})_{CR}} \quad (24)$$

$$(N_{tt})_{SR\mu\mu} = \left( (N_{\text{data}}^{\text{tag}})_{CR} - (N_{\text{non-}t\bar{t},MC}^{\text{tag}})_{CR} \right) \frac{(N_{\text{top},MC})_{SR\mu\mu}}{(N_{\text{top},MC})_{CR}} \quad (25)$$

where  $(N_{\text{data}})_{CR}$  is the number of events observed in a control region dominated by top pair events,  $(N_{\text{non-}t\bar{t},MC})_{CR}$  is the number of non- $t\bar{t}$  events in the control region, estimated from either Monte Carlo or data-driven techniques,  $(N_{\text{top},CR})_{MC}$  is the number of  $t\bar{t}$  events expected by Monte Carlo in the control region, and  $(N_{\text{top},SRxx})_{MC}$  (with  $xx = ee, \mu\mu, e\mu$ ) is the number of events expected by Monte Carlo in the signal region for each channel. The normalization of the  $t\bar{t}$  background is thus derived from data, while the Monte Carlo is used to extrapolate from the control region to the signal regions.

Process	$ee$	$\mu\mu$	$e\mu$	<b>total</b>
data	0	5	10	<b>15</b>
$t\bar{t}$	3.6	6.3	8.9	<b>18.8</b>
single top	0.2	0.2	0.3	<b>0.8</b>
$Z/\gamma + \text{jets}$	0.5	0.5	0.1	<b>1.1</b>
fakes	0.1	0.0	0.1	<b>0.2</b>
Diboson	0.1	0.2	0.1	<b>0.4</b>
Total non $t\bar{t}$	1.0	0.9	0.6	<b>2.5</b>
SU4	0.3	0.8	0.9	<b>2.1</b>

Table 22: Observed event counts and expected sample composition of control region for  $34.3 \text{ pb}^{-1}$ . The contamination by events from supersymmetry production for the SU4 model is also shown and is of the order of 10%.

Events with  $60 < E_T^{\text{miss}} < 80 \text{ GeV}$  and with a cotransverse mass tag has been chosen as control region. The lower limit on  $E_T^{\text{miss}}$  is required to reduce the contamination from Z events. The upper limit reduces the possible contamination from signal events.

Since the statistics available in the control region is limited, for all the channels the same control region obtained summing the  $ee$ ,  $e\mu$  and  $\mu\mu$  events is used and the MonteCarlo is relied upon to predict the fraction of events falling in each channel in the signal region. The uncertainty on these fractions is much smaller than both the systematic uncertainties associated to the extrapolation from the control region to the signal region and those due to the limited statistics in the control region.

#### CLOSURE TEST AND BACKGROUND PREDICTION

The method detailed above is validated on Monte Carlo by mixing the various Standard Model processes normalized with their respective cross sections. This allows to compute the expected composition of the signal and control regions. Table 22 shows the expected composition of the control region for an integrated luminosity of  $34.3 \text{ pb}^{-1}$ . The top, single top and double boson numbers are from Monte Carlo, while the Z has been normalized to data in the same flavour channels as described in Section 7.2 and the fakes have been estimated from data as described in Section 7.7. The number of observed data is also reported.

The last line shows the contamination by supersymmetry events as obtained for the SUSY model SU4. To test the validity of the signal-to-control region ratio method, it is applied on Monte Carlo, with and without SUSY contamination and the predicted number of  $t\bar{t}$  events in a signal region with  $E_T^{\text{miss}} > 100 \text{ GeV}$  is compared to its true number as directly predicted by the Monte Carlo and cross sections. The corresponding results are shown in Table 23, where the effect of the SUSY contamination has been estimated in the presence of the SUSY models MSSM27 and SU4. It appears that in presence of MSSM27 or SU4, the background is slightly overestimated by 10-15%. This has the disadvantage of reducing the significance for signal discovery. Nevertheless one should note that this contamination is rather modest, compared to method A3 and method B described in the Appendix H.

For the Monte Carlo study, where the numerator of Equation 23- 25 is put identical to  $(N_{top,MC}^{\text{tag}})_{CR}$ , in case of absence of SUSY the number of  $t\bar{t}$  events predicted in the signal region with this method is trivially the number predicted by the Monte Carlo. The total uncertainty of the estimate is of the order of 30%. This uncertainty arises from the total expected systematic uncertainty for an integrated luminosity of  $34.3 \text{ pb}^{-1}$ . The various sources of uncertainty are detailed in the next section.

#### SYSTEMATIC UNCERTAINTIES

	True	No signal	MSSM27	SU4
$N_{t\bar{t}}$	20.5	$20.5 \pm 6.6$	$23.0 \pm 7.4$	$23.4 \pm 7.5$
$N_{t\bar{t}} + N_{SUSY}$ in Signal Region		20.5	47.3	33.6

Table 23: True (2nd column) and predicted number of  $t\bar{t}$  events for  $E_T^{\text{miss}} > 100$  GeV in the following cases: no SUSY signal (3rd column), supersymmetry is present (MSSM27)(4th column) and supersymmetry is present (SU4) (last column). The last row gives the sum of the predicted number of  $t\bar{t}$  events and the predicted number of SUSY events. Event yields are predictions for an integrated luminosity of  $34.3 \text{ pb}^{-1}$ .

In the signal-to-control region method the ratios  $f_{MC}^{CR \rightarrow SR} = (N_{top,MC})_{SRxx}/(N_{top,MC}^{\text{tag}})_{CR}$  are extracted from the simulation. To understand the potential effect of discrepancies between data and the Monte Carlo modelling, these ratios are re-estimated for different samples, and by varying several potential sources of systematic errors. The resulting variation is then propagated to the  $N_{t\bar{t}}$  prediction. The resulting uncertainties on  $N_{t\bar{t}}$  are included in the error bars given in Table 23. The sources of systematic uncertainties that have been considered are the following.

*Generator Uncertainty* To investigate the effect of the generator on the ratio  $f_{MC}^{CR \rightarrow SR}$ , it is recalculated using sample generated with AcerMC, ALPGEN, POWHEG. The RMS of the differences with the MC@NLO generator (the reference) is used as systematic uncertainty.

*Initial and Final State Radiation (ISR/FSR)* This systematic uncertainty is obtained by varying the parameters controlling the amount of ISR and FSR in the Monte Carlo simulation. The ISR and FSR are varied up and down both separately and simultaneously, using AcerMC Monte Carlo samples.

*Parton shower modelling* The uncertainty due to the modelling of the parton showering is estimated by comparing the ratio  $f_{MC}^{CR \rightarrow SR}$  in a sample generated with POWHEG + PYTHIA with a second sample generated with POWHEG + HERWIG.

*Jet energy scale and resolution*, as discussed in section 5.

In addition to the uncertainty mentioned above, the uncertainty on the non- $t\bar{t}$  Standard Model contribution to the control regions (here called "background") and the control region statistics have been taken into account. The former has been estimated using the same techniques used for the signal region: the single top and boson pairs are taken from MonteCarlo, the fake contribution from the data-driven estimate, while the Z has been normalized to data in a control region.

The resulting uncertainties on the predicted  $t\bar{t}$  background are included in Table 23. Table 24 gives the breakdown of the relative systematic uncertainties on the predicted  $t\bar{t}$  event yield in the signal regions. The expected uncertainties are computed using the Monte Carlo prediction of the number of events in the control regions, while the observed uncertainties refer to the actual results using the measured number of events in data. The dominant systematic errors are the jet energy scale and the statistics in the control region.

## RESULTS

The observed number of events in the control region (Table 22) is significantly smaller than expected. In Fig. 26 the likelihood of the data in the control region, evaluated with a toy MonteCarlo, is shown as a function of the  $t\bar{t}$  scaling factor. The black curve includes only the statistical uncertainty, while the red one includes the systematics associated to the evaluation of the non- $t\bar{t}$  background in the control region. The uncertainties related to the extrapolation to the signal region, discussed previously, are not included.

Signal region Channel	$E_T^{\text{miss}} > 100 \text{ GeV}$			$E_T^{\text{miss}} > 150 \text{ GeV}$		
	$ee$	$e\mu$	$\mu\mu$	$ee$	$e\mu$	$\mu\mu$
Generator	7%			3%		
ISR/FSR	9%			23%		
Parton shower	2%			2%		
Jet energy scale and resolution	15%			23%		
Control region statistics (exp.)				24%		
Control region statistics (obs.)				33%		
Control region backgrounds (exp.)				8%		
Control region backgrounds (obs.)				12%		
MonteCarlo statistics	9%	7%	7%	17%	14%	14%
Total (expected)				32%		41%
Total (observed)				40%		44%

Table 24: The relative systematic uncertainties on the predicted number of  $t\bar{t}$  events in the signal region as predicted by the signal-to-control region ratio method.

The figure shows that the nominal top MonteCarlo rate (scaling factor 1) is compatible with the data in the control region at the level of 1.3 standard deviations.

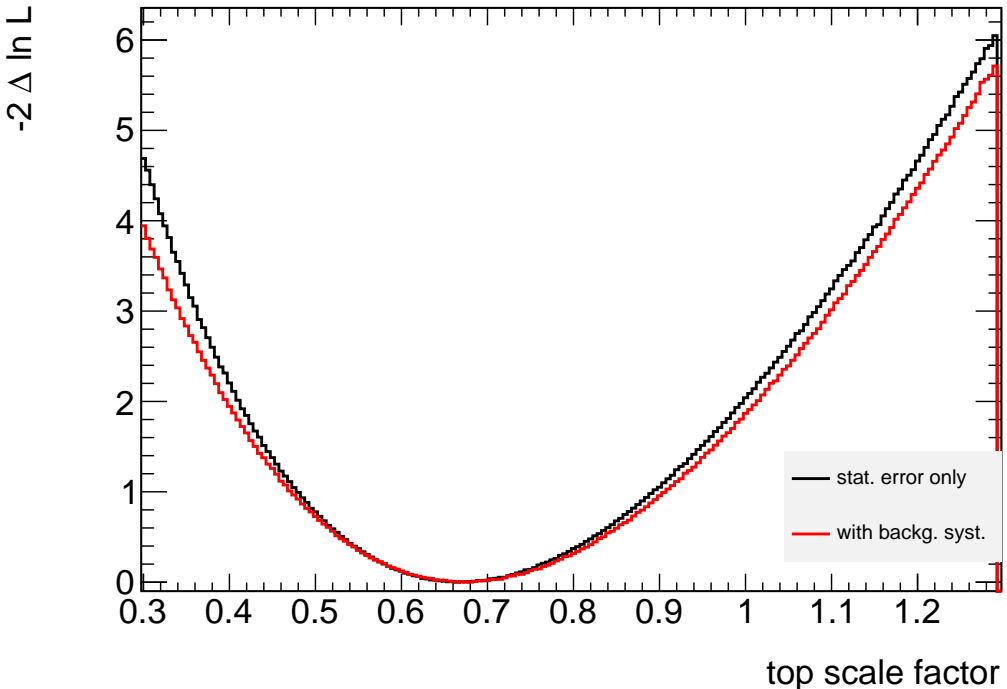


Figure 26: The likelihood for the number of events observed in the control region is shown as a function of the top background scaling factor.

The prediction of the top background in the signal region is reported in Table 25.

channel	ee	$\mu\mu$	$e\mu$	total
prediction $E_T^{\text{miss}} > 100 \text{ GeV}$	$2.50^{+1.03}_{-0.96}$	$4.71^{+1.87}_{-1.80}$	$6.61^{+2.72}_{-2.52}$	$13.8^{+5.6}_{-5.3}$
MC expectation $E_T^{\text{miss}} > 100 \text{ GeV}$	$3.7 \pm 0.9$	$7.0 \pm 1.6$	$9.8 \pm 2.3$	$20.5 \pm 4.8$
prediction $E_T^{\text{miss}} > 150 \text{ GeV}$	$0.62^{+0.31}_{-0.28}$	$1.00^{+0.50}_{-0.45}$	$1.24^{+0.62}_{-0.56}$	$2.8^{+1.4}_{-1.3}$
MC expectation $E_T^{\text{miss}} > 150 \text{ GeV}$	$0.92 \pm 0.27$	$1.48 \pm 0.43$	$1.83 \pm 0.53$	$4.2 \pm 1.2$

Table 25: The predicted number of  $t\bar{t}$  events in the signal regions and the MonteCarlo expectation are reported.

## 7.7 Z+jets background

The Standard Model description of  $Z/\gamma^*$  events predicts a relatively soft  $E_T^{\text{miss}}$  spectrum, compared to  $t\bar{t}$  and SUSY events. Therefore, we expect the contribution in the high- $E_T^{\text{miss}}$  range to be quite small. Nonetheless, we can acquire a precise estimate of the number of  $Z/\gamma^*$  events in the SUSY dilepton signal region (SR), defined by  $E_T^{\text{miss}} > 100 \text{ GeV}$  or  $E_T^{\text{miss}} > 150 \text{ GeV}$ , using a semi-data driven technique.

The expression for the number of  $Z/\gamma^*$  events in the SR,  $N_{Z/\gamma^*}^{\text{est,SR}}$ , is given by

$$N_{Z/\gamma^*}^{\text{est,SR}} = \beta \cdot N_{Z/\gamma^*}^{\text{data,CR}} \quad (26)$$

where  $N_{Z/\gamma^*}^{\text{data,CR}}$  is the number of  $Z/\gamma^*$  events from data in the control region (CR), defined by events with  $E_T^{\text{miss}} < 20 \text{ GeV}$  and  $81 < m_{\ell\ell} < 101 \text{ GeV}$ , and the scale factor,  $\beta$ , is defined by

$$\beta = \frac{N_{Z/\gamma^*}^{\text{MC,SR}}}{N_{Z/\gamma^*}^{\text{MC,CR}}} \quad (27)$$

Here,  $N_{Z/\gamma^*}^{\text{MC,SR}}$  is the number of OS dilepton events from  $Z/\gamma^*$  MC in the SR, and  $N_{Z/\gamma^*}^{\text{MC,CR}}$  is the number of OS dilepton events from  $Z/\gamma^*$  MC in the CR.

Using an approach such as this requires the MC to model well the  $E_T^{\text{miss}}$  in  $Z/\gamma^*$  events, which is demonstrated in figure 27. These distributions show the  $E_T^{\text{miss}}$  for ee (left) and  $\mu\mu$  (right) events with  $81 < m_{\ell\ell} < 101 \text{ GeV}$  for  $Z/\gamma^*$  MC (hatched) and for data, corrected for  $t\bar{t}$ ,  $W$ , and QCD (points). The MC events presented in these histograms are re-weighted according to the primary vertex distribution to account for pileup effects.

The number of  $Z/\gamma^*$  events from data in the CR,  $N_{Z/\gamma^*}^{\text{data,CR}}$  is estimated by correcting the data in this region for  $t\bar{t}$ ,  $W + \text{jets}$ , and QCD:

$$N_{Z/\gamma^*}^{\text{data,CR}} = (N_{Z/\gamma^*}^{\text{data}} - N_W^{\text{MC}} - N_{t\bar{t}}^{\text{MC}} - N_{\text{QCD}}^{\text{est}})^{\text{CR}} \quad (28)$$

where the number of  $W + \text{jets}$  ( $N_W^{\text{MC}}$ ) and  $t\bar{t}$  ( $N_{t\bar{t}}^{\text{MC}}$ ) events in the CR are estimated using MC and the number of QCD events in the CR ( $N_{\text{QCD}}^{\text{est}}$ ) is derived differently, depending on the channel:

- ee channel:

$$N_{\text{QCD}}^{\text{est,CR}} = (N_{\text{RobustLoose}}^{\text{data,CR}} - N_{Z/\gamma^*,\text{RobustLoose}}^{\text{MC,CR}}) \times \left( \frac{N_{\text{RobusterTight}}^{\text{data}}}{N_{\text{RobustLoose}}^{\text{data}}} \right) \Big|_{E_T^{\text{miss}} < 20 \text{ GeV}, 5 < m_{ee} < 60 \text{ GeV}} \quad (29)$$

where  $N_{\text{RobustLoose}}^{\text{data}} (N_{\text{RobusterTight}}^{\text{data}})$  is the number of the SS ee events with  $E_T^{\text{miss}} < 15 \text{ GeV}$  and  $5 < m_{ee} < 60 \text{ GeV}$  with selected electrons passing the RobustLoose (RobusterTight) criteria. The ratio of these numbers represents the fake rate of ee pairs in the region dominated by QCD background. The fake rate is applied to the number of events in the CR, correcting for non-QCD backgrounds.

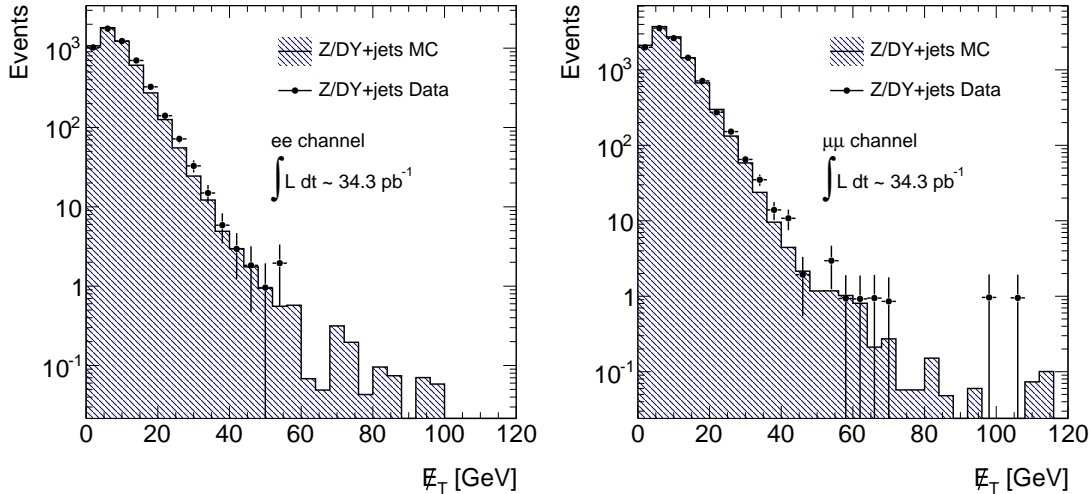


Figure 27: The  $E_T^{\text{miss}}$  distribution for  $ee$  (left) and  $\mu\mu$  (right) events falling under the  $Z$ -mass window,  $81 < m_{\ell\ell} < 101$  GeV. The hatched histograms are  $Z/\gamma^*$  MC events, whereas the points represent data corrected for top,  $W$ , and QCD.

- $\mu\mu$  channel:

$$N_{\text{QCD}}^{\text{est,CR}} = N_{\text{QCD}}^{\text{MC,CR}} \times \left( \frac{N_{\text{data}}^{\text{data}}}{N_{\text{QCD}}^{\text{MC}}} \right)^{\text{SS pairs}}_{E_T^{\text{miss}} < 15 \text{ GeV}, 5 < m_{\mu\mu} < 60 \text{ GeV}} \quad (30)$$

where  $N_{\text{data}}^{\text{data}}$  ( $N_{\text{QCD}}^{\text{MC}}$ ) is the number of SS di-muon data(MC, QCD) events with  $E_T^{\text{miss}} < 15$  GeV and  $5 < m_{\mu\mu} < 60$  GeV. The ratio represents the fake dimuon rate in the region dominated by QCD background. The fake rate is applied to the number of QCD events in the CR.

	$ee$	$\mu\mu$
$N_{\text{data,CR}}^{\text{data}}$	$4824 \pm 69(\text{stat.})$	$10347 \pm 102(\text{stat.})$
$N_{\text{non-Z}/\gamma^*}^{\text{est,CR}}$	$0.437 \pm 0.126(\text{stat.})$	$0.10 \pm 0.02(\text{stat.})$
$N_{Z/\gamma^*}^{\text{data,CR}}$	$4283.56 \pm 69(\text{stat.})$	$10346.9 \pm 102(\text{stat.})$
$N_{Z/\gamma^*}^{\text{MC,CR}}$	$4986.34 \pm 21.32(\text{stat.})$	$10714.9 \pm 31.5(\text{stat.})$

Table 26: The observed number of events from data in the  $Z$  CR, along with the contribution to this CR from non- $Z/\gamma^*$  sources. Using these two numbers, we estimate  $N_{Z/\gamma^*}^{\text{data,CR}}$ . The MC expectations for  $Z/\gamma^*$  events in this CR are also given.

In table 26, one can find the various observations and expectations used in estimating the number of  $Z/\gamma^*$  events in the CR. The non- $Z/\gamma^*$  sources consist of  $W$ ,  $t\bar{t}$ , and QCD. The latter is found to be consistent with zero for both  $ee$  and  $\mu\mu$ , using equations 29 and 30. This table shows that the contribution to the CR from non- $Z/\gamma^*$  sources is negligible.

Sources of systematic uncertainties for this method considered include variation of the  $E_T^{\text{miss}}$  and  $m_{\ell\ell}$  cuts in the  $Z/\gamma^*$  control region, jet energy scale and jet energy resolution uncertainties, and the effects of using MC from different event generators. Since the statistics in the SR are so low, the errors on such

errors are themselves quite large. The larger of the  $\text{JES}_\uparrow/\text{JES}_\downarrow$  uncertainties are considered for the final systematic.

Generator uncertainties were calculated by replacing the nominal  $Z(\rightarrow \ell\ell) + \text{jets}$  MC (**Alpgen**) with other samples. For comparison, we calculated results of this method using **Pythia** and **MC@NLO** MC and assessed a systematic. The larger variation of the two comparisons is used to compute the final uncertainty. Due to the low MC statistics in the **MC@NLO** sample, no uncertainty could be acquired for the  $ee$  case when  $E_T^{\text{miss}} > 150$  GeV; a similar argument holds for the  $e\mu$  channel in both SRs. Table 27 shows the contribution from each source of systematic uncertainty, as well as the total uncertainty, for all three flavor channels in both SRs.

	$E_T^{\text{miss}} > 100$ GeV	$E_T^{\text{miss}} > 150$ GeV
$ee$		
JER	+74%	+5.3%
$\text{JES}_\uparrow$	+34%	+1.9%
$\text{JES}_\downarrow$	-15%	-1.3%
MC@NLO	-75%	-
<b>Pythia</b>	-52%	-60%
Variation of CR	5%	3%
Total	100%	60%
$\mu\mu$		
JER	+7.1%	+71%
$\text{JES}_\uparrow$	+9.7%	+1%
$\text{JES}_\downarrow$	-14%	+69%
MC@NLO	-67%	-56%
<b>Pythia</b>	-42%	0%
Variation of CR	2%	1%
Total	69%	100%
$e\mu$		
JER	-16%	0%
$\text{JES}_\uparrow$	+28%	0%
$\text{JES}_\downarrow$	-33%	0%
MC@NLO	-	-
<b>Pythia</b>	-12%	-19%
Total	39%	19%

Table 27: Systematic uncertainties considered for each flavor channel and SR. The larger of the  $\text{JES}_\uparrow/\text{JES}_\downarrow$  and generator uncertainties are considered for the final systematic. Note that, due to low MC statistics, **Pythia** was used as the only generator alternative in some cases. Since we acquire the  $e\mu$  predictions from MC, no variation of the control region is defined for this channel.

Table 28 presents the estimation of the  $Z/\gamma^*$  contribution in the SUSY dilepton SR for  $34.3 \text{ pb}^{-1}$ . Due to the lack of statistics under the  $Z$ -peak in  $e\mu$  events, we use MC estimates for the SR for this channel.

		<i>ee</i>
$E_T^{\text{miss}} > 100 \text{ GeV}$	$\beta \times 10^5$	$7.263 \pm 2.965(\text{stat.}) \pm 7.263(\text{syst.})$
	$N_{Z/\gamma^*}^{\text{est,SR}}$	$0.399 \pm 0.151(\text{stat.}) \pm 0.399(\text{syst.})$
$E_T^{\text{miss}} > 100 \text{ GeV}$		<i><math>\mu\mu</math></i>
	$\beta \times 10^5$	$8.750 \pm 2.526(\text{stat.}) \pm 6.037(\text{syst.})$
$E_T^{\text{miss}} > 150 \text{ GeV}$	$N_{Z/\gamma^*}^{\text{est,SR}}$	$0.905 \pm 0.262(\text{stat.}) \pm 0.624(\text{syst.})$
		<i><math>e\mu</math></i>
	$N_{Z/\gamma^*}^{\text{MC,SR}}$	$0.36 \pm 0.16(\text{stat.}) \pm 0.14(\text{syst.})$
		<i>ee</i>
$E_T^{\text{miss}} > 150 \text{ GeV}$	$\beta \times 10^5$	$3.823 \pm 2.208(\text{stat.}) \pm 2.294(\text{syst.})$
	$N_{Z/\gamma^*}^{\text{est,SR}}$	$0.185 \pm 0.107(\text{stat.}) \pm 0.111(\text{syst.})$
$E_T^{\text{miss}} > 150 \text{ GeV}$		<i><math>\mu\mu</math></i>
	$\beta \times 10^5$	$1.343 \pm 0.950(\text{stat.}) \pm 1.343(\text{syst.})$
$E_T^{\text{miss}} > 150 \text{ GeV}$	$N_{Z/\gamma^*}^{\text{est,SR}}$	$0.139 \pm 0.098(\text{stat.}) \pm 0.139(\text{syst.})$
		<i><math>e\mu</math></i>
	$N_{Z/\gamma^*}^{\text{MC,SR}}$	$0.08 \pm 0.08(\text{stat.}) \pm 0.02(\text{syst.})$

Table 28: The scale factors and predictions for the  $Z/\gamma^*$  contribution for OS dileptons in the regions with  $E_T^{\text{miss}} > 100 \text{ GeV}$  and  $E_T^{\text{miss}} > 150 \text{ GeV}$ , for the  $ee$ ,  $\mu\mu$ , and  $e\mu$  channels. Due to suffering statistics,  $e\mu$  results are computed using MC.

## 8 Results and Interpretation

### 8.1 Same-Sign Analysis Results

#### 8.1.1 Expected and Observed Limits

The exclusion limits are obtained using the profile log likelihood ratio (LLR) method. The profile LLR is obtained from a simultaneous fit in the signal region to signal and background components. The likelihood function used for SS analysis is the product of a Poisson distributions for the signal region ( $P_{SR}$ ) and an additional distribution to include the constraints on systematic uncertainties ( $C_{Syst}$ ):

$$L(n|\mu, b, \vec{\theta}) = P_{SR} \times C_{Syst},$$

where  $n$  is the measured number of events in signal region,  $b$  is the number of background events,  $\mu$  is a signal normalization factor, also called signal strength. The nuisance parameters ( $\vec{\theta}$ ) parametrize systematic uncertainties, such as the luminosity or jet energy scale. The probability density function  $C_{Syst}$  is modeled with a product of Gaussian functions for each systematic uncertainty.

The exclusion fit tests for a specific signal model, the signal strength parameter  $\mu$  is left free in the fit. As a model-specific interpretation of the signal excess is made, the nuisance parameters for the signal cross-section uncertainty, the luminosity uncertainty, and signal Monte Carlo statistics uncertainty, are also left free in the fit.

The profile likelihood ratio is defined as:

$$\Lambda(\mu) = -2 \left( \ln L(n|\mu, \hat{b}, \hat{\vec{\theta}}) - \ln L(n|\hat{\mu}, \hat{b}, \hat{\vec{\theta}}) \right)$$

where  $\hat{\mu}$ ,  $\hat{b}$ ,  $\hat{\vec{\theta}}$  maximize the likelihood function, and  $\hat{b}$ ,  $\hat{\vec{\theta}}$  maximize the likelihood for the specific, fixed value of  $\mu$ . When testing specific models it is sufficient to consider tests for the nominal signal strengths  $\mu = 0$  and  $\mu = 1$ . The  $p$ -value for each model is obtained using pseudo-experiments and those with  $p$ -values smaller than 0.05 are said to be excluded with 95% confidence level. This procedure is suitable for the 0 observed events. More detail description about the profile LLR test and the statistical method are given in [1].

For each point in the signal grids, the number of expected events in the signal region has been computed for standard model background and signal processes. For the Standard Model background, two components were considered: (i) processes involving at least one fake lepton in the final state (QCD, W/Z+jets and  $t\bar{t}$ ), and (ii) processes involving two real leptons in the final state. The contribution from (i) was estimated using the data-driven fake background estimation techniques described in Section 7.2. The contribution from events of type (ii) (diboson WW, WZ and ZZ events) was taken from Monte Carlo (as determined in Section 6.3). The numbers of events for each of these background components in the signal regions for an integrated luminosity of  $34.3 \text{ pb}^{-1}$  are summarised in Table 29.

Table 29: The number of observed and expected events for each SS channel in the  $E_T^{\text{miss}} > 100 \text{ GeV}$  signal region at  $34.3 \text{ pb}^{-1}$ . The numbers are nominal, statistical errors and systematic errors respectively. For the  $e\mu$  channel the correlated errors with  $ee$  and  $\mu\mu$  channels are given for the fake rate method.

	Data(Observed)	Fake background (estimated)	Diboson (expected)	$t\bar{t}$ (charge-flip)
$e^\pm e^\mp$	0	$0.12 \pm 0.12 \pm 0.05$	$0.015 \pm 0.004 \pm 0.003$	$0.019 \pm 0.001 \pm 0.008$
$\mu^\pm \mu^\mp$	0	$0.014 \pm 0.01 \pm 0.005$	$0.035 \pm 0.005 \pm 0.011$	0.0
$e^\pm \mu^\mp$	0	$0.03 \pm 0.026 \pm 0.005(el) \pm 0.009(\mu)$	$0.021 \pm 0.004 \pm 0.008$	$0.026 \pm 0.001 \pm 0.011$

The uncertainties in this table are taken from Section 7.2 (for the fake contribution) and Table 16 for the diboson contribution. The errors are calculated in the following way for the exclusion limit computation :

- Statistical errors are added in quadrature for the fake backgrounds and for the MC diboson numbers for all the three channels. The total statistical error on the SM background becomes 0.123.
- Systematic errors for the fake backgrounds are followed in these steps :
  - The correlated errors between  $ee$  and  $e\mu$  are summed up linearly giving a value of 0.055. Similarly, the correlated errors between  $\mu\mu$  and  $e\mu$  are summed up linearly giving a value of 0.014.
  - The above two numbers are then added in quadrature considering  $ee$  and  $\mu\mu$  channels uncorrelated. This gives a value of 0.056 for the total systematic error on the fake background estimation
- The systematic errors for the diboson background and the systematic errors in the charge-flip method in the three channels are added in quadrature to the total systematic error from the fake background estimation. This yields a total systematic error on the SM background in the SS channel to be  $0.058 \approx 0.06$ .

We then add the total statistical error and the total systematic error in quadrature considering them to be uncorrelated. Thus the total number for the SM background events in the SS channel is :  $0.28 \pm 0.123$  (stat.)  $\pm 0.06$  (syst.)  $= 0.28 \pm 0.14$  (total).

For each signal point the uncertainties due to JES, JER, cross section weighted by acceptance are considered. The uncertainties on the signal points are detailed in the appendix.

We observe 0 events in the signal regions for an integrated luminosity of  $34.3 \text{ pb}^{-1}$ , as shown in Table 29. The number of observed events is consistent with the background prediction in all channels.

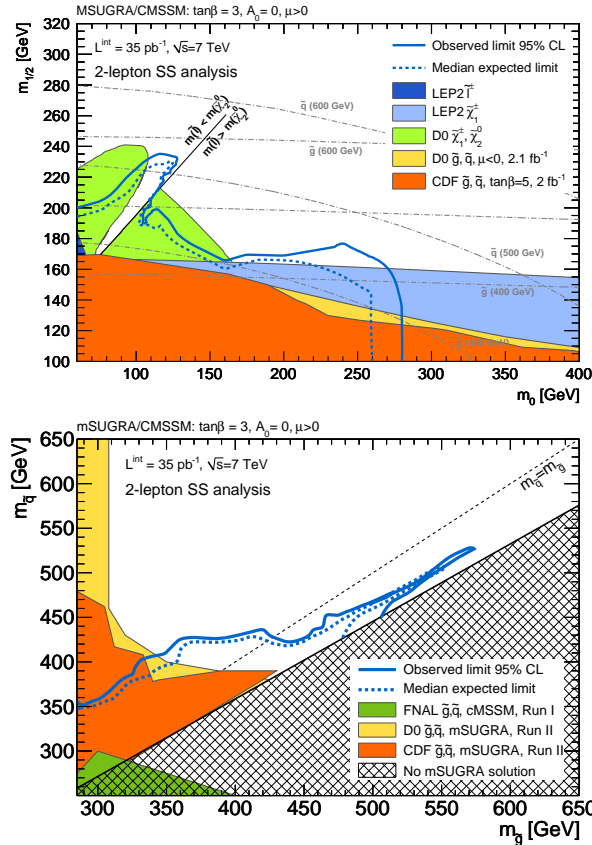


Figure 28: The expected and observed exclusion limits for mSUGRA in the  $m_0$ - $m_{1/2}$  plane (top) and in the  $m_{\tilde{q}}$ - $m_{\tilde{g}}$  plane (bottom). Figure shows the limit obtained using the signal region with a  $E_T^{\text{miss}}$  cut  $> 100 \text{ GeV}$ .

In Figure 28, the observed limit and the expected limit are illustrated in mSUGRA parameter space for a signal region with  $E_T^{\text{miss}} > 100 \text{ GeV}$ . Similar exclusion limits are computed for the Phenogrid points and they are illustrated in Figure 29 for Phenogrid2 and Figure 30 for Phenogrid3 signal points.

We limit on the mass of the sparticle based on the mSUGRA and Phenomenological signal grids. The limit on the mass is lower than 425 GeV for  $m_{\tilde{q}} = m_{\tilde{g}}$  in the mSUGRA scenario. The limit on the squark mass for the ‘compressed spectrum’ (‘light neutralino’) scenarios are 410 (519) GeV for the SS analysis.

By comparing the SM expectations with the numbers of events observed in the SS channel, we put 95% confidence limits on the ‘effective cross section’ (cross section times branching ratio times acceptance) for new physics processes producing SS lepton pairs and  $E_T^{\text{miss}}$  of 0.07 pb.

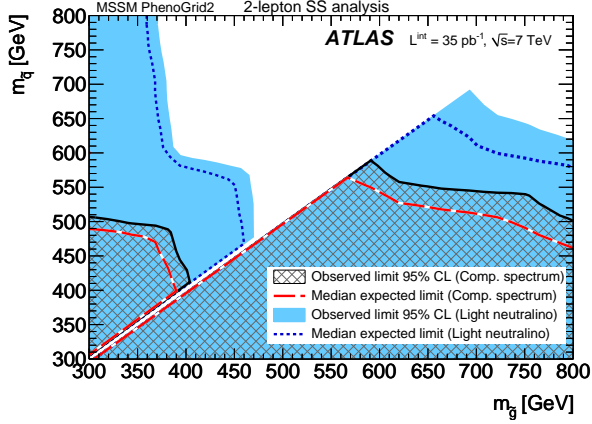


Figure 29: Expected and Observed exclusion limits as a function of the squark and gluino masses, for the subset of PhenoGrid2 with compressed spectrum and with light neutralino scenarios.

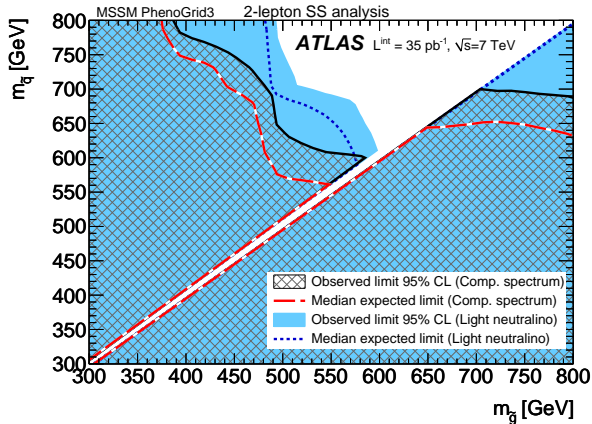


Figure 30: Expected and Observed exclusion limits as a function of the squark and gluino masses, for the subset of PhenoGrid3 with compressed spectrum and with light neutralino scenarios.

## 8.2 Opposite-Sign Analysis Results

Table 30: The total number of observed events with  $E_T^{\text{miss}} > 100 \text{ GeV}$  (upper table) and  $E_T^{\text{miss}} > 150 \text{ GeV}$  (lower table) and the background expectation is reported for each OS channel at an integrated luminosity of  $34.3 \text{ pb}^{-1}$ . For the total background, the components correlated and uncorrelated with signal uncertainties are provided. Also, the negative numbers are taken as zero when computing the total number of events.

$E_T^{\text{miss}} > 100 \text{ GeV}$	$e^\pm e^\pm$	$e^\pm \mu^\pm$	$\mu^\pm \mu^\pm$
Data,	4	13	13
$t\bar{t}$	$2.50^{+1.03}_{-0.96}$	$6.61^{+2.72}_{-2.52}$	$4.71^{+1.87}_{-1.80}$
Z+jets	$0.37 \pm 0.15$	$0.36 \pm 0.13$	$0.91 \pm 0.26$
fakes	$0.31 \pm 0.24$	$-0.15 \pm 0.46$	$0.01 \pm 0.01$
single top	$0.13 \pm 0.08$	$0.70 \pm 0.21$	$0.67 \pm 0.20$
WW+WZ+ZZ	$0.30 \pm 0.15$	$0.36 \pm 0.18$	$0.61 \pm 0.30$
cosmics	0	$0.42 \pm 1.07$	$-1.39 \pm 1.43$
total	$3.56^{+1.24}_{-1.12}(\text{uncorr.}) \pm 0.36(\text{corr.})$	$8.23^{+3.21}_{-2.72}(\text{uncorr.}) \pm 0.94(\text{corr.})$	$6.82^{+2.57}_{-1.93}(\text{uncorr.}) \pm 0.67(\text{corr.})$
$E_T^{\text{miss}} > 150 \text{ GeV}$	$e^\pm e^\pm$	$e^\pm \mu^\pm$	$\mu^\pm \mu^\pm$
Data	1	4	4
$t\bar{t}$	$0.62^{+0.31}_{-0.28}$	$1.24^{+0.62}_{-0.56}$	$1.00^{+0.50}_{-0.45}$
Z+jets	$0.19 \pm 0.15$	$0.08 \pm 0.08$	$0.14^{+0.17}_{-0.14}$
fakes	$-0.02 \pm 0.02$	$-0.05 \pm 0.04$	0
single top	$0.03^{+0.05}_{-0.03}$	$0.06^{+0.08}_{-0.06}$	$0.10 \pm 0.07$
WW+WZ+ZZ	$0.09 \pm 0.03$	$0.06 \pm 0.03$	$0.15 \pm 0.03$
cosmics	0	$-0.20 \pm 0.18$	$-0.43 \pm 1.27$
total	$0.92^{+0.40}_{-0.34}(\text{uncorr.}) \pm 0.14(\text{corr.})$	$1.43^{+1.42}_{-0.48}(\text{uncorr.}) \pm 0.28(\text{corr.})$	$1.39^{+1.39}_{-0.48}(\text{uncorr.}) \pm 0.23(\text{corr.})$

We have observed 4, 12 and 13 events respectively in each channel ( $e^\pm e^\mp$ ,  $e^\pm \mu^\mp$  and  $\mu^\pm \mu^\pm$ ) in the signal region with  $E_T^{\text{miss}} > 100 \text{ GeV}$ . Of these, 1, 4 and 4 events respectively have  $E_T^{\text{miss}} > 150 \text{ GeV}$ . The expected background for each channel is reported in Table 30. The top background has been determined with the partially data-driven method "A2" described in Section 7.6. The Z+jets background has been determined with the partially data-driven method described in Section 7.7 for the same flavour channels and with Monte Carlo for the  $e\mu$  channel. The background with fake leptons has been determined with the data-driven methods explained in Section 7.3. The double boson and single top backgrounds have been determined with Monte Carlo. The cosmic background was estimated by the matrix method described in Section 7.5.

The uncertainty on the total background estimate has been determined as

$$\sigma = \sqrt{\sigma_{tt,\text{stat}}^2 + (|\sigma_{tt,bkg} - \sigma_{\text{non-}tt}| + \sigma_{tt,MC})^2} \quad (31)$$

In Eq. 31,  $\sigma_{\text{non-}tt}$  is the uncertainty on the backgrounds other than  $t\bar{t}$  in the signal region; the uncertainties on the single background sources have been summed linearly as they are very correlated.  $\sigma_{tt,bkg}$  is the contribution to the  $t\bar{t}$  background uncertainty which comes from the subtraction of the non- $t\bar{t}$  contamination in the top control region; it has been considered completely correlated with the uncertainties on the same backgrounds in the signal region but since the two terms contribute to the total background with opposite sign they become anticorrelated.  $\sigma_{tt,MC}$  is the uncertainty on the extrapolation from the top

control regions to the signal region. This has been summed linearly to the term due to the non- $t\bar{t}$  backgrounds in order to be conservative, as the two terms are correlated. The term  $\sigma_{tt,stat}$  is the uncertainty due to the statistic of the top control regions, which is not correlated with the rest.

For the cosmic background the central value provided by the Matrix Method described in Section 7.5 is compatible with zero, and often negative. The negative values have been taken as zero when computing the total number of events, and the downward uncertainty taken as zero too.

In determining the exclusion limits, the downward uncertainties on the backgrounds were considered, so that the cosmics uncertainty does not contribute. Also, the uncertainty on the background due to jet energy scale, jet energy resolution, and luminosity has been treated as completely correlated with the corresponding uncertainties on the signal rate. This component of background uncertainty is reported in Table 30 as "correlated background uncertainty". The uncorrelated background uncertainty term, also reported in the table, is the component due to the top control region statistics, the non- $t\bar{t}$  uncertainties, and the theoretical uncertainties on the top extrapolation from the control region to the signal regions, which are not correlated to the signal uncertainties.

### 8.2.1 Expected and Observed Limits

Limits are computed using the profile likelihood method as detailed in the zero-lepton supporting note [1]. For each point in the signal grids, the number of expected events in the signal region and in the top background control region has been computed. The expected signal contamination in the control region has been used to correct the prediction of the top background under the assumption that the signal under consideration exists. Since this leads to a smaller estimated background, this correction results in weaker limits. For each point the uncertainties on the signal cross section and acceptance are computed and the compatibility of the observed number of events with the signal hypothesis has been tested.

The number of observed events with  $E_T^{\text{miss}} > 150$  GeV is slightly larger than the background prediction. The combined probability to observe a number of events larger than the observed number, under the Standard Model only hypothesis, has been found to be 12.8%, corresponding to a 1.1 standard deviations excess.

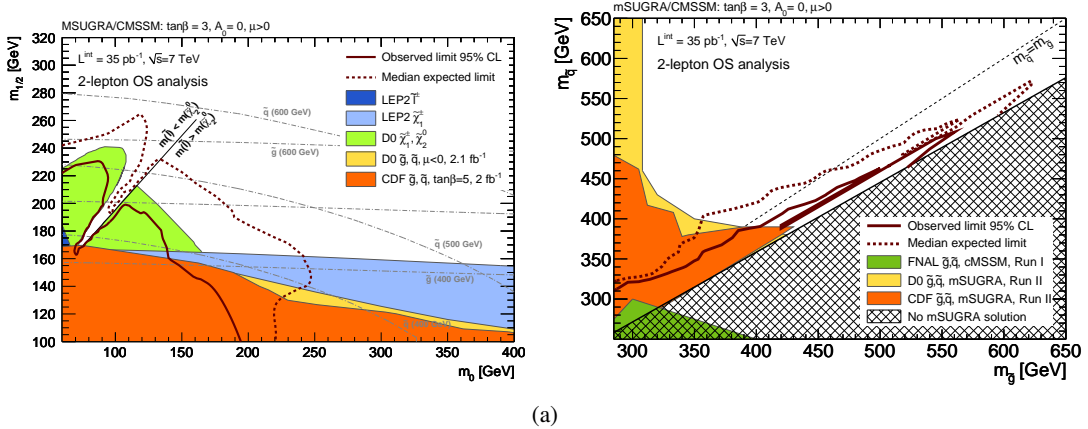


Figure 31: The expected and observed exclusion limits for mSUGRA in the  $m_0$ - $m_{1/2}$  plane (left) and in the  $m_{\tilde{q}}$ - $m_{\tilde{g}}$  plane (right). Figure shows the limit obtained using the signal region with a  $E_T^{\text{miss}}$  cut  $> 150$  GeV.

In Figure 31, the expected and observed limits in mSUGRA space are illustrated. The more stringent selection  $E_T^{\text{miss}} > 150$  GeV has been used.

In Fig. 32 the expected and observed limits are reported for the PhenoGrid2 and in Fig. 33 for the PhenoGrid3. For an equal value of the squark and gluino masses, the observed limit is 445 GeV and 543 GeV for the PhenoGrid2 with the compressed and favourable mass spectrum respectively, and it is 432 GeV and 541 GeV for the PhenoGrid3 with the compressed and favourable mass spectrum respectively,

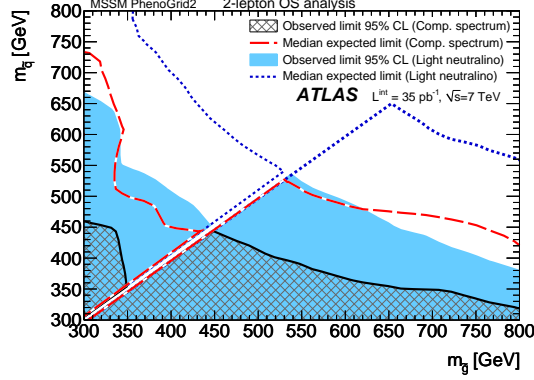


Figure 32: Expected exclusion limits as a function of the squark and gluino masses, for the subset of PhenoGrid2 with a compressed spectrum and with a light neutralino.

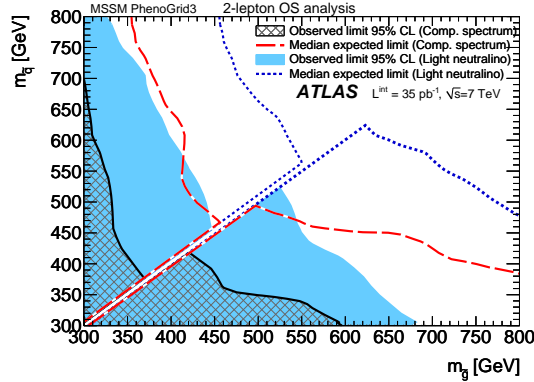


Figure 33: Expected exclusion limits as a function of the squark and gluino masses, for the subset of PhenoGrid3 with a compressed spectrum and with a light neutralino.

## 8.3 Flavour Subtraction Results

### 8.3.1 Summary

This section will introduce a quantity,  $\mathcal{S}$ , which is the excess of same-flavour opposite-sign events multiplied by the product of the electron and muon reconstruction efficiencies. This quantity will be predicted for standard model events using the data-driven estimations of the number of events in each opposite-sign channel in Sections 7.3, 7.6 and 7.7. Cosmic sources of background are neglected, but an underestimate of  $\mathcal{S}$  sets a conservative limit. This quantity will also be predicted using the purely Monte Carlo based estimates of each background given in Section 6.3. As already discussed both these background predictions will be small. The dominant standard model backgrounds naturally cancel in a flavour-subtraction analysis. The excess of same-flavour events remaining, and the uncertainty on it, will both be small.

When carrying out a flavour subtraction, in order to achieve the expected natural cancellation the subtraction must take into account: (i) differences in the electron and muon reconstruction efficiencies, and (ii) differences in the muon and electron trigger efficiencies. It will, however, be shown that the impact on the predicted same flavour excess from uncertainties on the reconstruction and identification efficiencies is small. Given how near the trigger efficiencies are to unity, uncertainties on the trigger efficiencies have a negligible impact on the predicted same flavour excess. The trigger efficiencies and the ratio of electron to muon reconstruction efficiencies are easily derived from data.

Standard Model Monte Carlo alone will be demonstrated to predict a mean excess of:

$$\mathcal{S}_{MC} = 1.8 \pm 1.1(\text{sys.}) \pm 0.87(\text{stat.}) \quad \text{at } 34.3 \text{ pb}^{-1}$$

This prediction is small, and the systematic (which is dominated by the luminosity, scale and resolution uncertainties) is comparable to the statistical error. Diboson,  $t\bar{t}$  and  $Z+\text{jets}$  events contribute to this excess – but the  $t\bar{t}$  contribution is consistent with zero within the statistical uncertainty it carries.

The data-driven estimates of the background in each opposite-sign channel will predict a mean excess of:

$$\mathcal{S}_{pred.} = 2.06 \pm 0.78(\text{sys.}) \pm 0.79(\text{stat.}) \quad \text{at } 34.3 \text{ pb}^{-1}$$

This is consistent with the purely Monte Carlo based prediction. This data-driven estimate includes the contributions from: (i) Diboson and  $Wt$  single top (from MC), (ii)  $t\bar{t}$ , (iii)  $Z+\text{jets}$  and (iv) fake dilepton (semi-leptonic  $t\bar{t}$ , QCD and  $W+\text{jets}$ ) events.

In data at  $34.3 \text{ pb}^{-1}$  we observe the following excess:

$$\mathcal{S}_{obs.} = 1.98 \pm 0.15(\text{sys.}\beta) \pm 0.02(\text{sys.}\tau_e) \pm 0.06(\text{sys.}\tau_\mu)$$

Taking account of the statistical and systematic uncertainties, this observation in data will be shown to set an upper limit on  $\mathcal{S}$  calculated from supersymmetric events alone of  $\sim 10$  (i.e. a limit on the excess same-flavour events from supersymmetry, multiplied by the product of reconstruction efficiencies), when a sixth of the total same-flavour events arise from flavour-blind processes, at  $34.3 \text{ pb}^{-1}$  at 95% confidence. For MSSM points with a high  $\tilde{\chi}_2^0 \rightarrow \tilde{\chi}_1^0 l^\pm l^\mp$  branching ratio, Monte Carlo predicts a significant excess of same-flavour events. For example, the point MSSM27 predicts  $\mathcal{S}_{SUSY}$  of 26.7 at  $34.3 \text{ pb}^{-1}$ , safely excluded by the limit set. Many points in the PhenoGrid also predict excesses above this limit. This limit will be obtained using a frequentist approach. This limit is driven by the expected observations in each channel ( $e^\pm e^\mp$ ,  $e^\pm \mu^\mp$  and  $\mu^\pm \mu^\mp$ ) which give the distribution of expected  $\mathcal{S}$  its width. Systematic uncertainties on the mean value of this distribution, and on the event rates in each channel, have a com-

paratively small effect on the limit.

*The sections which follow detail how the limit was set, how  $S$  was determined in each case and how the systematic uncertainties were obtained. Although the systematics and backgrounds are detailed at length for completeness – this should not dilute the statements made so far – (i) that the background is negligible, and (ii) that the analysis is only weakly sensitive to systematics. At this luminosity the measurement is a statistics dominated one.*

### 8.3.2 Method

Observation has been made of the number of  $e^\pm e^\mp$  events,  $N(e^\pm e^\mp)$ , the number of  $e^\pm \mu^\mp$  events,  $N(e^\pm \mu^\mp)$ , and the number of  $\mu^\pm \mu^\mp$  events,  $N(\mu^\pm \mu^\mp)$ . This observation has been made after event selection, and in the signal region (Section 6.3).

The excess of same-flavour events, after ‘flavour subtraction’, is given by Equation 32 where  $\tau_e$  and  $\tau_\mu$  are the electron and muon trigger efficiencies respectively, and the triggers are assumed to be at plateau for all  $p_T > 20$  GeV leptons. This equation takes into account the different electron and muon reconstruction efficiencies,  $\epsilon_e$  and  $\epsilon_\mu$  respectively, whose ratio,  $\epsilon_e/\epsilon_\mu$ , is defined as  $\beta$ . This ratio must take into account differences in both reconstruction efficiencies and acceptance. This equation does not exactly equal the excess of same-flavour events, but instead equals the excess of same flavour events multiplied by the product of  $\epsilon_e$  and  $\epsilon_\mu$ .

$$S = \frac{N(e^\pm e^\mp)}{\beta(1 - (1 - \tau_e)^2)} - \frac{N(e^\pm \mu^\mp)}{1 - (1 - \tau_e)(1 - \tau_\mu)} + \frac{\beta N(\mu^\pm \mu^\mp)}{(1 - (1 - \tau_\mu)^2)} \quad (32)$$

The denominators on the same-flavour counts correct for the loss of events in which both leptons of the same kind fail the appropriate trigger, the denominator of the different-flavour count correcting for the loss of events when neither the electron, nor the muon, trigger catches the  $e\mu$  event (see Appendix C for a detailed derivation of  $S$ ). Given appropriate estimates of  $\beta$ ,  $\tau_e$  and  $\tau_\mu$  this equation predicts zero contribution to  $S$  from standard model processes which give equal rates of same flavour and opposite flavour events.

### 8.3.3 The Determination of $\beta$ , $\tau_e$ and $\tau_\mu$

- **Determining Trigger Efficiencies,  $\tau_e$  and  $\tau_\mu$ .**

The trigger efficiencies (as a function of  $p_T$ ) for electrons and muons, triggered by the appropriate period dependent triggers, are given in Figure 34. In these figures, and the discussion and trigger efficiency calculations which follow – the electrons and muons considered are those which pass the object definitions used throughout this note (that is, we consider the efficiency for triggering the electrons and muons which pass our object definitions). The efficiency of the electron triggers (a) are noticeably higher than the muon trigger efficiencies (b), which are strongly  $\eta$  dependent. These turn on curves are obtained for the electron triggers using independently triggered events in the muon stream, and for the muon triggers using independently triggered events in the egamma stream. The electron and muon trigger efficiencies,  $\tau_e$  and  $\tau_\mu$  respectively, are determined separately for data and Monte Carlo as follows. For an estimate of the trigger efficiencies in data – events in the muon stream containing one selected electron with  $p_T > 20$  GeV are counted, firstly all events and secondly only those events for which the appropriate electron trigger was fired. The ratio of the numbers of events in these two event samples gives the overall efficiency of the electron triggers. The appropriate uncertainty is the binomial error on this efficiency. Conversely, the efficiency of the muon triggers can be determined for events using single muon events in the egamma

stream. To determine the Monte Carlo trigger efficiency, counts are made simply of the single electron events triggered, and those not triggered in the Monte Carlo (and similarly of the single muon events triggered, and those not triggered). Undertaking this procedure gives the following trigger efficiencies (using the SU4 sample for Monte Carlo):

Monte Carlo:  $\tau_e = 98.7 \pm 0.6\%$ ,  $\tau_\mu = 84.9 \pm 1.7\%$

Data:  $\tau_e = 98.5 \pm 1.1\%$ ,  $\tau_\mu = 83.7 \pm 1.9\%$

The efficiencies,  $\tau_\mu$  for data and Monte Carlo can be decomposed into separated trigger efficiencies for the barrel and the end-cap:

MC:  $\tau_\mu = 82.3 \pm 2.2\%$  (90.4  $\pm 2.5\%$ ) barrel (endcap)

Data:  $\tau_\mu = 75.6 \pm 3.3\%$  (90.5  $\pm 2.1\%$ ) barrel (endcap)

These barrel and end-cap efficiencies are consistent with those estimated in [2]<sup>1</sup>.

Using instead for Monte Carlo the  $t\bar{t}$  sample, the average  $\tau_\mu$  is  $84.1 \pm 0.5\%$ , and the barrel (endcap) efficiency  $80.4 \pm 0.5\%$  ( $90.2 \pm 0.7\%$ ), in agreement with the efficiencies quoted for the SU4 sample. The quoted average muon trigger efficiency in data gives a multiplicative scaling factor of  $\frac{1}{1-(1-\tau_\mu)^2}$  equal to 1.03 to apply to the number of  $\mu^\pm\mu^\mp$  events, in the calculation of  $S$ . This is a negligible correction compared to the statistical and systematic uncertainty on the number of  $\mu^\mp\mu^\pm$  events, and compared to the efficiency and acceptance factor  $\beta$ . Although the muon trigger efficiency in the end-cap is different to the efficiency in the barrel, the  $\tau_\mu$  which will be used is the quoted average muon trigger efficiency, and the multiplicative factor the one which results from using this  $\tau_\mu$ . In the unlikely worst case scenario that in fact all muon pair events were located in the barrel, the multiplicative scaling factor would only increase by 3%. This would have a negligible impact on the analysis. The estimates of  $\tau_\mu$  obtained for data (and Monte Carlo) have integrated over the actual  $\eta$  distribution of the muons in the single muon events considered. The muon  $\eta$  distribution in double muon events may be slightly different to this, but any difference will only have a small effect on the analysis (far smaller than the size of the effect demonstrated for the un-realistic case in which all muons actually like in the end-cap). No systematic is assigned for this uncertainty in the  $\eta$  distribution as the  $t\bar{t}$  and SU4 samples give agreement on the average trigger efficiency, and for data the estimate of  $\tau_\mu$  has been obtained by averaging over the  $\eta$  distribution of a sample of muons in the data events considered. But were an increased systematic included, this would have a negligible impact on the analysis. The trigger corrections - though applied - are minor corrections.

In summary we take the following as the trigger efficiencies for data and Monte Carlo (where the Monte Carlo is the estimate from  $t\bar{t}$ , as most events in the signal region are expected to be from  $t\bar{t}$ , and this estimate benefits from a smaller statistical uncertainty):

Data  $\tau_e = 98.5 \pm 1.1\%$ ,  $\tau_\mu = 83.7 \pm 1.9\%$

Monte Carlo  $\tau_e = 99.1 \pm 0.2\%$ ,  $\tau_\mu = 84.1 \pm 0.5\%$

- o **Determining  $\beta$ .**

This analysis is not sensitive to the individual reconstruction efficiencies,  $\epsilon_e$  and  $\epsilon_\mu$ , only their ratio. There are numerous approaches to determining  $\beta$ :

**(1) Z+jets Control Region** In a suitable Z+jets control region, the ratio of  $e^\pm e^\mp$  events to  $\mu^\pm\mu^\mp$  events,  $R$ , is given by:

---

<sup>1</sup>The method used here, of taking independently triggered single lepton events, and taking the ratio of the number events for which the appropriate trigger was fired to the total will only give an in-accurate estimate of the efficiency in the unlikely case that there were was actually an additional lepton of the appropriate flavour in the event (in addition to the muon and the electron), which actually fired the trigger, but failed the object cuts. This should be a small effect, and indeed the agreement between these numbers and those obtained in [2] using tag-and-probe methods confirms this to be the case.

$$R = \frac{N(e^\pm e^\mp)}{N(\mu^\mp \mu^\pm)}$$

After correcting the two different event rates for differing reconstruction efficiencies and trigger efficiencies, the ratio  $R$  should equal one. Therefore,  $\beta$ , the ratio of electron to muon reconstruction efficiencies can be obtained using the relation:

$$\beta = \sqrt{\frac{N_Z(e^\pm e^\mp)(1-(1-\tau_\mu)^2)}{N_Z(\mu^\mp \mu^\pm)(1-(1-\tau_e)^2)}} \text{ where the } N_Z \text{ are the numbers of } e^\pm e^\mp \text{ and } \mu^\mp \mu^\pm \text{ events in the electron-pair and muon-pair Z control-regions respectively.}$$

This calculation can be carried out for data and Monte Carlo separately. The statistical uncertainty can be calculated appropriately, and a systematic assigned based on the variation obtained on the estimate of  $\beta$  from slight variations in the control regions used.

**(2) Performance Group Studies** The individual reconstruction efficiencies,  $\epsilon_e$  and  $\epsilon_\mu$ , are well studied for tight electrons and muons with  $p_T > 20$  GeV from inclusive spectra. These estimates can be used to obtain an estimate of  $\beta$ , and an appropriate uncertainty.

**(3) Detailed Monte Carlo Studies** These can evaluate how  $\beta$  depends on the physics process simulated – kinematics, event and so on.

Using (1), and varying a low  $E_T^{miss}$ , appropriate  $m_{ll}$ , control-region, estimates of  $\beta$  are obtained. Method (3) is then used to assess the systematic on this  $\beta$ . These resulting  $\beta$  and systematic assigned are (see Appendix D for full details):

Monte Carlo:  $\beta = 0.69 \pm 0.03(\text{sys.})$

Data:  $\beta = 0.69 \pm 0.03(\text{sys.})$

The statistical error is negligible in comparison to the systematic one. The estimates of  $\beta$  in Monte Carlo and data agree at the quoted level of accuracy.

*The resulting systematic on  $S$  from this uncertainty on  $\beta$  will be small. Even were the systematic much larger, the resulting uncertainty on  $S$  will still be small. The  $\beta$  uncertainty is a negligible part of the overall systematic on  $S$ .*

### 8.3.4 Experimental and Theoretical Uncertainties

The impact on  $S$  of each experimental and theoretical uncertainty is detailed in this section. These uncertainties are to be evaluated for each background separately. The overall subtracted quantity,  $S$ , is then constructed as the sum of the different background contributions, and the systematic and statistical uncertainties combined appropriately. This treatment assumes that either (i) *the uncertainty on  $S$  is being determined for a standard model Monte Carlo based prediction,  $S_{MC}$* , or that (ii) *the uncertainty is being determined for a subtraction,  $S_{pred.}$ , based on data-driven estimates of each type of background*. Ultimately a systematic uncertainty will be assigned to both the Monte Carlo estimate, (i), but also to the data-driven prediction, (ii) (where uncertainties in the trigger efficiencies, and uncertainties on  $\beta$  will be derived from data). A measurement of the subtraction,  $S_{obs.}$ , observed in data from the  $N(e^\pm e^\mp)$ ,  $N(e^\pm \mu^\mp)$  and  $N(\mu^\pm \mu^\mp)$  will also be made.

To create the large subtracted counts predicted by true processes, like supersymmetry, which do create excesses of same-flavour events, would require more than just using an incorrect  $\beta$  or an incorrect trigger efficiency. The excesses which can be created from false trigger efficiencies and reconstruction efficiencies are small (as will be seen in the resulting systematics on  $S_{pred.}$  and  $S_{MC}$ ). The quantity  $S$  is the excess of same-flavour two-lepton events in the signal region (multiplied by  $\epsilon_e \epsilon_\mu$ ). The uncertainties on  $S$  to be considered are the same uncertainties as are detailed in Section 5, plus the uncertainties on  $\beta$ ,  $\tau_e$  and  $\tau_\mu$ , which we have already noted will be a small part of the overall uncertainty on  $S$ . Exactly how these uncertainties impact  $S$  is now detailed for each systematic:

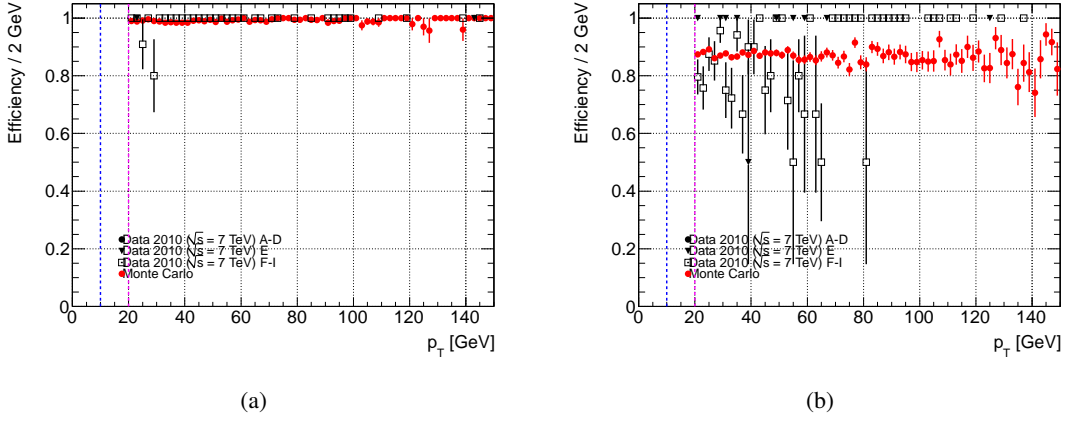


Figure 34: The efficiency of the chosen electron and muon triggers as a function of electron  $p_T$  and muon  $p_T$ . Only selected and identified electrons and muons are considered, and trigger rates are determined from independently triggered events. Illustrated errors are binomial for both data (black) and Monte Carlo (red).

- **Luminosity**

$\frac{\Delta S}{S}$  due to uncertainty on  $\mathcal{L}$ : 11% [22]

The luminosity uncertainty will be applied to the Monte Carlo estimate of  $S$ .

- **Cross-sections**

$\frac{\Delta S}{S}$  due to uncertainty on each  $\sigma$ : sample dependent, currently taken to be  $\sim 5\%$  for all Monte Carlo samples (based on [23, 24]) - with the exception of  $t\bar{t}$  which carries a 7% uncertainty.

The cross-section uncertainty is only to be applied to the Monte Carlo estimate of  $S$ .

The  $\sim 5\%$  uncertainty on each samples cross-sections is conservative, but compatible with the uncertainties attached to various cross-section measurements in ATLAS (see also Section 3.2).

- **Electron and muon trigger efficiencies**

Absolute  $\Delta S$  due to uncertainty on  $\tau_\mu$  (evaluating  $(\Delta S)^2 = (\frac{\partial S}{\partial \tau_\mu})^2 (\Delta \tau_\mu)^2$ ):

$$\left| \left( \frac{N(e^\pm \mu^\mp)(1 - \tau_e)}{(1 - (1 - \tau_e) * (1 - \tau_\mu))^2} - 2 \frac{\beta(1 - \tau_\mu)N(\mu^\pm \mu^\mp)}{(1 - (1 - \tau_\mu)^2)^2} \right) (\Delta \tau_\mu) \right| \quad (33)$$

taking  $\Delta \tau_\mu = 0.5\%$  in Monte Carlo and  $\Delta \tau_\mu = 1.9\%$  in Data (see Figure 34, Monte Carlo turn on curve (red), turn on curve for data (black) and discussion in previous sub-section)

*This formula quantifies how negligible the uncertainty on  $S$  due to uncertainties on the triggers is.*

Absolute  $\Delta S$  due to uncertainty on  $\tau_e$  (evaluating  $(\Delta S)^2 = (\frac{\partial S}{\partial \tau_e})^2 (\Delta \tau_e)^2$ ):

$$\left| \left( \frac{N(e^\pm \mu^\mp)(1 - \tau_\mu)}{(1 - (1 - \tau_e) * (1 - \tau_\mu))^2} - 2 \frac{(1 - \tau_e)N(e^\pm e^\mp)}{\beta(1 - (1 - \tau_e)^2)^2} \right) (\Delta \tau_e) \right| \quad (34)$$

taking  $\Delta \tau_e = 0.2\%$  in Monte Carlo and  $\Delta \tau_e = 1.1\%$  in Data (see Figure 34, Monte Carlo turn on curve (red), turn on curve for data (black) and discussion in previous sub-section)

*This formula quantifies how negligible the uncertainty on  $S$  due to uncertainties on the triggers is.*

- o **Electron and muon identification efficiencies**

Absolute  $\Delta S$  due to uncertainty on  $\epsilon_\mu$  (expanding  $\beta = \frac{\epsilon_e}{\epsilon_\mu}$  and evaluating  $(\Delta S)^2 = (\frac{\partial S}{\partial \epsilon_\mu})^2 (\Delta \epsilon_\mu)^2$ ):

$$\left| \left( \frac{N(e^\pm e^\mp)}{\beta(1 - (1 - \tau_e)^2)} - \frac{\beta N(\mu^\pm \mu^\mp)}{(1 - (1 - \tau_\mu)^2)} \right) \left( \frac{\Delta \epsilon_\mu}{\epsilon_\mu} \right) \right| \quad (35)$$

taking  $\frac{\Delta \epsilon_\mu}{\epsilon_\mu} \sim 4\%$  [24]

Absolute  $\Delta S$  due to uncertainty on  $\epsilon_e$  (expanding  $\beta = \frac{\epsilon_e}{\epsilon_\mu}$  and evaluating  $(\Delta S)^2 = (\frac{\partial S}{\partial \epsilon_e})^2 (\Delta \epsilon_e)^2$ ):

$$\left| \left( \frac{N(e^\pm e^\mp)}{\beta(1 - (1 - \tau_e)^2)} - \frac{\beta N(\mu^\pm \mu^\mp)}{(1 - (1 - \tau_\mu)^2)} \right) \left( \frac{\Delta \epsilon_e}{\epsilon_e} \right) \right| \quad (36)$$

taking  $\frac{\Delta \epsilon_e}{\epsilon_e} \sim 5\%$  [24]

(composed of uncertainty from OTX, pile-up effect on  $\epsilon_e$  and so on)

These results show that although there is some uncertainty on  $\epsilon_e$  and  $\epsilon_\mu$ , the subtracted result  $S$  is surprisingly insensitive to these uncertainties.

An alternative procedure is to measure just  $\beta$ , and express the overall uncertainty on  $S$  in terms of  $\beta$  and  $\Delta \beta$ . For a data-derived subtraction, obtaining a measurement of  $\beta$  is likely easier than obtaining separate measurements of  $\epsilon_e$  and  $\epsilon_\mu$ . In this instance the absolute  $\Delta S$  due to uncertainty on  $\beta$  is:

$$\left| \left( -\frac{N(e^\pm e^\mp)}{\beta^2(1 - (1 - \tau_e)^2)} + \frac{N(\mu^\pm \mu^\mp)}{(1 - (1 - \tau_\mu)^2)} \right) \Delta \beta \right| \quad (37)$$

Quantifying the uncertainty on  $S$  through an uncertainty on  $\beta$  will be adopted for the data observation of  $S$ , the Monte Carlo estimate of  $S$  and data-driven estimates of  $S$ . The values of  $\beta$ ,  $\epsilon_e$  and  $\epsilon_\mu$  and their uncertainties can be taken from performance studies ultimately (but  $\beta$  can be also predicted from the  $Z \rightarrow ll + \text{jets}$  control region). As these leptons have  $p_T > 20$  GeV, the differing reconstruction rates, and uncertainties on them are well studied by the performance groups (see discussion above); we are dealing with leptons in well studied environments.

*This formula quantifies the statements already made about how small the systematic on  $S$  due to uncertainties on  $\beta$  is. Even large uncertainty on  $\beta$  gives an uncertainty on  $S$  will a small part of the overall uncertainty on  $S$ .*

- o **Fake rate uncertainties**

An additional uncertainty can be applied to the Monte Carlo estimates of backgrounds which arise from fake leptons in events. This uncertainty, even if as large as  $\sim 10\%$ , will still have negligible impact on  $S$ , because it is so small.

- o **Parton distribution function uncertainties**

The parton distribution function uncertainty is to be estimated as follows (only applicable to Monte Carlo estimate of  $S$ ). Generated events are re-weighted according to Bjorken-x values of the interacting partons from the production process, and its scale  $Q^2$  as given by the appropriate parton distribution function of the Monte Carlo, and those of the CTEQ 6.6 central next-to-leading order error set. The full set of eigenvectors of CTEQ 6.6 are considered and the errors combined according to the Master Equation in [25]. This gives an estimate of the spread of next-to-leading order predictions, and an upper and lower uncertainty on the CTEQ 6.6 prediction. A separate uncertainty term is perhaps needed to take into account the switch from the used parton distribution function to the CTEQ 6.6 error-set.

Figure 35 shows the effect of this procedure on the experimental distributions. In this figure the

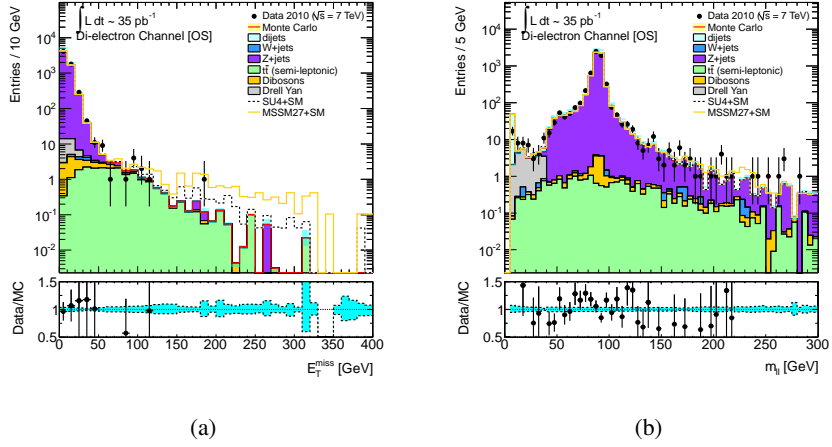


Figure 35: Parton distribution function uncertainties on  $E_T^{miss}$  (a) and  $m_{ll}$  (b) for opposite-sign electron pairs. A conservative uncertainty statistic of 5% could be applied based on these distributions. Errors on data points are 68% Poisson confidence limits, error band on Monte Carlo is purely that given by parton distribution function re-weighting.

variation on the  $E_T^{miss}$  and  $m_{ll}$  distributions, due to the parton distribution function re-weighting procedure, is illustrated by the cyan uncertainty band. A conservative error of  $\sim 5\%$  is assigned based on these figures.

- **$E_T^{miss}$  scale and other uncertainties**

The remaining uncertainties are: JES, JER,  $res_e$ ,  $E_{e,up/down}$ ,  $\mu_{ID,up/down}$  and  $\mu_{MS,up/down}$  (Section 5). The JES/JER uncertainties impact  $E_T^{miss}$  only (they effect overlap removal, but only very negligibly). The remainder of these uncertainties change both the number of leptons passing selection criteria, and  $E_T^{miss}$ . In Table 13 the impact of all these uncertainties on the number of opposite-sign events in the signal region, in each channel, were given. For each uncertainty the results in this table can be used to evaluate the corresponding uncertainty on  $\mathcal{S}$  for each source. That is, the new event rates for each channel after additional smearing or scale increase are used to recompute  $\mathcal{S}$ . The difference between this new  $\mathcal{S}$  and the original is taken as the uncertainty. The overall uncertainty on  $\mathcal{S}$  from all these sources is then the combination of all of these errors in quadrature. All these uncertainties combine to give a conservative overall uncertainty of  $\frac{\Delta \mathcal{S}}{\mathcal{S}}$  of 55% (see Table 35 for a detailed breakdown).

*It has been shown quantitatively how uncertainties on  $\beta$ ,  $\tau_e$  and  $\tau_\mu$  will give small and negligible uncertainties on  $\mathcal{S}$  – as advertised in the introductory section of this flavour subtraction note. The remaining uncertainties, which are fractional uncertainties on  $\mathcal{S}$  due to luminosity, cross-section and scale are the dominant ones. Because the predicted background  $\mathcal{S}$  is small - fractional events in most cases (at worst  $\sim 1-2$  events at this luminosity), the overall absolute systematic uncertainty is comparable to the statistical one. Even if it were inflated, signals still predict  $\sim 15 - 20+$  events – well clear of the small  $\sim 1 - 2$  event background rate.*

## 8.4 Results

Note that the estimates of  $\mathcal{S}$  which follow ( $\mathcal{S}_{MC}$  and  $\mathcal{S}_{pred.}$ ) are the predicted mean values of  $\mathcal{S}$ . Since  $\mathcal{S}$  is constructed from observations in three channels, with relatively low expected event rates, the width

of the distribution of possible  $\mathcal{S}$  values will be quite large because of the statistical fluctuations in the event counts (see later discussion of limit setting). The estimated event rates in each channel are used to predict the mean  $\mathcal{S}$ . In the limit setting section these estimates will also predict the width of the  $\mathcal{S}$  distribution when limits are set using a frequentist approach.

#### 8.4.1 Data-driven Prediction

The  $\beta$ ,  $\tau_e$  and  $\tau_\mu$  as derived from data are used to derive the data-driven prediction for  $\mathcal{S}$ :

$$\mathcal{S}_{pred.} = \mathcal{S}_{t\bar{t}} + \mathcal{S}_f + \mathcal{S}_Z + \mathcal{S}_t + \mathcal{S}_d$$

where  $\mathcal{S}_{t\bar{t}}$  is the contribution to  $\mathcal{S}$  from  $t\bar{t}$ ,  $\mathcal{S}_Z$  the contribution from  $Z+jets$  events,  $\mathcal{S}_f$  the contribution from fakes and  $\mathcal{S}_t$  and  $\mathcal{S}_d$  the contributions from single top and diboson events respectively (both of which are estimated from Monte Carlo).

- o  $t\bar{t}$  (see Section 7.6)

The data-driven estimates of  $t\bar{t}$  event rates in the signal-region are (assuming no signal, and using the results of Method A2):

- (i)  $N(e^\pm e^\mp) = 2.50 \pm 0.22(stat.) \pm 0.92(sys.)$ ,
- (ii)  $N(e^\pm \mu^\mp) = 6.61 \pm 0.46(stat.) \pm 2.42(sys.)$ ,
- (iii)  $N(\mu^\mp \mu^\pm) = 4.71 \pm 0.33(stat.) \pm 1.73(sys.)$ .

at  $34.3 \text{ pb}^{-1}$

The systematic uncertainties included in the systematic term are uncertainties which are perfectly correlated between each channel. This includes uncertainties due to: choice of generator, ISR/FSR, parton showering, jet energy scale and resolution, control region statistics and the control region backgrounds (as detailed in Section 7.6). The statistical uncertainty quoted arises from the limited Monte Carlo statistics (Section 7.6). The resulting prediction for  $\mathcal{S}_{t\bar{t}}$  is therefore:

$$\mathcal{S}_{t\bar{t}} = 0.34 \pm 0.61(stat.) \pm 0.13(sys.) \pm 0.01(\beta_{sys.}) \pm 0.01(\tau_e.sys) \pm 0.02(\tau_\mu.sys) \text{ at } 34.3 \text{ pb}^{-1}.$$

- o Fakes:  $W+jets$ , Dijets, semi-leptonic  $t\bar{t}$  (see Section 7.3)

This term gives the predicted contribution from events with one or two fake leptons.

The predicted rates of  $e^\pm e^\mp$ ,  $e^\pm \mu^\mp$  and  $\mu^\pm \mu^\mp$  events where one lepton is a fake are:

- (i)  $N(e^\pm e^\mp) = 0.31 \pm 0.21(stat.) \pm 0.11(sys.e)$
- (ii)  $N(e^\pm \mu^\mp) = -0.15 \pm 0.05(stat.) \pm 0.06(sys.e) \pm 0.01(sys.\mu)$
- (iii)  $N(\mu^\pm \mu^\mp) = 0.014 \pm 0.010(stat.) \pm 0.004(sys.\mu)$

at  $34.3 \text{ pb}^{-1}$ .

The systematic uncertainties are perfectly correlated between each channel.

$$\mathcal{S}_f = 0.46 \pm 0.31(stat.) \pm 0.10(sys.) \pm 0.02(\beta_{sys.}) \text{ at } 34.3 \text{ pb}^{-1}.$$

The prediction for  $N(e^\pm \mu^\mp)$  is set to zero to give an estimate which will set a conservative limit.

The uncertainties due to  $\tau_e$  and  $\tau_\mu$  are negligible compared to the other uncertainties.

- o  $Z+jets$  and Drell Yan (see Section 7.7)

The predicted rates for  $Z+jets$  events in the signal region are:

- (i)  $N(e^\pm e^\mp) = 0.399 \pm 0.151(stat.) \pm 0.326(sys.)$
- (iii)  $N(\mu^\pm \mu^\mp) = 0.905 \pm 0.262(stat.) \pm 0.11(sys.)$

at  $34.3 \text{ pb}^{-1}$ .

The systematic quoted has been estimated by varying the  $E_T^{miss}$  and  $m_{ll}$  cuts used in the  $Z/\gamma^*$  control region, and considering the effects of JES and JER uncertainties.

These estimates are combined with the prediction for  $N(e^\pm \mu^\mp)$  from Monte Carlo alone:

- (ii)  $N(e^\pm \mu^\mp) = 0.36 \pm 0.16(stat.) \pm 0.13(sys.)$

Considering the JES, JER and control region uncertainties, and adding an additional uncertainty on  $\mathcal{S}$  for generator effects: using  $e^\pm e^\pm$  and  $\mu^\pm \mu^\mp$  uncertainties of 70%, perfectly correlated with a

Table 31: Breakdown of uncertainty on data-driven prediction for  $\mathcal{S}$ ,  $\mathcal{S}_{pred.}$ , from all sources of systematics. The various systematics are detailed, then combined together to give a total uncertainty (expressed as an absolute uncertainty). Numbers are given at  $34.3 \text{ pb}^{-1}$  in the signal region.

	$\mathcal{S}$	$\mathcal{L}_{sys.}$	$pdf_{sys.}$	$\sigma_{sys.}$	other <sub>sys.</sub>	JES	JER	$E_e$	$res_e$	$\beta_{sys.}$	stat.
$\mathcal{S}_t$	-0.10	-0.01	-0.01	-0.01	-	0.05	-0.05	0.01	0.03	0.01	0.23
$\mathcal{S}_d$	0.51	0.06	0.03	0.03	-	0.08	0.00	0.05	0.00	0.00	0.04
$\mathcal{S}_f$	0.46	-	-	-	0.10	-	-	-	-	0.02	0.31
$\mathcal{S}_{t\bar{t}}$	0.34	-	-	-	0.12	0.05	0.00	-	-	0.01	0.61
$\mathcal{S}_Z$	0.86	-	-	-	0.49	0.16	0.53	-	-	0.00	0.33
$\mathcal{S}_{pred.}$	2.06	0.05	0.02	0.03	0.52	0.34	0.48	0.06	0.03	0.05	0.80

100% uncertainty on  $e^\pm\mu^\mp$  for generator systematics (Table 27) the resulting prediction for  $\mathcal{S}$  is:  
 $\mathcal{S}_Z = 0.86 \pm 0.33(\text{stat.}) \pm 0.74(\text{sys.}) \pm 0.003(\beta_{sys.})$  at  $34.3 \text{ pb}^{-1}$ .

The uncertainties due to  $\tau_e$  and  $\tau_\mu$  are negligible compared to the other uncertainties.

Combining these estimates of  $\mathcal{S}$  for the different background contributions, and their uncertainties appropriately, with the Monte Carlo prediction for the contribution to  $\mathcal{S}$  from diboson events ( $\mathcal{S}_d$ ) and single top ( $\mathcal{S}_t$ ) as detailed in Section 8.4.2, Table 34, gives a data-driven prediction of:

$$\boxed{\mathcal{S}_{pred.} = 2.06 \pm 0.78(\text{sys.}) \pm 0.79(\text{stat.})}$$

A detailed break-down of the overall systematic uncertainty on  $\mathcal{S}_{pred.}$  is given in Table 31. Note that the s-channel and t-channel contributions to the single top Monte Carlo event rate are negligible. These two channels are taken into account by the fake component estimated from data, only the estimate of single top events in the Wt-channel is needed from Monte Carlo. In the column ‘other<sub>sys.</sub>’ the uncertainties given are those which are particular to each data-driven background estimation, and so are therefore not correlated between backgrounds. For  $t\bar{t}$  this includes the generator and ISR/FSR uncertainties, for fakes this includes the uncertainties from  $e$  and  $\mu$  and for Z+jets this includes the uncertainties from varying the control-region chosen, and the large generator uncertainty. The luminosity, parton distribution function, JES+JER, electron scale and resolution and  $\beta$  uncertainties are all uncertainties which are perfectly correlated between the backgrounds. These are each summed linearly for all backgrounds in each channel. The cross-section uncertainties are not correlated between the backgrounds, and are therefore added in quadrature. The systematics due to the ID and MS muon momentum measurements, and the trigger efficiency uncertainties, are neglected as they are small. Finally, the estimates for each source of uncertainty on the overall estimate,  $\mathcal{S}_{pred.}$ , are added in quadrature to give the total systematic uncertainty.<sup>2</sup>

<sup>2</sup>Note that for single top, some entries in the table are negative. The negative sign is included in the table to make clear the cases where as one uncertainty is explored two different background components change in different directions i.e. there are negative correlations. This ensures that when each column is added up, the resulting uncertainty is the same as what it would have been had the background not been decomposed into its components. Similarly, when evaluating the uncertainties on  $\mathcal{S}$  due to resolution uncertainties (JER and  $res_e$ ), the new event rates in each channel after the additional smearings are applied are simply fed into the formula for  $\mathcal{S}$  to yield the new estimate of  $\mathcal{S}$ . In instances where the additional smearing increases one channel, yet decreases another, no attempt is made to take the modulus of the increase in each channel (and in doing so making the argument that all channels should increase or decrease together) and re-calculate  $\mathcal{S}$ . This approach sets conservative limits - but will ultimately have only a very small effect on them (changing the numerical limits by at most  $\sim 0.3$ ).

Table 32: Number of events in each of the three possible charge-flavour channels at  $34.3 \text{ pb}^{-1}$  after event selection. Errors on the Monte Carlo prediction are purely statistical.

	$e^\pm e^\mp$	$e^\pm \mu^\mp$	$\mu^\pm \mu^\mp$
$t\bar{t}$	$20.2 \pm 0.8$	$51.7 \pm 1.2$	$34.8 \pm 1.0$
Dibosons	$11.9 \pm 0.1$	$12.8 \pm 0.2$	$23.9 \pm 0.2$
Drell Yan	$22.47 \pm 1.28$	$0.00 \pm 0.00$	$56.7 \pm 2.0$
Z+jets	$6023 \pm 25$	$37 \pm 2$	$13011 \pm 37$
$W+$ jets	$2.5 \pm 0.6$	$2.7 \pm 0.7$	$0.6 \pm 0.3$
Dijets	$49 \pm 5$	$53 \pm 35$	$215 \pm 61$
Single Top	$1.6 \pm 0.3$	$4.5 \pm 0.4$	$3.4 \pm 0.4$
Total SM	$6131 \pm 26$	$162 \pm 35$	$13345 \pm 71$
MSSM27	$18.0 \pm 1.4$	$6.6 \pm 0.8$	$21.8 \pm 1.5$

Table 33: Number of events in each of the three possible charge-flavour channels at  $34.3 \text{ pb}^{-1}$  after an  $E_T^{miss}$  cut of 100 GeV. Errors on the Monte Carlo prediction are purely statistical.

	$e^\pm e^\mp$	$e^\pm \mu^\mp$	$\mu^\pm \mu^\mp$
$t\bar{t}$	$3.7 \pm 0.3$	$9.8 \pm 0.5$	$7.0 \pm 0.4$
Dibosons	$0.30 \pm 0.02$	$0.36 \pm 0.03$	$0.61 \pm 0.03$
Drell Yan	$0 \pm 0$	$0 \pm 0$	$0 \pm 0$
Z+jets	$0.4 \pm 0.2$	$0.4 \pm 0.2$	$1.0 \pm 0.3$
$W+$ jets	$0 \pm 0$	$0 \pm 0$	$0 \pm 0$
Dijets	$0 \pm 0$	$0 \pm 0$	$0 \pm 0$
Single Top	$0 \pm 0$	$1 \pm 0$	$1 \pm 0$
Total SM	$4.5 \pm 0.4$	$11.3 \pm 0.6$	$9.2 \pm 0.6$
MSSM27	$13.8 \pm 1.2$	$4.5 \pm 0.7$	$16.2 \pm 1.3$

#### 8.4.2 Monte Carlo Prediction

The predicted numbers of standard model events after event selection, and in the signal region, are detailed in Tables 32 and 33 (from Monte Carlo). This information was also given in Section 6.3 and Table 12. Table 32 illustrates the dominance of Z+jets before a transverse missing energy cut is made. The MSSM27 predictions are also detailed in these tables for comparison. The reduction to the standard model background in Table 33 is significant, but the impact to the MSSM prediction much smaller.

The predicted numbers of standard model events remaining after subtraction are detailed in Table 34. These estimates are based purely on Monte Carlo. The trigger efficiencies,  $\tau_e$  and  $\tau_\mu$ , and the ratio of reconstruction efficiencies,  $\beta$ , used are those obtained from Monte Carlo (Section 8.3.3). The overall estimate of  $\mathcal{S}$ , obtained from combining the individual background estimates, and their uncertainties, in Table 34, is:

$$\mathcal{S}_{MC} = 1.8 \pm 1.1(\text{sys.}) \pm 0.87(\text{stat.})$$

As expected, and shown in Table 34 in the detailed break-down, the systematic is comparable to the statistical uncertainty (dominated by the  $t\bar{t}$  statistics). The conservative uncertainty from JES/JER, and electron/muon scale and resolution systematics – denoted ‘scale<sub>sys.</sub>’ in this table, is the dominant systematic. The sources which are combined to give this single uncertainty term are detailed in Table 35. These uncertainties have been estimated by combining the uncertainty from each source on the event

Table 34: Predicted composition of background in the flavour subtracted signal region. The various components which make up the total systematic, *Total sys.*, are detailed. The column labelled ‘ $\text{scale}_{\text{sys.}}$ ’ includes the JES/JER,  $\text{res}_e$ ,  $E_{e,\text{up/down}}$  and  $\mu_{ID/MS,\text{up/down}}$  uncertainties.

	$\mathcal{S}$	$\mathcal{L}_{\text{sys.}}$	$\text{pdf}_{\text{sys}}$	$\sigma_{\text{sys}}$	$\beta_{\text{sys}}$	$\tau_{e,\text{sys}}$	$\tau_{\mu,\text{sys}}$	$\text{scale}_{\text{sys.}}$	Total sys.	stat.
$t\bar{t}$	0.52	0.057	0.026	0.036	0.017	0.0029	0.0081	0.52	0.53	0.76
Dibosons	0.51	0.056	0.025	0.025	0.00039	9.9e-05	0.00073	0.099	0.12	0.043
Drell Yan	0	0	0	0	0	0	0	0	0	0
Z+jets	0.89	0.098	0.044	0.044	0.0052	9.3e-05	0.0012	0.52	0.54	0.35
W+jets	0	0	0	0	0	0	0	0	0	0
Dijets	0	0	0	0	0	0	0	0	0	0
Single Top	-0.096	-0.011	-0.0048	-0.0048	0.012	0.00023	0.00079	0.079	0.081	0.23

Table 35: Breakdown of uncertainty on subtraction from systematics which impact  $E_T^{\text{miss}}$ . The various systematics are detailed, then combined together to give a total uncertainty (expressed as an absolute uncertainty). Numbers are given at  $34.3 \text{ pb}^{-1}$  in the signal region.

	Events	$\text{JES}_{\text{up}}$	$\text{JES}_{\text{down}}$	JER	$E_{e,\text{up}}$	$E_{e,\text{down}}$	$\text{res}_e$	$\mu_{MS,\text{up}}$	$\mu_{MS,\text{down}}$	$\mu_{ID,\text{up}}$	$\mu_{ID,\text{down}}$	$\text{scale}_{\text{sys.}}$
Z+jets	0.89	0.26	-0.06	0.37	0.26	-0.09	0.05	0.00	-0.07	0.00	0.00	0.52
$t\bar{t}$	0.52	0.20	0.11	0.39	-0.19	-0.21	-0.18	-0.01	-0.03	0.00	0.01	0.52
Dibosons	0.51	0.08	-0.06	-0.00	0.05	-0.03	-0.00	0.01	0.00	-0.00	-0.00	0.10
Single Top	-0.10	0.05	-0.02	-0.05	0.01	0.00	0.03	0.00	0.00	0.00	0.00	0.08
Total SM	1.82	0.59	-0.02	0.71	0.13	-0.33	-0.11	-0.00	-0.09	-0.00	0.01	0.99

rates in each channel (Table 13) appropriately. The size of the uncertainty from  $\beta$  depends on the events observed in each channel – but for all backgrounds it is smaller than the luminosity uncertainty.

The expected contributions to  $\mathcal{S}_{\text{SUSY}}$  (i.e.  $\mathcal{S}$  calculated from supersymmetric events alone) from a variety of points in the MSSM are detailed in Table 36. These predictions for  $\mathcal{S}$  are substantially higher than the standard model predictions, both  $\mathcal{S}_{\text{MC}}$  and  $\mathcal{S}_{\text{pred.}}$ . A wider variety of signal points will be discussed in Section 8.4.4, where the limit which can be obtained from  $\mathcal{S}_{\text{obs.}}$  is detailed and a variety of signal points with predicted contributions above this limit are illustrated.

Table 36: Predicted mean excess of same-flavour events,  $\mathcal{S}_{\text{SUSY}}$  for a variety of MSSM points, at  $34.3 \text{ pb}^{-1}$  after an  $E_T^{\text{miss}}$  cut of 100 GeV for selected signal points. Errors on the Monte Carlo prediction are statistical.

Point	$\mathcal{S}_{\text{MSSM}}$
MSSM22	$21.22 \pm 1.45$
MSSM27	$26.67 \pm 1.43$
MSSM29	$18.29 \pm 1.27$
MSSM26	$24.40 \pm 1.44$
MSSM28	$28.29 \pm 1.46$

Table 37: Number of events in each of the three possible charge-flavour channels at  $34.3 \text{ pb}^{-1}$  before and after an  $E_T^{\text{miss}}$  cut of 100 GeV. Error on the Monte Carlo prediction is purely statistical, errors on data are Poisson 68% confidence limits (see Tables 12 and 33 for breakdown of the Monte Carlo into individual background components).

	$e^\pm e^\mp$	$e^\pm \mu^\mp$	$\mu^\pm \mu^\mp$
Data	$6250^{+80}_{-79}$	$131^{+12}_{-11}$	$12774^{+114}_{-113}$
Total SM	$6131 \pm 26$	$162 \pm 35$	$13345 \pm 71$
Data ( $E_T^{\text{miss}} > 100 \text{ GeV}$ )	$4^{+3.2}_{-1.9}$	$13^{+4.7}_{-3.6}$	$13^{+4.7}_{-3.6}$
Total SM ( $E_T^{\text{miss}} > 100 \text{ GeV}$ )	$4.5 \pm 0.4$	$11.3 \pm 0.6$	$9.2 \pm 0.6$

### 8.4.3 Observation from Data

The recorded events in data before and after the high  $E_T^{\text{miss}}$  cut are detailed, alongside the Monte Carlo prediction, in Table 37. The agreement between Monte Carlo and data both before and after the missing transverse energy cut are applied is reasonable. In this section, which presents the observed excess of same-flavour over different flavour events, the trigger efficiencies,  $\tau_e$  and  $\tau_\mu$ , and  $\beta$  are those derived from data (see Section 8.3.3). The observed  $\mathcal{S}$  from data is:

$$\mathcal{S}_{\text{obs.}} = 1.98 \pm 0.15(\text{sys.}\beta) \pm 0.02(\text{sys.}\tau_e) \pm 0.06(\text{sys.}\tau_\mu)$$

#### 8.4.4 Confidence Limits and Interpretation

In this section two complementary limit setting approaches are described. Both approaches will be shown to give compatible results, but only the first method (Toy Monte Carlo) will be used to set the limits from this analysis. A limit is set on  $S_{SUSY}$ , which is the excess same flavour events from supersymmetry multiplied by the product of electron and muon reconstruction efficiencies ( $\epsilon_e$  and  $\epsilon_\mu$ , which include both efficiency and acceptance).

#### Toy Experiments

We have predictions for the average number of events we should observe in the three different opposite-sign flavour channels:  $\bar{N}(e^\pm e^\mp)$ ,  $\bar{N}(e^\pm \mu^\mp)$  and  $\bar{N}(\mu^\pm \mu^\mp)$  (in the absence of beyond the standard model physics). That is, if we ran the experiment millions of times we would expect the average observation made of the number of events in each channel to be equal to these predictions. These predictions carry uncertainties - both statistical and systematic. These predictions exist for (a) data-driven approaches, and (b) purely Monte Carlo driven approaches – each set of predictions carrying a different set of uncertainties. Using these, the observation  $S_{obs.}$  can be converted to an observed limit on  $S_{SUSY}$ , the excess same-flavour events from supersymmetry multiplied by acceptances (i.e. the value of  $S$  calculated from supersymmetric events alone).

A single toy experiment can be set up as follows:

- Set the expected mean observations of  $e^\pm e^\mp$ ,  $e^\pm \mu^\mp$  and  $\mu^\pm \mu^\mp$  events to be the predicted observations (the  $\bar{N}$ ), multiplied by a series of random numbers drawn from gaussian distributions with unit means and sigmas set to equal the various fractional uncertainties. This includes a gaussian for the statistical uncertainty on the estimates of the mean values, as well as gaussians for the systematics. If an uncertainty is correlated between the channels, then a single random number is drawn and each expected observation multiplied by this same random number. If the uncertainties are perfectly correlated, but different in magnitude between the channels, then this is corrected for. For the case of uncorrelated uncertainties - such as the statistical uncertainty - the expected observation in each channel is multiplied by a different random number (and in the case of the statistical uncertainty, the gaussians are different for each channel). The  $\bar{N}$  are taken as the sum of the contributions from the different background components. This allows uncertainties specific to a particular background estimate to affect the appropriate component of the total only.
- Take the number of events the particular experiment observed, in each channel, as random numbers from three Poisson distributions with means equal to the expected observations as calculated above.
- Take also an observed number of same-flavour  $e^\pm e^\mp$  supersymmetric events and an observed number of same-flavour  $\mu^\pm \mu^\mp$  supersymmetric events, from Poisson distributions with means equal to the *hypothesised mean number of same-flavour supersymmetric events in the given channel* at the considered luminosity. That is, assume the true  $e^\pm e^\mp$  and  $\mu^\pm \mu^\mp$  production rates are the same, that there is no  $e^\pm \mu^\mp$  production and set the hypothesised mean number of  $e^\pm e^\mp$  and  $\mu^\pm \mu^\mp$  events to  $\bar{s} \times \beta(1 - (1 - \tau_e)^2)$  and  $\bar{s}(1 - (1 - \tau_\mu)^2)/\beta$  respectively. The  $\bar{s}$  is therefore the true rate of production, but the mean number observed takes into account the trigger and reconstruction efficiencies.
- Draw  $\beta$  and trigger efficiencies from gaussian distributions with means of the expected values, and sigmas set to the uncertainties. This accounts for the effect on  $S$  of our uncertainties the trigger efficiencies and reconstruction ratio.

- Calculate  $\mathcal{S}$  for each pseudo-experiment, with the drawn  $\beta$ ,  $\tau_e$  and  $\tau_\mu$  and the standard model plus supersymmetry event observations drawn from the Poisson distributions.

If we run one million toy experiments we get a distribution of all possible observed  $\mathcal{S}$  values, *for the particular hypothesised true number of same-flavour supersymmetric events, multiplied by acceptances, in each same-flavour channel,  $\bar{s}$* . The *limit to be set on  $\bar{s}$ , is the value of this which when hypothesised gives only 5% of experiments with  $\mathcal{S}_{obs}$ , less than or equal to what we actually observed in the experiment we ran*. This limit is on the mean of the Poisson distribution from which the  $e^\pm e^\mp$  and  $\mu^\pm \mu^\mp$  supersymmetry event numbers were drawn. This translates to a limit on  $\mathcal{S}$  from supersymmetry,  $\mathcal{S}_{SUSY}$ , of  $2\bar{s}$ .

For example, we take the Monte Carlo predictions for the  $\bar{N}$  in each channel at  $34.3 \text{ pb}^{-1}$ :  $\bar{N}(e^\pm e^\mp) = 4.5$ ,  $\bar{N}(e^\pm \mu^\mp) = 11.3$  and  $\bar{N}(\mu^\pm \mu^\mp) = 9.3$ . We draw a single random number from each of: (i) a gaussian with unit mean, and sigma 0.11 for the luminosity uncertainty, (ii) a gaussian with unit mean, and sigma 0.05 for the parton distribution function uncertainty and so on for all the uncertainties which are perfectly correlated between the channels and backgrounds. We multiply the estimates in each channel: 4.5, 11.3 and 9.3 by each of these random numbers. We then consider the statistical uncertainties. These are 0.4, 0.6 and 0.6 respectively. The estimate in  $e^\pm e^\mp$  channel, for example, is therefore multiplied by a random number drawn from a gaussian with unit mean and sigma of  $0.4/4.5$ . Additional Gaussians are drawn for each uncertainty on the event rates in each channel, for each background, taking account of correlations. Random numbers are drawn as described for  $\beta$ ,  $\tau_e$  and  $\tau_\mu$ . Two final random numbers are then drawn for the additional same flavour excesses from supersymmetry (from the same distribution, as detailed above).  $\mathcal{S}$  is then calculated using these expected observations, and efficiencies. This processes of drawing random numbers and calculating  $\mathcal{S}$  is repeated a million times. The hypothesised same flavour excess is varied, and the series of experiments repeated. The distribution of  $\mathcal{S}$  values for the hypothesised excess of same-flavour events which gives  $\mathcal{S}$  of 1.98 (our observation) or less, only 5% of the time is illustrated in Figure 36. The Poisson mean,  $\bar{s}$ , for this is 5.1 corresponding to  $\mathcal{S}_{SUSY}$  of 10.2. The limit is driven by the width of this distribution. The Poisson fluctuations which result from drawing the three different observations in each channel give this distribution its width. The impact of the uncertainties on these means has a much smaller impact on the width than the fluctuations do.

The final limits will be set using the data-driven background estimations of the expected events in each channel given in Section 8.4.1, not the Monte Carlo predictions as the data-driven predictions are a better estimate of the backgrounds. The results of using the Monte Carlo predictions are given here for interest. The data-driven estimates will give slightly better limits because the predicted number of  $t\bar{t}$  events in each channel is larger in Monte Carlo than the data-driven prediction. Although the limits differ, the simulated grid points excluded by both background estimations when we consider the mSUGRA exclusions are the same. The limit quoted so far of 10.2 on  $\mathcal{S}_{SUSY}$  at  $34.3 \text{ pb}^{-1}$  has been set using the Monte Carlo estimates, and uncertainties, of the events in each channel (and of  $\beta$ ,  $\tau_e$  and  $\tau_\mu$ ).

If the data-driven estimates are used, and their uncertainties (both statistical and systematic), the limit is 8.8. This first limit has been set using the assumption that *supersymmetry does not introduce a ‘flavour-blind’ component*. That is, supersymmetric events have been assumed to be only of the same-flavour kind. However, it is possible to have supersymmetric events with two-leptons for which there are equal quantities of different-flavour and same-flavour types – and these are what we call flavour-blind processes. Adding more flavour-blind physics does not change  $\mathcal{S}_{SUSY}$ , since flavour-blind processes contribute zero events after flavour-subtraction (by definition), but it does change the width of the distribution of observed  $\mathcal{S}$  values. The greater the ‘contamination’ in same-flavour events from flavour-blind supersymmetric processes, the wider the  $\mathcal{S}$  distribution. This will impact the limit. The more contamination there is in a SUSY point, the harder it is to exclude. We consider now exactly how the limit

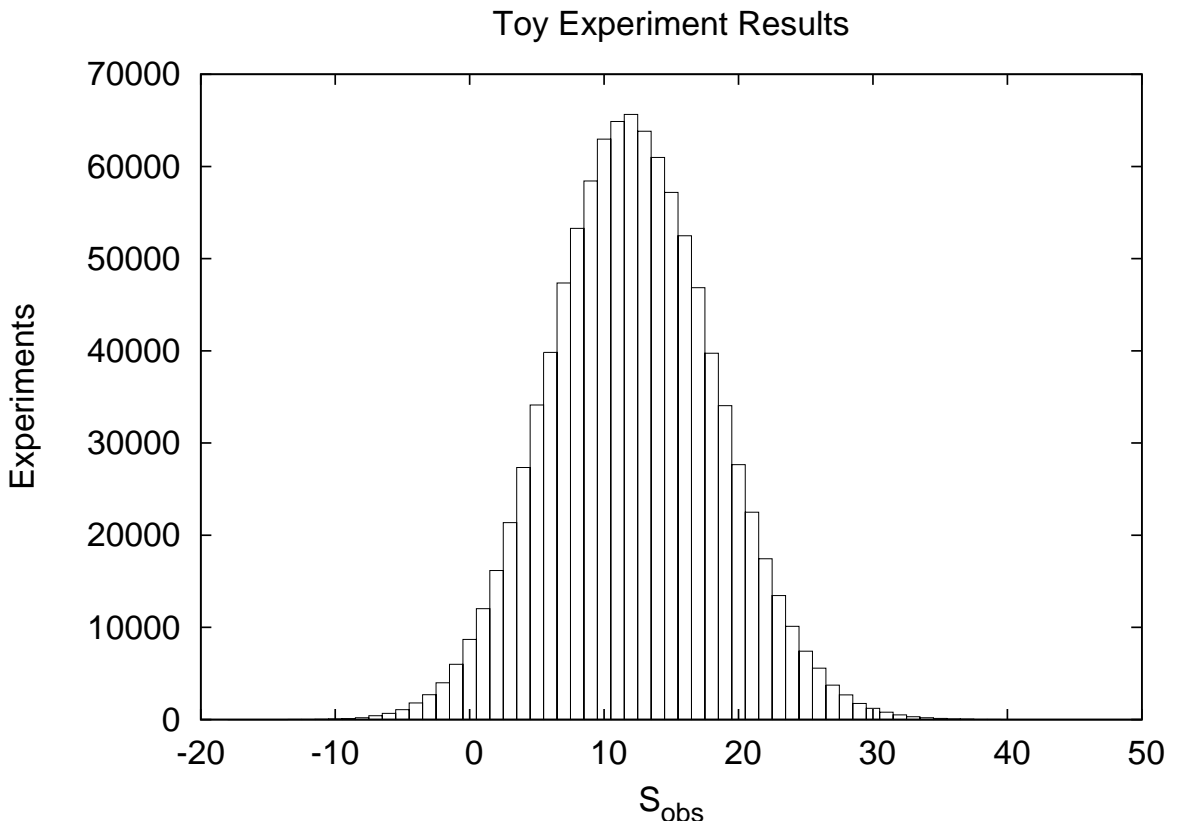


Figure 36: Observed  $\mathcal{S}$  values for one million toy experiments, based on the expected number of standard model events in each channel from Monte Carlo, and a hypothesis of on average 10.2 same-flavour supersymmetry events ( $\mathcal{S}_{SUSY}$ ) at  $34.3 \text{ pb}^{-1}$ . Our particular experiment observed  $\mathcal{S}_{obs}$  of 1.98 at  $34.3 \text{ pb}^{-1}$ , only 5% of the illustrated experiments for the chosen rate of supersymmetric event production recorded a value less than this observation. That is to say, if the hypothesised rate – or a higher rate – of same flavour event production was occurring, over 95% of experiments would have given a higher  $\mathcal{S}$  than ours. A limit on  $\mathcal{S}_{SUSY}$  of 10.2 at  $34.3 \text{ pb}^{-1}$  is therefore set as the 95% confidence limit.

Contamination	Data-Driven	MC
0	8.8	10.2
1/6	9.2	10.5
1/3	10.4	12.0
1/2	12.6	14.0

Table 38: Observed limit on  $\mathcal{S}_{SUSY}$  obtained using the data-driven estimates of the contributions in each channel from SM background, and the purely Monte Carlo estimates of the contributions in each channel from SM background. The observed limits assume that the rates of production of  $e^\pm e^\mp$  and  $\mu^\pm \mu^\mp$  events from SUSY are the same. Limits are given for various degrees of contamination by flavour-blind SUSY processes which contribute not just  $e^\pm e^\mp$  and  $\mu^\pm \mu^\mp$  events but also  $e^\pm \mu^\mp$  events.

changes if we account for this contamination. For the point illustrated in Section 8.4.2, MSSM27, just one sixth of the total  $e^\pm e^\mp$  events arise from flavour-blind processes. The limit setting procedure using Toy Monte Carlo can be extended to include flavour-blind processes. In addition to drawing  $e^\pm e^\mp$  and  $\mu^\pm \mu^\mp$  events for supersymmetry, we can draw further  $e^\pm e^\mp$  and  $\mu^\mp \mu^\pm$  events – but events which have  $e^\pm \mu^\mp$  counterparts. If the mean of the flavour-blind processes is adjusted so that one sixth of the total same flavour events are flavour-blind, the limit  $\mathcal{S}_{SUSY}$  becomes 9.2. If the flavour-blind component becomes large ( $\sim 50\%$ ), then the limit reaches 12.6. The flavour-subtraction analysis is designed to search for an excess of same-flavour events from supersymmetry – if the leptons are predominantly from flavour-blind processes, the analysis is less sensitive. The equivalent limits set using purely Monte Carlo estimates are 10.5 and 14.0. The limits obtained for different degrees of contamination are summarised in Table 38.

As an aside, we can run these toy experiments for just the standard model background predictions. That is, we add in zero supersymmetry events. The resulting  $\mathcal{S}_{obs}$  for these one million experiments are illustrated in Figure 37. This figure illustrates the likely possible observations with just the standard model. Our observation of  $\mathcal{S}_{obs} = 1.98$  is a likely value given this distribution. The mean of this distribution is what it has been predicted in detail to be, the width is driven by the expected event rates in each channel.

The limit set on  $\mathcal{S}$  calculated for the supersymmetric events only, the  $\mathcal{S}_{SUSY}$ , can be illustrated in various parameter spaces. In Figure 38 the same-flavour excesses multiplied by  $\epsilon_e \epsilon_\mu$ , so the  $\mathcal{S}$  calculated for supersymmetric events alone, for a variety of points in the ‘PhenoGrids’ are given at  $34.3 \text{ pb}^{-1}$ . In these grids there are 5 parameters:  $m(\tilde{g})$ ,  $m(\tilde{q}_L)$ ,  $m(\tilde{\chi}_2^0 \tilde{\chi}_1^\pm)$ ,  $m(\tilde{l}_L)$  and  $m(\tilde{\chi}_1^0)$ . In the first of the three PhenoGrids, the sleptons have masses 2 TeV and therefore the same flavour excesses at these luminosities are small. For the other two PhenoGrids, however, there is significant production of same-flavour dilepton events in excess of the different-flavour production, as these figures show. The cross-sections of the second PhenoGrid points are higher, which is reflected in the higher same-flavour excesses given for these grid points. In Figure 38 these points are illustrated in squark-gluino space. Each PhenoGrid contains 32 points – but two points for each squark and gluino mass pairing. However, sixteen of these points are associated with a ‘lighter LSP’, sixteen with a ‘heavier LSP’. These thirty two points are therefore divided according to this LSP classification and the sixteen points in each division all have different squark and gluino masses. The lepton  $p_T$  in these grids is influenced by the mass difference between the  $\tilde{\chi}_2^0/\tilde{\chi}_1^\pm$  and  $\tilde{l}$  particles, and also the difference between the  $\tilde{\chi}_1^0$  and  $\tilde{l}$  masses. These points are set up so that the minimum mass difference is constant (50 GeV), whilst the maximum differences varies between 50 and 200 GeV. So alternatively, the light LSP points are those with the maximum difference between these masses, and the heavier LSP points those with the minimum difference between these masses. In

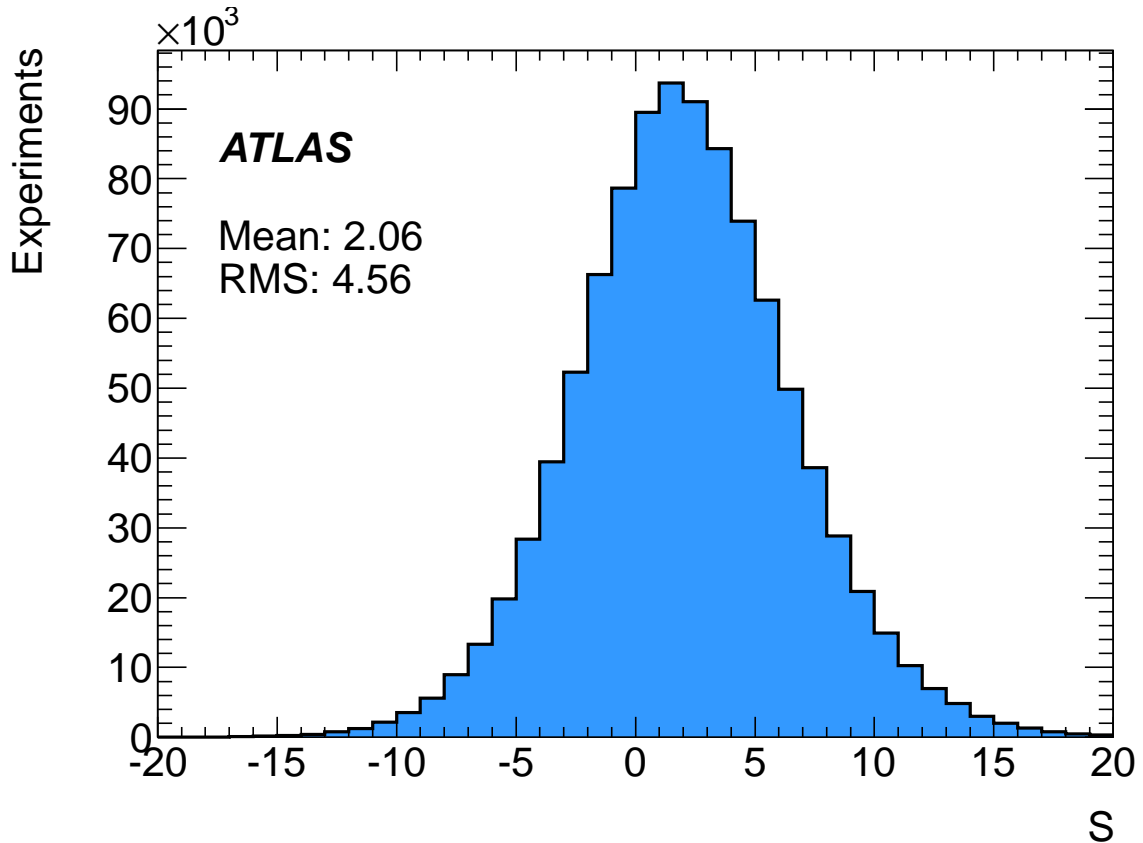


Figure 37: Observed  $S$  values for one million toy experiments in the just standard model case. This figure illustrates that our particular observation,  $S_{obs} = 1.98$ , is not unexpected. Whilst this distribution has a mean near zero, the low numbers of events in each channel at  $34.3 \text{ pb}^{-1}$  give this distribution its width. The total opposite-sign event rate is predicted to be  $\sim 25$  events, so we would roughly expect this distribution to approximate a Gaussian distribution with  $\sigma \sim 5$ .

PhenoGrid3 the flavour-blind contamination can be as much as 50% of the total same-flavour component (implying limits of 14.0 and 12.6 with the Monte Carlo and data-driven estimates respectively), for PhenoGrid2 the contamination is only a third the total same-flavour component (implying limits of 12.0 and 10.4);

In Figure 39 the  $\mathcal{S}_{SUSY}$  is illustrated for each point in mSUGRA parameter space. The majority of points with low  $m_0$  and low  $m_{1/2}$  have just one-fifth contamination by flavour-blind SUSY events.

To draw an exclusion contour through Figures 38 and 39 we need to take into account uncertainties in the number of signal events in each channel. The Monte Carlo predicts the number of events in each channel for each point, and so we can also rather than a set a limit based on assumed contamination take each point individually and consider whether or not it is excluded by our observation. Here we will draw the observed exclusions for the partially data-driven background predictions only. The limit setting procedure and systematic uncertainties are treated as before but now:

- For each point in a given grid, signal events in each channel are drawn from Poisson distributions with means equal to the predicted number of events from Monte Carlo. The JES, JER and parton distribution function uncertainties in the signal are treated as uncertainties correlated with the corresponding systematic uncertainties on the background predictions. To account for these, the means are each multiplied by the single numbers drawn from the appropriate Gaussian distributions described for the background, but corrected in size to keep the relative sizes of the correlated uncertainties between signal and background in proportion. Additional Gaussians are used for signal uncertainties not correlated to any background uncertainties.
- The  $\beta$ ,  $\tau_e$  and  $\tau_\mu$  are drawn as described, the subtraction is then performed.

For each signal point, the one million toy experiments are run. The resulting p-value (the % of experiments measuring  $\mathcal{S}$  less than our  $\mathcal{S}_{obs}$  of 1.98) is recorded. These are then converted into significances, and the appropriate 95% confidence limit drawn through them. This procedure uses all the information we have about each point to avoid making assumptions about the contamination and the size of the signal uncertainties. The default ROOT interpolation is not reliable for the PhenoGrid, and so a more considered interpolation (as is done for the opposite-sign and same-sign limits) is used for these. The exclusion limits are given in Figure 41.

Note that - the inclusion of 80 new mSUGRA points around the gap in the D0 tri-lepton exclusions reveals that this feature is also present, as one would expect, in this analysis. Initially it is not seen because of the coarse granularity of the grid - see Figure 40. The marked line is where  $m(\tilde{l}) = m(\tilde{\chi}_2^0)$ . Just to the left of this line  $m(\tilde{l})$  is just less than  $m(\tilde{\chi}_2^0)$ . As a result the lepton from the  $\tilde{\chi}_2^0 \rightarrow \tilde{l}^\pm l^\mp$  decay is soft. For these points the signal acceptance for same flavour events is reduced, and so there is no longer a significant excess of same flavour events over those of different flavour.

In Table 36 the predicted same-flavour excesses for a variety of points in the MSSM were illustrated. This again illustrates that significant  $\tilde{\chi}_2^0 \rightarrow \tilde{\chi}_1^0 t^+ t^-$  branching ratio supersymmetry points with high cross-sections may be excluded by this search.

*These Toy Monte Carlo experiments have demonstrated that the limit is driven not by the systematic uncertainties, but by the predicted numbers of events in each of the three flavour channels at this luminosity. The width of the distribution of possible values of  $\mathcal{S}$  is roughly given by the sum of the predicted*

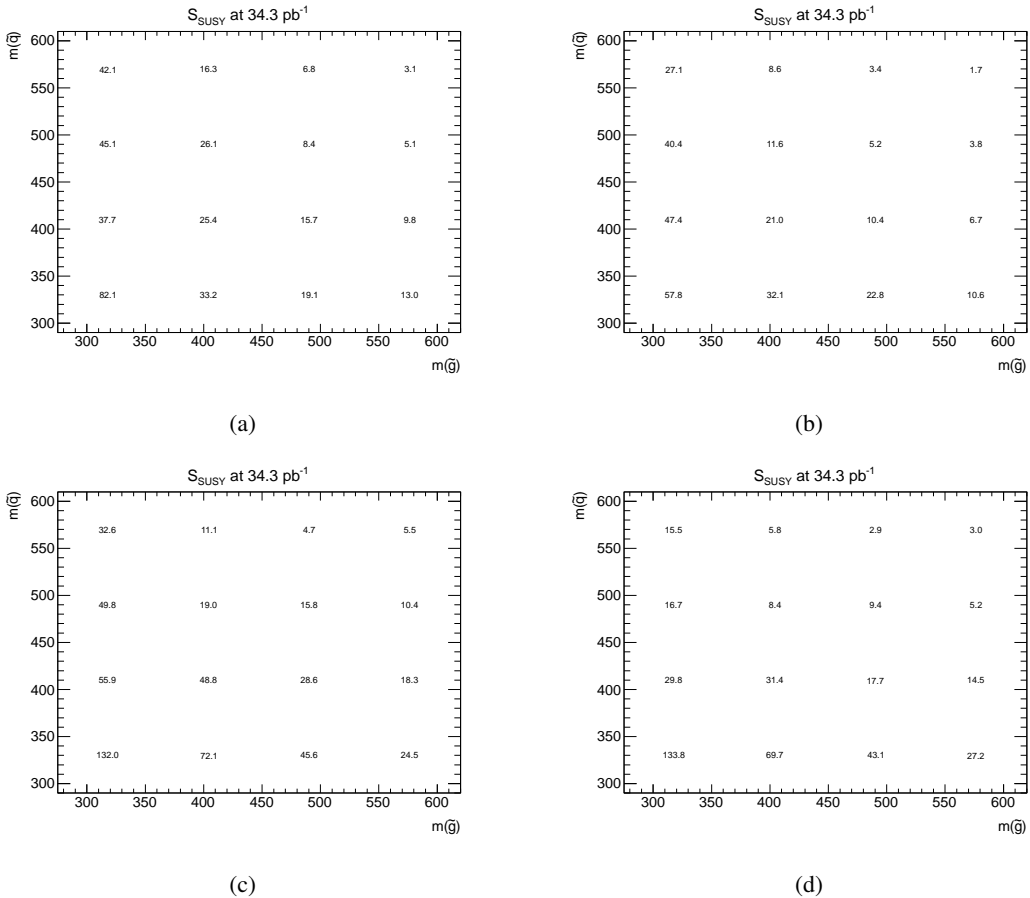


Figure 38: Predicted same-flavour excess multiplied by  $\epsilon_e \epsilon_\mu$  (i.e.  $S$ , from supersymmetry events only) at  $34.3 \text{ pb}^{-1}$  for a variety of points in the PhenoGrids. EachPhenoGrid contains 32 points – but two points for each squark and gluino mass pairing. However, sixteen of these points are associated with a ‘lighter LSP’, sixteen with a ‘heavier LSP’. These thirty two points are therefore divided according to this LSP classification and the sixteen points in each division all have different squark and gluino masses. The lighter-LSP points are illustrated in (a) and (c) for Phenogrid3 and Phenogrid2 respectively. Correspondingly, (b) and (d) illustrate the heavier-LSP points. In (c) and (d) the higher rates arise from the higher cross-section for supersymmetric event production. NB:  $S$  values in this figure are produced with slightly out-dated definitions, but are very similar to the  $S$  values obtained with the most up-to-date definitions.

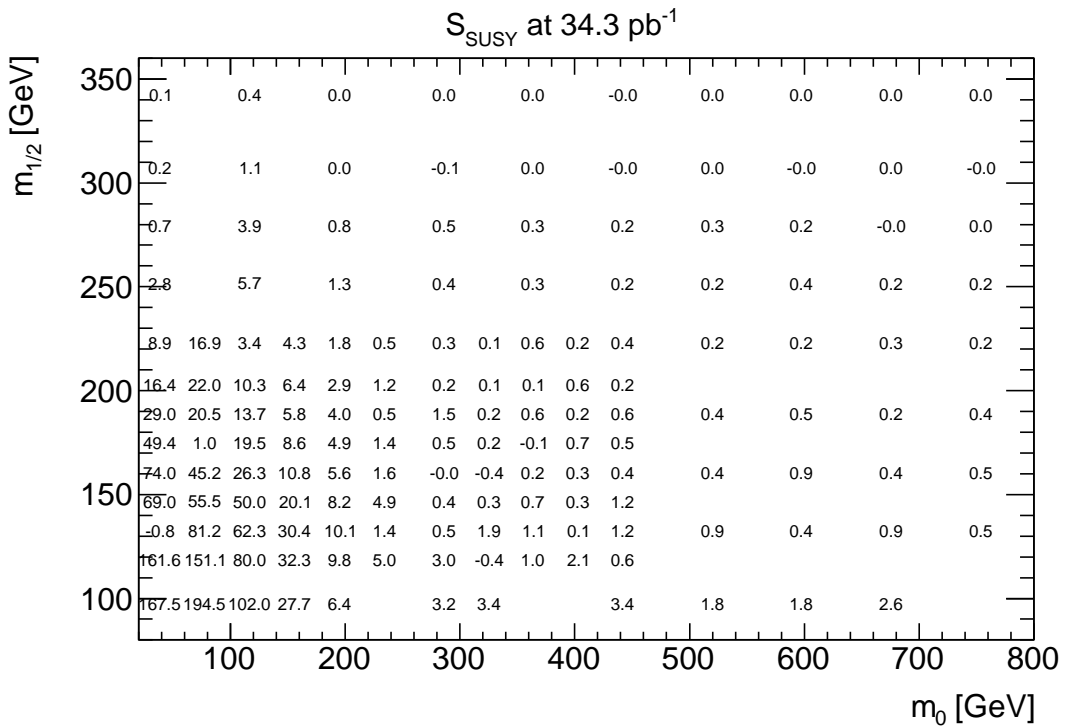


Figure 39: Predicted same-flavour excess multiplied by  $\epsilon_e \epsilon_\mu$  (i.e.  $\mathcal{S}$ , from supersymmetry events only) at  $34.3 \text{ pb}^{-1}$  for the mSUGRA parameter space grid. The majority of the points in the bottom left corner have a contamination of roughly one-fifth. NB:  $\mathcal{S}$  values in this figure are produced with slightly outdated definitions, but are very similar to the  $\mathcal{S}$  values obtained with the most up-to-date definitions.

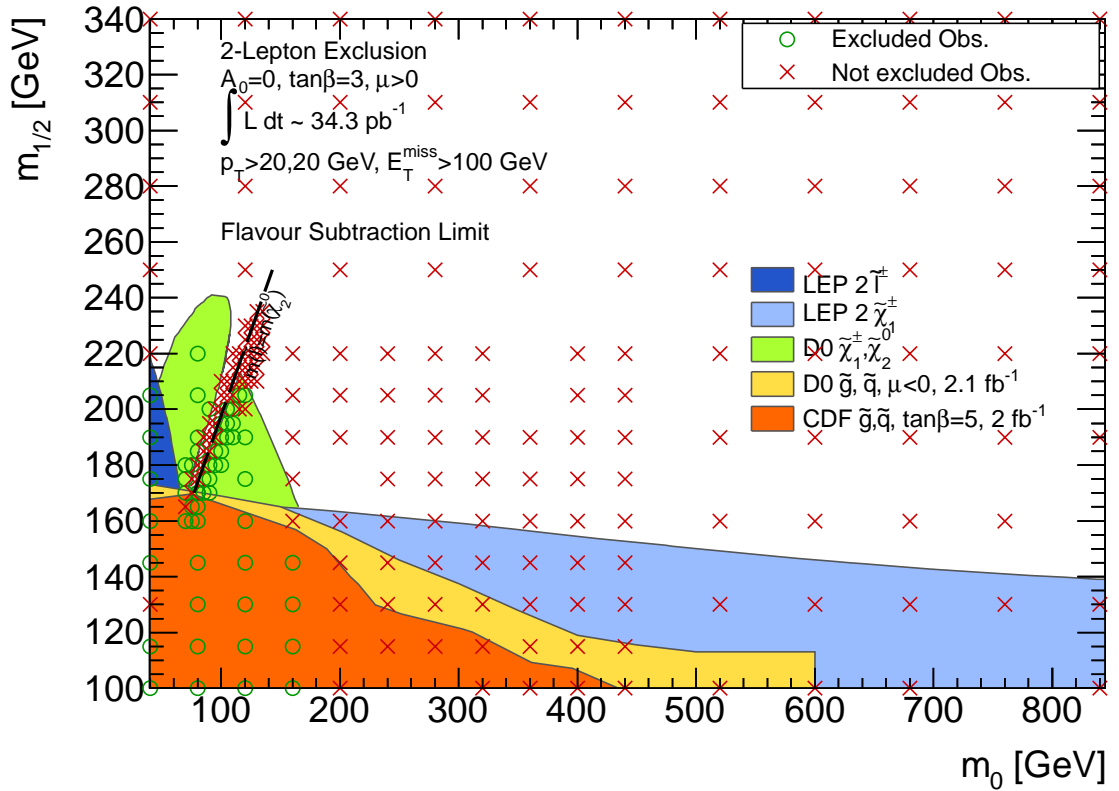


Figure 40: Points excluded and not excluded in mSUGRA parameter space. The marked line is where  $m(\tilde{l}) = m(\tilde{\chi}_2^0)$ . Just to the left of this line  $m(\tilde{l})$  is just less than  $m(\tilde{\chi}_2^0)$ . As a result the lepton from the  $\tilde{\chi}_2^0 \rightarrow \tilde{l}^\pm l^\mp$  decay is soft. For these points the signal acceptance for same flavour events is reduced, and so there is no longer a significant excess of same flavour events over those of different flavour.

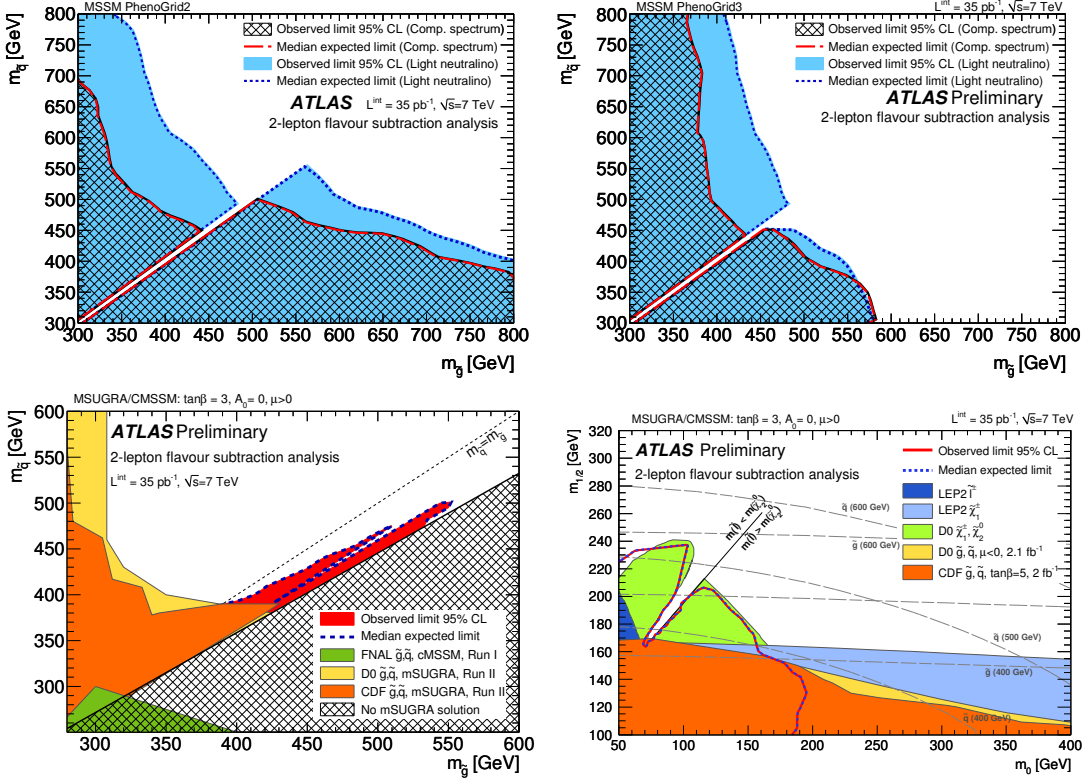


Figure 41: Observed and expected exclusion limits for PhenoGrid2 ‘lighter LSP and compressed spectrum/‘heavier’ LSP points (a) and PhenoGrid3 (b). The mSUGRA expected and observed limits in the  $m_{\tilde{g}} - m_{\tilde{q}}$  (c) and  $m_0 - m_{1/2}$  planes (d).

*numbers of events in each flavour channel. The impact on the width of systematic and statistical uncertainties is small in comparison to this initial width. Similarly, the shift in mean possible from the uncertainties on the mean value of  $S$ , is small compared to the width. At this luminosity we are limited by the low expected event rates in each channel, not by systematic uncertainties.*

## Profile Likelihood

The aim is to test the hypothesis that the subtracted count  $\mathcal{S}$  is consistent with the standard model. In the scenario considered here, the expectation is that true event rates  $\lambda_{e^\pm e^\mp}$ ,  $\lambda_{e^\pm \mu^\mp}$  and  $\lambda_{\mu^\pm \mu^\mp}$  have the composition detailed in Equations 38 to 40. That is, the total events of type  $\lambda_{e^\pm e^\mp}$  and  $\lambda_{\mu^\pm \mu^\mp}$ , are made up of events from a process, with rate  $\lambda_{sub}$ , that also produces events of type  $\lambda_{e^\pm \mu^\mp}$ . In the scenario here  $\lambda_{sub}$  includes  $W+jets$ ,  $t\bar{t}$  and  $WW$  standard model processes. Unfortunately, the same-flavour event rates ( $\lambda_{e^\pm e^\mp}$  and  $\lambda_{\mu^\pm \mu^\mp}$ ) will also include a contribution from processes which do not also produce events of the type  $\lambda_{e^\pm \mu^\mp}$ . In the scenario here,  $WZ$  is the major process contributing only to the same flavour counts. The rate of this process is denoted by  $\lambda_n$ .

$$\lambda_{e^\pm e^\mp} = \lambda_n + \lambda_{sub} \quad (38)$$

$$\lambda_{e^\pm \mu^\mp} = 2 \times \lambda_{sub} \quad (39)$$

$$\lambda_{\mu^\pm \mu^\mp} = \lambda_n + \lambda_{sub} \quad (40)$$

The design of the experiment has been such that  $\mathcal{S}$  is measured in a region where  $\lambda_n$  is expected to be small.

For a particular experiment the subtraction,  $\mathcal{S} = \frac{N(e^\pm e^\mp)}{\beta(1-(1-\tau_e)^2)} - \frac{N(e^\pm \mu^\mp)}{1-(1-\tau_e)*(1-\tau_\mu)} + \frac{N(\mu^\pm \mu^\mp)\beta}{1-(1-\tau_\mu)^2}$ , is constructed out of the number of measured events in the three different opposite-sign channels. The value of  $\mathcal{S}$  for a given experiment is dependent upon the true  $\beta$ ,  $\tau_e$  and  $\tau_\mu$  as well as the particular event counts which were observed. The distribution of all possible measurements of  $\mathcal{S}$  is given by Equation 41.

$$\mathcal{P}(\mathcal{S}) = \left( \frac{1}{\beta(1-(1-\tau_e)^2)} \right) \mathcal{P}(\lambda) - \left( \frac{1}{1-(1-\tau_e)*(1-\tau_\mu)} \right) \mathcal{P}(\mu) + \left( \frac{\beta}{1-(1-\tau_\mu)^2} \right) \mathcal{P}(\nu) \quad (41)$$

In this Equation  $\mathcal{P}(\lambda)$ ,  $\mathcal{P}(\mu)$  and  $\mathcal{P}(\nu)$  are Poisson distributions with means  $\lambda$ ,  $\mu$  and  $\nu$  respectively (the observed event counts,  $N(e^\pm e^\mp)$ ,  $N(e^\pm \mu^\mp)$  and  $N(\mu^\pm \mu^\mp)$  can only take integer values). These means will not exactly equal the expected rates  $\lambda_{e^\pm e^\mp}$ ,  $\lambda_{e^\pm \mu^\mp}$  and  $\lambda_{\mu^\pm \mu^\mp}$  detailed in Equations 38 to 40. Different detector acceptances and reconstruction efficiencies for electrons and muons will slightly alter the rates of events reconstructed (and is indeed why these rates are corrected for using the terms in  $\beta$ ,  $\tau_e$  and  $\tau_\mu$ ). Equations 42 to 44 give the means  $\lambda$ ,  $\mu$  and  $\nu$  in terms of true rates, and the experimental parameters.

$$\lambda = (\lambda_n + \lambda_{sub}) \left( \beta(1 - (1 - \tau_e)^2) \right) \quad (42)$$

$$\mu = 2 \times \lambda_{sub} \left( 1 - (1 - \tau_e) * (1 - \tau_\mu) \right) \quad (43)$$

$$\nu = (\lambda_n + \lambda_{sub}) \left( \frac{(1 - (1 - \tau_\mu)^2)}{\beta} \right) \quad (44)$$

These rates,  $\lambda$ ,  $\mu$  and  $\nu$ , can be estimated from the Monte Carlo event counts  $N_{MC}(e^\pm e^\mp)$ ,  $N_{MC}(e^\pm \mu^\mp)$  and  $N_{MC}(\mu^\pm \mu^\mp)$  and the values of  $\beta$ ,  $\tau_e$  and  $\tau_\mu$  from Monte Carlo. The construction of  $\mathcal{S}$  is such that its expected value is  $2 \times \lambda_n$ . Without the corrective scale factors in front of each of the  $\mathcal{P}$  distributions of observed counts this would not be the case. The  $\lambda$ ,  $\mu$  and  $\nu$  can be set using Equations 45 to 47.

$$\lambda = N_{MC}(e^\pm e^\mp) \quad (45)$$

$$\mu = N_{MC}(e^\pm \mu^\mp) \quad (46)$$

$$\nu = N_{MC}(\mu^\pm \mu^\mp) \quad (47)$$

The uncertainties on  $N_{MC}$  due to luminosity, parton distribution functions, cross-sections and missing energy scale must be taken into account, as must the uncertainties on  $\beta$ ,  $\tau_e$  and  $\tau_\mu$  when this model is explored. The appropriate model for the possible values of  $\mathcal{S}$  obtainable when  $\lambda$ ,  $\mu$  and  $\nu$  are what have been assumed to be here, and an experiment has the  $\beta$ ,  $\tau_e$  and  $\tau_\mu$  here is given in Equation 48.

$$\mathcal{P}(\mathcal{S}) = f_{pdf} \times f_{lumi} \times f_\sigma \times f_{E_T^{miss}} \left( \left( \frac{\mathcal{P}(N_{MC}(e^\pm e^\mp))}{f_\beta(1 - (1 - f_{\tau_e})^2)} \right) - \left( \frac{\mathcal{P}(N_{MC}(e^\pm \mu^\mp))}{1 - (1 - f_{\tau_e}) \times (1 - f_{\tau_\mu})} \right) + \left( \frac{f_\beta \times \mathcal{P}(N_{MC}(\mu^\pm \mu^\mp))}{1 - (1 - f_{\tau_\mu})^2} \right) \right) \quad (48)$$

In this Equation,  $f_{pdf}$ ,  $f_{lumi}$ ,  $f_\sigma$  and  $f_{E_T^{miss}}$  are assumed to be Gaussian distributions, with unit mean and sigma given by the appropriate uncertainty (as detailed in Section 8.3.4). The terms  $f_\beta$ ,  $f_{\tau_e}$  and  $f_{\tau_\mu}$  are assumed to be Gaussian distributions, with means equal to  $\beta$ ,  $\tau_e$  and  $\tau_\mu$  respectively, and sigma given by the appropriate uncertainty (as detailed in Section 8.3.4).

It is possible to test the agreement between the observed  $\mathcal{S}$  in data and the standard model prediction for  $\mathcal{S}$  (Section 8.4.2), a background only hypothesis, using the profile likelihood method.

It is perhaps possible to simplify the model for  $\mathcal{S}$  in Equation 48 by considering the following argument. Whilst the zero-lepton and one-lepton analysis channels, can assume that their observed event count,  $x$ , is modelled by a Poisson distribution (with a mean formed of varying proportions of signal and background), the observation here,  $\mathcal{S}$ , is clearly not appropriately approximated by a Poisson model. The quantity  $\mathcal{S}$  is not formed from the sum of different Poisson distributions, it is instead formed from a sum and a subtraction of different Poisson distributions.

The probability distribution of the difference  $n_1 - n_2$  of two statistically independent random variables,  $n_1$  and  $n_2$ , each Poisson distributed with mean  $\mu_1$  and  $\mu_2$  is called the Skellam Distribution (Equation 49, where  $I_k(z)$  is the modified Bessel function of the first kind).

$$f(k; \mu_1, \mu_2) = e^{-(\mu_1 + \mu_2)} \left( \frac{\mu_1}{\mu_2} \right)^{k/2} I_{|k|}(2 \sqrt{\mu_1 \mu_2}) \quad (49)$$

If the skewness,  $(\mu_1 - \mu_2)/(\mu_1 + \mu_2)$ , is small and the kurtosis,  $1/(\mu_1 + \mu_2)$ , small then the Skellam is closely modelled by a Gaussian with mean  $\mu_1 - \mu_2$  and variance  $\mu_1 + \mu_2$ .

In the case considered here, however, we are not quite dealing with two (or more) independent variables with Poisson distributions which combine in this way. The ‘scaling’ factors in front of each Poisson term complicates this picture. So it is not necessarily enough to be in the limit where skewness is small and kurtosis is small. The expressions  $\mathcal{P}(\alpha\lambda)$  and  $\alpha\mathcal{P}(\lambda)$  differ in their allowable values, though not in their shared mean and variance. For a count given by the expression  $\mathcal{P}(\alpha\lambda)$ , the count can take any integer value. In the case of  $\alpha\mathcal{P}(\lambda)$ , the allowable values are instead only 0,  $\alpha$ ,  $2\alpha$  and so on. In the model for  $\mathcal{S}$ , the allowable values of  $\mathcal{S}$  will not only be discrete, but the discrete fringes will not sit at all integer values and will instead sit at different non-integer values of  $\mathcal{S}$ , given by the different scaling factors. This can be pictured as a ‘three-dimensional lattice’ of possible values of  $\mathcal{S}$ . As the uncertainties in  $\beta$ ,  $\tau_e$  and  $\tau_\mu$  are explored through the  $f_\beta$ ,  $f_{\tau_e}$  and  $f_{\tau_\mu}$  terms a ‘smearing’ out of the ‘comb’ of the discrete fringes so that for some  $\beta$ ,  $\tau_e$  and  $\tau_\mu$  and their uncertainties the Gaussian limit is once again recovered.

In the Gaussian approximation the likelihood function is the product of the Gaussian model for  $\mathcal{S}$  and the distributions which enforce the systematic uncertainty constraints (i.e. the Gaussian  $f$  distributions). In the Gaussian approximation the mean of the Gaussian is given by Equation 50 and the variance by Equation 51. The newly introduced  $\lambda_{SUSY}$  is the true rate of production of Supersymmetric events. The background only null hypothesis that  $\lambda_{SUSY} = 0$  can be tested.

$$\bar{\mathcal{S}} = \left( \left( \left( \frac{(N_{MC}(e^\pm e^\mp))}{f_\beta(1 - (1 - f_{\tau_e})^2)} \right) - \left( \frac{(N_{MC}(e^\pm \mu^\mp))}{1 - (1 - f_{\tau_e}) \times (1 - f_{\tau_\mu})} \right) + \left( \frac{f_\beta \times (N_{MC}(\mu^\pm \mu^\mp))}{1 - (1 - f_{\tau_\mu})^2} \right) \right) f_\sigma f_{E_T^{miss}} + \lambda_{SUSY} \right) \times f_{lumi} \times f_{pdf} \quad (50)$$

$$(\Delta S)^2 = \left( \left( \left( \frac{(N_{MC}(e^\pm e^\mp))}{f_\beta(1 - (1 - f_{\tau_e})^2)} \right) + \left( \frac{(N_{MC}(e^\pm \mu^\mp))}{1 - (1 - f_{\tau_e}) \times (1 - f_{\tau_\mu})} \right) + \left( \frac{f_\beta \times (N_{MC}(\mu^\pm \mu^\mp))}{1 - (1 - f_{\tau_\mu})^2} \right) \right) f_\sigma f_{E_T^{miss}} + \lambda_{SUSY} \right) \times f_{lumi} \times f_{pdf} \quad (51)$$

### 95% confidence limit on $S$

Using the profile likelihood method in the Gaussian approximation gives a 95% upper confidence limit of  $\sim 8.8$  events without contamination compared to a limit of  $\sim 9.0$  events from the toy experiments (at  $15.7 \text{ pb}^{-1}$ ).

## Summary

The toy experiment approach, and the RooStats Profile Likelihood approach have been shown to give comparable results. Either approach to setting a limit can be taken – the first approach, using toy experiments, is favoured for its simplicity (but its simplicity makes it no less sound).

## 9 Summary and Conclusions

This note has presented the details and results of three different searches for two-lepton, high missing transverse energy events. These analyses have searched for: (i) excesses of same-sign lepton pairs, and (ii) excesses of opposite-sign lepton pairs. In the latter case, a third analysis (iii) was considered, in which the opposite-sign leptons were further studied and a search performed for an excess of lepton pairs with same-flavour, over events with different-flavour leptons. These three searches when carried out in parallel are sensitive to a variety of supersymmetric decays. These analyses observed no significant deviations from standard model predictions. For all analyses predictions were made using both Monte Carlo and (partially-) data-driven estimates of the standard model backgrounds in all charge-flavour channels. These predictions were used to set limits. In all three cases exclusions limits were set based on the observed two-lepton events in  $34.3 \text{ pb}^{-1}$  of  $\sqrt{s} = 7 \text{ TeV}$  integrated luminosity in mSUGRA parameter space, and for the introduced PhenoGrids.

## 10 Acknowledgements

## References

- [1] The ATLAS Collaboration, *Search for Supersymmetry with jets and missing transverse momentum at  $\sqrt{s} = 7 \text{ TeV}$  (supporting INT note)*, .
- [2] The ATLAS Collaboration, *Search for Supersymmetry with jets and missing transverse momentum and one lepton at  $\sqrt{s} = 7 \text{ TeV}$  (supporting INT note)*, .

- [3] ATLAS Collaboration, *Expected performance of the ATLAS experiment: detector, trigger and physics*, arXiv:0901.0512 [hep-ex] (2009) .
- [4] <http://indico.cern.ch/getFile.py/access?contribId=4&resId=0&materialId=slides&confId=110062>.
- [5] J. Butterworth, E. Dobson, U. Klein, B. Mellado Garcia, T. Nunnemann, J. Qian, D. Rebuzzi, and R. Tanaka, *Single Boson and Diboson Production Cross Sections in pp Collisions at  $\sqrt{s} = 7 \text{ TeV}$* , Tech. Rep. ATL-COM-PHYS-2010-695, CERN, Geneva, Aug, 2010.
- [6]
  - <https://twiki.cern.ch/twiki/bin/view/AtlasProtected/JetEtmissDataAnalysisRecommendationSummer2010>.
- [7] ATLAS Collaboration, T. A. collaboration, *Measurement of the  $W \rightarrow l\nu$  and  $Z/\gamma\gamma^* \rightarrow ll$  production cross sections in proton-proton collisions at  $\sqrt{s} = 7 \text{ TeV}$  with the ATLAS detector*, arXiv:1010.2130 [hep-ex].
- [8] <https://twiki.cern.ch/twiki/bin/view/AtlasProtected/MCPAnalysisGuidelinesRel15>.
- [9] S. Moch and P. Uwer, *Theoretical status and prospects for top-quark pair production at hadron colliders*, Phys. Rev. **D78** (2008) 034003, arXiv:0804.1476 [hep-ph].
- [10] U. Langenfeld, S. Moch, and P. Uwer, *New results for  $t \bar{t}$  production at hadron colliders*, arXiv:0907.2527 [hep-ph].
- [11] <https://twiki.cern.ch/twiki/bin/view/AtlasProtected/JESUncertaintyProvider>.
- [12] T. A. collaboration, *Jet energy scale and its systematic uncertainty in ATLAS for jets produced in proton-proton collisions at  $\sqrt{s} = 7 \text{ TeV}$* , Tech. Rep. ATLAS-COM-CONF-2010-056, CERN, Geneva, Jul, 2010.
- [13] T. A. collaboration, *Jet energy resolution and selection efficiency relative to track jets from in-situ techniques with the ATLAS Detector Using Proton-Proton Collisions at a Center of Mass Energy  $\sqrt{s} = 7 \text{ TeV}$* , Tech. Rep. ATLAS-CONF-2010-054, CERN, Geneva, Jul, 2010.
- [14] <https://twiki.cern.ch/twiki/bin/view/AtlasProtected/EnergyScaleResolutionRecommendations>.
- [15] <https://twiki.cern.ch/twiki/bin/view/AtlasProtected/MCPAnalysisGuidelinesRel15>.
- [16] <https://twiki.cern.ch/twiki/bin/view/AtlasProtected/HowToCleanJets>.
- [17] <https://twiki.cern.ch/twiki/bin/view/AtlasProtected/EfficiencyMeasurements>.
- [18] W. J. S. A. Kulesza, *Like-sign  $W$  boson production at the LHC as a probe of double parton scattering*, Phys. Lett. B **475** (2000) 168.
- [19] T. A. collaboration, *Measurement of the missing transverse momentum based on tracks in proton-proton collisions at  $s = 900 \text{ GeV}$  centre-of-mass energy with the ATLAS detector*, Tech. Rep. ATLAS-COM-CONF-2010-056, CERN, Geneva, Jul, 2010.
- [20] D. Tovey, *On measuring the masses of pair-produced semi-invisibly decaying particles at hadron colliders*, JHEP **0804** (2008) 034.
- [21] G. Polesello and D. Tovey, *Supersymmetric particle mass measurement with the boost-corrected contransverse mass*, JHEP **1003** (2010) 030.

- [22] The ATLAS Collaboration, *Luminosity Determination Using the ATLAS Detector*, .
- [23] The ATLAS Collaboration, *Measurement of the  $W \rightarrow l\nu$  production cross-section and observation of  $Z \rightarrow ll$  production in proton-proton collisions at  $\sqrt{s} = 7$  TeV with the ATLAS detector*, .
- [24] The ATLAS Collaboration, *Measurement of the  $Z \rightarrow ll$  production cross section in proton-proton collisions at  $\sqrt{s} = 7$  TeV with the ATLAS detector*, .
- [25] A. D. Martin, W. J. Stirling, R. S. Thorne, and G. Watt, *Parton distributions for the LHC*, Eur. Phys. J. **C63** (2009) 189–285, arXiv:0901.0002 [hep-ph].
- [26] W. Beenakker, R. Hopker, M. Spira, P.M. Zerwas, Squark and gluino production at hadron colliders, Nucl. Phys. B492 (1997), 51.
- [27] The CDF Collaboration, *Inclusive Search for Squark and Gluino Production in  $p\bar{p}$  Collisions at  $\sqrt{s} = 1.96$  TeV*, Phys. Rev. Lett. **102** (2009) 121801.
- [28] The D0 Collaboration, *Search for squarks and gluinos in events with jets and missing transverse energy using  $2.1fb^{-1}$  of  $p\bar{p}$  data at  $\sqrt{s} = 1.96$  TeV*, Phys. Lett. B **660** (2008) 449–457.

## A Same Sign Distributions by Flavour

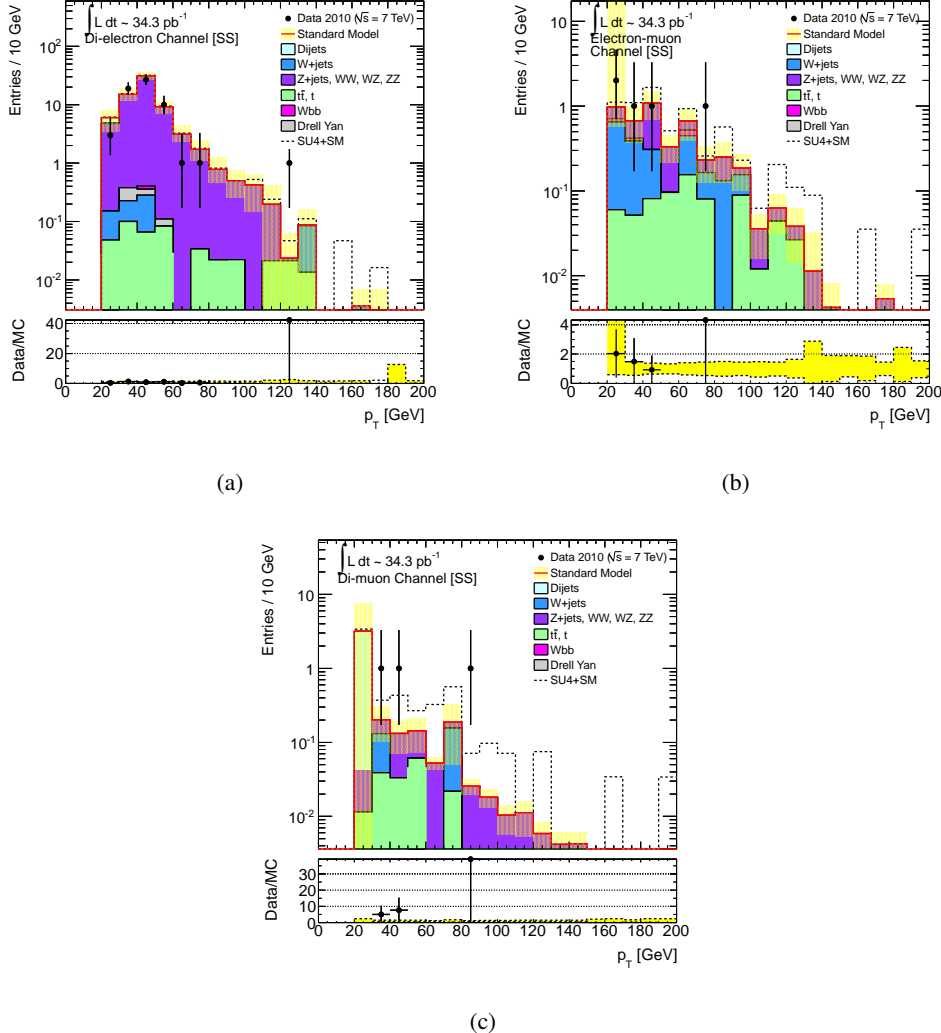


Figure 42: Distributions of the  $p_T$  of the leading lepton in two-lepton events in data and Monte Carlo. The two lepton events are divided into the three opposite-sign and three same-sign charge flavour channels,  $e^\mp e^\mp$  (a),  $e^\pm \mu^\pm$  (b) and  $\mu^\mp \mu^\mp$  (c). Errors on data points are 68% Poisson confidence limits, error band on Monte Carlo represents the statistical, jet energy scale and resolution, lepton energy scale and resolution, cross-section and luminosity uncertainties (as detailed in the text).

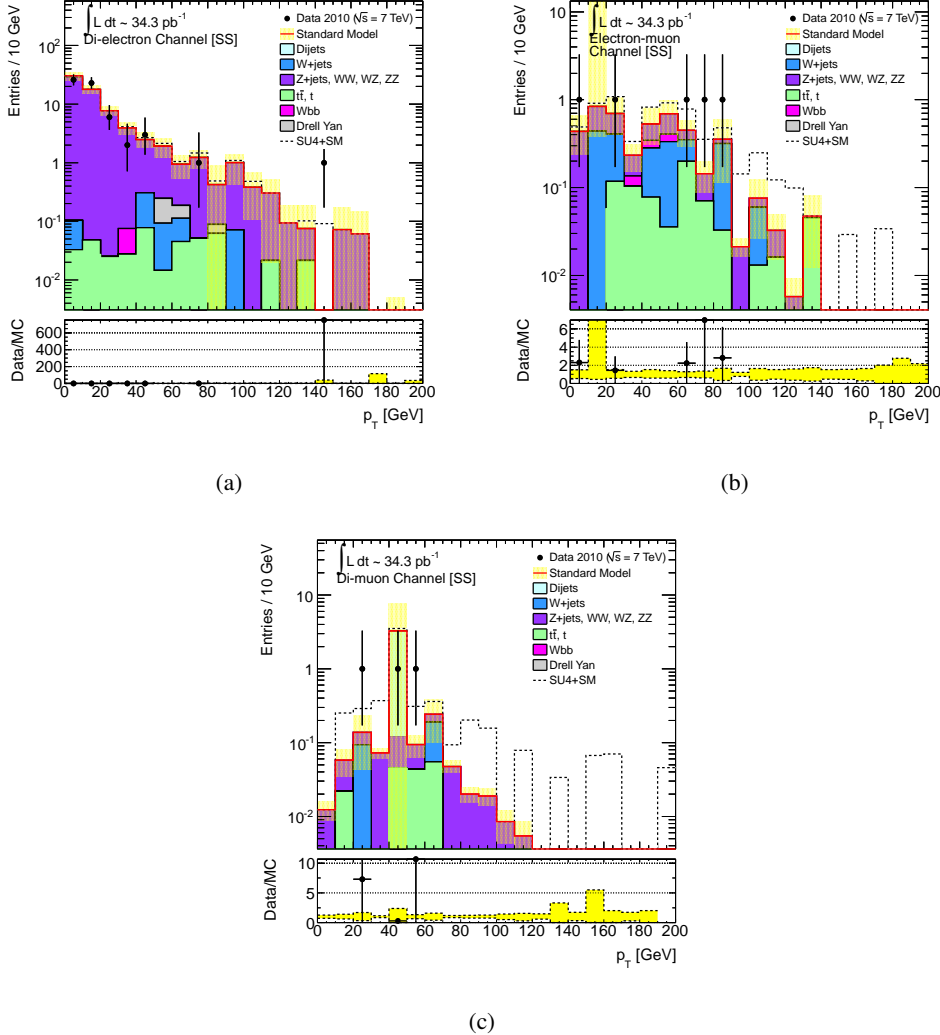


Figure 43: Distributions of the  $p_T$  of the lepton-pair in two-lepton events in data and Monte Carlo. The two lepton events are divided into the three opposite-sign and three same-sign charge flavour channels,  $e^\mp e^\mp$  (a),  $e^\pm \mu^\pm$  (b) and  $\mu^\mp \mu^\mp$  (c). Errors on data points are 68% Poisson confidence limits, error band on Monte Carlo represents the statistical, jet energy scale and resolution, lepton energy scale and resolution, cross-section and luminosity uncertainties (as detailed in the text).

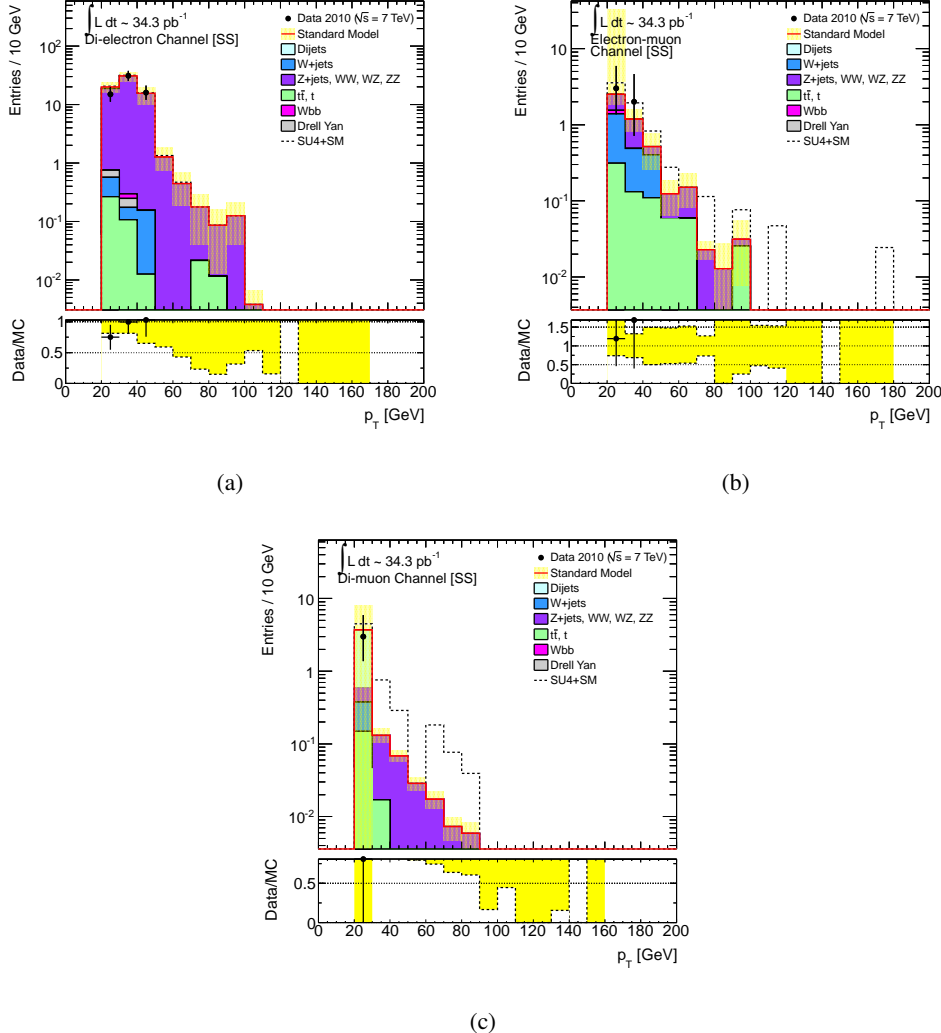


Figure 44: Distributions of the  $p_T$  of the sub-leading lepton in two-lepton events in data and Monte Carlo. The two lepton events are divided into the three opposite-sign and three same-sign charge flavour channels,  $e^\mp e^\mp$  (a),  $e^\pm \mu^\pm$  (b) and  $\mu^\mp \mu^\mp$  (c). Errors on data points are 68% Poisson confidence limits, error band on Monte Carlo represents the statistical, jet energy scale and resolution, lepton energy scale and resolution, cross-section and luminosity uncertainties (as detailed in the text).

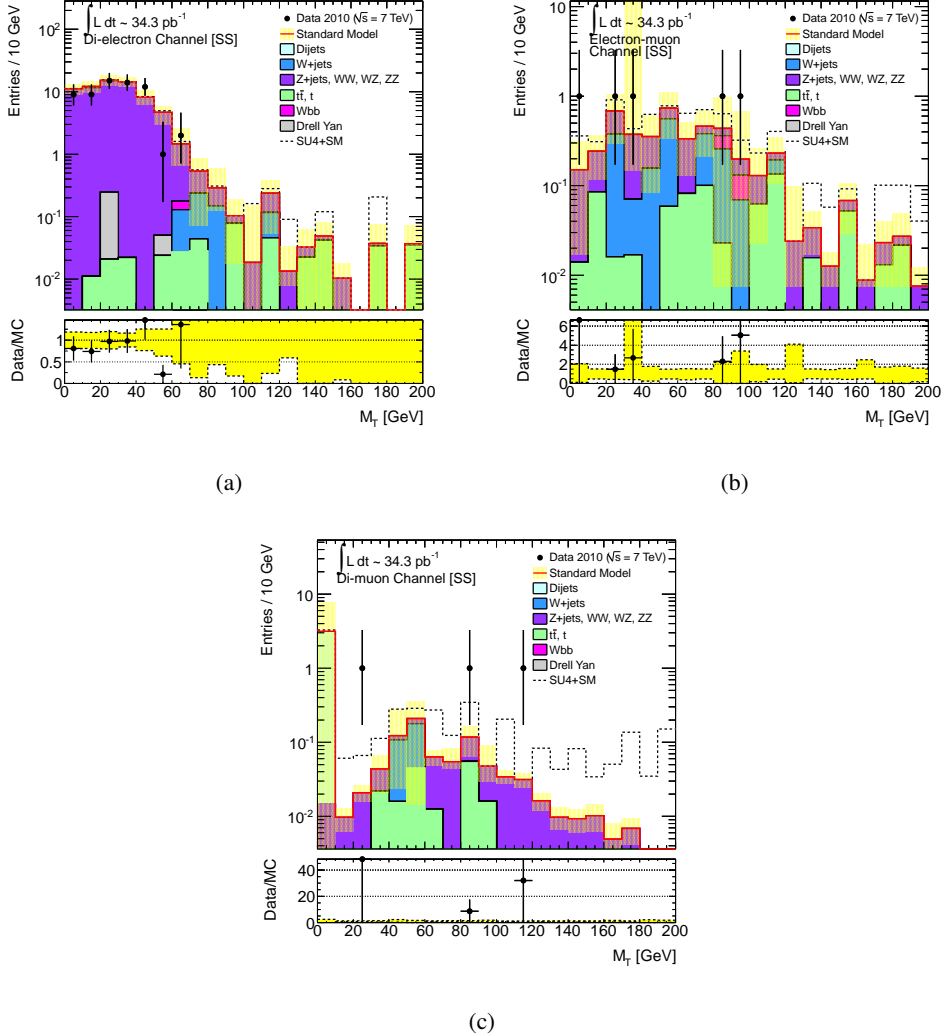


Figure 45: Distributions of the transverse mass ( $M_T$ ) of the highest  $p_T$  lepton in two-lepton events in data and Monte Carlo. The two lepton events are divided into the three opposite-sign and three same-sign charge flavour channels,  $e^\mp e^\mp$  (a),  $e^\pm \mu^\pm$  (b) and  $\mu^\mp \mu^\mp$  (c). Errors on data points are 68% Poisson confidence limits, error band on Monte Carlo represents the statistical, jet energy scale and resolution, lepton energy scale and resolution, cross-section and luminosity uncertainties (as detailed in the text).

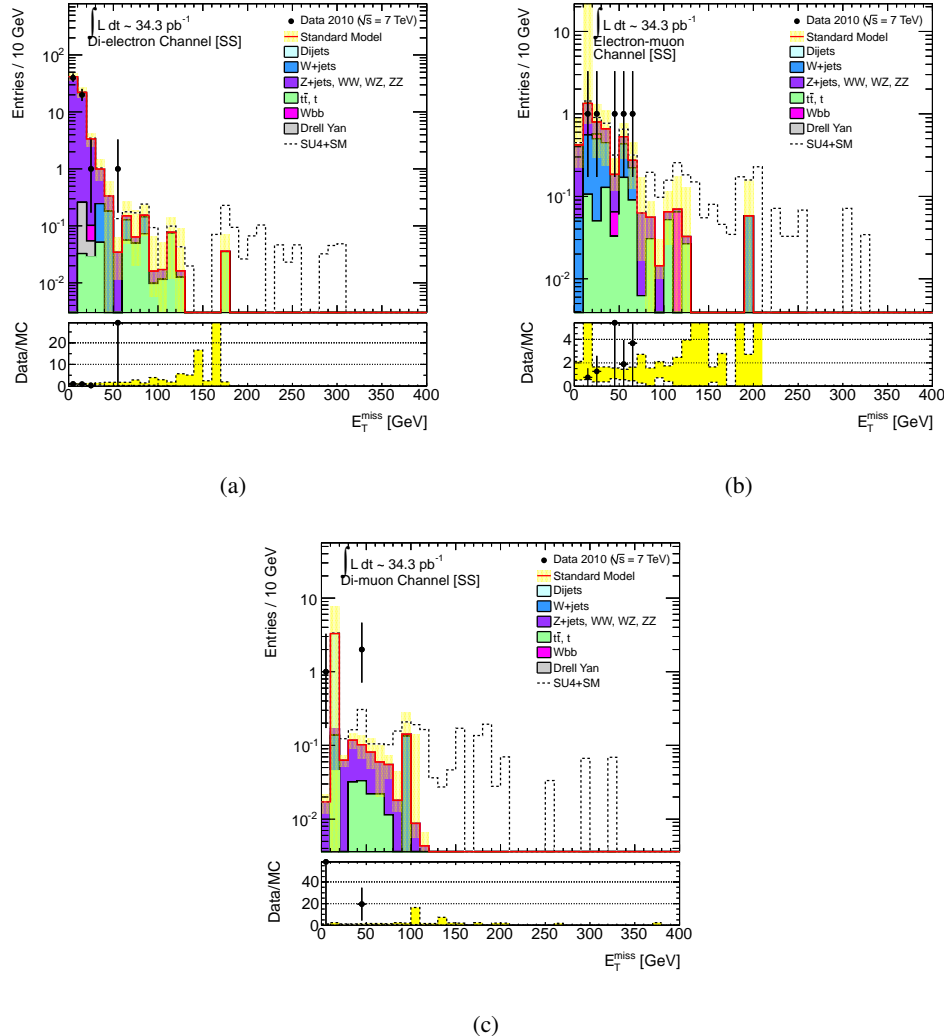


Figure 46: Distributions of the transverse missing energy ( $E_T^{miss}$ ) of two-lepton events in data and Monte Carlo. The two lepton events are divided into the three opposite-sign and three same-sign charge flavour channels,  $e^\mp e^\mp$  (a),  $e^\pm \mu^\pm$  (b) and  $\mu^\mp \mu^\mp$  (c). Errors on data points are 68% Poisson confidence limits, error band on Monte Carlo represents the statistical, jet energy scale and resolution, lepton energy scale and resolution, cross-section and luminosity uncertainties (as detailed in the text).

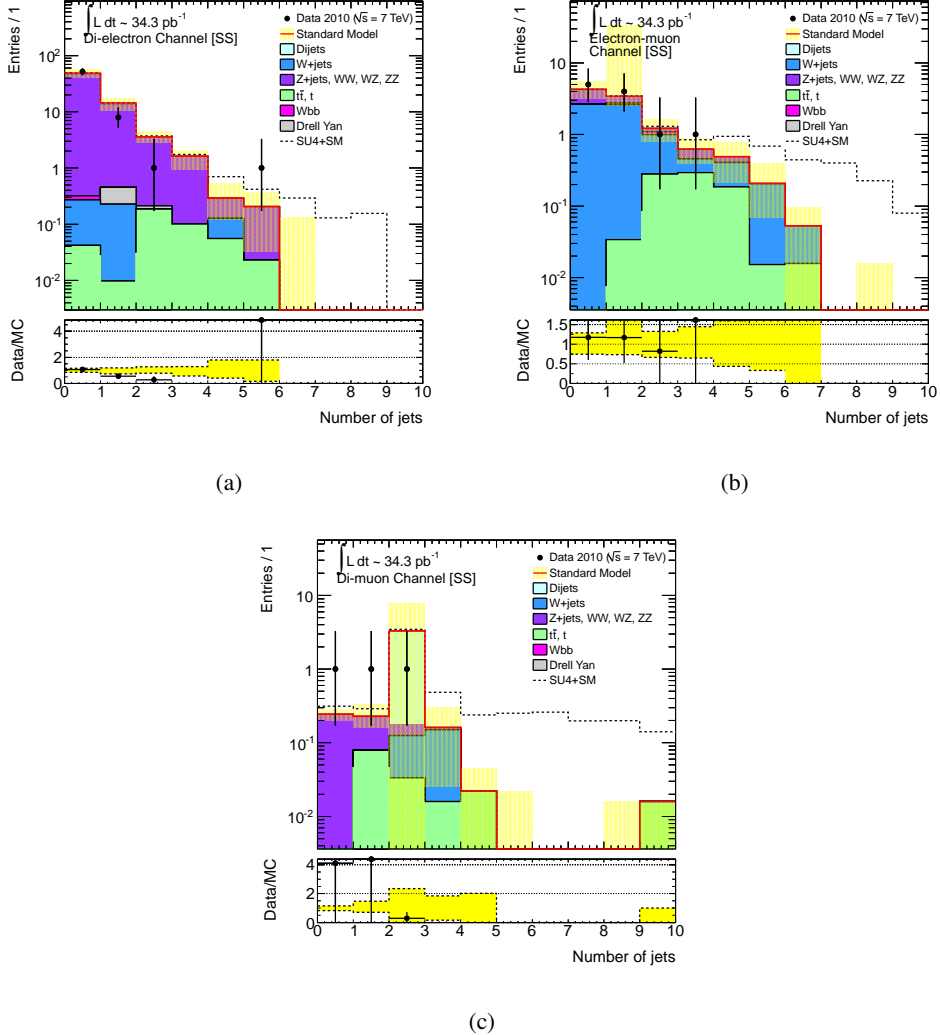


Figure 47: Distributions of the total number of jets in the two-lepton events in data and Monte Carlo. The two lepton events are divided into the three opposite-sign and three same-sign charge flavour channels,  $e^\mp e^\mp$  (a),  $e^\pm \mu^\pm$  (b) and  $\mu^\mp \mu^\mp$  (c). Errors on data points are 68% Poisson confidence limits, error band on Monte Carlo represents the statistical, jet energy scale and resolution, lepton energy scale and resolution, cross-section and luminosity uncertainties (as detailed in the text).

## B Opposite-Sign/Flavour-Subtraction Signal Region Events

In the three different opposite-sign flavour channels, there are the following numbers of events in the signal region.

(a)  $N(e^\pm e^\mp)$ : 4, (b)  $N(e^\pm \mu^\mp)$ : 13 and (c)  $N(\mu^\pm \mu^\mp)$ : 13, where the  $N(e^\pm \mu^\mp)$  are all derived from the egamma stream.

The event numbers and run numbers of these events are:

- o  $e^\pm e^\mp$  Events:

Run Number: 165767, Event Number: 79945104,  $E_T^{miss}$ : 105.417 GeV (Period G)  
 Run Number: 166786, Event Number: 60573764,  $E_T^{miss}$ : 118.49 GeV (Period H)  
 Run Number: 167607, Event Number: 54473522,  $E_T^{miss}$ : 113.559 GeV (Period I)  
 Run Number: 167607, Event Number: 83835161,  $E_T^{miss}$ : 187.651 GeV (Period I)

- o  $e^\pm \mu^\mp$  Events:

Run Number: 162623, Event Number: 58803424,  $E_T^{miss}$ : 113.153 (Period F)  
 Run Number: 162764, Event Number: 17478556,  $E_T^{miss}$ : 101.506 (Period F)  
 Run Number: 165591, Event Number: 15545300,  $E_T^{miss}$ : 177.588 (Period G)  
 Run Number: 165732, Event Number: 92405434,  $E_T^{miss}$ : 112.876 (Period G)  
 Run Number: 166198, Event Number: 23388408,  $E_T^{miss}$ : 142.947 (Period G)  
 Run Number: 167575, Event Number: 471786,  $E_T^{miss}$ : 114.583 (Period I)  
 Run Number: 167576, Event Number: 14944716,  $E_T^{miss}$ : 107.668 (Period I)  
 Run Number: 167576, Event Number: 24477091,  $E_T^{miss}$ : 100.636 (Period I)  
 Run Number: 167576, Event Number: 117937804,  $E_T^{miss}$ : 147.546 (Period I)  
 Run Number: 167607, Event Number: 73166366,  $E_T^{miss}$ : 184.668 (Period I)  
 Run Number: 167661, Event Number: 19488920,  $E_T^{miss}$ : 187.143 (Period I)  
 Run Number: 167776, Event Number: 27878443,  $E_T^{miss}$ : 151.366 (Period I)  
 Run Number: 167776, Event Number: 178060130,  $E_T^{miss}$ : 101.105 (Period I)

- o  $\mu^\pm \mu^\mp$  Events :

Run Number: 165632, Event Number: 44357054,  $E_T^{miss}$ : 143.117 (Period G)  
 Run Number: 165632, Event Number: 50114155,  $E_T^{miss}$ : 622.083 (Period G)  
 Run Number: 165732, Event Number: 40984283,  $E_T^{miss}$ : 162.492 (Period G)  
 Run Number: 165732, Event Number: 89733137,  $E_T^{miss}$ : 105.602 (Period G)  
 Run Number: 166142, Event Number: 46995983,  $E_T^{miss}$ : 111.523 (Period G)  
 Run Number: 167576, Event Number: 52027837,  $E_T^{miss}$ : 130.257 (Period I)  
 Run Number: 167576, Event Number: 72997270,  $E_T^{miss}$ : 158.393 (Period I)  
 Run Number: 167576, Event Number: 123404137,  $E_T^{miss}$ : 109.371 (Period I)  
 Run Number: 167607, Event Number: 53509962,  $E_T^{miss}$ : 115.106 (Period I)  
 Run Number: 167607, Event Number: 86148444,  $E_T^{miss}$ : 106.297 (Period I)  
 Run Number: 167607, Event Number: 122440648,  $E_T^{miss}$ : 128.727 (Period I)  
 Run Number: 167776, Event Number: 129360643,  $E_T^{miss}$ : 160.669 (Period I)  
 Run Number: 167776, Event Number: 55021180,  $E_T^{miss}$ : 100.9 (Period I)

## C Notes on the Flavour Subtraction Analysis

### C.1 The Expression $\mathcal{S}$

The formula for  $\mathcal{S}$  is derived as follows:

- If there are  $N_{true}(e^\pm e^\mp)$   $e^\pm e^\mp$  events produced, and the probability of triggering an electron  $\tau_e$  then:
  - $N_{true}(e^\pm e^\mp) \times (1 - \tau_e) \times (1 - \tau_e)$  events of this kind will not be triggered (i.e both  $e$  must fail the trigger)
  - $N_{true}(1 - (1 - \tau_e)^2)$  events will therefore be observed
  - i.e.  $N(e^\pm e^\mp) = N_{true}(1 - (1 - \tau_e)^2)$
  - and so  $N_{true}(e^\pm e^\mp) = \frac{N(e^\pm e^\mp)}{(1 - (1 - \tau_e)^2)}$
  - where  $N(e^\pm e^\mp)$  is the number of observed  $e^\pm e^\mp$  events
  - both electrons must also be reconstructed
  - if the reconstruction efficiency is  $\epsilon_e$
  - $N(e^\pm e^\pm) = N_{true}(1 - (1 - \tau_e)^2) \times (\epsilon_e)^2$  (both electrons must be reconstructed)
  - and so  $N_{true}(e^\pm e^\mp) = \frac{N(e^\pm e^\mp)}{\epsilon_e^2(1 - (1 - \tau_e)^2)}$
- If there are  $N_{true}(\mu^\pm \mu^\mp)$   $\mu^\pm \mu^\mp$  events produced, the muon reconstruction efficiency  $\epsilon_\mu$  and the probability of triggering a muon  $\tau_\mu$  then similarly:
  - $N_{true}(\mu^\pm \mu^\mp) = \frac{N(\mu^\pm \mu^\mp)}{\epsilon_\mu^2(1 - (1 - \tau_\mu)^2)}$
- In the  $e^\pm \mu^\mp$  case:
  - $N_{true}(e^\pm \mu^\pm)(1 - (1 - \tau_e)(1 - \tau_\mu))$  events will not be observed because of the trigger
  - i.e. both the electron and muon must fail their respective triggers
  - $N_{true}(e^\pm \mu^\mp) = \frac{N(e^\pm \mu^\mp)}{\epsilon_e \epsilon_\mu (1 - (1 - \tau_e)(1 - \tau_\mu))}$
- The true excess of same-flavour events:  $N_{true}(e^\pm e^\mp) + N_{true}(\mu^\pm \mu^\mp) - N_{true}(e^\pm \mu^\mp)$  is therefore given by –
  - $\frac{N(e^\pm e^\mp)}{(1 - (1 - \tau_e)^2)\epsilon_e^2} - \frac{N(e^\pm \mu^\mp)}{(1 - (1 - \tau_e)(1 - \tau_\mu))\epsilon_e \epsilon_\mu} + \frac{N(\mu^\pm \mu^\mp)}{\epsilon_\mu^2(1 - (1 - \tau_\mu)^2)}$
  - multiplying this expression by  $\epsilon_\mu \epsilon_e$  and introducing  $\beta = \frac{\epsilon_e}{\epsilon_\mu}$  returns the advertised formula for  $\mathcal{S}$ .
  - i.e.  $\mathcal{S} = \frac{N(e^\pm e^\mp)}{\beta(1 - (1 - \tau_e)^2)} - \frac{N(e^\pm \mu^\mp)}{1 - (1 - \tau_e)(1 - \tau_\mu)} + \frac{\beta N(\mu^\pm \mu^\mp)}{(1 - (1 - \tau_\mu)^2)}$

### C.2 Determining Uncertainties

The uncertainties on  $\mathcal{S}$  from  $\beta$ ,  $\epsilon_e$ ,  $\epsilon_\mu$  and  $\beta$  are derived by noting that:

- if  $Z = Z(A, B, \dots)$  (where  $A$  and  $B$  are independent) then
- $(\sigma_Z)^2 = \left(\frac{\partial Z}{\partial A}\sigma_A\right)^2 + \left(\frac{\partial Z}{\partial B}\sigma_B\right)^2 + \dots$
- i.e. the absolute uncertainty on  $\mathcal{S}$  from  $\beta$  is given by:
- $\left(\frac{\partial \mathcal{S}}{\partial \beta}\right)(\sigma_\beta)$
- the overall error on  $\mathcal{S}$  follows from summing the contribution from  $\beta$  above to the similarly obtained contributions from  $\tau_e$  and  $\tau_\mu$  in quadrature

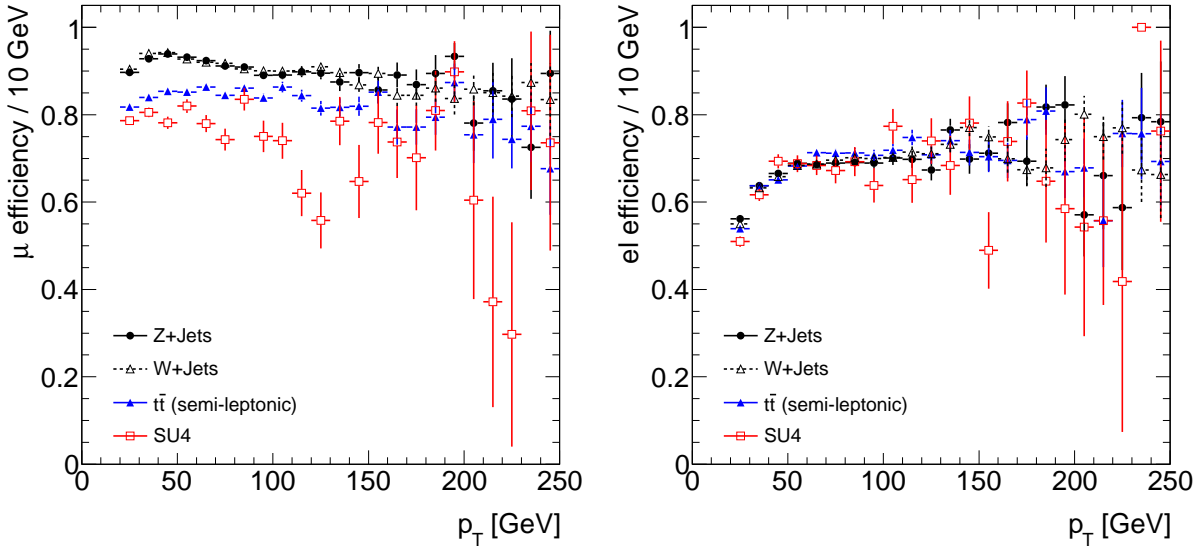


Figure 48: Muon efficiency over  $p_T$  (left) and electron efficiency over  $p_T$  (right) determined for Monte-Carlo samples via truth-matching

## D Systematic uncertainty on $\beta$ the ratio of the lepton reconstruction efficiencies

In this section the systematic uncertainties due to the variation of the ratio of the electron reconstruction efficiency over the muon reconstruction efficiency is investigated in detail. In order to study if  $\beta$  is expected to vary for different processes  $\beta$  is analyzed for several Monte-Carlo samples which are expected to be the main background of the flavor subtracting analysis. A variation of the lepton efficiency for different processes has to be taken into account as systematic, when measuring the efficiencies in a control region and extrapolating these values into the signal region. The reconstruction efficiencies for electrons and muons are determined for Monte-Carlo samples using a truth-matching method.

In the second approach a data-driven study is done in a control region around the Z peak. This region has a very high purity and is well understood. Using this region  $\beta$  can be measured as the ratio of the reconstructed number of di-electron and di-muon events. Before summarizing the contribution to the variation of  $\beta$  a cross-check of  $p_T$  dependency of  $\beta$  data-driven only is presented.

### D.1 Systematics on $\beta$ analyzed for different processes

First,  $\beta$  is determined using the reconstruction efficiency of the muons and electrons based on truth-matching information.  $\beta$  is defined as the ratio of electron efficiency over muon efficiency:

$$\beta = \frac{\epsilon_e}{\epsilon_\mu}$$

Monte-Carlo samples described detail in section 2 have been analysed in order to study the reconstruction efficiencies and the object definition cuts in detail. The reconstruction efficiencies in Fig. 48 include the object definitions (see Sec. 2), the overlap removal between electrons and jets and muons and jets and an event veto against electrons in the crack region ( $1.37 < |\eta| < 1.52$ ). No additional event selections have been applied. The efficiencies are determined as the ratio of reconstructed lepton ( $e/\mu$ )

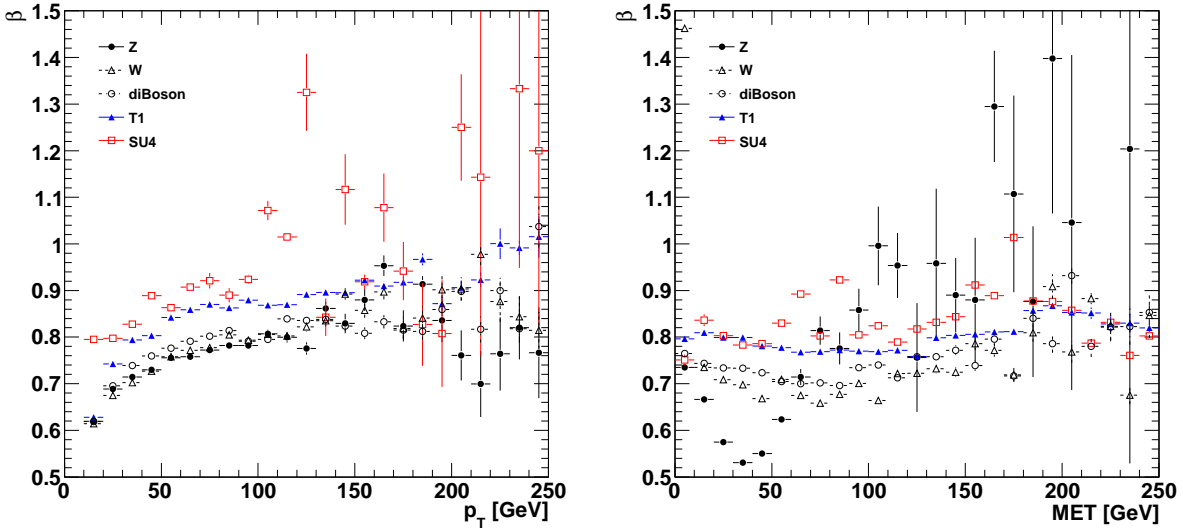


Figure 49: Both ratios  $\beta(p_T)$  (left) and  $\beta(MET)$  (right) of different MC samples are determined via truth-matching.

Table 39: Cutflow for muon object definition in MC samples. Relative fraction of candidates passing the different object identification cuts.

cut	Z	W	$t\bar{t}$	SU4
eta, pt	0.601	0.558	0.398	0.228
combined low pT	0.992	0.993	0.991	0.986
Pix or SCT hits	0.995	0.995	0.994	0.994
eta and TRT	0.999	0.999	0.998	0.998
TRT outliers	0.999	0.999	0.998	0.995
$\chi^2 < \text{max}$	0.997	0.997	0.996	0.990
MS extrapol	0.996	0.996	0.994	0.987
pT cone	0.981	0.982	0.835	0.698
OR	0.980	0.984	0.928	0.903

matched to a simulated (true) lepton ( $e/\mu$ ) divided by the total number of true leptons<sup>3</sup>:

$$\epsilon_e = \frac{\text{reconstructed} \rightarrow \text{truth-matched}}{\text{truth}}$$

Comparing the efficiencies of signal (SU4) and several Standard Model MC samples, it turns out that the muon efficiencies differ according to the different processes (Fig. 48 (left)). Events with more particles in the detector like  $t\bar{t}$  or SU4 show lower muon efficiency than Z decays. This maybe explained by the object isolation criteria such as the pT cone cut and the overlap removal (see Tab. 39 last two rows).

The difference between the electron jet and muon jet overlap removal is that in case of electron overlap removal in a first step jets in a cone of  $\Delta R < 0.2$  around an electron are removed and in a second step electrons in a cone around jets smaller  $\Delta R < 0.4$  are rejected. The muon jet overlap removal applies only step two. According to this method more muon candidates than electron candidates are rejected by

<sup>3</sup> $e/\mu$  true lying in the acceptance of the detector  $p_T > 20 \text{ GeV}$ ,  $|\eta| < 2.47$  e (2.4  $\mu$ ) and e not in crack region

Table 40: Cutflow for electron object definition in MC samples. Relative fraction of candidates passing several object identification cuts.

cut	Z	W	$t\bar{t}$	SU4
eta, pt	0.198	0.169	0.221	0.293
author	0.871	0.904	0.583	0.420
OTX	0.911	0.911	0.912	0.911
El ID	0.542	0.588	0.176	0.058
EtCone	0.986	0.984	0.963	0.937
OR	1.000	1.000	0.993	0.985

the overlap removal in busy events. The variation of the muon efficiency yields the variation of the ratio  $\beta$  for the different processes.

Figure 49 shows  $\beta$  for several Monte-Carlo samples. Large fluctuations of the SU4 sample in higher  $p_T$  bins is due to the kinematics of the SU4 benchmark point which yield larger statistical errors in higher  $p_T$  bins (Fig.49 left). More important for the discrepancy of  $\beta$  from SU4 sample in comparison to the SM distributions is the lower muon efficiency for low  $p_T$  muons. Apart from  $\beta_Z(MET)$  the  $\beta(MET)$  distributions are reasonably flat.  $\beta_Z(MET)$  drops with MET in low MET region ( $MET < 50$  GeV) and runs out of statistics in high MET region. The V-shape of  $\beta_Z(MET)$  can be explained by two different effects. The decrease is due to the decreasing electron efficiency with larger MET up to 50 GeV. A priori there is no missing transverse energy expected in  $Z \rightarrow ee$  processes. MET below 50 GeV in  $Z \rightarrow ee$  events is caused by not reconstructed electrons. The not reconstructed electron cause the reduced  $\beta$ . The increase for slightly higher MET values is due to the contribution of  $Z \rightarrow \tau\tau \rightarrow ll$  events. There the missing transverse energy is caused by escaping neutrinos.

Table 41: Reconstruction and identification efficiencies for electrons and muons and the ratio  $\beta$  for W, Z,  $t\bar{t}$ , and SU4 samples determined by Monte-Carlo truth-matching method. Applying object definition, overlap removal, and crack veto.

sample	$\epsilon_e$	$\epsilon_\mu$	$\beta$
W	$62.811 \pm 0.098$	$92.826 \pm 0.027$	$0.677 \pm 0.001$
Z	$63.263 \pm 0.079$	$92.310 \pm 0.042$	$0.685 \pm 0.001$
$t\bar{t}$	$64.915 \pm 0.261$	$84.100 \pm 0.194$	$0.772 \pm 0.004$
SU4	$61.972 \pm 0.628$	$78.318 \pm 0.521$	$0.791 \pm 0.010$

Calculating the variation of  $\beta$  based on the difference between the SM processes with largest difference  $\beta_W$  and  $\beta_{t\bar{t}}$  (0.095) the variance can be determined to  $\Delta\beta_{SM} = 0.027$ . Taking into account the higher  $\beta$  value for SU4 benchmark point another contribution of  $\Delta\beta_{SM-SU4} = 0.08$  has to be added.

## D.2 Data-driven $\beta$ determination in the Z control region

The Z control region is defined by missing transverse energy ( $MET < 40$  GeV) and an invariant mass of two leptons in a window around the Z mass ( $80$  GeV  $< m_{ll} < 100$  GeV). After applying those cuts Zee and  $Z\mu\mu$  are the dominating events which are left as SM contribution. This subsample can be used to determine  $\beta$  as the ration of  $N_{ee}$  over  $N_{\mu\mu}$ .

$\beta$  is defined as the ratio of the reconstruction efficiencies only. When comparing  $\beta_{meas.}$  with  $\beta$  derived by the truth-matching method the trigger has to be taken into account as follows:

$$\beta_{meas.}^2 = \frac{N_{ee}}{N_{\mu\mu}} = \frac{(1 - (1 - \tau_{el})^2) \cdot \epsilon_e^2}{(1 - (1 - \tau_\mu)^2) \cdot \epsilon_\mu^2} = \frac{(1 - (1 - \tau_{el})^2)}{(1 - (1 - \tau_\mu)^2)} \cdot \beta^2$$

Table 42: Comparison of  $\beta$  derived from Z control region data and MC.

	$\beta_{meas.} = \sqrt{\frac{N_{ee}}{N_{\mu\mu}}}$	$\beta$
Zee/Z $\mu\mu$	$0.686 \pm 0.002$	$0.686 \pm 0.003$
SM all data	$0.686 \pm 0.002$	$0.686 \pm 0.003$
	$0.691 \pm 0.006$	$0.688 \pm 0.009$

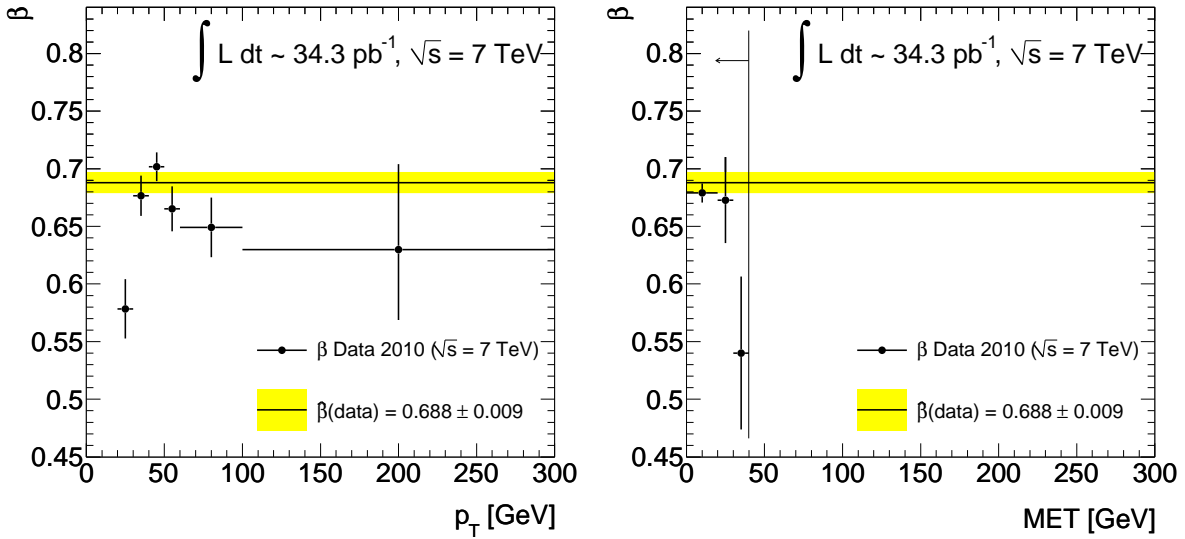


Figure 50: Ratio  $\beta(p_T) = \sqrt{\frac{1-(1-\tau_\mu)^2}{1-(1-\tau_e)^2} \frac{N_{ee}(p_T)}{N_{\mu\mu}(p_T)}}$  binned in  $p_T$  for the leading lepton derived from data (left) and  $\beta(MET)$  with Z control region missing transverse energy cut at 40 GeV (right).

With trigger efficiencies of 99.9% for electrons and 96.3% for muons in MC samples, and trigger efficiencies of 97.8% for electrons and 90.6% for muons in data  $\beta$  can be calculated from  $\frac{N_{ee}}{N_{\mu\mu}}$ . The results are given in Tab. 42.

The  $\beta$  values from standard model MC and Z (Tab. 42) extracted from the Z control region by counting the di-lepton events is in perfect agreement with  $\beta$  determined from Z samples via truth-matching (Tab. 41). No additional systematics for the data-driven  $\beta$  determination has to be taken into account. The  $\beta$  value derived from data only ( $\beta = 0.6880 \pm 0.0085$ ) is in good agreement with the Monte-Carlo results.

### D.3 Data-driven $\beta$ determination in the Z control region checking $p_T$ dependency

The  $p_T$  and MET dependency of  $\beta$  can be studied in a completely data-driven way. Therefore e.g.  $\beta(p_T) = \sqrt{\frac{1-(1-\tau_\mu)^2}{1-(1-\tau_e)^2} \frac{N_{ee}(p_T)}{N_{\mu\mu}(p_T)}}$  derived from the ratio  $N_{ee}$  over  $N_{\mu\mu}$  including the trigger efficiencies is plotted in Fig. 50 left for the leading lepton binned in  $p_T$  bins.  $N_{ee}$  over  $N_{\mu\mu}$  for different MET is plotted in Fig. 50 right. The drop of  $\beta(MET)$  in the third bin is in agreement with the Monte-Carlo study above (cp. 49). The variation of  $\beta(p_T)$  and  $\beta(MET)$  determined via the data-driven method is neglected.

#### D.4 Summary

In conclusion, three systematics have been studied. According to the different muon reconstruction efficiencies for different processes, the variation of  $\beta$  ( $\Delta\beta_{SM} = 0.027$ ) has to be taken into account (and another variation for SU4 predictions of  $\Delta\beta_{SU4} = 0.08$ ). The data-driven approach is in good agreement with the Monte-Carlo truth-matching results ( $\beta_{Z \text{ peak}} \approx 0$ ) and can be neglected. The uncertainty of  $\beta$  in  $p_T$  is also neglected so far.

$$\Delta\beta_{MC \text{ } SM \text{ samples}} = 0.027$$

$$\Delta\beta_{SM-SU4} = 0.08$$

$$\Delta\beta_{Z \text{ peak}} \approx 0.$$

$$\Delta\beta_{p_T} \approx 0.$$

$$\Delta\beta_{tot} = 0.084$$

The total variation of  $\beta$  including SU4 predictions is  $\Delta\beta_{tot} = 0.084$ .

Figure 51: NLO production cross section in pb as a function of  $M_0$  and  $M_{1/2}$  summed over all the production processes considered.

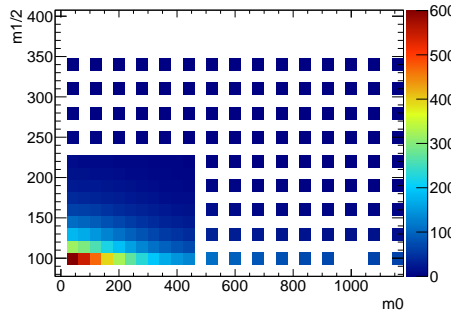
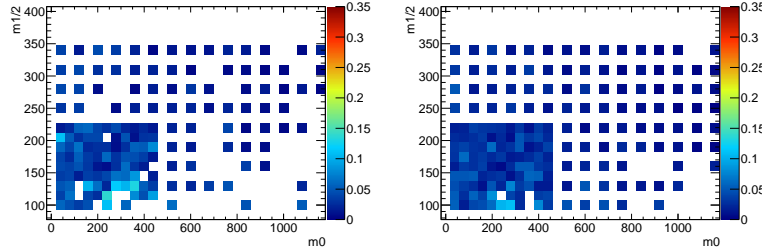


Figure 52: Percentage of excluded production processes in the Herwig Monte Carlo as a function of  $M_0$  and  $M_{1/2}$  for the same sign channel (left) and the opposite sign channel (right)



## E SUSY signal models

### E.1 Theoretical uncertainties on mSUGRA grid

There are various production mechanisms with different  $2 \rightarrow 2$  processes involved. Each process can have a different K-factor and different acceptance, and the PDF and Scale uncertainties can vary for each production process. Therefore the production is divided into 24 separate channels: squark–gluino, gluino–gluino, squark–squark, squark–antisquark, stop 1 pair, stop 2 pair, sbottom 1 pair, sbottom 2 pair and the 16 production processes associating a neutralino or a chargino to a gluino or a squark. The NLO cross section of these processes is calculated with Prospino 2.1 [26] and the total cross section as a function of  $M_0$  and  $M_{1/2}$  of these processes can be seen in Fig. 51. For some channels no NLO cross section and no PDF and Scale uncertainties were available, so they were not included. These excluded processes are mostly sbottom–gluino or sbottom–squark processes and to some degree also stop production. According to Herwig the contribution from those channels is only a few percent, as shown in Fig. 52. The relative contributions at production level of the included processes is shown in Fig. 53. The k-factor as calculated by Prospino is pictured in Fig. 54.

#### E.1.1 Acceptance

The acceptance is the fraction of events that pass all cuts of the 2 lepton analysis at the truth level. To study the acceptance the following set of object definitions and cuts was defined, trying to stay as close

Figure 53: Relative contribution to the total production rate as a function of  $M_0$  and  $M_{1/2}$  for (from top left to bottom right) squark–gluino production, gluino–gluino production, squark–squark production, squark–antisquark production, stop 1 pair production, stop 2 pair production, sbottom 1 pair production, sbottom 2 pair production and other production processes. Note the different scales.

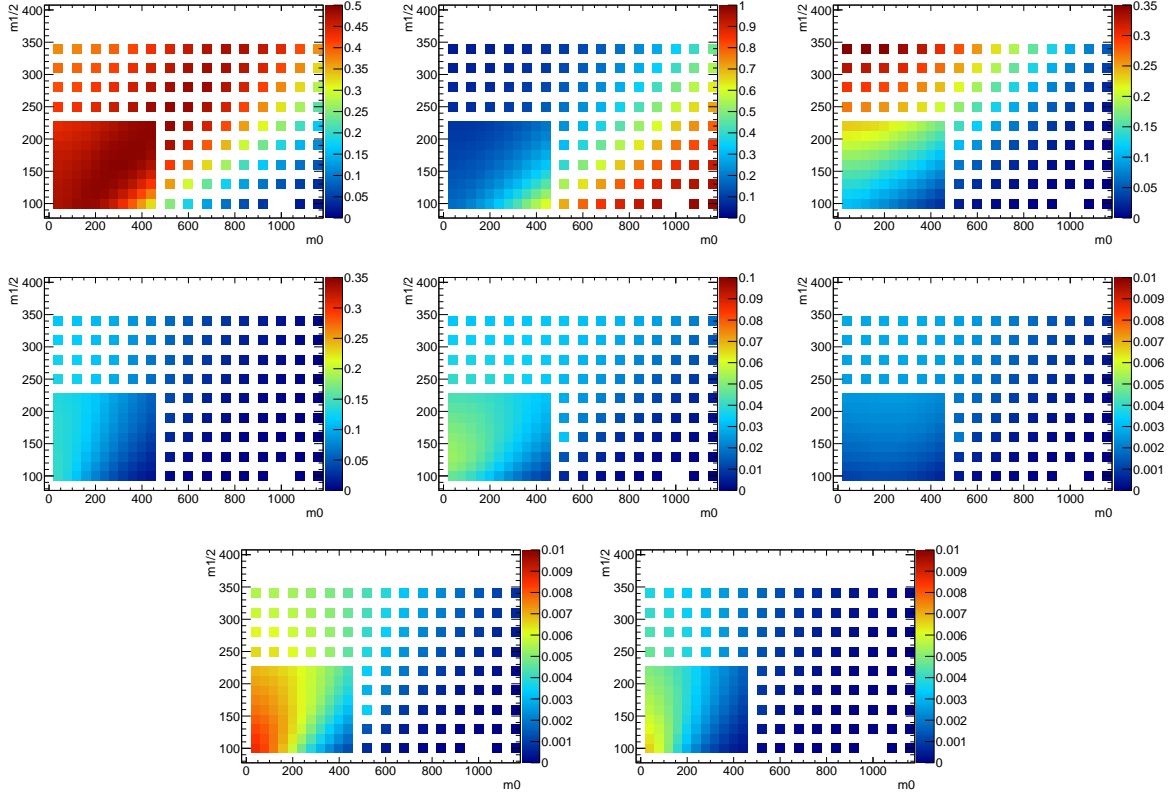
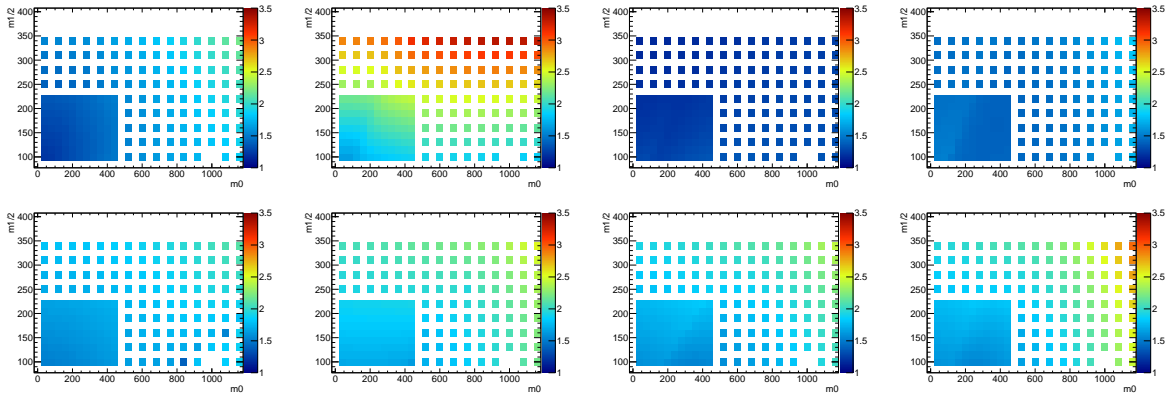


Figure 54: K-factor as a function of  $M_0$  and  $M_{1/2}$  for (from top left to bottom right) squark–gluino production, gluino–gluino production, squark–squark production, squark–antisquark production, stop 1 pair production stop 2 pair production, sbottom 1 pair production and sbottom 2 pair production.



as possible to the cuts used on the reconstruction level:

Object Definition:

- Jets from *jet\_AntiKt4TruthJets\_\** with  $p_T > 20 \text{ GeV}$  and  $|\eta| < 2.5$
- electrons from *mc\_\** with  $p_T > 20 \text{ GeV}$  and  $|\eta| < 2.47$
- muons from *mc\_\** with  $p_T > 20 \text{ GeV}$  and  $|\eta| < 2.4$
- $E_T^{\text{miss}}$  from *MET\_Truth\_NonInt\_et*

Overlap removal:

- Remove all jets with  $\Delta R < 0.2$  to electrons
- Remove all muons with  $\Delta R < 0.4$  to jets
- Remove all electrons with  $0.2 < \Delta R < 0.4$  to jets

Analysis Cuts:

- Require exactly 2 leptons with  $p_T > 20$
- Remove event for which one of those 2 leptons is an electron in the crack region
- $m_{ll} > 5 \text{ GeV}$
- $E_T^{\text{miss}} > 100 \text{ GeV}$
- Divide into same-sign or opposite-sign channel

On truth level no isolation on calorimeter level is available. The OTX cuts are not applied, as they are not part of the detector acceptance but a temporary reduction in reconstruction efficiency. The acceptance of these cuts depends on the sparticles produced, therefore the acceptance  $\epsilon_i$  is calculated individually for each production channel  $i$ , using:

$$\epsilon_i = \frac{\#(\text{accepted events})}{\#(\text{total events})}$$

In Fig. 55 the acceptance of each cut is shown for the squark–gluino production. One can see that the probability of producing 2 leptons depends on both  $M_0$ ,  $M_{1/2}$ , while the cut on  $E_T^{\text{miss}}$  mostly affects the low  $M_{1/2}$  regions.

When weighting the acceptances  $\epsilon_i$  with the cross section  $\sigma_i$  of the according process one can calculate the overall acceptance shown in Fig. 56, the number of expected events for  $20 \text{ pb}^{-1}$  shown in Fig. 56 or the percentage each production channel contributes to the total cross section. The latter is shown for the opposite sign channel in Fig. 58 and for the same sign channel in Fig. 57. For some production channels the number of produced events is small and thus the relative statistical error on the acceptance is high. However, the small cross section of those channels reduces the impact of those contributions.

### E.1.2 Scale and PDF uncertainties

The uncertainty caused by the PDF used to calculate the signal cross section is studied using Prospino. The default PDF set used in the computation of the cross section is CTEQ6.6. The uncertainty on the PDF is represented by 22 sets of eigenvectors  $X$ , that all have an upper and a lower bound, giving in total 44 variations. The uncertainty caused by the PDF is then evaluated using the Hessian method

Figure 55: Acceptance, as a function of  $M_0$  and  $M_{1/2}$  for the squark–gluino process, of the various cuts (from top left to bottom right): Two leptons with  $p_T > 20$  and  $10 \text{ GeV}$ ,  $m_{ll} > 5 \text{ GeV}$ ,  $E_T^{\text{miss}} > 100 \text{ GeV}$ , and the percentage of events in the same-sign channel.

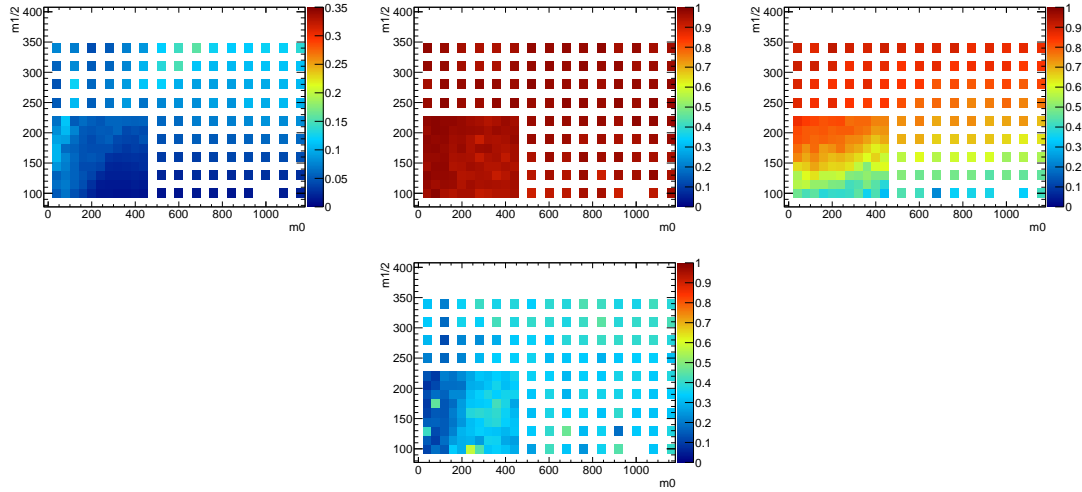


Figure 56: Acceptance for the Opposite Sign channel after all cuts (left) and number of events expected at the truth level in the signal region for  $20 \text{ pb}^{-1}$  (right) as a function of  $M_0$  and  $M_{1/2}$  after combining all the processes.

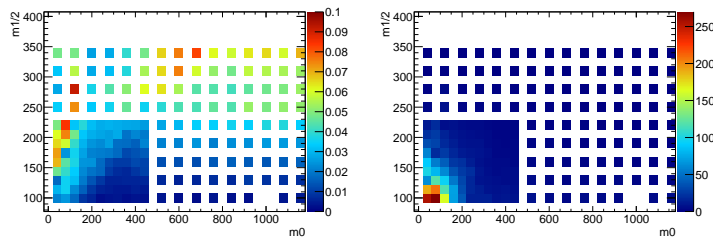


Figure 57: Relative contribution to the selected events for the opposite sign channel as a function of  $M_0$  and  $M_{1/2}$  for (from top left to bottom right) squark–gluino production, gluino–gluino production, squark–squark production, squark–antisquark production, stop 1 pair production, stop 2 pair production, sbottom 1 pair production, sbottom 2 pair production. Note the differences to Fig. 53 and see text for discussion on low statistics in some bins

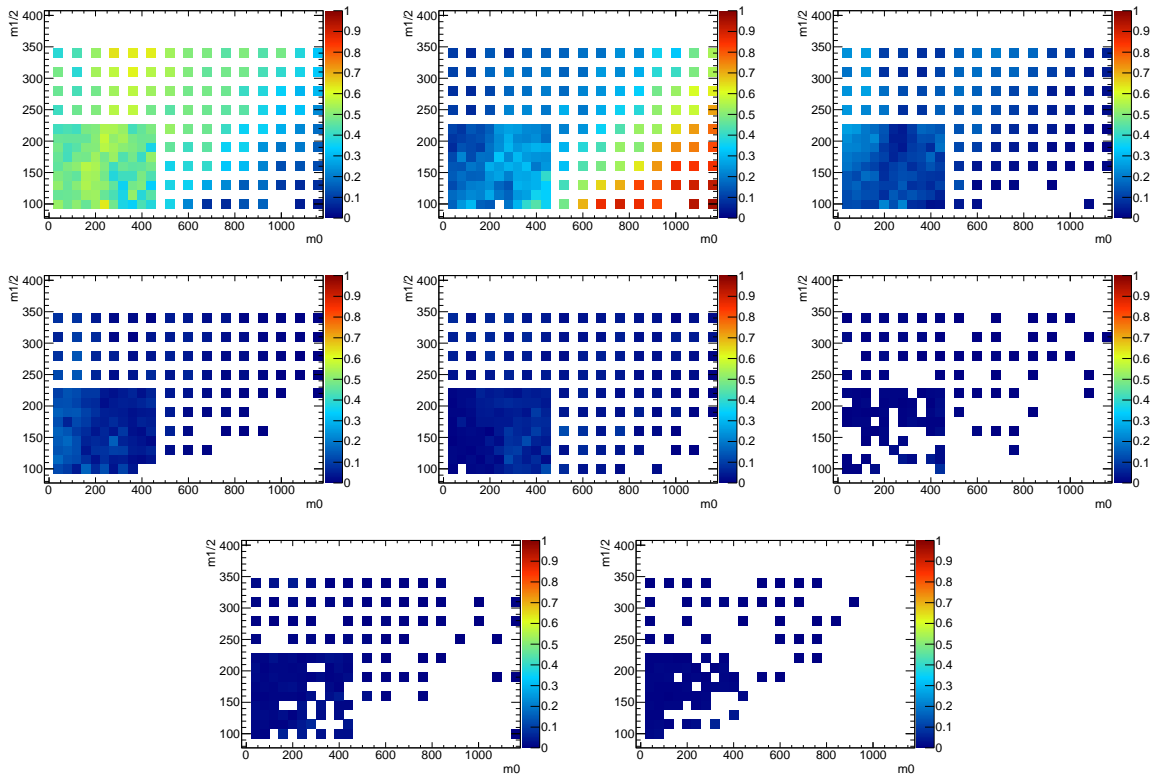
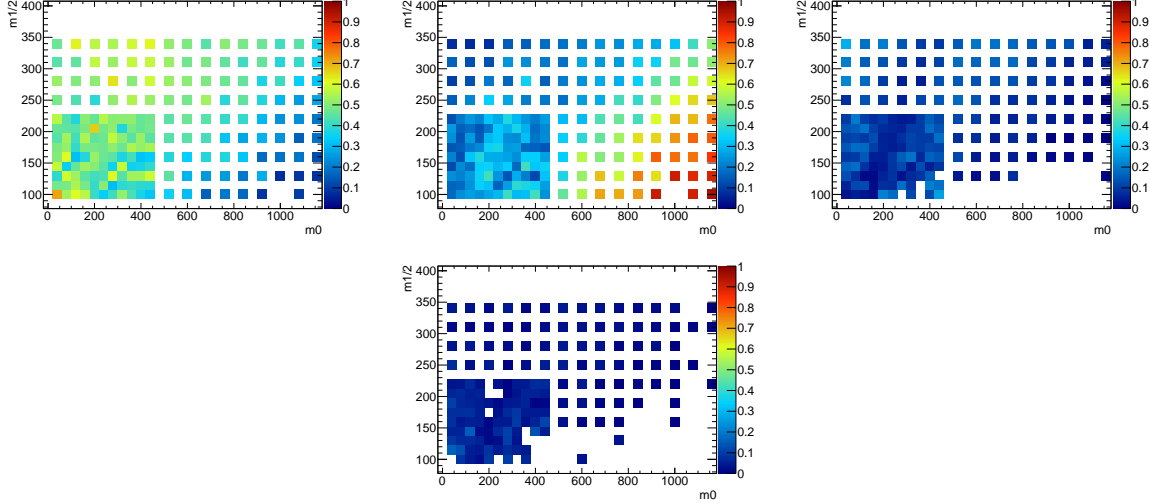


Figure 58: Relative contribution to the selected events for the same sign channel as a function of  $M_0$  and  $M_{1/2}$  for the four most important channels (from top left to bottom right) squark–gluino production, gluino–gluino production, squark–squark production, squark–antisquark production. Note the differences to Fig. 57



$$\Delta_{PDF}(\sigma_{NLO}) = \frac{1}{2 \times 1.645} \sqrt{\sum_X (\sigma(X^+) - \sigma(X^-))^2},$$

where  $\sigma_{NLO}$  is calculated for the 44 variations  $X^\pm$  of the PDF and where the factor 1.645 is used to transform the 90% CL uncertainty into a 68% CL one.

The scale uncertainty is given by a variation of the factorisation and renormalisation scales by a factor of 2 up and down. The nominal scale  $Q$  is given by  $Q = (M_{sq} + M_{gl})/2$ ,  $Q = M_{gl}$  or  $Q = M_{sq}$ , depending on the production process at play. The uncertainty due to the scale variation is calculated by comparing the NLO cross section with scale variation to the cross section of the nominal sample for each production process; the uncertainty increases in particular with an increase of  $m_0$  and to smaller extent with an increase of  $m_{1/2}$  and it is found to be the largest for gluino–gluino production for which it reaches values of around 20%. One should note that for production processes involving squarks and gluinos, the higher cross section is obtained when decreasing the scales and vice-versa.

In Fig. 59, 60 and 61 the uncertainties for a scale  $Q = 2Q_{nominal}$ , a scale  $Q = \frac{1}{2}Q_{nominal}$  and the PDF uncertainties are shown for the 4 most important channels.

Those uncertainties can now be summed over all production channels using the contribution weights shown in Fig. 58 and Fig. 57 respectively. The result is shown in Fig. 62 for the scale uncertainties and in Fig. 63 for the PDF uncertainties.

## E.2 Theoretical uncertainties on pheno grids

Identical studies have been performed for the various pheno grids, and the results have been supplied to the limit setting group. The PDF uncertainty is below 7% for phenogrid 2 and below 14% for phenogrid 3. The uncertainty due to scale uncertainties is between 10 and 14% for both phenogrid 2 and 3.

Figure 59: Relative error on the cross section as a function of  $M_0$  and  $M_{1/2}$  for a scale increase by a factor of 2 for the four dominant production processes (from left to right) squark–gluino production, gluino–gluino production, squark–squark production and squark–antisquark production.

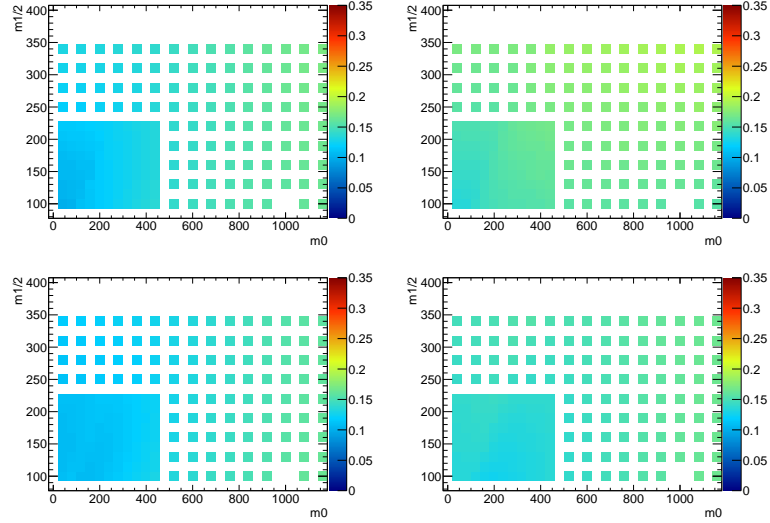


Figure 60: Relative error on the cross section as a function of  $M_0$  and  $M_{1/2}$  for a scale decrease by a factor of 2 for the four dominant production processes (from left to right) squark–gluino production, gluino–gluino production, squark–squark production and squark–antisquark production.

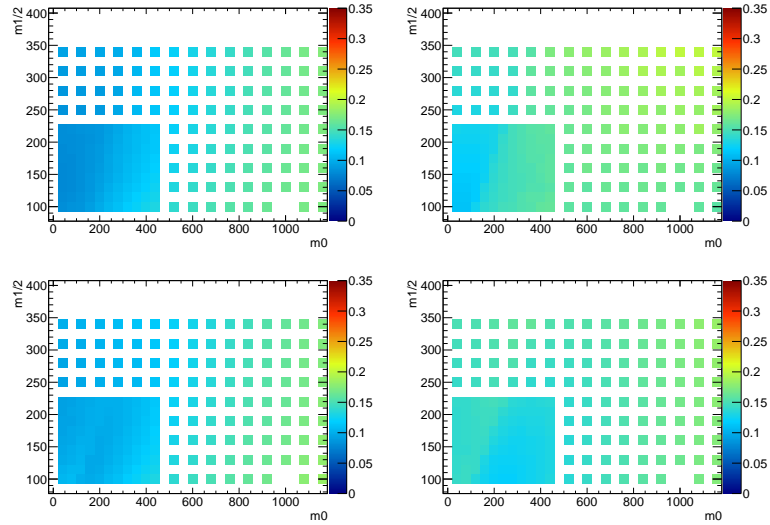


Figure 61: Relative error on the cross section as a function of  $M_0$  and  $M_{1/2}$  for the PDF variation for the four dominant production processes (from left to right) squark–gluino production, gluino–gluino production, squark–squark production and squark–antisquark production.

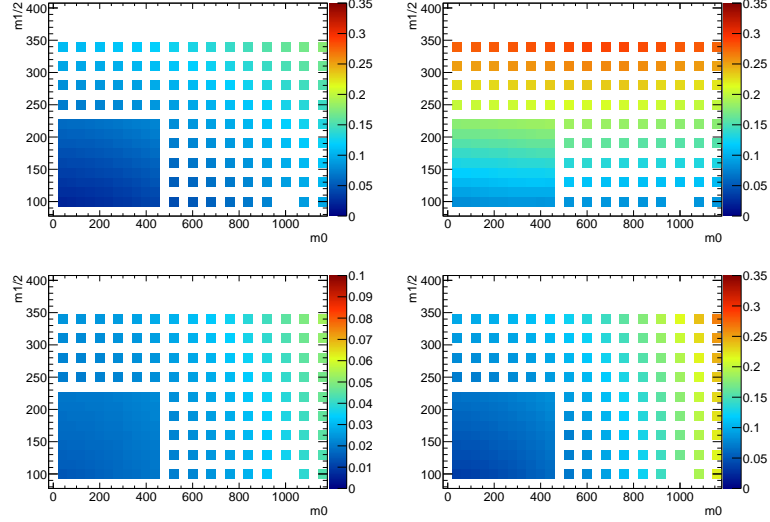


Figure 62: Relative error on the total acceptance as a function of  $M_0$  and  $M_{1/2}$  due to a scale decrease by a factor of 2 (top) or to a scale increase by a factor 2 (bottom) for the same sign channel (left) and the opposite sign channel (right).

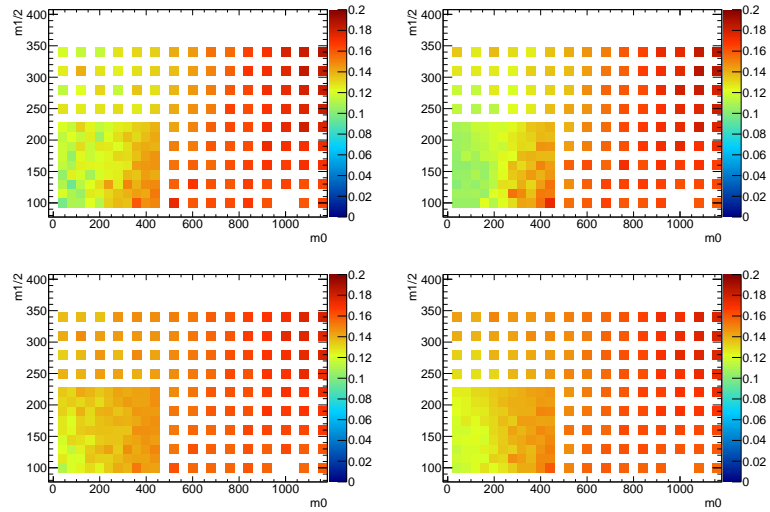


Figure 63: Relative error on the cross section weighted by acceptance of each subprocess as a function of  $M_0$  and  $M_{1/2}$  for the PDF variation for the same sign channel (left) and the opposite sign channel (right).

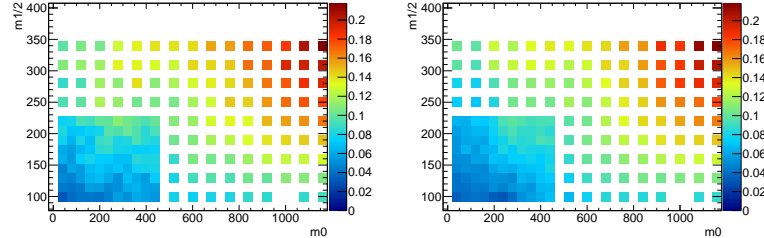


Figure 64: Relative error on the cross section weighted by acceptance of each subprocess as a function of  $M_0$  and  $M_{1/2}$ : upper error (top) and lower error (bottom) for the same sign channel (left) and the opposite sign channel (right).

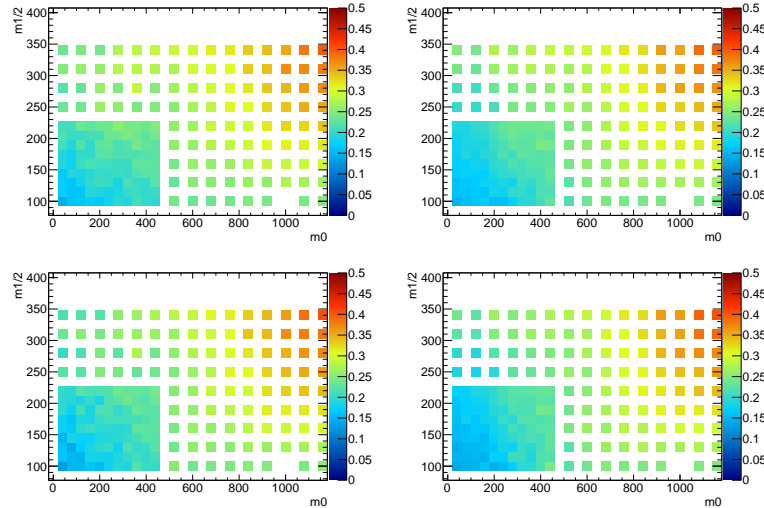
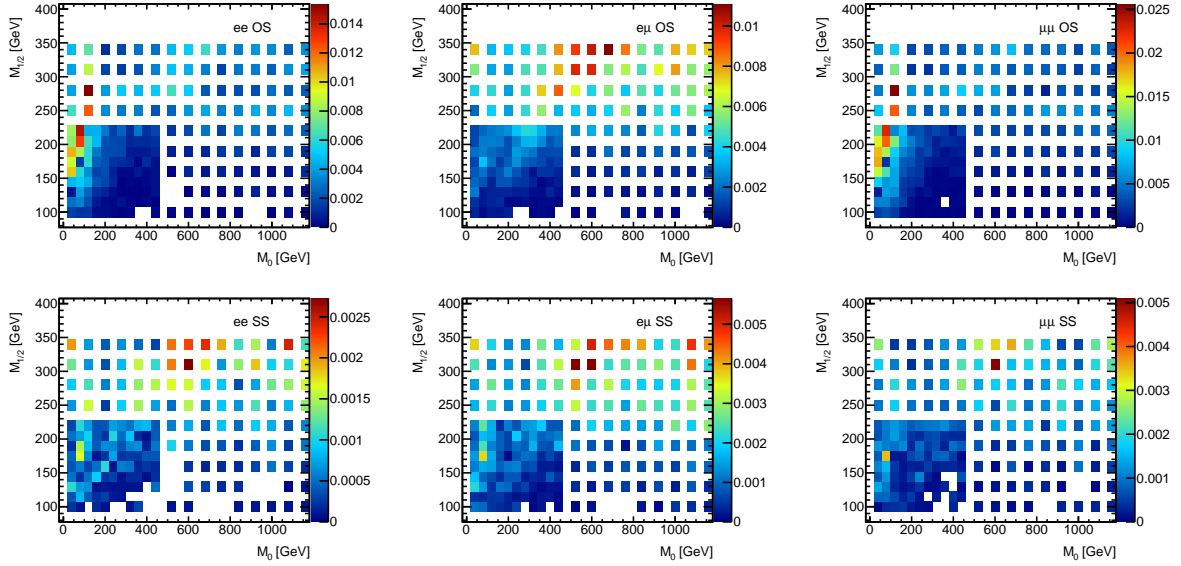


Figure 65: Total efficiency after the MET requirement as a function of  $M_0$  and  $M_{1/2}$  for all lepton (flavour and sign) combinations.



### E.3 Reconstruction efficiency for the mSUGRA grid

The efficiency of a given cut is defined as the ratio between the fraction of events selected by this cut at reconstruction level and the number of Monte Carlo events before any cut is applied<sup>4</sup>. The total efficiency after the  $E_T^{\text{miss}}$  cut (at 150 GeV for the OS channel and at 100 GeV for SS) is shown in Fig. 65. The efficiencies for OS events are  $\sim 5$  times larger than those for SS events for most of the parameter space. The highest reconstruction efficiencies can be found in the OS dimuon channel ( $\sim 2\%$ ) and OS dilepton channel ( $\sim 1\%$ ). Those large efficiencies can be found in a small part of the parameter space, with  $M_0 < 100$  GeV and  $150 < M_{1/2} < 250$  GeV. For most of the parameter space the total efficiency is on the order of a few per mille. Highest efficiency for SS ( $0.1\text{-}0.5\%$ ) and OF OS events ( $0.1\%$ ) are found for large  $M_0$  (greater than 500 GeV) and  $M_{1/2}$  (greater than 200 GeV). The points which show large deviations from the average are due to low statistics in the Monte Carlo samples.

The number of events expected after all cuts at the reconstruction level is shown in Fig 66 for all lepton (flavour and sign) combinations for an integrated luminosity of  $34.3 \text{ pb}^{-1}$ . The highest event yields are to be expected for low  $M_0$  and  $M_{1/2}$  due to the high cross section. In the best cases, one can expect  $\sim 100$  OS events, and  $\sim 30$  SS events. In Fig 67 and 68 one can find the event yields for both SS and OS channels divided by process, as a function of  $M_0$  and  $M_{1/2}$ , and of the squark and gluino masses respectively. The process giving the highest contribution is gluino-squark production.

#### E.3.1 Systematics

Systematic errors on the reconstructed objects will affect the efficiency shown in the last section and hence the number of expected signal events. Unlike the theoretical errors on the acceptance presented above, these errors should be correlated between the signal and the background expectations. The largest systematic errors are related to the lepton reconstruction efficiencies, jet energy scale and jet energy resolution. Other systematic errors (lepton energy scale and resolution) are expected to be small in

<sup>4</sup>This is also sometimes defined as efficiency times acceptance.

Figure 66: Number of events expected after all cuts at the reconstruction level as a function of  $M_0$  and  $M_{1/2}$  for all lepton (flavour and sign) combinations for  $34.3 \text{ pb}^{-1}$ .

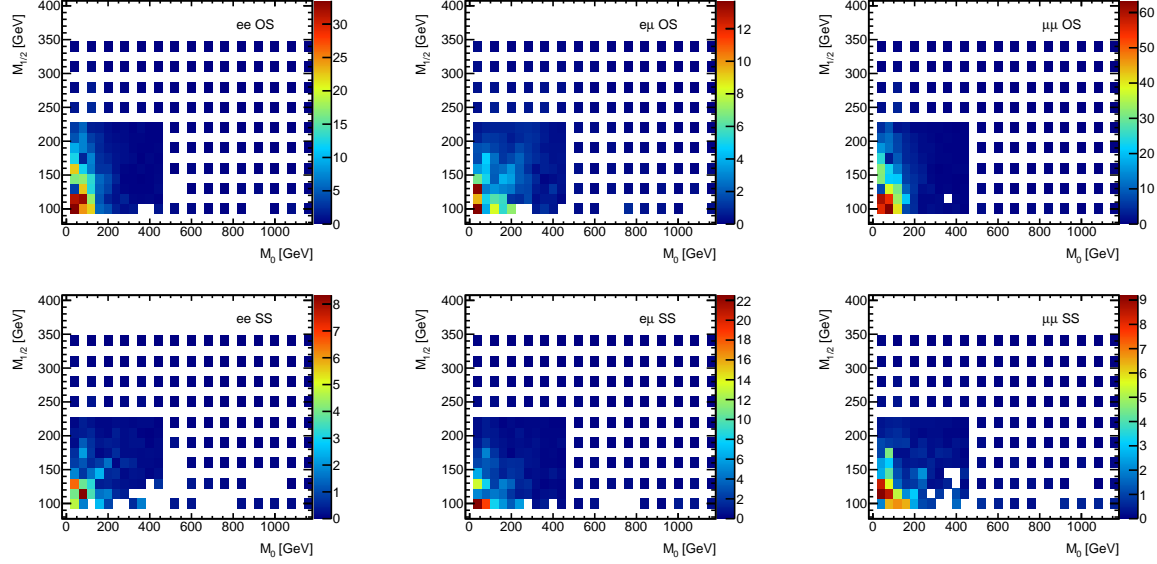


Figure 67: Number of events expected after all cuts (SS and OS channels combined) at the reconstruction level as a function of  $M_0$  and  $M_{1/2}$  for different processes for  $34.3 \text{ pb}^{-1}$ .

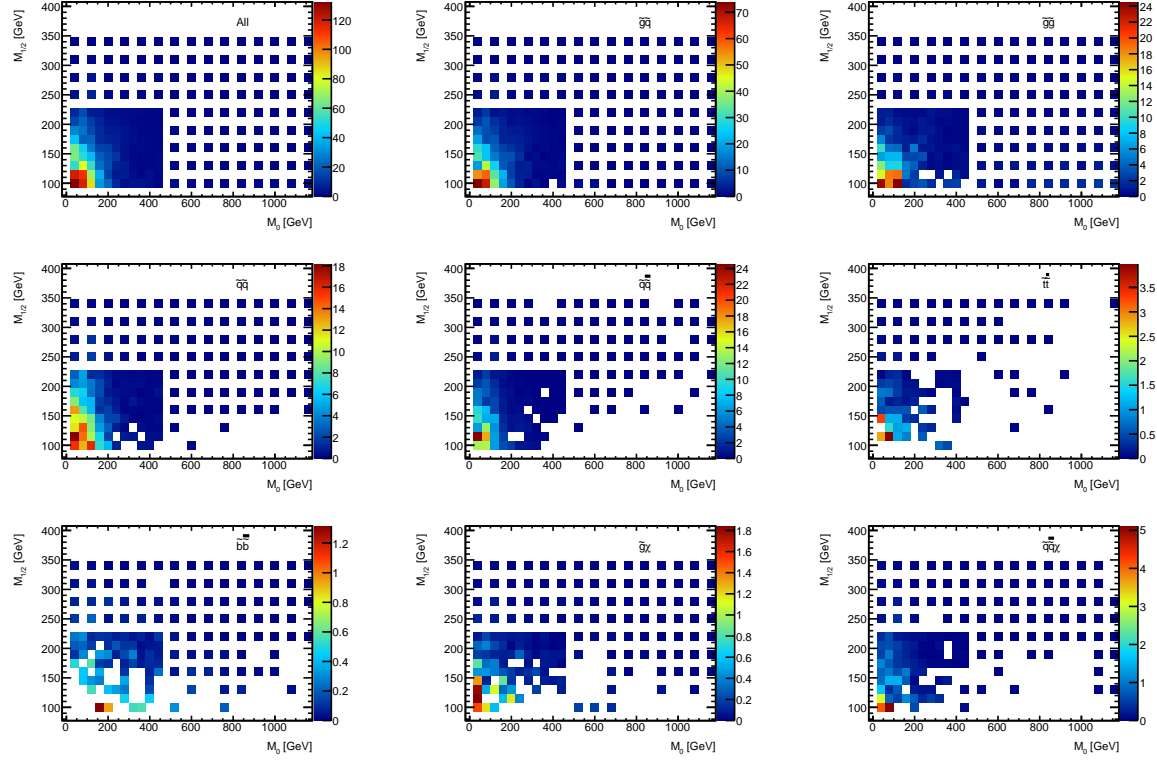


Figure 68: Number of events expected after all cuts (SS and OS channels combined) at the reconstruction level as a function of the squark mass  $M_{\tilde{q}}$  and the gluino mass  $M_{\tilde{g}}$  for different processes for  $34.3 \text{ pb}^{-1}$ .

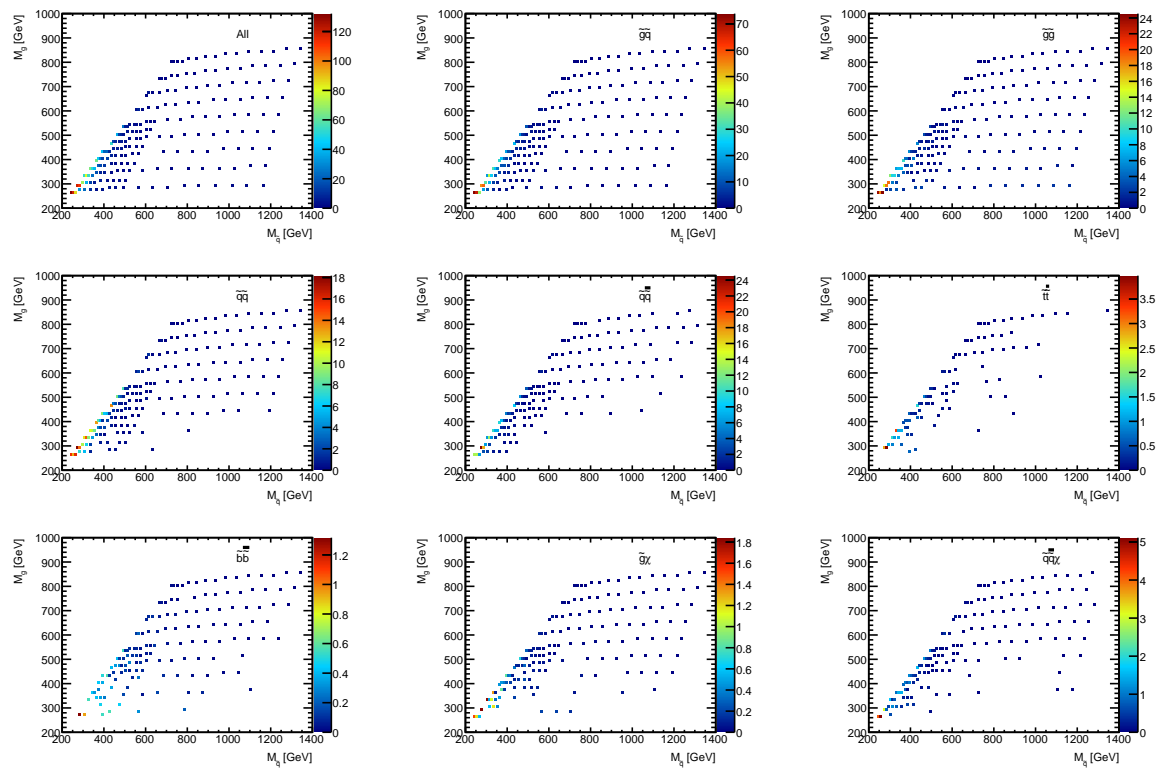


Figure 69: Relative error on the efficiency after the  $E_T^{\text{miss}}$  cut due to the muon (right) and electron (left) reconstruction efficiency, as a function of  $M_0$  and  $M_{1/2}$ .

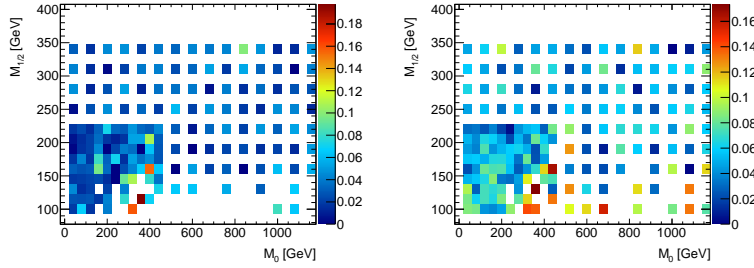
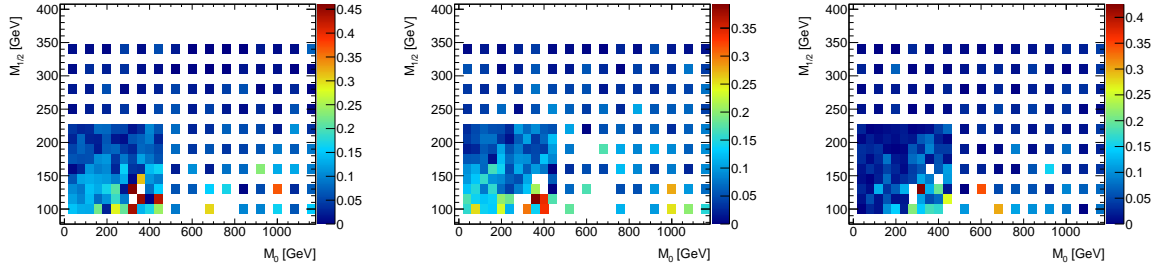


Figure 70: Relative error on the efficiency after the  $E_T^{\text{miss}}$  cut due to the jet energy resolution (right) and jet energy scale: upper (left) and lower (center), as a function of  $M_0$  and  $M_{1/2}$ .



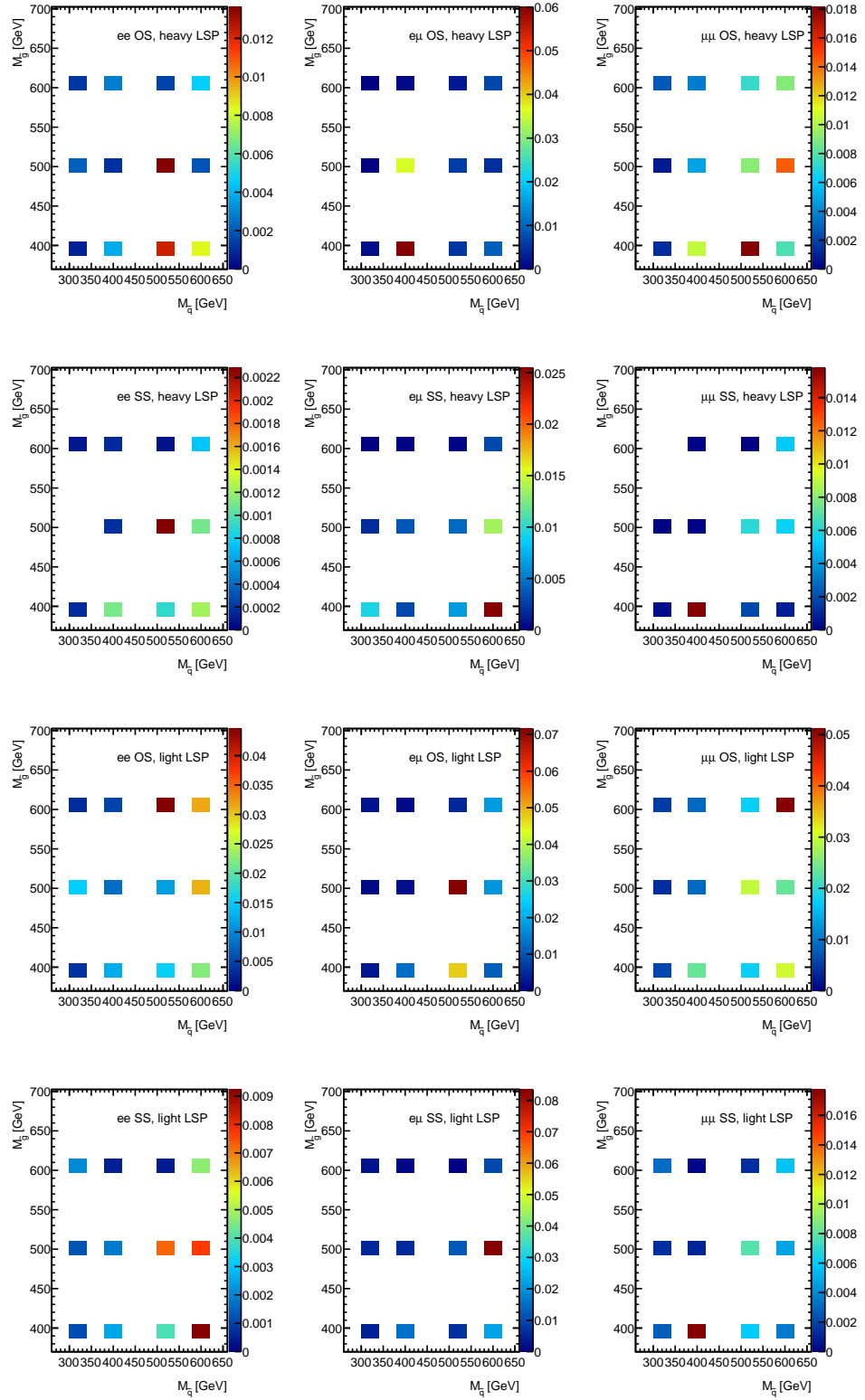
comparison; this assumption was checked on the SU4 benchmark point ( $M_0 = 200 \text{ GeV}$ ,  $M_{1/2} = 160 \text{ GeV}$ ,  $\tan\beta = 10$ ,  $\mu > 0$  and  $A_0 = -400 \text{ GeV}$ ). The systematic uncertainty on the muon and electron reconstruction efficiency was estimated by randomly rejecting 5% of the selected leptons. As shown in Fig. 69, this uncertainty is less than 10% for most of the parameter space (disregarding fluctuations due to low Monte Carlo statistics at low  $M_{1/2}$ ). The systematic uncertainties due to jet energy scale and resolution are shown in Fig. 70. As done for the background, these errors were propagated to all kinematic variables based on jets. As can be seen in the figure, the error related to the jet energy scale is less than 20% for most of the parameter space, while the one related to the jet energy resolution is mainly below 10%.

#### E.4 Reconstruction efficiency for the PhenoGrids

As in the previous section, the efficiency of a given cut is defined as the ratio between the fraction of events selected by this cut at reconstruction level and the number of Monte Carlo events before any cut is applied. The total efficiency after the  $E_T^{\text{miss}}$  requirement (at 150 GeV for the OS channel and at 100 GeV for SS) is shown in Fig. 71 for the PhenoGrid2. The lower 6 plots have maximum  $E_T^{\text{miss}}$ , and jets and leptons as hard as possible, whereas the upper 6 plots have unfavourable kinematics. Efficiencies are  $\sim 3$  times larger in the case of a light LSP. The highest reconstruction efficiencies can be found in the OS SF channels ( $\sim 4\%$ ) for large values of  $M_{\tilde{g}}$  and  $M_{\tilde{q}}$ . For most of the parameter space the total efficiency is of the order of a few percent.

The number of events expected after all cuts at the reconstruction level is shown in Fig. 72 for all lepton (flavour and sign) combinations for an integrated luminosity of  $34.3 \text{ pb}^{-1}$ . The highest event

Figure 71: Total efficiency after the  $E_T^{\text{miss}}$  requirement as a function of  $M_{\tilde{g}}$  and  $M_{\tilde{q}}$  for a variety of PhenoGrid2 points for all lepton (flavour and sign) combinations.



yields are to be expected for low  $M_{\tilde{g}}$  and  $M_{\tilde{q}}$  due to the higher cross section. In the best cases, one can expect  $\sim 70$  events. The processes giving the highest contribution are gluino-gluino and gluino-squark production (see Fig 73).

#### E.4.1 Systematics

Systematic errors on the reconstructed objects will affect the efficiency shown in the last section and hence the number of expected signal events. The largest systematic errors are related to the lepton reconstruction efficiencies, jet energy scale and jet energy resolution (see E.3.1). The uncertainties due to electron and muon reconstruction efficiencies are shown in Fig. 74, whereas the uncertainties due to jet energy scale and resolution can be found in Fig. 75. The uncertainty on the lepton reconstruction efficiency is less than 5% for most of the parameter space. The error related to the jet energy scale is less than 20% for most of the parameter space (disregarding fluctuations due to low Monte Carlo statistics), while the one related to the jet energy resolution is mainly below 10%.

Figure 72: Number of events expected after the  $E_T^{\text{miss}}$  cut as a function of  $M_{\tilde{g}}$  and  $M_{\tilde{q}}$  for a variety of PhenoGrid2 points for all lepton (flavour and sign) combinations for  $34.3 \text{ pb}^{-1}$ .

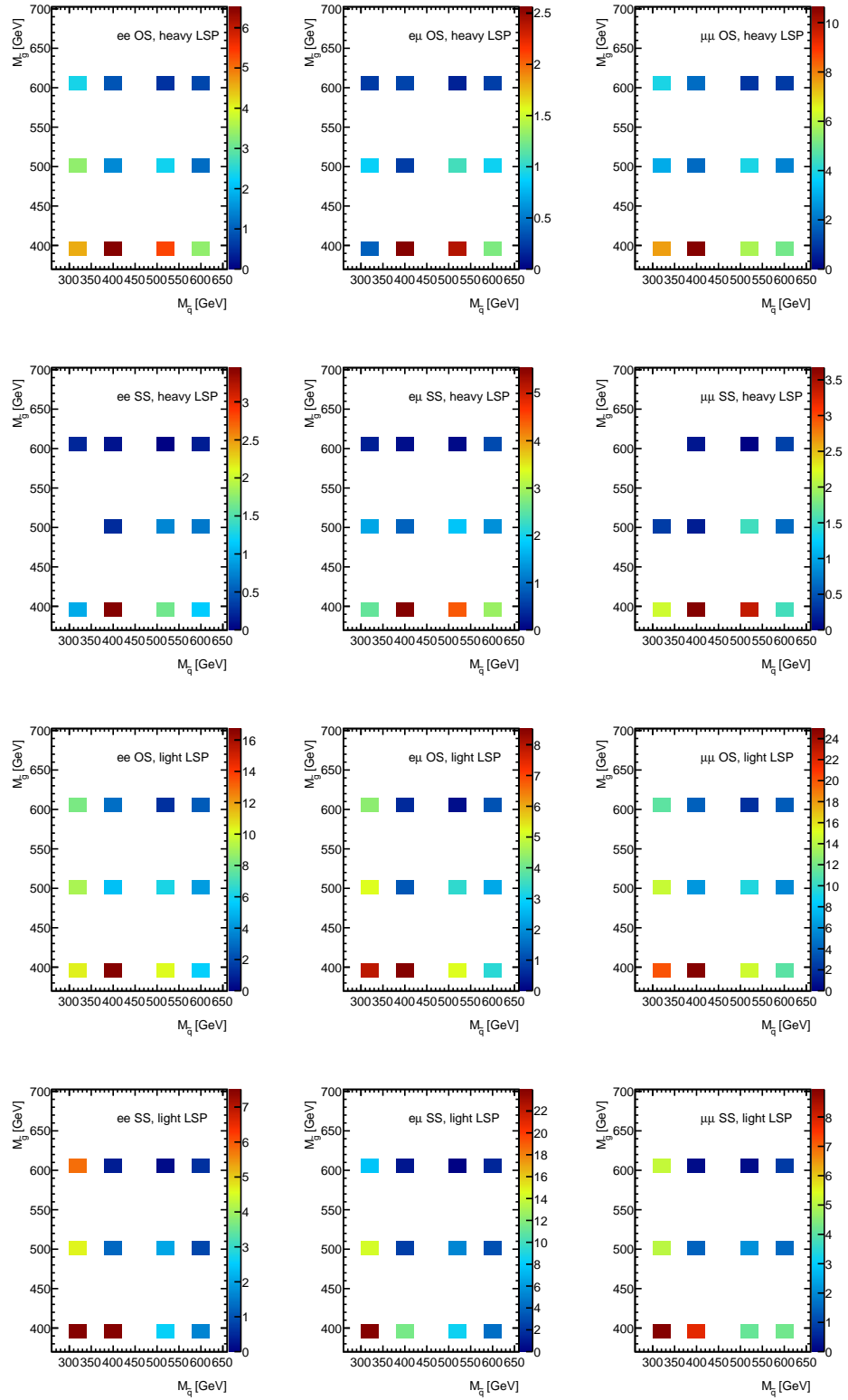


Figure 73: Number of events expected after the  $E_T^{\text{miss}}$  cut as a function of  $M_{\tilde{g}}$  and  $M_{\tilde{q}}$  for a variety of PhenoGrid2 points for various processes for  $34.3 \text{ pb}^{-1}$ .

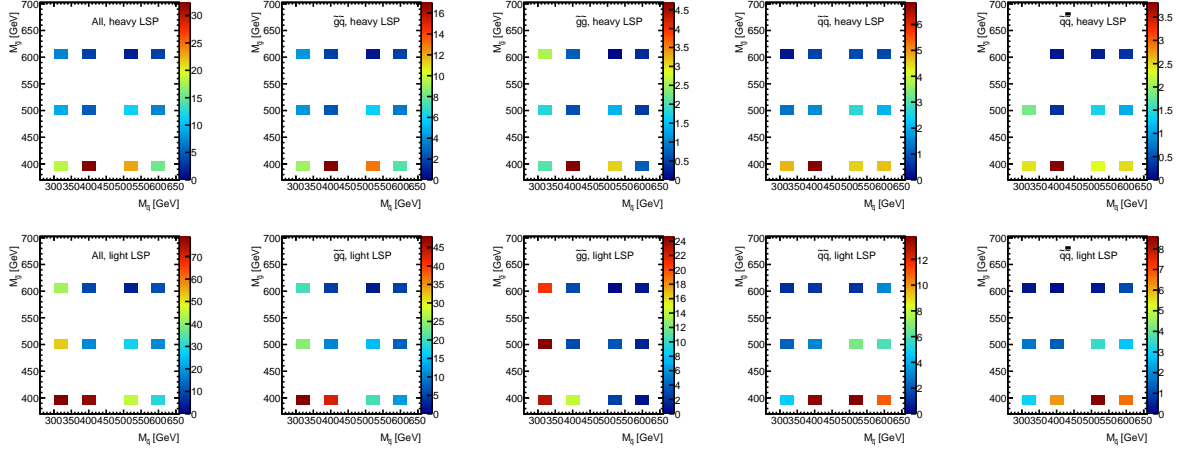


Figure 74: Relative error on the efficiency after the  $E_T^{\text{miss}}$  cut due to the muon (right) and electron (left) reconstruction efficiency, as a function of  $M_{\tilde{g}}$  and  $M_{\tilde{q}}$  for a variety of PhenoGrid2 points.

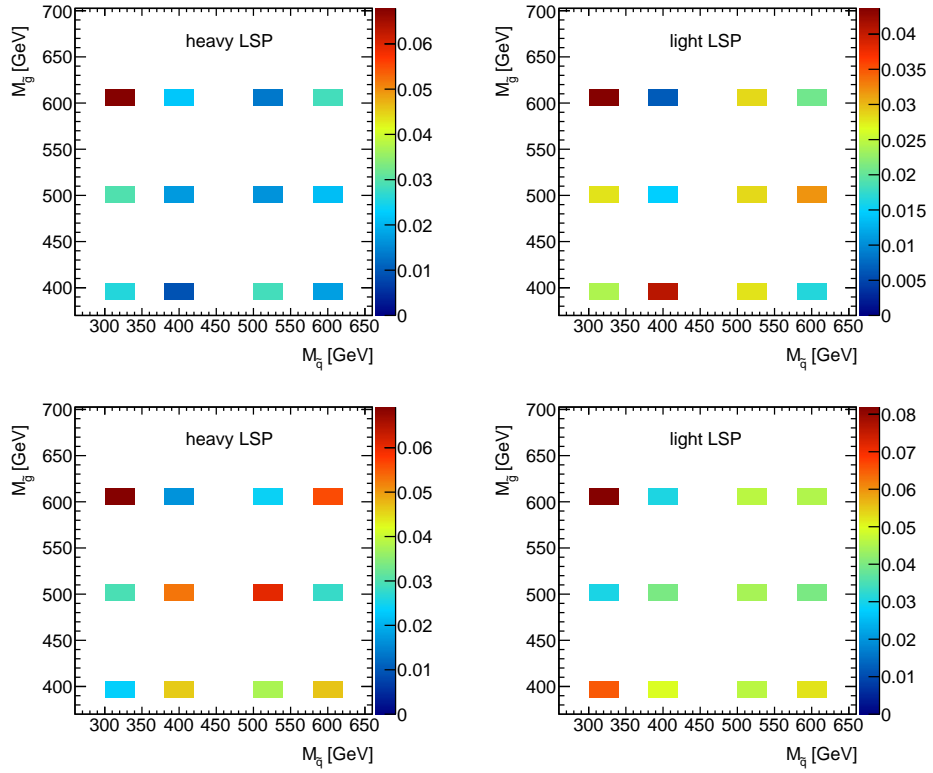
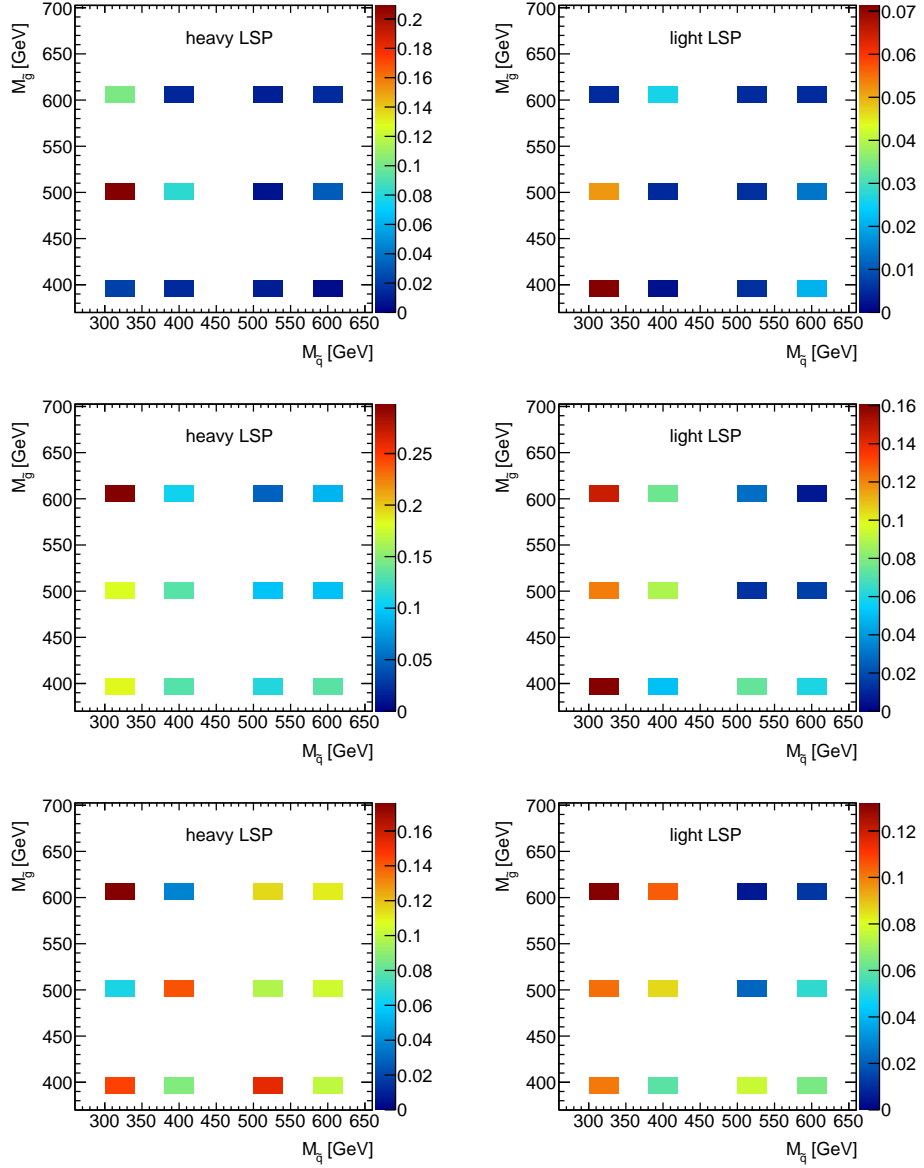


Figure 75: Relative error on the efficiency after the  $E_T^{\text{miss}}$  cut due to the jet energy resolution (upper plots) and jet energy scale: upper (middle) and lower (bottom), as a function of  $M_{\tilde{g}}$  and  $M_{\tilde{q}}$  for a variety of PhenoGrid2 points.



## F Charge misidentification rate

We focus on the measurement of electron charge mis-identification rate using a data-driven approach based on  $Z/\gamma^* \rightarrow e^+e^-$  events. It consists of tagging a clean sample of events using one electron, and then measuring the charge mis-identification rate using the second electron from the  $Z/\gamma^*$  boson decay.

### F.1 Tag-and-Probe Method

The tag condition typically requires an electron identified with RobusterTight cuts. Both electrons are also required to be above a pT threshold consistent with the trigger used. The invariant mass of the lepton pair is then fitted using a Gaussian distribution convoluted with a Breit-Wigner plus an exponential function, to identify the number of tag-probe events,  $N_1$ , where the secend selected electron has the same sign with the first one, and a sample  $N_2$ , where the second has the opposite sign with the first one. The charge mis-identification rate for a given signature is given by the ratio between  $N_1$  and  $(N_1+N_2)$ . A quantitative comparison between the charge mis-identification rate obtained from real data and from the Monte Carlo is used to validate the tag-and-probe method.

### F.2 Electron Charge Mis-identification Rate

The identification of electrons is based on seed-clusters in the electromagnetic calorimeter matched to tracks. The tag electron is a reconstructed electron selected using RobusterTight cuts and also required to pass the trigger EF\_e15\_medium. The electron is also required to be outside the barrel/end-cap transition region ( $1.37 < \eta < 1.52$ ). The probe electron is selected by identifying a cluster in the opposite hemisphere, such that the azimuthal difference between tag and probe electrons is  $\Delta\phi > 3/4\pi$ . Both tag and probe electrons are required to be isolated and have  $pT > 20$  GeV. The invariant mass of the lepton pair is required to be between 60 and 120 GeV for the  $Z$  mass fit region. The reconstructed probe electron was checked against RobustMedium and RobusterTight selection cuts.

Considering the background contamination, we require "good events" which defined by SUSY group, and also remove the events with missing transverse energy larger than 20GeV.. The standard model background is estimated as a part of background in  $Z$  mass peak fit process.

Table 43 summarise the charge mis-identification rate obtained in Tag-and-Probe method.

Figure 1 and Figure 2 show the invariant mass, with the two level probe electron.

Table 43: electron charge mis-identification rate.

	misID rate $\pm$ stat(%)	
criteria	DATA	MC
RobustMedium	$1.96 \pm 0.20$	$2.05 \pm 0.13$
RobusterTight	$0.75 \pm 0.14$	$1.08 \pm 0.11$

### F.3 Statistical and Systematic Uncertainties

Several uncertainties may affect these tag-and-probe measurements, are listed in Table 44

- **Differences between DATA and MC:**

The charge mis-identification rate difference between DATA and MC is 0.09% for RobusetMedium electron , and 0.33% for RobusterTight electron, assuming that the statistical error on MC is negligible.

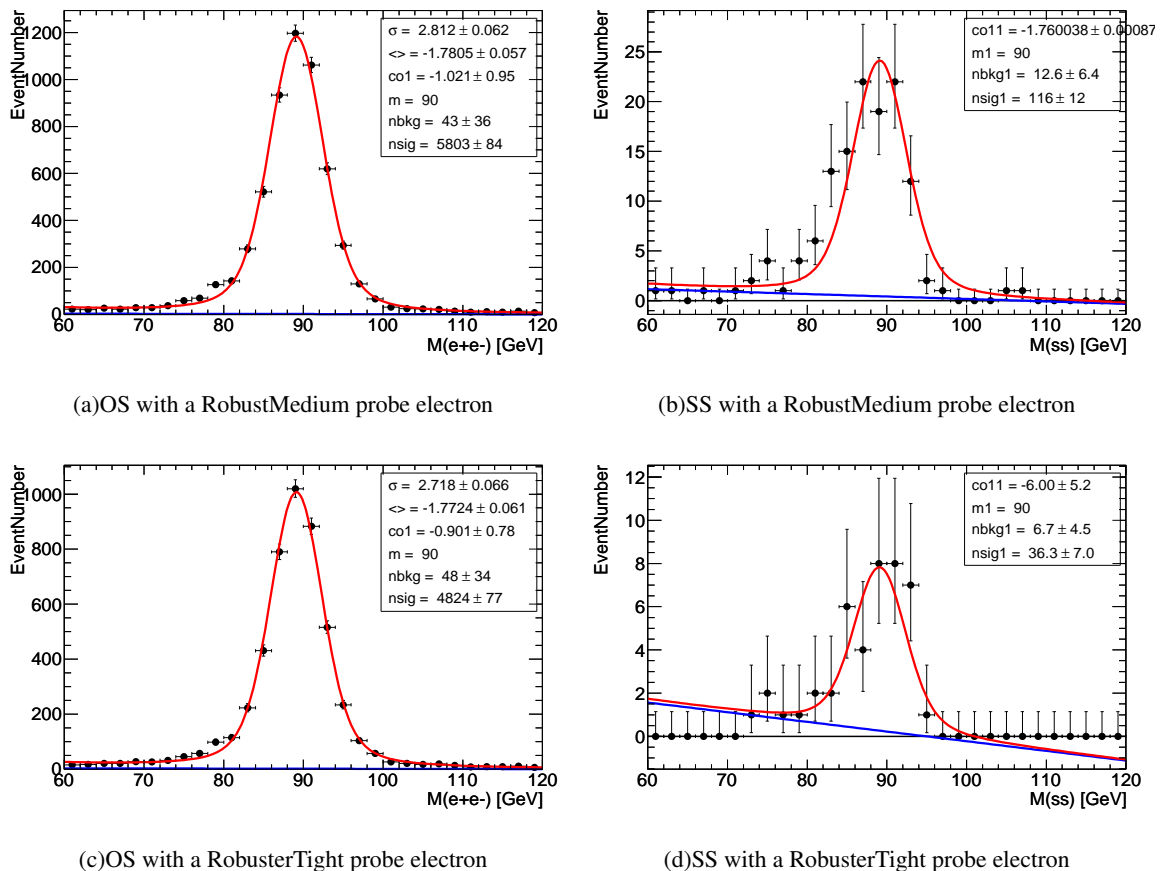


Figure 76:  $Z/\gamma^*$  invariant mass from data

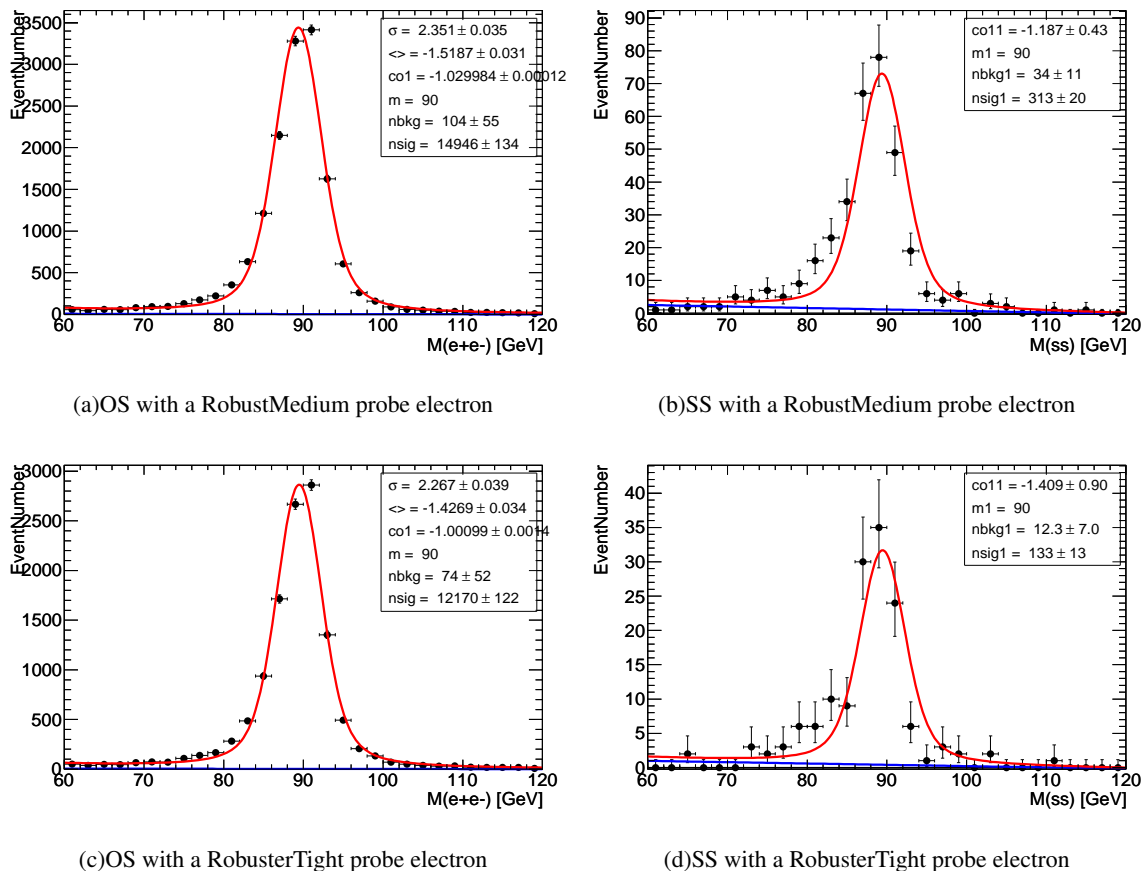


Figure 77:  $Z/\gamma^*$  invariant mass from Zee

- **Fit Region:**

Another source of systematic error comes from varying the selection of invariant mass region from 60-120GeV to 50-130GeV. The Uncertainty is 0.14% for RobusetMedium positron , and 0.11% for RobusterTight positron.

- **Fit Shape Uncertainty:**

We estimate the shape effect by fitting the background with different order Chebychev polynomials. The charge mis-identification rate uncertainty introduced by Z invariant mass fit method is 0.39% for RobusetMedium electron , and 0.05% for RobusterTight electron.

- **Statistical Uncertainty:**

The statistic uncerntainty for electron charge mis-identification rateis is 0.20% for RobusetMedium electron , and 0.14% for RobusterTight electron.

**Table 44: Uncertainties**

	uncertainty (%)	
	RobustMedium	RobusterTight
DATA MC	0.09	0.33
fit region	0.14	0.11
fit shape	0.39	0.05
statistical error	0.20	0.14
total	0.47	0.38

## F.4 Conclusion

Studies of the strategies for measuring electron charge mis-identification rates in early data show that the tag-and-probe method is a good tool to estimate the electron charge mis-identification rate and to eliminate the effect of other standard model background. With data  $4.3 pb^{-1}$  , the electron charge mis-identification rate of RobustMedium and RobusterTight is 1.96%and 0.75% respectively.

The method is limited by the statistics of the Z sample, whereas its systematic uncertainty is less than 0.47% for RobustMedium electron and 0.38% for RobusterTight electron.The large uncertainty in Ro-busterTight electron charge mis-identification between data and MC is under investigation.

## G Complementary results on fake background estimation using the matrix method

### G.1 Introduction

We apply the matrix method described in section 7.2, on the same flavour channels  $ee$  and  $\mu\mu$ . We can reduce the 4x4 matrix to 3x3 since in the same flavour channel we do not need to distinguish between the two leptons.

All leptons follow the standard SUSY object definitions as described in the note, with some exceptions. Leptons used to extract the QCD Control regions are only required to satisfy  $p_T > 10\text{GeV}$ , and not 20 GeV, as the standard object preselection requires. This is necessary in order to gain sufficient statistics especially in the 2-lepton QCD Control regions. A loose electron must, as the tight electron, pass the b-layer requirement. This is in order to suppress fake contribution from conversions. A loose electron needs only fulfill the RobustMedium quality requirement. In addition, the isolation requirement is loosened to  $\text{etcone}20/\text{pt} < 0.5$ , instead of the usual  $\text{etcone}20/\text{pt} < 0.15$ . A loose muon is not subject to overlap removal, nor include any additional isolation.

We study two main QCD control regions, defined by either containing exactly 1-lepton, or 2 same-sign leptons. Several variations over these two control regions are studied, and the resulting fake-rates can be found in table 45.

Efficiencies are obtained from clean  $Z$  decays into 2 leptons, by tagging a tight lepton and using tight-tight  $N_{TT}$  and tight-exclusive loose  $N_{lT}$  lepton pairs. Fake-rates from the 2-lepton QCD control regions are extracted using “anti-tag-and-probe”, i.e. by tagging a “exclusive loose lepton” (passes loose requirement, but fails tight). Lepton combinations exclusive loose-exclusive loose  $N_{ll}$  and tight-exclusive loose  $N_{lT}$  are used in the fake-rate calculation.

Single lepton efficiency is extracted via the ratio

$$\tilde{\epsilon}_{real} = \frac{N_{TT}}{2 \cdot N_{lT} + N_{TT}}$$

where  $\tilde{\epsilon}_{real}$  is the pseudo-efficiency we calculate when operating with lepton pairs. The factor 2 comes from the combination of  $N_{lT}^o + N_{Tl}^o = 2 \cdot N_{lT}$ , where the superscript  $o$  indicates the ordered pair. Assuming all lepton pairs in this region are real, the single-lepton efficiency  $r$  is found by noting that  $N_{TT} = rr \cdot N_{LL}^{real}$ , and correspondingly  $N_{Tl} = r \cdot (1 - r) \cdot N_{LL}^{real}$  and  $N_{ll} = (1 - r) \cdot (1 - r) \cdot N_{LL}^{real}$ .  $N_{LL}^{real}$  is the full set of 2 inclusive loose lepton events. We then have the relation

$$\tilde{\epsilon}_{real} = \frac{rr}{2r(1 - r) + rr} \implies r = \frac{2\tilde{\epsilon}_{real}}{1 + \tilde{\epsilon}_{real}} \quad (52)$$

Similarly we get the single fake-rate  $f$ , by now assuming  $N_{LL}^{fake}$  as the full set of 2 inclusive loose lepton events.

$$\tilde{\epsilon}_{fake} = \frac{2 \cdot N_{lT}}{N_{ll} + 2 \cdot N_{lT}} = \frac{2(1 - f)f}{(1 - f)(1 - f) + 2(1 - f)f} \implies f = \frac{\tilde{\epsilon}_{fake}}{2 - \tilde{\epsilon}_{fake}} \quad (53)$$

The fake-rates from the 1 lepton QCD control regions are simply defined as

$$f = \frac{N_l}{N_l + N_T} \quad (54)$$

Variations over the following main control regions are studied:

#### 1. Z control region

- Lepton pairs mainly from clean Z events are used to extract efficiencies. A clean real control region is obtained by tagging a tight lepton, and requiring the second lepton (either exclusive loose, or tight) to be of opposite sign and same flavour, and their di-lepton mass to be within 5 GeV of the Z mass (86-96 GeV).

#### 2. QCD control region 1-lepton

- The incentive for requiring exactly 1 lepton is to avoid a large contamination of Z + jets in our control region, in addition to large event-statistics. The W+jets background is suppressed by removing events where  $\Delta\phi(\text{lep}, E_T^{\text{miss}}) < 0.5$  (or 1.0), and one can in addition apply a Z veto to remove the surviving Z + jets contribution.

#### 3. QCD control region 2 same-sign leptons

- A clean QCD region is obtained by requiring exactly 2 leptons with equal charge. Real leptons from Z contribute due to charge mis-identification in the electron channel, especially for the tight-exclusive loose pairs. To avoid leptons from Z pushing the fake-rate up, we can in addition exclude events where the leptons fall inside the Z mass peak, to better reflect the actual QCD contribution.

In the following distributions we choose not to include any QCD MC, as the uncertainty is so large. The electroweak contribution is much better understood so we rather infer the QCD contribution from the gap between data and the sum of MC (excluding QCD).

## G.2 Validation plots for the real lepton control region

A highly pure real-lepton enhanced region is obtained by selecting the Z mass window  $86 < mll < 96$  GeV. From figure 78 we see that under the mass peak, only a negligible amount of other processes contribute. We obtain an electron and muon efficiency of 87.6% and 97.3% respectively. Numbers can be found in table 45. MC SM processes do not include QCD. The MC Drell-Yan contribution ends abruptly due to the invariant mass cut on generator level, separating this contribution from Z processes.

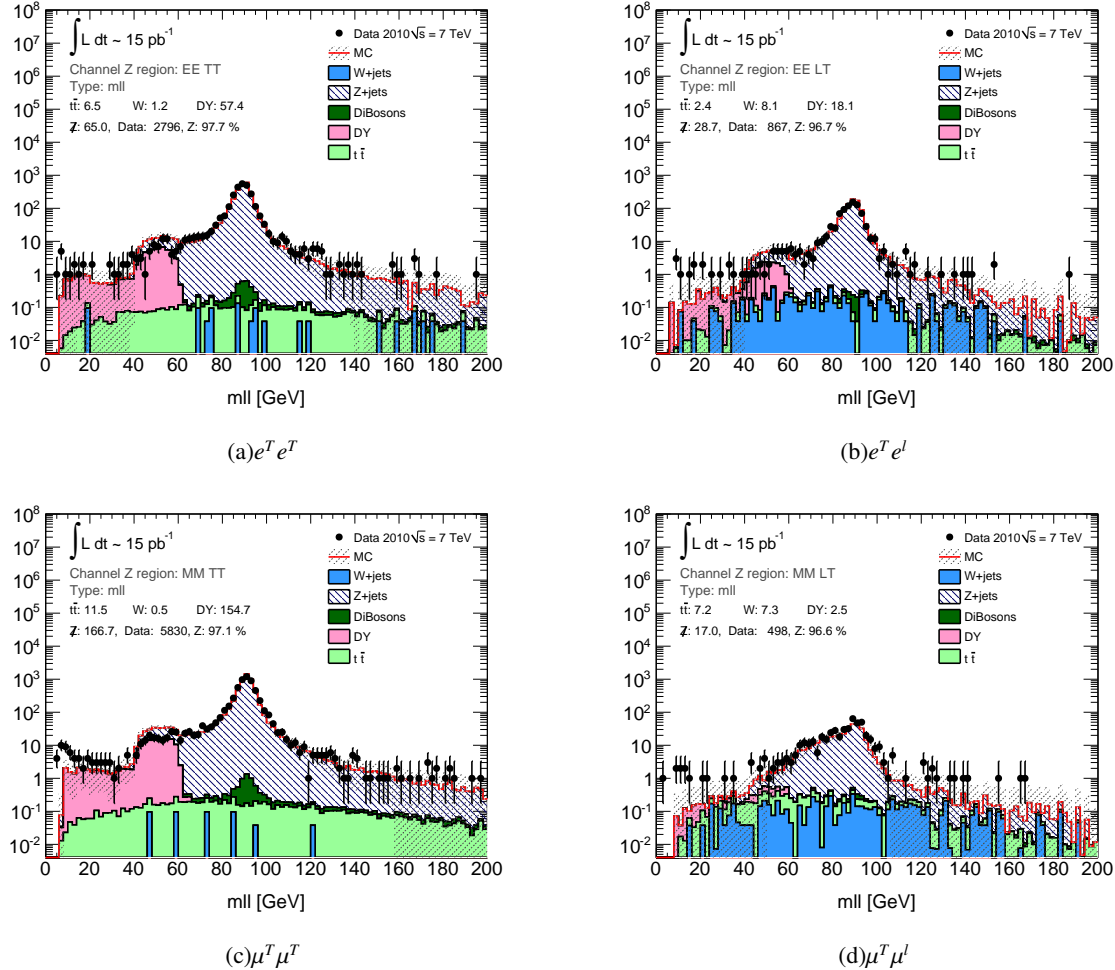


Figure 78: Invariant mass of opposite sign di-lepton pairs. Z region used for computing the efficiency is chosen in the Z mass peak within  $\Delta mll(2lep, Z) < 5\text{GeV}$ . Left column tight-tight pairs, right column tight-exclusive loose pairs. Top row shows the di-electron channel, bottom row the di-muon channel.  $Z$  is the sum of all SM MC events except Z and QCD. The ratio  $(\text{Data} - Z)/\text{Data}$ , is shown in percent.

### G.3 Validation plots for the same-sign QCD region

Figure 79 show the same-sign QCD Control region before applying any Z veto. In these distributions we have required  $N^{jets} \geq 1$  and  $E_T^{\text{miss}} < 20$  GeV. Except for the Z contribution stemming from misidentified charge, all electroweak SM processes are highly suppressed. Finally applying a Z veto removing events where  $\Delta m(2l, Z) < 10$  GeV, results in a sufficiently clean QCD control region.

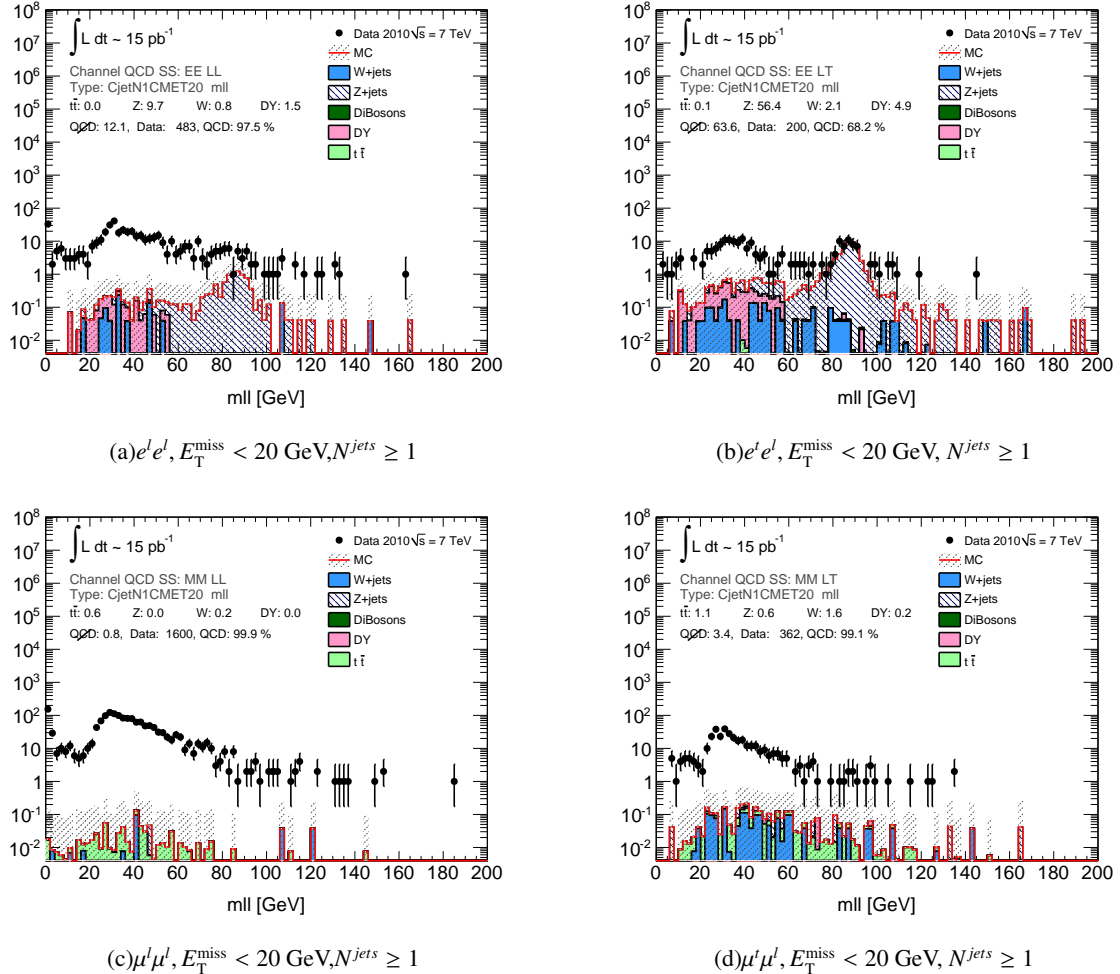


Figure 79: Invariant mass distribution of the 2 leptons defining the same-sign QCD Control region after requiring  $E_T^{\text{miss}} < 20$  GeV, and at least one jet. The final Z-veto removes Z contamination especially in the electron channel. Electron channel (top) and muon channel (bottom), exclusive loose-loose combination  $e^l e^l$  (left) and tight-exclusive loose combination (right). The integrated number of events,  $N_{ll}$  and  $N_{ll}$  are used to calculate fake-rates.  $QCD$  is the sum of all SM MC events except QCD. The ratio (Data -  $QCD$ )/Data, is shown in percent.

## G.4 Validation plots for the 1-lepton QCD region

The 1-lepton QCD control regions naturally has much higher event-statistics than the 2-lepton same-sign QCD control region. In the electron channel the Z contribution can be handled by vetoing the event if the selected lepton, together with any other lepton in the event, match the Z mass. Since we in this region require exactly 1 lepton, the second lepton has not passed loose object preselection. As mentioned above, the expected high W background is suppressed by a cut on  $\Delta\phi(\text{lep}, E_T^{\text{miss}})$ . A higher purity can be obtained in the muon channel by an additional  $M_T < 40 \text{ GeV}$  cut.

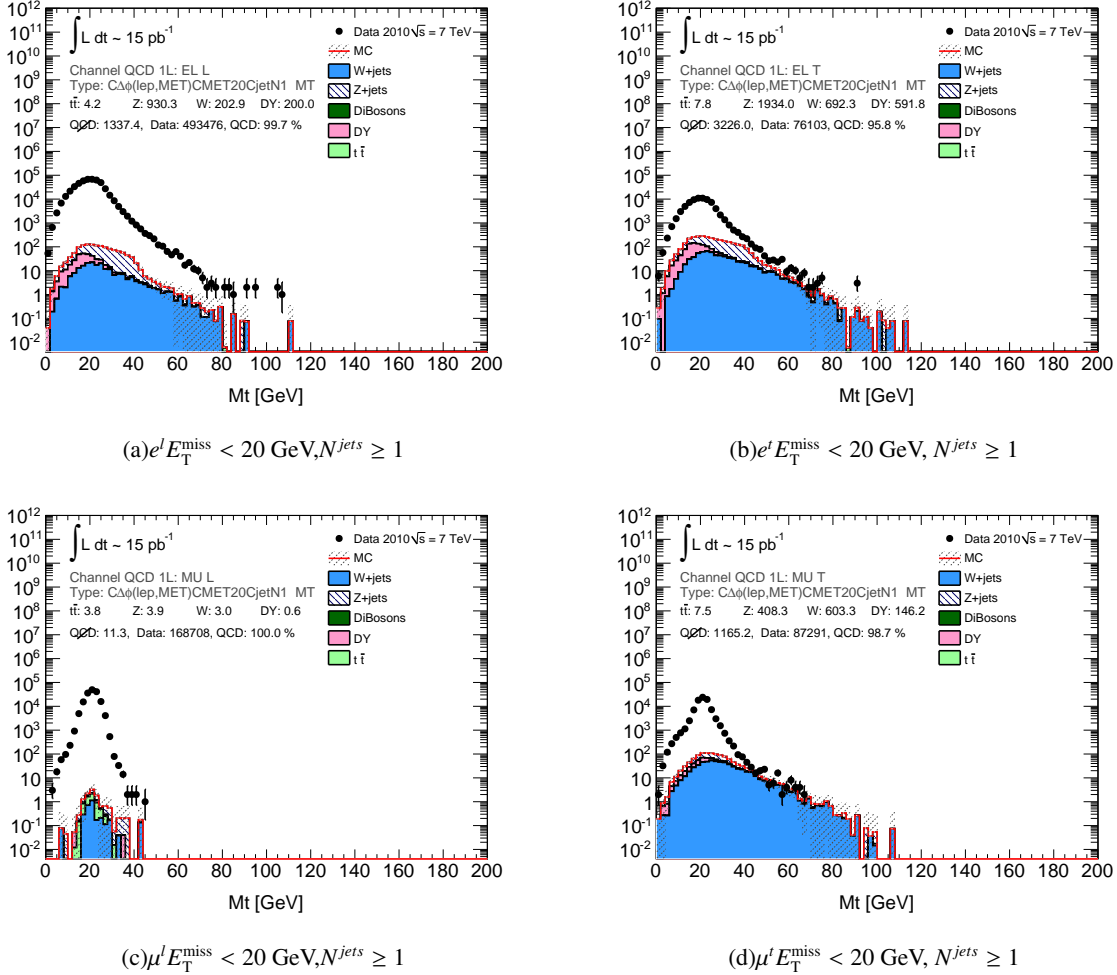


Figure 80: Transverse mass in the 1-lepton QCD Control region after requiring  $E_T^{\text{miss}} < 20 \text{ GeV}, N^{\text{jets}} > 1$  and  $\Delta\phi(\text{lep}, E_T^{\text{miss}}) < 0.5$ . Top row shows the electron channel and bottom row the muon channel. Exclusive loose leptons to the left, and tight leptons to the right.  $QCD$  is the sum of all SM MC events except QCD. The ratio  $(\text{Data} - QCD)/\text{Data}$ , is shown in percent.

## G.5 Efficiencies from the real and fake control regions

Table 45 shows fake-rates including event statistics and errors respectively, obtained from various definitions of the 1-lepton and the 2-lepton QCD control regions. We see that the fake-rate for electrons varies from about 16 % to as low as 4 %, and from 37% to slightly below 7% for muons.

There are at least two main considerations to take into account when applying the matrix method. These are the purity of the control samples, and the event topology and composition in the control samples compared to the signal region. In a fake control region (QCD control region) “contaminated” with a lot of real leptons from for instance W decays, the fake-rate extracted will be artificially high, and will not reflect a fake lepton’s probability to pass tight object requirements, which is what we aim to measure in this control region. In the real control region (Z region) the efficiency would be less if the region is not sufficiently pure, and again the efficiency would not reflect the probability of a real lepton to fail tight object preselection.

In the control regions we have chosen, the validation plots in sections including, and following section G.2 show that both our fake and real control regions are very well selected. This consideration is therefore sufficiently well taken care of.

The second consideration is if the event topology or composition in our control region is significantly different compared to our signal region. Since the fakes come from various sources like conversions and heavy and light flavour jets, and the fake-rate for each of the contributions will vary, it is important that we evaluate the fake-rate in a QCD control region that has similar mixture of these types compared to the signal region, and if not to, correct for this. The event topology, for instance number of jets, and the kinematic properties of the event could also affect the result.

The large difference we observe in fake-rate between the 1-lepton and the 2-lepton QCD control regions could to be explained by arguments like this. The fake-rate obtained from a 1-lepton QCD region is not necessarily compatible with the 2-lepton kinematics of the SUSY final state. A more detailed study is needed in order to apply the fake-rates from the 1 lepton QCD control region to the 2-lepton signal region. A way to correct for this possible effect could be to “balance” the one lepton with a hard jet. It is probably not surprising that when requiring in addition at least 2 jets, the 1-lepton fake-rates seem to agree with those obtained from the 2-lepton same-sign sample.

From the list of more or less refined control regions, we choose  $f_{12}$ , which is a compromise between statistics and a sufficiently QCD dominated region. A summary of the fake estimations by using fake-rates from several of the other regions, is documented in the final section.

## G.6 Efficiency and fake-rate for the selected same-sign QCD Control region versus $\eta$ , $p_T$ and $E_T^{\text{miss}}$

Figures 81 and 82 shows efficiency and fake-rate versus  $\eta$ ,  $p_T$  and  $E_T^{\text{miss}}$  for electrons and muons respectively. The fake-rates are calculated using the same-sign QCD control region  $f_{12}$ , with event requirements  $N^{jets} \geq 1$ . The  $\eta$  and  $p_T$  distributions have an additional  $E_T^{\text{miss}} < 20$  GeV cut. The largest dependency is on  $p_T$ , leading to an upward going fake-rate for harder leptons. In the figures some bins have a fake-rate or efficiency of exactly 1. This is due to the event containing, in the fake-rate case, a single loose-tight lepton pair, and in the efficiency, a single tight-tight pair. The weight of these points is however so small that they do not significantly contribute to the overall rates.

Table 45: Fake-rates and event statistics for 13 different QCD control regions, and the efficiency extracted from the Z control region. The 2 lepton region use equations 52 and 53 to convert the 2-lepton ratio to single lepton efficiency and fake-rate respectively.  $\Delta\phi_{lE_T}$  is a short-hand notation of  $\Delta\phi(lep, E_T^{\text{miss}})$ .  $\mathbb{Z}$  means that a Z veto is required, rejecting event if  $m(ll, Z) < 10$  GeV. In the 1 lepton case, the additional lepton is any other lepton in the event that did not pass the loose lepton object definition.

	Electrons	Muons	Cuts
1L	0.1313 (27649/210611) $\pm 0.0007$	0.3660 (20565/56181) $\pm 0.0020$	$f_1: E_T < 20$ GeV, $N_j \geq 1, \Delta\phi_{lE_T} < 0.5$
1L	0.1297 (29246/225570) $\pm 0.0007$	0.3442 (64662/187843) $\pm 0.0011$	$f_2: M_T < 30$ GeV, $N_j \geq 1, \Delta\phi_{lE_T} < 0.5$
1L	0.0312 (4017/128896) $\pm 0.0005$	0.1110 (7532/67880) $\pm 0.0012$	$f_3: M_T < 30$ GeV, $N_j \geq 2, \Delta\phi_{lE_T} < 0.5, \mathbb{Z}$
1L	0.1340 (44924/335195) $\pm 0.0006$	0.3497 (38726/110743) $\pm 0.0014$	$f_4: E_T < 20$ GeV, $N_j \geq 1, \Delta\phi_{lE_T} < 1.0, \mathbb{Z}$
1L	0.0920 (91063/990142) $\pm 0.0003$	0.1533 (103939/678023) $\pm 0.0004$	$f_5: E_T < 20$ GeV, $N_j \geq 1$
1L	0.1454 (13058/89780) $\pm 0.0012$	0.0503 (3374/67062) $\pm 0.0008$	$f_6: M_T < 60$ GeV, $\Delta\phi_{E_T,j} < 0.1$
2L	0.166(297/1787) $\pm 0.009$	0.137(807/5893) $\pm 0.004$	$f_7: \text{SS}$
2L	0.152(258/1694) $\pm 0.009$	0.111(614/5554) $\pm 0.004$	$f_8: N_j \geq 1$
2L	0.125(192/1534) $\pm 0.008$	0.109(593/5421) $\pm 0.004$	$f_9: \mathbb{Z}, N_j \geq 1$
2L	0.061(65/1073) $\pm 0.007$	0.067(296/4442) $\pm 0.004$	$f_{10}: \mathbb{Z}, N_j \geq 2$
2L	0.137(178/1298) $\pm 0.010$	0.150(596/3982) $\pm 0.006$	$f_{11}: \mathbb{Z}, E_T < 20$ GeV
2L	0.118(144/1222) $\pm 0.009$	0.113(414/3660) $\pm 0.005$	$f_{12}: \mathbb{Z}, E_T < 20$ GeV, $N_j \geq 1$
2L	0.040(34/846) $\pm 0.007$	0.067(201/2991) $\pm 0.005$	$f_{13}: \mathbb{Z}, E_T < 20$ GeV, $N_j \geq 2$
2L	0.876(3968/4532) $\pm 0.005$	0.973(8768/9008) $\pm 0.002$	$r_1: \Delta m(ll, Z) < 10$ GeV

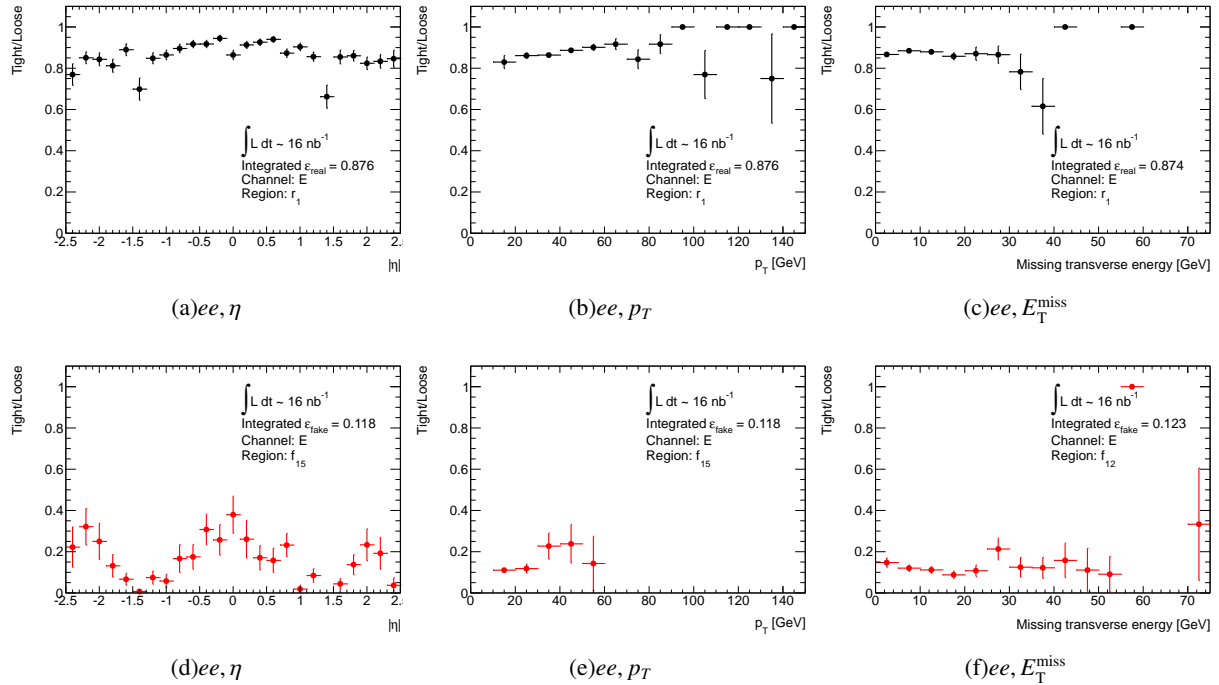


Figure 81: Electron channel real (top) and fake (bottom) efficiencies versus  $\eta$ ,  $p_T$  and  $E_T^{\text{miss}}$

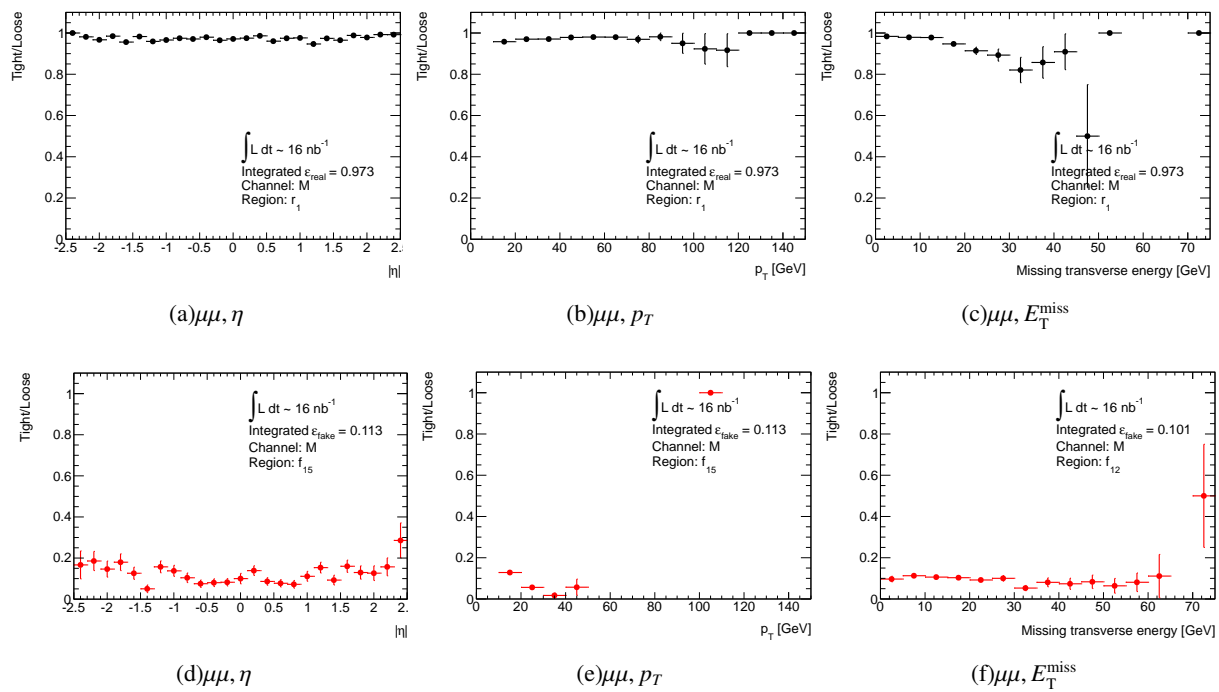


Figure 82: Muon channel efficiency (black) and fake-rate (red) versus  $\eta$ ,  $p_T$  and  $E_T^{\text{miss}}$

## G.7 Resulting fake estimation using constant efficiency and fake-rate

We apply the matrix method to our 2-lepton region defined as in section 6.3, which only includes events after full event cleaning, exactly two di-electrons or di-muons and  $m(l, l) > 5$  GeV. Extracting the fake-rate from the 2-lepton same-sign QCD Control region marked  $f_{12}$  and efficiency from table 45 gives for electrons,  $f_e = 11.8\%$ ,  $r_e = 87.6\%$  and for muons  $f_\mu = 11.3\%$ ,  $r_\mu = 97.3\%$ . Using these values together with the number of events with one pair of exclusive loose- exclusive loose  $N_{ll}$ , tight- exclusive loose  $N_{lT}$  and tight-tight  $N_{TT}$ , we calculate the number of estimated fake-fake  $N_{ff}$ , fake-real  $N_{fr}$  and real-real  $N_{rr}$  lepton pairs by matrix inversion. The exact same procedure is used for all the 4 channels: opposite sign electrons (OSee), opposite sign muon channel (OS $\mu\mu$ ), same-sign electron channel (SSee) and same-sign muon channel (SS $\mu\mu$ ). The fake contribution is taken as the combination of real-fake sources and fake-fake sources. Errors are purely statistical, and obtained by error propagation. By extracting the total number of events - two inclusive loose leptons  $N_{LL}$ , and introducing instead of the event counts, event ratios  $N_{ll}/N_{LL}$ ,  $N_{lT}/N_{LL}$  and  $N_{TT}/N_{LL}$  we can apply binomial errors on those numbers.

Results below use the full dataset from period A-I with an integrated luminosity of  $34 \text{ pb}^{-1}$ .

### Opposite sign channel

In the opposite sign electron channel we observe a total of 6282 tight-tight lepton pairs, where the estimated fake contribution amounts to  $35.5 \pm 9.9$ , as seen from figure 83 and corresponding table 46. After requiring  $E_T^{\text{miss}} > 100$  GeV, 3 events are observed, and  $1.4 \pm 0.6$  fake background events are estimated. In the opposite sign muon channel, 12857 events are observed. Estimated fake background events are  $38.1 \pm 6.6$ . At  $E_T^{\text{miss}} > 100$  GeV, 11 events are observed, with  $1.30 \pm 0.5$  estimated to originate from fake background sources.

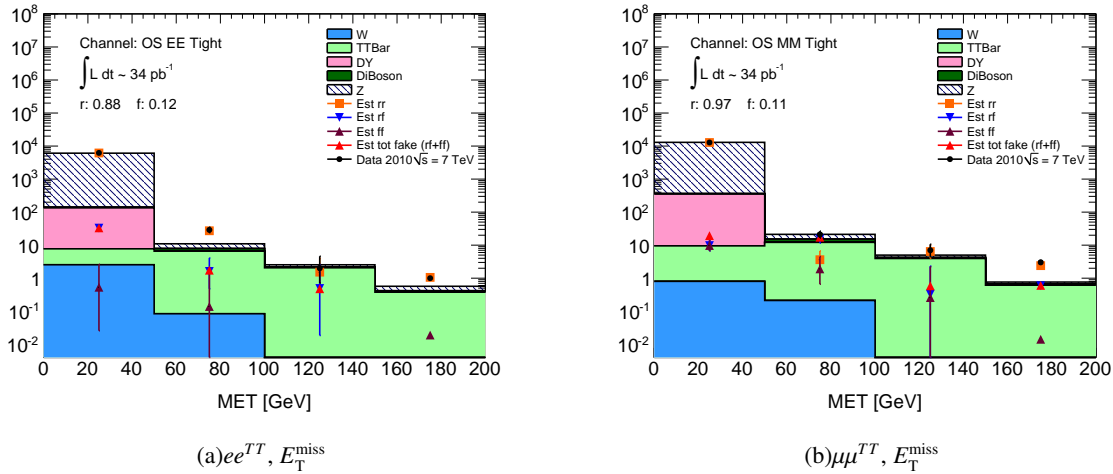


Figure 83: Opposite sign channel, electrons (left) and muons (right). Tight-tight lepton pairs from data and SM MC together with estimates for fake-fake  $ff$ , real-real  $rr$  and fake-real  $rf$ . The tight-tight MC QCD contribution is present, but vanishingly small compared to the other SM contributions, in both the electron and the muon channel. The MC QCD prediction is not shown.

Table 46: Results for the opposite sign electron (top) and muon channel (bottom). Number of events and the estimated numbers of real-real  $rr$ , real-fake  $rf$  and fake-fake  $ff$  lepton pairs, in bins of  $E_T^{\text{miss}}$

Bin [GeV]	Data	fakerate	eff	est(rr)	est(rf)	est(ff)	est(rf+ff)
0 - 50	6205	0.12	0.88	6171.7	32.8	0.5	$33.3 \pm 9.9$
50 - 100	29	0.12	0.88	27.3	1.6	0.1	$1.7 \pm 0.7$
100 - 150	2	0.12	0.88	1.5	0.5	-0.0	$0.5 \pm 0.2$
150 - 200	1	0.12	0.88	1.1	-0.1	0.0	$-0.1 \pm 0.2$
> 200	0	0.12	0.88	0.0	0.0	0.0	$0.0 \pm 0.0$
					Tot	$35.5 \pm 9.9$	
					Tot rf+ff with > 100 GeV	$1.4 \pm 0.6$	
Bin [GeV]	Data	fakerate	eff	est(rr)	est(rf)	est(ff)	est(rf+ff)
0 - 50	12825	0.11	0.97	12805.6	9.7	9.7	$19.4 \pm 6.4$
50 - 100	21	0.11	0.97	3.6	15.5	1.9	$17.4 \pm 1.2$
100 - 150	7	0.11	0.97	6.4	0.3	0.3	$0.6 \pm 0.4$
150 - 200	3	0.11	0.97	2.4	0.6	0.0	$0.6 \pm 0.2$
> 200	1	0.11	0.97	0.9	0.1	0.0	$0.1 \pm 0.2$
					Tot	$38.1 \pm 6.6$	
					Tot rf+ff with > 100 GeV	$1.3 \pm 0.5$	

### Same sign channel

The results for the same-sign channels are shown in figure 84 and corresponding table 47. We observe 62 tight-tight lepton pairs in the same-sign electron channel. Of these  $15.6 \pm 1.3$  are estimated to origin from fake background. No events in the signal region  $E_T^{\text{miss}} > 100$  GeV are observed and estimation of fake contribution amounts to  $1.6 \pm 0.6$  events. In the muon channel 3 events are observed in the whole  $E_T^{\text{miss}}$  region, and  $-0.4 \pm 2.1$  events are estimated. No events are observed in the signal region, while  $1.9 \pm 0.6$  fake background events are estimated. All errors quoted up to now, are purely statistical.

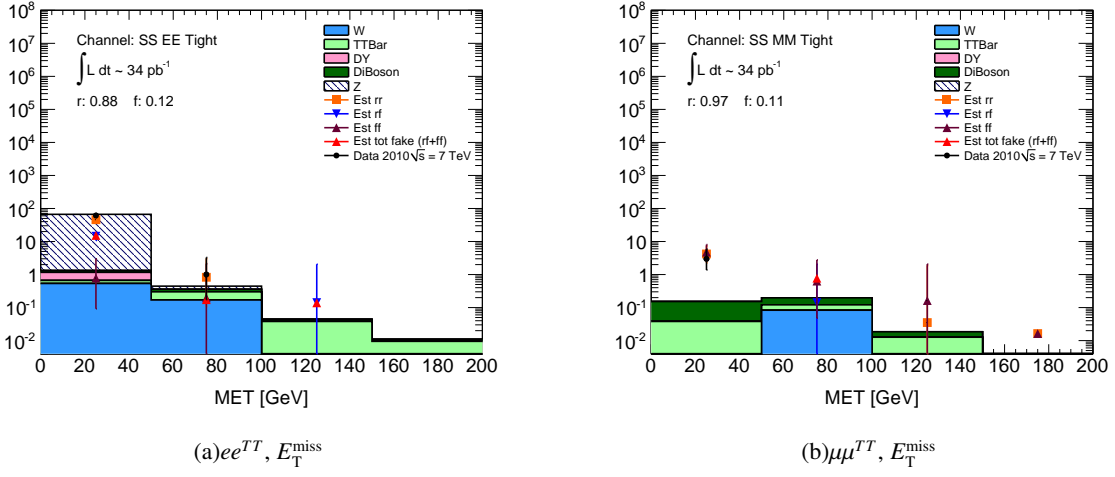


Figure 84: Opposite sign channel, electrons (left) and muons (right). Tight-tight lepton pairs from data and SM MC together with estimates for fake-fake  $ff$ , real-real  $rr$  and fake-real  $rf$ . The tight-tight MC QCD contribution is present, but vanishingly small compared to other SM processes in the electron channel. The MC QCD prediction is not shown.

Table 47: Results for the same sign electron (top) and muon channel (bottom). Number of events and the estimated numbers of real-real  $rr$ , real-fake  $rf$  and fake-fake  $ff$  lepton pairs, in bins of  $E_T^{\text{miss}}$

Bin [GeV]	Data	fakerate	eff	est(rr)	est(rf)	est(ff)	est(rf+ff)
0 - 50	61	0.12	0.88	45.7	14.5	0.8	$15.3 \pm 1.2$
50 - 100	1	0.12	0.88	0.8	-0.0	0.2	$0.2 \pm 0.4$
100 - 150	0	0.12	0.88	-0.1	0.1	-0.0	$0.1 \pm 0.1$
150 - 200	0	0.12	0.88	0.0	0.0	0.0	$0.0 \pm 0.0$
> 200	0	0.12	0.88	0.0	0.0	0.0	$0.0 \pm 0.0$
						Tot	$15.6 \pm 1.3$
						Tot rf+ff with > 100 GeV	$1.6 \pm 0.6$

Bin [GeV]	Data	fakerate	eff	est(rr)	est(rf)	est(ff)	est(rf+ff)
0 - 50	3	0.11	0.97	4.2	-6.0	4.8	$-1.2 \pm 2.0$
50 - 100	0	0.11	0.97	-0.8	0.1	0.6	$0.8 \pm 0.7$
100 - 150	0	0.11	0.97	0.0	-0.2	0.2	$-0.0 \pm 0.4$
150 - 200	0	0.11	0.97	0.0	-0.0	0.0	$-0.0 \pm 0.1$
> 200	0	0.11	0.97	-0.1	0.1	0.0	$0.1 \pm 0.1$
						Tot	$-0.4 \pm 2.1$
						Tot rf+ff with > 100 GeV	$1.9 \pm 0.6$

### G.7.1 Fake background estimations varying the fake-rate

Using the minimal and maximal fake-rate as calculated from the 2-lepton same-sign QCD control region, we can evaluate the effect on the systematic uncertainty from this fake-rate.

Table 48: Estimated number of fake events in the opposite sign (left) and same sign (right) electron (top) and muon (bottom) channel, when using low to high fake-rates obtained from three different same-sign lepton QCD control regions. Electron and muon efficiency is 87.6% and 97.3% respectively.

Fakerate	Opposite sign		Fakerate	Same sign	
	Tot fake	> 100 GeV fake		Tot fake	> 100 GeV fake
Electrons					
0.04	$11.1 \pm 3.0$	$0.5 \pm 0.2$	0.04	$5.0 \pm 0.4$	$0.6 \pm 0.2$
0.12	$35.5 \pm 9.9$	$1.4 \pm 0.6$	0.12	$15.6 \pm 1.3$	$1.6 \pm 0.6$
0.17	$52.8 \pm 15.2$	$1.9 \pm 1.0$	0.17	$22.7 \pm 2.0$	$2.1 \pm 1.0$
Muons					
0.07	$24.4 \pm 3.6$	$0.8 \pm 0.2$	0.07	$1.2 \pm 0.9$	$1.2 \pm 0.3$
0.11	$38.1 \pm 6.6$	$1.3 \pm 0.5$	0.11	$-0.4 \pm 2.1$	$1.9 \pm 0.6$
0.14	$43.8 \pm 8.5$	$1.5 \pm 0.7$	0.14	$-2.2 \pm 3.0$	$2.3 \pm 0.9$

It must be noted that the total number of observed events does not completely correspond to the numbers quoted in cutflows from section 6.3. This is due to a necessary manipulation of the events in order to separate the tight and loose leptons. In the electron channel we observe 13 tight-tight events less than the quoted 6250 opposite sign electron pairs. In the muon channel we observe a surplus of 85 events compared to the quoted 12772 opposite sign muon pairs. This difference does however not affect the relative fake background estimation.

A rough evaluation of the systematics based on table 48 for the opposite and same-sign channels can be done by subtracting the lowest estimation from the highest estimations in the two channels, and dividing the resulting difference by two. In the opposite-sign channels, we arrive to a systematic uncertainty of  $\pm 0.7$  in the electron and 0.4 in the muon channel. In the same-sign electron channel the systematic uncertainty is evaluated to be  $\pm 0.8$ , while the muon channel gives a systematic uncertainty of  $\pm 0.6$ . The predicted fake estimation is therefore, including statistical and systematic errors:  $1.4 \pm 0.9$  in the opposite sign electron channel,  $1.3 \pm 0.6$  in the opposite sign muon channel,  $1.6 \pm 1.0$  in the same-sign electron channel and  $1.9 \pm 0.8$  in the same-sign muon channel, when taking the errors in quadrature. These estimates are slightly higher than those quoted in section 7.3, but compatible within 2 sigma.

	Z-veto tagger			Contransverse mass tagger		
	$60 < E_T^{\text{miss}} < 80$ GeV	$60 < E_T^{\text{miss}} < 80$ GeV		$E_T^{\text{miss}} > 100$ GeV	$E_T^{\text{miss}} > 150$ GeV	
control region		A1	A2	A3	A3	
Process	$ee$	$\mu\mu$	$e\mu$	<b>total</b>	<b>total</b>	$e\mu$
data	1	5	13	<b>19</b>	<b>15</b>	<b>10</b>
$t\bar{t}$	3.7	6.1	10.7	<b>20.5</b>	<b>18.8</b>	<b>8.2</b>
single top	0.4	0.7	0.9	<b>1.9</b>	<b>0.8</b>	<b>0.3</b>
Z/ $\gamma$ +jets	0.3	1.4	0.2	<b>2.0</b>	<b>1.1</b>	<b>0.2</b>
fakes	0.1	0.1	0.4	<b>0.6</b>	<b>0.2</b>	<b>-0.1</b>
Diboson	0.6	1.4	1.9	<b>4.0</b>	<b>0.4</b>	<b>0.1</b>
Total non $t\bar{t}$	1.4	3.7	3.4	<b>8.5</b>	<b>2.5</b>	<b>0.5</b>
SU4	0.5	1.0	1.2	<b>2.6</b>	<b>2.1</b>	<b>4.5</b>
						2.49

Table 49: Observed event counts and expected sample composition of the three alternative control regions for  $34.3 \text{ pb}^{-1}$ . The contamination by events from supersymmetry production for the SU4 model is also shown.

## H Alternative top background estimates

### H.1 Signal to control region ratio with alternative control regions

The top background estimate method described in Section 7.6 relies on the data observed in an appropriate control region for the  $t\bar{t}$  background estimate, while the MonteCarlo is relied up for extrapolation to the opposite sign signal regions.

Three different choices for the control region have been considered:

- *Method A1*: Events with  $60 < E_T^{\text{miss}} < 80$  GeV and with the invariant mass of the two leptons outside the Z mass windows, if the leptons have the same flavour.
- *Method A2*: Events with  $60 < E_T^{\text{miss}} < 80$  GeV and with a cotransverse mass tag<sup>5</sup>.
- *Method A3*: Events in the  $e\mu$  channel, with  $E_T^{\text{miss}} > 100$  GeV or  $E_T^{\text{miss}} > 150$  GeV and with a cotransverse mass tag.

The A2 control region has been found to give the most precise estimate and has been thus used as baseline. In this section, we report the results obtained with the other two control regions and compare them with the baseline estimate, which has been described in Section 7.6.

#### CLOSURE TEST AND BACKGROUND PREDICTION

The expected composition of the control regions is reported in Table 49. The  $t\bar{t}$ , single top, and double boson rates have been obtained by MonteCarlo, while the the Z has been normalised to data in the same flavour channels as described in Section 7.2 and the fakes have been estimated from data as described in Section 7.7. The number of observed data is also reported. The last line shows the contamination by supersymmetry events as obtained for the SUSY model SU4.

The effect of the signal contamination on the  $t\bar{t}$  prediction is shown in Table 23,

To test the validity of the methods, they are applied on Monte Carlo, with and without SUSY contamination and the predicted number of  $t\bar{t}$  events in a signal region with  $E_T^{\text{miss}} > 100$  GeV is compared to its true number as directly predicted by the Monte Carlo and cross sections. The corresponding results

---

<sup>5</sup>See Section 7.6 for a description of the cotransverse mass top tagger algorithm

$N_{t\bar{t}}$	True	No signal	MSSM27	SU4
Contransverse mass tagger, $60 < E_T^{\text{miss}} < 80$ GeV	20.5	$20.5 \pm 6.6$	$23.0 \pm 7.4$	$23.4 \pm 7.5$
Z-veto, $60 < E_T^{\text{miss}} < 80$ GeV	20.5	$20.5 \pm 7.2$	$24.0 \pm 8.5$	$23.0 \pm 8.1$
Cotransverse mass tagger, $E_T^{\text{miss}} > 100$ GeV	20.5	$20.5 \pm 7.6$	$24.8 \pm 9.2$	$32.1 \pm 11.8$
$N_{t\bar{t}} + N_{SUSY}$ in Signal Region		20.5	47.3	33.6

Table 50: True (2nd column) and predicted number of  $t\bar{t}$  events for  $E_T^{\text{miss}} > 100$  GeV using the Z-veto and contransverse mass tagger control regions in the following cases: no SUSY signal (3rd column), supersymmetry is present (MSSM27)(4th column) and supersymmetry is present (SU4) (last column). The last row gives the sum of the predicted number of  $t\bar{t}$  events using method A, and the predicted number of SUSY events. Event yields are predictions for an integrated luminosity of  $34.3 \text{ pb}^{-1}$ .

are shown in Table 50, where the effect of the SUSY contamination has been estimated in the presence of the SUSY models MSSM27 and SU4. It appears that in presence of MSSM27 or SU4, the background predicted by methods A1 and A2 are slightly overestimated by 10-15%. This has the disadvantage of reducing the significance for signal discovery. The effect is however rather modest compared to method A3, which would not be sensitive to an SU4-like signal at all.

#### SYSTEMATIC UNCERTAINTIES

The effect of systematic uncertainty has been evaluated as described in Section 7.6 and are reported in Table 51 for a signal region with  $E_T^{\text{miss}} > 100$  GeV and in Table 52 for a signal region with  $E_T^{\text{miss}} > 150$  GeV.

For method A3, tagged  $e\mu$  events are used to normalize the top estimated to data and thus excluded from the signal region; this introduce an important difference between the systematic of the MonteCarlo extrapolation factor for same flavour and opposite flavour channels. In the former case, the extrapolation factor is proportional to the inverse of the top tagger efficiency  $1/\epsilon_{\text{tag}}$  while in the latter it is proportional to  $(1-\epsilon_{\text{tag}})/\epsilon_{\text{tag}}$ . Since the value of  $\epsilon_{\text{tag}}$  is larger than 80% the opposite flavour estimate is about 5 times more sensitive to uncertainties on the tagger efficiency. The statistics of the Monte Carlo samples is also an important limitation in evaluating the tagger efficiency. Since the high statistics baseline top MC samples shows that the dependence of the tagging efficiency on  $E_T^{\text{miss}}$  is within 5%, we evaluate the systematics on the tagging efficiency using a looser selection on  $E_T^{\text{miss}}$  and add a 5% uncertainty on the assumption that the tagging efficiency would be the same in the signal region.

#### RESULTS

The predictions of the top background in the signal region is reported in Table53. for the three variants of method A described here, as well as for the method B described in the next section.

#### DISCUSSION OF THE RESULTS

The A1 and A2 methods control regions are largely overlapping, so not surprisingly these two methods give a similar estimate for the top background in the signal region. The expected precision of A2 is slightly better, mostly because of the more effective suppression of the non-top processes by the cotransverse mass tagger. The A3 method has a comparable precision for a cut of  $E_T^{\text{miss}} > 100$  GeV for the signal region, but for the tighter selection  $E_T^{\text{miss}} > 150$  GeV it runs out of statistics in the control region (only 1.4 top events are expected). As a result, we use the prediction of the method A2 for the estimation of the top background.

Top estimate method	A1	A2	A3, SF	A3, OF
Generator	6%	7%	3%	19%
ISR/FSR	6%	9%	2%	10%
Parton shower	1%	2%	2%	10%
Jet energy scale and resolution	16%	15%	2%	11%
tagger eff. dependence on $E_T^{\text{miss}}$	-	-	5%	5%
Control region statistics (exp.)	26%	24%	36%	36%
Control region statistics (obs.)	41%	33%	33%	33%
Control region backgrounds (exp.)	15%	8%	6%	6%
Control region backgrounds (obs.)	29%	12%	5%	5%
Total (expected)	35%	32%	37%	47%
Total (observed)	54%	40%	34%	42%

Table 51: The relative systematic uncertainties on the predicted number of  $t\bar{t}$  events in the signal region as predicted by the signal-to-control region ratio method using the Z-veto and contranverse mass taggers, for a signal region with  $E_T^{\text{miss}} > 100 \text{ GeV}$ . The A3 method systematics are different for same flavour (SF) and opposite flavour (OF) channels.

Top estimate method	A1	A2	A3,SF	A3,OF
Generator	4%	3%	3%	19%
ISR/FSR	8%	23%	2%	10%
Parton shower	1%	2%	2%	10%
Jet energy scale and resolution	26%	23%	2%	11%
tagger eff. dependence on $E_T^{\text{miss}}$	-	-	5%	5%
Control region statistics (exp.)	26%	24%	83%	83%
Control region statistics (obs.)	41%	33%	69%	69%
Control region backgrounds (exp.)	15%	8%	9%	9%
Control region backgrounds (obs.)	29%	12%	7%	7%
Total (expected)	41%	41%	84%	98%
Total (observed)	57%	44%	70%	78%

Table 52: The relative systematic uncertainties on the predicted number of  $t\bar{t}$  events in the signal region as predicted by the signal-to-control region ratio method using the Z-veto and contranverse mass taggers, for a signal region with  $E_T^{\text{miss}} > 150 \text{ GeV}$ . The A3 method systematics are different for same flavour (SF) and opposite flavour (OF) channels.

method	A1	A2	A3	B
$ee$	$1.91 \pm 1.42$	$2.50^{+1.03}_{-0.96}$	$4.32 \pm 1.47$	$6.7 \pm 3.5$
$\mu\mu$	$3.59 \pm 2.68$	$4.71^{+1.87}_{-1.80}$	$8.11 \pm 2.76$	$7.1 \pm 4.1$
$e\mu$	$5.03 \pm 3.76$	$6.61^{+2.72}_{-2.52}$	$11.38 \pm 3.88$	$10.1 \pm 5.3$
total	$10.5 \pm 7.8$	$13.8^{+5.62}_{-5.28}$	$23.8 \pm 8.0$	$23.9 \pm 9.0$
MC expectation	$20.5 \pm 4.8$	$20.5 \pm 4.8$	$20.5 \pm 4.8$	$20.5 \pm 4.8$

Table 53: The predicted number of  $t\bar{t}$  events in the signal region with  $E_T^{\text{miss}} > 100 \text{ GeV}$  is reported for the three variants of the method A as well as for the method described in Appendix H.2 The MonteCarlo expectation is also reported for comparison.

## H.2 Matrix method using the kinematic top tagger

In this section we present an alternative data-driven technique designed to estimate the  $t\bar{t}$  background in the signal region. This estimate has systematics and assumptions which are orthogonal to those of the method presented in Section 7.6. Thus the different methods complement each other and allow to reach a solid understanding of the  $t\bar{t} \rightarrow \ell\ell$  background.

### KINEMATIC TAGGER

The kinematic tagger uses the prior knowledge of the top quark and  $W$  boson masses. For a  $t\bar{t}$  event decaying as follows:  $t\bar{t} \rightarrow (W^+ b)(W^- \bar{b}) \rightarrow (\ell^+ \nu_\ell b) (\ell^- \bar{\nu}_\ell \bar{b})$  we can write the following kinematic constraints:

$$\begin{aligned} (p_\nu + p_{\ell^+})^2 &= m_W^2 \\ (p_{\bar{\nu}} + p_{\ell^-})^2 &= m_W^2 \\ (p_\nu + p_{\ell^+} + p_b)^2 &= m_t^2 \\ (p_{\bar{\nu}} + p_{\ell^-} + p_{\bar{b}})^2 &= m_t^2 \\ p_{\nu_x} + p_{\bar{\nu}_x} &= E_{T,x}^{\text{miss}} \\ p_{\nu_y} + p_{\bar{\nu}_y} &= E_{T,x}^{\text{miss}} \end{aligned} \tag{55}$$

If an event has exactly two jets  $j_1, j_2$  with  $p_T > 20$  GeV, then there are two ways to associate the jets and leptons to the top and anti-top quark:  $t\bar{t} \rightarrow (\ell^+ j_1)(\ell^- j_2)$  and  $t\bar{t} \rightarrow (\ell^+ j_1)(\ell^- j_2)$ . If there are three or more jets with  $p_T > 20$  GeV, the 3 leading jets are considered and 6 permutations are built. For each permutation one attempts to solve the equation system above. If there is at least one permutation with at least one solution, the event is considered as top-tagged.

### DESCRIPTION

This method estimates the  $t\bar{t}$  background by studying directly within the signal region the rate at which the data passes the kinematic top-tagger. If the probability for a  $t\bar{t}$  event ( $\epsilon_{tt}$ ) and a supersymmetry event ( $\epsilon_{SUSY}$ ) to be top-tagged are approximately known, the number of events in the signal region  $N_{SR}$  and the number of events with a kinematic tag in the signal region  $N_{SR}^{\text{tag}}$  can be combined to derive the number of  $t\bar{t}$  background events. More precisely one can write:

$$\begin{aligned} (N)_{SR} &= (N_{tt})_{SR} &+ (N_{SUSY})_{SR} &+ (N_{\text{non-}t\bar{t}})_{SR} \\ (N^{\text{tag}})_{SR} &= \epsilon_{tt}(N_{tt})_{SR} &+ \epsilon_{SUSY}(N_{SUSY})_{SR} &+ \epsilon_{\text{non-}t\bar{t}}(N_{\text{non-}t\bar{t}})_{SR} \end{aligned} \tag{56}$$

where  $\epsilon_{tt}$ ,  $\epsilon_{\text{non-}t\bar{t}}$  and  $\epsilon_{SUSY}$  are the efficiency of the top tagger for  $t\bar{t}$ , non- $t\bar{t}$  and SUSY events in the signal region. The number of events  $(N_{tt})_{SR}$ ,  $(N_{\text{non-}t\bar{t}})_{SR}$  and  $(N_{SUSY})_{SR}$  are the number of events in the signal region for  $t\bar{t}$ , non- $t\bar{t}$  and SUSY.

The contribution from non- $t\bar{t}$  events can be dealt with in two ways. The number of non- $t\bar{t}$  background events in the signal region can be estimated from Monte Carlo or dedicated data driven techniques and subtracted from  $(N)_{SR}$  and  $(N^{\text{tag}})_{SR}$ . Since the non- $t\bar{t}$  backgrounds represents only 10% of the signal region, even a very large systematic uncertainty on  $(N_{\text{non-}t\bar{t}})_{SR}$  and  $\epsilon_{\text{non-}t\bar{t}}$  will give little effect on the final result. The second option arises from the observation that  $\epsilon_{\text{non-}t\bar{t}}$  for various SM processes fall well within

the range of possible values for  $\epsilon_{SUSY}$ . In this situation one can make the assumption  $\epsilon_{non-tt} = \epsilon_{SUSY}$ , which simplifies the above system of equation to:

$$\begin{aligned}(N)_{SR} &= (N_{tt})_{SR} + (N_{SUSY,non-tt})_{SR} \\ (N^{tag})_{SR} &= \epsilon_{tt}(N_{tt})_{SR} + \epsilon_{SUSY}(N_{SUSY,non-tt})_{SR}\end{aligned}\quad (57)$$

where  $(N_{SUSY,non-tt})_{SR}$  is equal to  $(N_{non-tt})_{SR} + (N_{SUSY})_{SR}$ . The validity of  $\epsilon_{non-tt} = \epsilon_{SUSY}$  will be discussed further below. It is the approach that is chosen for this analysis.

When this technique is applied to the analysis, the number of events in the signal region  $(N)_{SR}$  and the number of top-tagged events in the signal region  $(N^{tag})_{SR}$  are directly counted from the data. Together with an approximate knowledge of the efficiencies  $\epsilon_{tt}$  and  $\epsilon_{SUSY}$  the above equations system can be solved and the number of  $t\bar{t}$  events in the signal region can be estimated. This method relies on the simulation to derive the efficiencies  $\epsilon_{tt}$  and  $\epsilon_{SUSY}$  and various systematic uncertainties are investigated. An additional complication arises from the fact that  $\epsilon_{SUSY}$  depends on the SUSY model that might be present in the signal region. The study of  $\epsilon_{SUSY}$  is studied in detail below over several grids of SUSY models. Finally one should note that this matrix method with the kinematic top tagger can only be applied on events with at least 2 or more jets. The signal region used in this analysis comprises events of all jet multiplicities, including those with zero or one jet, while the top kinematic tagger can only be applied in events with at least two jets.

For this reason the  $t\bar{t}$  contribution is first estimated in events with 2 or more jets, and then extrapolated to all jet multiplicities. This extrapolation is described in the subsection “Ratio of  $N_{t\bar{t}}$  in 2 more jets sample and all jet multiplicities”. All numbers up to that section refer to events with at least two jets. The closure test and application to data incorporate the extrapolation to the full signal region.

Finally one should note that for SUSY models where  $\epsilon_{SUSY}$  has a value very close to that of  $\epsilon_{tt}$ , the system of equation above becomes degenerate, and this method cannot be applied. In practice, for such models, the uncertainty on the data driven  $t\bar{t}$  estimate becomes very large, thus removing any sensitivity.

#### MODEL DEPENDENCE OF THE TAGGER EFFICIENCY FOR SUSY EVENTS

The efficiency for the kinematic top-tagger is estimated for each point of four different SUSY model grids. Depending on the exact SUSY particle mass hierarchy, some SUSY models can look more top-like than others. Therefore the exact value of  $\epsilon_{SUSY}$  is model dependent and can in some cases become indistinguishable from  $t\bar{t}$  production. To estimate the range of validity of the matrix method with kinematic top tagger  $\epsilon_{SUSY}$  is studied on four different SUSY model grids. The grids and their motivations are described in Sec. 1.

The model grids that have been investigated are the MSSM22, MSSM27, MSSM29, an mSUGRA grid with  $\tan\beta = 3$ ,  $A_0 = 0$ ,  $sgn(\mu) = +$  and varying  $M_0$ ,  $M_{1/2}$ , the MSSM “PhenoGrid 2” and “PhenoGrid 3”. Table 54 summarizes the observed variations of  $\epsilon_{SUSY}$  for the four model grids. In the case of the Pheno Grid 2 and Pheno Grid 3, the value of  $\epsilon_{SUSY}$  is well bound between 0 and 0.4 and can be approximated by a single number in the middle of the range and with an uncertainty covering the whole range of observed  $\epsilon_{SUSY}$  values. This is referred to as the “range of  $\epsilon_{SUSY}$ ” and is given in the last column of Table 54. The value of  $\epsilon_{SUSY}$  computed on the Pheno Grid 2 and 3 is shown in Fig. 85 in the plane  $M_{\tilde{l}} - M_{\chi_1^0}$ ,  $M_{\chi_2^0} - M_{\chi_1^0}$ . Only the highest value taken by  $\epsilon_{SUSY}$  is shown in each mass bin (if there are more than one model entering that bin).

The MSSM lepton grid has a somewhat larger observed range for  $\epsilon_{SUSY}$ . One should nevertheless note that the points in the MSSM lepton grid with  $\epsilon_{SUSY} > 0.4$  have all very small cross section times dilepton branching ratio and are well beyond the experimental reach of the present analysis.

The value of  $\epsilon_{SUSY}$  over the SUGRA parameter space is studied in the plane  $M_0$ ,  $M_{1/2}$ . The result is shown in Fig. 86 and illustrates that there are two characteristic regions with high values of  $\epsilon_{SUSY}$ .

Model Grid	Minimum $\epsilon_{SUSY}$	Maximum $\epsilon_{SUSY}$	Range of $\epsilon_{SUSY}$
Pheno Grid 2	0.01±0.01	0.40±0.04	0.20±0.20
Pheno Grid 3	0.01±0.01	0.35±0.05	0.18±0.17
MSSM lepton grid	0.0 ±0.3	0.53±0.10	0.26±0.26
mSUGRA grid $\tan\beta = 3$	0.0 ±0.1	0.68±0.15	N/A

Table 54: Observed ranges of  $\epsilon_{SUSY}$  on four SUSY model grids. For all SUSY grids except SUGRA one builds an interval containing all observed values, the corresponding intervals are given in the last column under Range of  $\epsilon_{SUSY}$ .

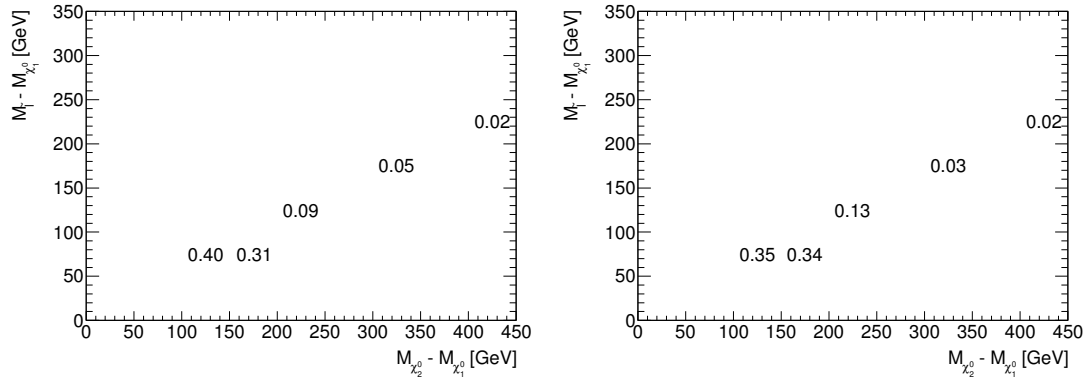


Figure 85: The efficiency of the kinematic top tagger  $\epsilon_{SUSY}$  in the plane  $M_{\tilde{t}} - M_{\chi_1^0}$ ,  $M_{\chi_2^0} - M_{\chi_1^0}$ , for the PhenoGrid 2 (left) and the PhenoGrid 3 (right). In the case of several models entering the same mass bin, only the highest observed value of  $\epsilon_{SUSY}$  is shown.

First in the region around  $(M_0, M_{1/2}) \sim (300, 120)$  GeV and secondly for models with  $M_{1/2} \sim 100$  GeV at all values of  $M_0 > 250$  GeV. One should note that most of these regions have been excluded by earlier experiments [27, 28]. The approach chosen for limit setting over the SUGRA parameter space is to consider for each SUGRA point the  $\epsilon_{SUSY}$  of that particular SUGRA point and derive the corresponding number of  $t\bar{t}$  background events and its associated uncertainty. In the case of SUSY points where SUSY is top-like, i.e.  $\epsilon_{SUSY} \sim \epsilon_{tt}$ , the uncertainty on the data-driven  $t\bar{t}$  background becomes very large and one is unable to test that particular SUSY model. It is relatively natural that a data driven method designed to derive the  $t\bar{t}$  background from data breaks down in the case of a signal with the same characteristics. In the ‘‘Closure Test’’ Section below, a closure test is performed for each model of the SUGRA model grid.

#### OTHER SYSTEMATIC UNCERTAINTIES ON THE TAGGER EFFICIENCY FOR SUSY EVENTS

In addition to the model dependence, the efficiency of the kinematic top tagger is affected to other sources of systematic errors such as the jet energy scale, the jet energy resolution, the mean number of minimum bias collisions per bunch crossing and the generator used to produce the events.

The effect of these uncertainties is estimated using the SUSY mSUGRA model SU4. The resulting relative systematic uncertainties on  $\epsilon_{SUSY}$  are listed in Table 55. The generator uncertainty is derived by comparing  $\epsilon_{SUSY}$  obtained with HERWIG + JIMMY and HERWIG++. The effect of pile up is studied by comparing  $\epsilon_{SUSY}$  obtained on samples generated i) without pileup, ii) with a mean pileup of 2 and iii) with a mean pileup of 5. The systematic labelled as ‘‘more pileup’’ and ‘‘less pileup’’ in Table 55 are obtained by using the sample with mean pile up of two as the reference. The pile up is considered here as a source of systematic uncertainty (while it is not in the case of  $t\bar{t}$ ) because the SUSY grid samples are only available without pile up simulation. The jet energy scale and jet energy resolutions are derived in

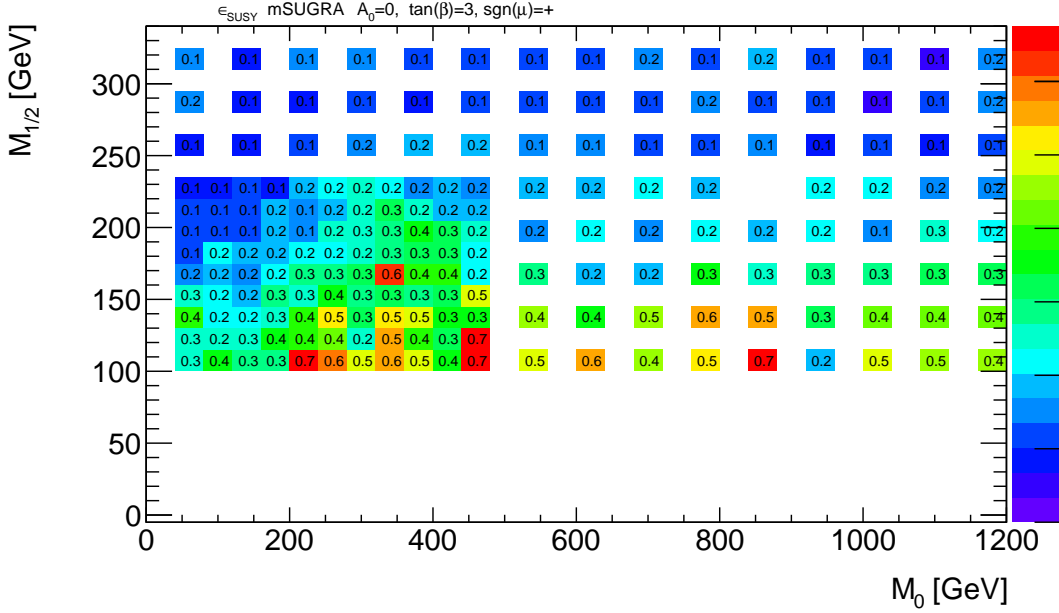


Figure 86: The efficiency of the kinematic top tagger  $\epsilon_{SUSY}$  in the SUGRA plane  $M_0, M_{1/2}$ . In the case of several models entering the same mass bin, only the highest observed value of  $\epsilon_{SUSY}$  is shown.

Source of uncertainty	Relative effect on $\epsilon_{SUSY}$
Generator	15%
Jet energy scale $+1\sigma$	-13%
Jet energy scale $-1\sigma$	+13%
More pile up	-6%
Less pile up	+3%
Jet energy resolution	11%

Table 55: Relative systematic uncertainties on  $\epsilon_{SUSY}$ .

the same way as described in the previous sections. The size of the systematic uncertainties on  $\epsilon_{SUSY}$  are relatively modest compared to the variations due to model dependence. In the case of the SUGRA grid, the specific value of  $\epsilon_{SUSY}$  is used for each point, such reducing considerably the uncertainty on  $\epsilon_{SUSY}$ . In this case the uncertainties listed in Table 55, together with the uncertainty associated to the extrapolation to all jet multiplicities (See section “Ratio of  $N_{\bar{t}\bar{t}}$  in 2 more jets sample and all jet multiplicities”) are the only uncertainties considered. For PhenoGrid 2 and 3 and the MSSM lepton grid the dominant systematic uncertainty is always the model dependence. In these cases one could also possibly consider to have  $\epsilon_{SUSY}$  as a function of the point on the SUSY grid.

#### TAGGER EFFICIENCY FOR NON- $t\bar{t}$ STANDARD MODEL PROCESSES

The efficiency of the kinematic top tagger is computed for non- $t\bar{t}$  standard model processes contaminating the signal region. Non- $t\bar{t}$  processes represent only 10% of the signal region backgrounds, thus even a large systematic uncertainty on  $\epsilon_{non-tt}$  has little impact on the overall background uncertainty. The dominating non- $t\bar{t}$  backgrounds are  $Z/\gamma$  and  $W+\text{jets}$ . The value of  $\epsilon_{non-tt}$  on  $Z/\gamma$  is estimated in two ways.

First it is computed in Monte Carlo samples by counting the fraction of top tagged  $Z/\gamma$  events in the signal region. In this case the statistical error on  $\epsilon_{non-tt}$  is large due to insufficient Monte Carlo statistics.

Process	$ee, \mu\mu$	$e\mu$
$Z/\gamma + \text{jets}$	$0.06 \pm 0.06$	$0.38 \pm 0.07$
$W + \text{jets}$		$0.20 \pm 0.18$
$WW$		$0.29 \pm 0.04$
$WZ, ZZ$	$0.14 \pm 0.02$	$0.35 \pm 0.04$

Table 56: Estimated values of  $\epsilon_{non-t\bar{t}}$  for the non- $t\bar{t}$  standard model backgrounds.

The efficiencies are computed on various  $Z/\gamma$  samples generated with ALPGEN, PYTHIA and MC@NLO. The weighted average of the efficiencies over the samples are formed. It is found that  $\epsilon_{non-t\bar{t}}$  is  $0.22 \pm 0.21$  in the dielectron channel,  $0.05 \pm 0.06$  in the di-muon channel and  $0.38 \pm 0.07$  in the electron muon channel.

To circumvent the problem of low statistics, a second method is used. The  $E_T^{\text{miss}}$  spectrum of  $Z/\gamma$  events after all the selections of the signal region except for  $E_T^{\text{miss}} > 100$  GeV, is parameterized in the region  $E_T^{\text{miss}} > 25$  GeV with a falling exponential. A second parameterization is derived for the  $E_T^{\text{miss}}$  spectrum of the top tagged  $Z/\gamma$  events. The ratio of the two parameterizations is then used to predict the efficiency of the kinematic tagger in the region  $E_T^{\text{miss}} > 100$  GeV. This procedure yields  $\epsilon_{non-t\bar{t}}$  consistent within errors with the above mentioned values. It is interesting to note that the value of  $\epsilon_{non-t\bar{t}}$  derived in this way is the same for the dielectron and the dimuon channel and is rather insensitive to the lower bound of the  $E_T^{\text{miss}}$  spectrum considered to derive the parameterization. For this reason we consider a single value of  $\epsilon_{non-t\bar{t}} = 0.06 \pm 0.06$  for both the electron and the muon channels. This technique cannot be straightforwardly applied to the  $Z/\gamma \rightarrow \tau\tau \rightarrow e\mu$  where the  $E_T^{\text{miss}}$  spectrum is harder due to the presence of the neutrinos.

The problem with insufficient Monte Carlo statistics becomes even more pronounced for the determination of  $\epsilon_{non-t\bar{t}}$  on  $W + \text{jets}$  events. Various samples are considered. In total only 5 events are found in the signal region and only one is tagged by the kinematic top tagger, this yields  $\epsilon_{non-t\bar{t}} = 0.2 \pm 0.18$ .

The efficiency of the tagger is also computed on diboson processes on Monte Carlo samples produced with HERWIG. For  $WW$  production one observes that  $\epsilon_{non-t\bar{t}}$  is the same within uncertainties between the dielectron, dimuon and electron muon channels with  $\epsilon_{non-t\bar{t}} = 0.29 \pm 0.04$ . In the case of  $WZ$  and  $ZZ$  production it is found that both processes have similar efficiencies in the dielectron and dimuon channels and significantly higher efficiencies in the electron-muon channel. Table 56 summarizes the values of  $\epsilon_{non-t\bar{t}}$  for the non- $t\bar{t}$  standard model backgrounds.

#### TAGGER EFFICIENCY FOR $t\bar{t}$ EVENTS AND SYSTEMATICS

The efficiency of the tagger for  $t\bar{t}$  events is estimated on Monte Carlo for events which pass all the selections defining the signal region. To take into account the effect of possible discrepancies in the Monte Carlo modelling the effect of a range of systematic uncertainties on  $\epsilon_{tt}$  is estimated. The same systematic uncertainties as those studied in the signal-to-control region ratio method are estimated. The results are summarized in Table 57. The largest uncertainties are the jet energy scale and the amount of Initial/Final State Radiation.

#### RATIO OF $N_{t\bar{t}}$ IN 2 MORE JETS SAMPLE AND ALL JET MULTIPLICITIES

The kinematic top-tagger can only be applied in events with 2 or more jets, while the signal region used in this analysis does not require any specific number of jets. For this reason the matrix method with the kinematic top-tagger is first applied in the subset of the signal region with 2 or more jets. The ratio between the number of  $t\bar{t}$  events with 0 or more jets and with 2 or more jets is derived from the simulation. The uncertainty on this ratio is estimated to 5% after comparing MC@NLO with POWHEG and taking into account jet energy scale systematics and a possible uncertainty of 5% on the jet

Source	Relative uncertainty
Generator	$\pm 3\%$
More ISR/FSR	+6%
Less ISR/FSR	+14%
Parton shower	5%
Jet energy scale $+1\sigma$	-11%
Jet energy scale $-1\sigma$	+11%
Jet energy resolution	$\pm 3\%$

Table 57: The relative systematic uncertainties on  $\epsilon_{tt}$ .

	Data	Monte Carlo
Z region $ee$ channel	$0.25 \pm 0.03$	$0.31 \pm 0.03$
Z region $\mu\mu$ channel	$0.29 \pm 0.02$	$0.30 \pm 0.03$
Top region $ee$ channel	$0.64 \pm 0.15$	$0.71 \pm 0.08$
Top region $\mu\mu$ channel	$0.50 \pm 0.13$	$0.70 \pm 0.06$
Top region $e\mu$ with $e$ trigger channel	$0.85 \pm 0.10$	$0.72 \pm 0.08$
Top region $e\mu$ with $\mu$ trigger channel	$0.67 \pm 0.16$	$0.72 \pm 0.09$

Table 58: Comparison of the fraction of events passing the kinematic top-tagger in data and Monte Carlo in the “Z region” and the “Top region” defined in the text. Errors are statistical only.

reconstruction efficiency. This uncertainty on the ratio between the number of  $t\bar{t}$  events with 0 or more jets and with 2 or more jets is propagated to the total uncertainty on the predicted number of  $t\bar{t}$  events in the signal region.

#### VALIDATION OF THE KINEMATIC TAGGER EFFICIENCY WITH DATA

Although the efficiencies of the tagger for SUSY and  $t\bar{t}$  events are taken from Monte Carlo, one can check in data samples with larger statistics than the signal region that the efficiency of the tagger is in agreement with that of the Monte Carlo. Two control regions are defined, a “Z region” selected by requiring two jets and the invariant mass of the two leptons to be within 10 GeV of the Z mass and a “Top region” selected by requiring two jets,  $E_T^{\text{miss}} > 30$  GeV and with the lepton invariant mass at least 10 GeV away from the Z mass. The fraction of top-tagged events in each of these regions is computed and compared between data and Monte Carlo. The results are shown in Table 58 and it appears that for the 6 regions considered, all data-Monte Carlo deviations are less than  $1.5\sigma$ . Therefore one concludes that the efficiency of the tagger is reasonably well modelled by the Monte Carlo.

#### CLOSURE TEST

To test the method and check that it does not introduce a bias it is applied to a mix of Monte Carlo samples representing the various Standard Model processes in the control region. Both cases where SUSY is present or absent are considered. The closure tests are carried out for the four considered SUSY model grids, namely the MSSM lepton grid, the Pheno Grids 2 and 3 and the SUGRA grid described earlier.

Figure 87 shows the predicted number of  $t\bar{t}$  events in the plane  $M_0$ ,  $M_{1/2}$ , for the three channels dielectron, dimuon and electron-muon summed up and for an integrated luminosity of  $35 \text{ pb}^{-1}$ . Figure 88 shows the total uncertainty on this prediction. The uncertainty arises from the systematic uncertainties on  $\epsilon_{SUSY}$  and  $\epsilon_t$  discussed in the earlier subsections and from the limited statistics in the signal region. The limited statistics of the signal region is the dominant source of uncertainty on the data driven prediction.

At each SUGRA point the value of  $\epsilon_{SUSY}$  specific that point is used. The non- $t\bar{t}$  backgrounds are simply treated by assuming that  $\epsilon_{non-t\bar{t}} = \epsilon_{SUSY}$ . The true number of  $t\bar{t}$  events predicted by the Monte Carlo is 31.6. Given the uncertainties on the  $t\bar{t}$  prediction given in Fig. 88 one can see that the predicted value is always consistent within errors with the true value.

One should note that there are two regions of parameter space where SUSY events are so top-like that the data driven method can no longer differentiate between  $t\bar{t}$  and SUSY. These regions consist of i) a wedge shape area in the  $M_0, M_{1/2}$  plane located around  $(M_0, M_{1/2}) \sim (300, 120)$  GeV and ii) a band with  $M_{1/2} < 150$  GeV.

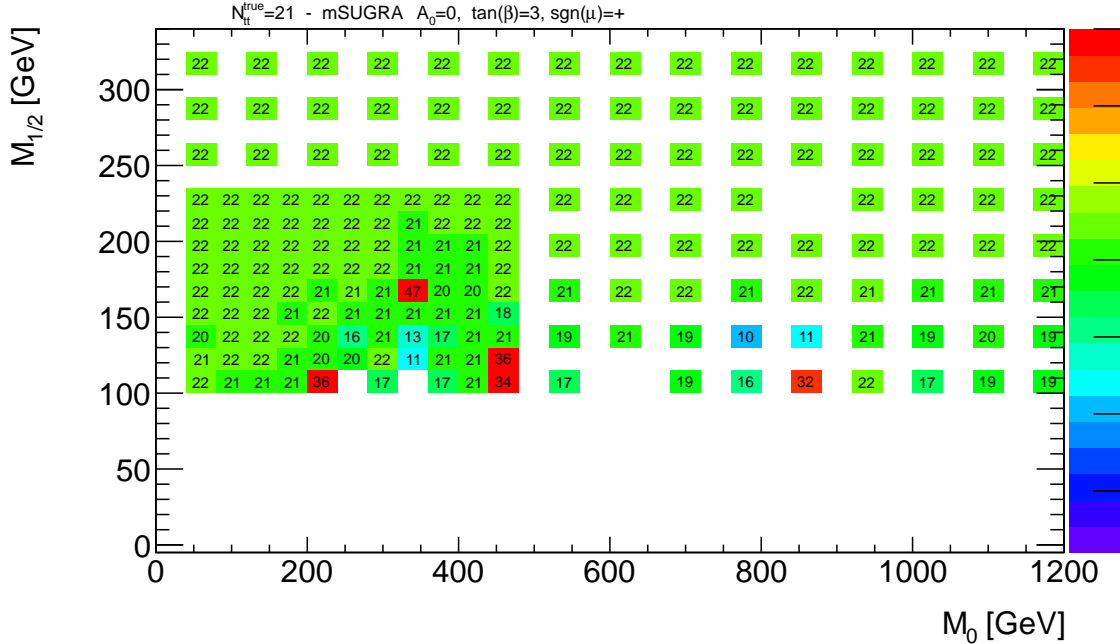


Figure 87: The predicted number of  $t\bar{t}$  events in the dielectron, dimuon and electron-muon channels for  $35 \text{ pb}^{-1}$ , in the signal region, as obtained by the matrix method with the kinematic tagger. The expected prediction from Monte Carlo only is 21 events.

The closure test is also performed on the MSSM one lepton grid. Table 59 shows the result of the matrix method with the kinematic tagger applied on the Monte Carlo using Point 29 of the MSSM24 grid for events with at least two jets. In this case the generic value of  $\epsilon_{SUSY} = 0.2 \pm 0.2$  was used. The predicted number of  $t\bar{t}$  events is within errors in agreement with the true number of  $t\bar{t}$  events.

## RESULTS

The matrix method with kinematic tagger is applied to the ATLAS data for period E to I. The Opposite Sign analysis has 4, 13 and 13 candidates in the  $ee$ ,  $e\mu$  and  $\mu\mu$  analyses respectively. In the sample with two jets with  $p_T > 20$  GeV these event yields reduce to 4, 11 and 7 events. Finally it is found that the number of events tagged by the kinematic tagger are 3, 6 and 4 in the  $ee$ ,  $e\mu$  and  $\mu\mu$  final states. The resulting data driven prediction of the number of  $t\bar{t}$  events in the signal region (zero or more jets) is given in Fig. 89 and the corresponding total uncertainty is given in Fig. 90. For a large portion of parameter space this data driven estimate of the  $t\bar{t}$  background yields about 22-23 events with an uncertainty of 5-6 events. We conclude that the sample is fully consistent with the hypothesis of being entirely from  $t\bar{t}$  production.

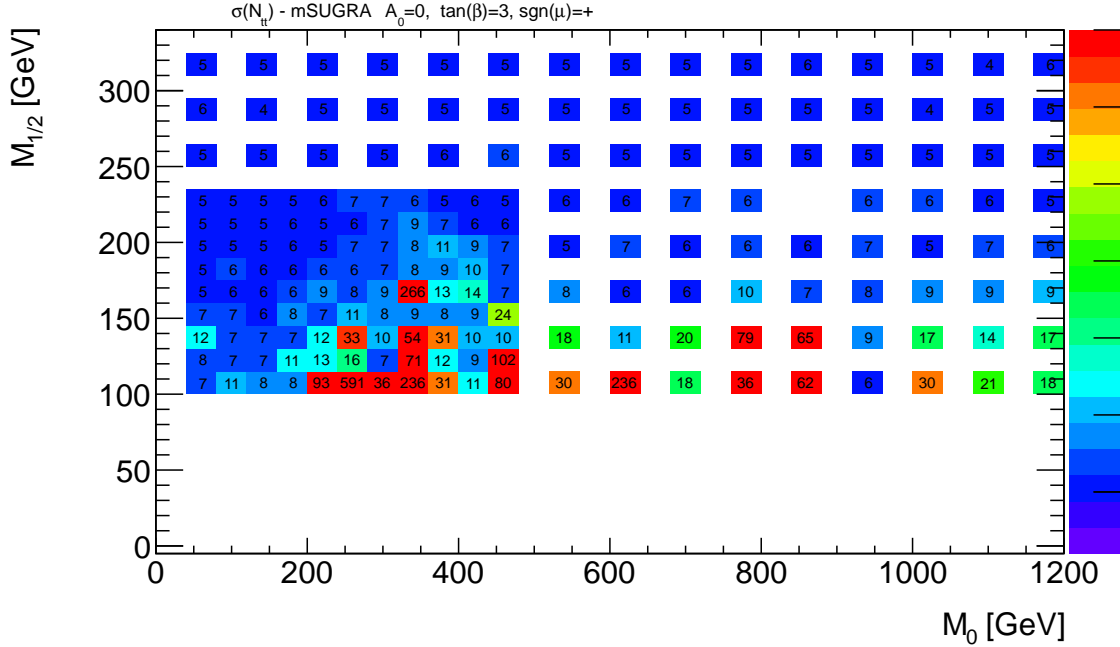


Figure 88: The total uncertainty on the predicted number of  $t\bar{t}$  events in the dielectron, dimuon and electron muon channels for  $35 \text{ pb}^{-1}$ , using the matrix method with the kinematic tagger.

$N_{tt}$	True	No SUSY		MSSM29	MSSM29
				Specific $\epsilon_{SUSY}$	Generic $\epsilon_{SUSY}$
$ee$	3.4	3.4±1.4		3.6±2.1	1.5±10.8
$\mu\mu$	6.6	6.6±2.1		6.0±3.0	2.4±17.8
$e\mu$	9.7	9.8±2.7		10.1±3.1	8.8±7.8

Table 59: True (2nd column) and predicted number of  $t\bar{t}$  events (3rd to 5th columns) for an integrated luminosity of  $35 \text{ pb}^{-1}$  in the three OS dilepton channels, with the additional requirement of the presence of 2 jets. The 3rd column illustrates the result of the matrix method with the top tagger when no SUSY events are present and using the value  $\epsilon_{SUSY} = 0.2 \pm 0.18$  which applies PhenoGrid 2 and PhenoGrid 3. The 4th column shows the result of the matrix method in the case of the presence of SUSY from the MSSM29 model when the value of  $\epsilon_{SUSY}$  used is that of MSSM29. Finally the last column gives the results in the presence of MSSM29 SUSY and for the generic value of  $\epsilon_{SUSY} = 0.2 \pm 0.18$ . The errors include both statistics and systematics. In the case of the generic value of  $\epsilon_{SUSY}$  an additional uncertainty from model dependence is also taken into account.

The SUSY limit setting can be performed with a particular  $N_{t\bar{t}}$  for each SUSY grid point and each value can have its own uncertainty. In regions of the SUSY grid where  $\epsilon_{SUSY} \sim \epsilon_{tt}$  the method does not work anymore. Practically the uncertainty on the  $t\bar{t}$  becomes so large that the sensitivity to a potential SUSY signal is null. This naturally happens in region of parameter space where SUSY events are very  $t\bar{t}$  like. In such a situation it is very difficult if not impossible to make a data driven estimate of the  $t\bar{t}$  background using the signal region. In such a situation the SUSY events would be so  $t\bar{t}$  like that they would likely fall into the standard  $t\bar{t}$  analysis and lead to an increased  $t\bar{t}$  cross section or  $t\bar{t}$  modified differential cross section. Such SUSY could be detected by studying the detailed kinematic properties of  $t\bar{t}$  sample and would lead to deviation from Standard Model prediction of quantities such as the top boost.

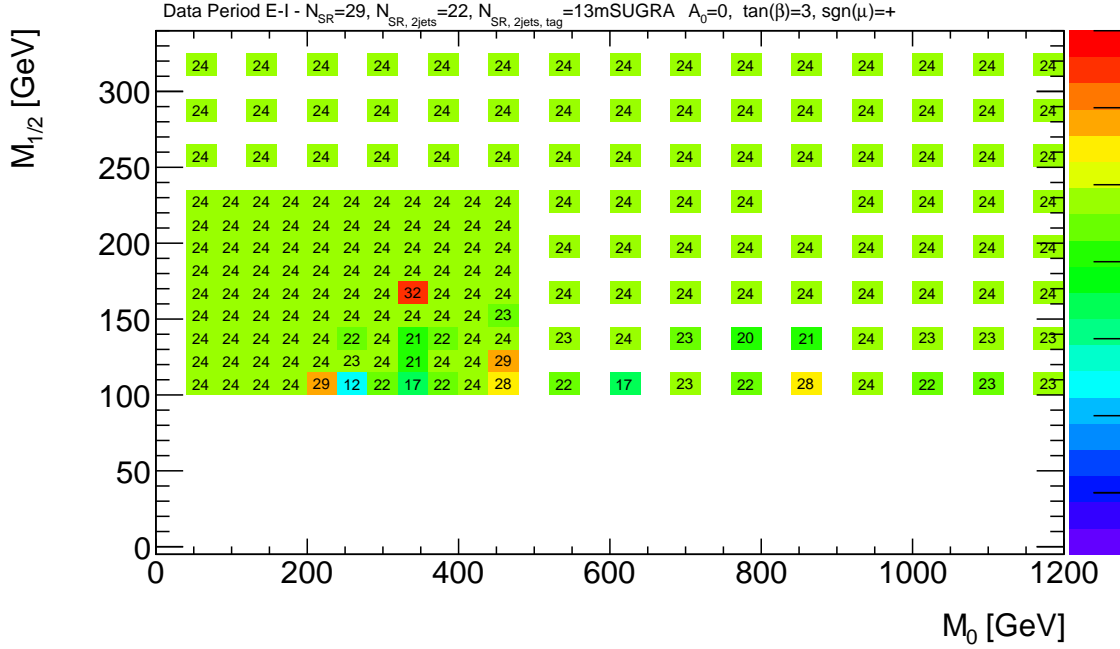


Figure 89: The data driven prediction of the number of  $t\bar{t}$  events in the dielectron, dimuon and electron-muon channels given the data of period E to I, as obtained by the matrix method with the kinematic tagger.

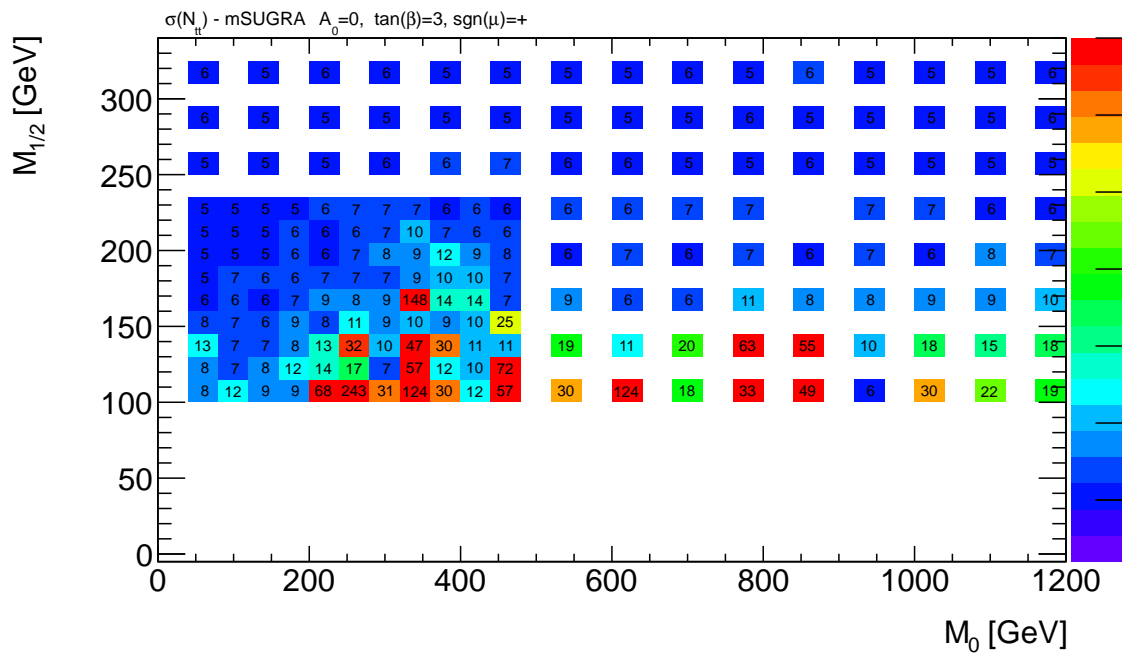


Figure 90: The total uncertainty on the data driven prediction of the number of  $t\bar{t}$  events in the dielectron, dimuon and electron muon channels given the data of period E-I, using the matrix method with the kinematic tagger.